Modeling and Simulation of Vibration in Deviated Wells

By

© Mejbahul Sarker, B. Eng., M. Eng.

A Thesis submitted to the School of Graduate Studies

in partial fulfillment of the requirement for the degree of

Doctor of Philosophy

Faculty of Engineering and Applied Science

Memorial University of Newfoundland

May, 2017

St. John's Newfoundland and Labrador Canada

Modeling and Simulation of Vibration in Deviated Wells

© Copyright 2016
Mejbahul Sarker
All rights reserved

Abstract

Modeling and Simulation of Vibration in Deviated Wells

by

Mejbahul Sarker

Doctor of Philosophy in Oil and Gas Engineering

Memorial University of Newfoundland, St. John's, NL

Thesis Supervisor: Dr. Geoff Rideout and Dr. Stephen Butt

During the engineering of deviated well, drillstring is in the complicated moving state, strong vibration is the main reason that induces drillstring failure. Drillstring vibrations usually have axial vibration, lateral vibration, torsional vibration and the drillstring near the bottom of well usually coupled vibrates strongly. A dynamic model to predict the effect of drillstring parameters on the type and severity of vibration is desired by the oil industry, to understand and prevent conditions that lead to costly downhole tool failures and expensive tripping or removal of the string from the wellbore. High-fidelity prediction of lateral vibrations is required due to its coupling with potentially destructive axial and torsional vibration.

This research work analyses the dynamics of a horizontal oilwell drillstring. In this dynamics, the friction forces between the drillstring and the borehole are relevant and uncertain. Drillstring contact with its borehole, which can occur continuously over a line of contact for horizontal shafts such as drillstrings, generates normal forces using a user-definable stiff spring constitutive law. Tangential contact forces due to friction between the

drillstring and borehole must be generated in order for whirl to occur. The potential for backward whirl and stick-slip requires the transition between static and dynamic Coulomb friction. The proposed model computes the relative velocity between sliding surfaces when contact occurs, and enforces a rolling-without-slip constraint as the velocity approaches zero. When the surfaces become 'stuck', a force larger than the maximum possible static friction force is required to break the surfaces loose, allowing sliding to resume.

The drillstring bottom-hole-assembly has been modeled using a three-dimensional multibody dynamics approach implemented in vector bond graphs. Rigid lumped segments with 6 degrees of freedom are connected by axial, torsional, shear, and bending springs to approximate continuous system response. Parasitic springs and dampers are used to enforce boundary conditions. A complete deviated drillstring has been simulated by combining the bottom-hole-assembly model with a model of drill pipe and collars. The pipe and collars are modeled using a lumped-segment approach that predict axial and torsional motions.

The proposed dynamic model has been incorporated the lumped segment approach which has been validated with finite element representation of shafts. Finally, the proposed contact and friction model have been validated using finite element LS-DYNA® commercial software.

The model can predict how axial and torsional bit-rock reactions are propagated to the surface, and the role that lateral vibrations near the bit plays in exciting those vibrations and stressing components in the bottom-hole-assembly. The proposed model includes the mutual dependence of these vibrations, which arises due to bit-rock interaction and friction dynamics between drillstring and wellbore wall.

The model can simulate the downhole axial vibration tool (or Agitator®). Simulation results show a better weight transfer to the bit, with a low frequency and high amplitude force excitation giving best performance but can increase the severity of lateral shock. The uniqueness of this proposed work lies in developing an efficient yet predictive dynamic model for a deviated drillstring.

Indexing terms: horizontal drilling, bottom-hole-assembly, wellbore friction, bit-rock interaction, rate of penetration, bond graph, multibody dynamics, finite element, vibration, downhole tool.

Acknowledgments

I would like to thank several people for making the success of this thesis possible. First, I must express my deepest gratitude to my supervisor, Dr. Geoff Rideout, for his professional supervision, critical discussions and immeasurable contributions. Without his encouragement and ideas this work would have never been completed.

I would like to thank my supervisor, Dr. Stephen Butt for having me in his laboratory. When I first came to MUN, I was a fresh college graduate and rather a theory-minded person. He trained and guided me to think how to explore the knowledge in the petroleum engineering application. Now I always think how better research can be made to tackle problems facing petroleum industries. To him also belongs the credit for proposing the research project and attracting several sources of funding.

I would like to thank my colleagues in the Advance Drilling Laboratory at MUN for their continuous help with matters of drilling research challenges.

I would also like to thank the Atlantic Canada Opportunity Agency (AIF Contract no. 781-2636-1920044), Husky Energy, and Suncor Energy for funding this research. Finally, I wish to thank the Faculty of Engineering and Applied Science at Memorial University for financial support.

Dedicated to my parents

Note on the Units of Measurements

Throughout this thesis, S.I. and imperial units of measurements are used. Where appropriate and possible however, the S.I. metric equivalent of imperial units have been provided. The reason for adopting imperial units is justified by the following:

1. This work is oriented towards technical advances in the drilling industry. However, the drilling industry worldwide commonly in the United States where imperial units uses.

2. Most drilling equipment conforms to API standards which recently are generally in non-S.I. units. Issues like thread size, pipe dimensions, pressure gauges etc. will likely continue to be based on traditional units since it is too entrenched in the industry. As well, the traditional units are a mixture of imperial (weight, length) and American (1 usg = 3.785 L and 1 short ton = 2000 lbs).

3. The majority of previous publications relating to the thesis research were in imperial units.

On this basis, it was decided to maintain imperial units for all subsequent data presentation and calculations. The following page provides a Table of Conversion for imperial units to their metric equivalents.

TABLE OF CONVERSION; IMPERIAL TO METRIC

Imperial	Multiplying factor	Metric
feet	0.3048	m
in	25.4	mm
ft/hr	0.3048	m/hr
psi	0.0069	MPa
lb mass	0.4536	kg
rev/min (rpm)	0.1047	rad/s
ft-lb	1.36	N.m

Table of contents

Abstract i
Acknowledgments iv
Note on the Units of Measurements vi
Table of contents viii
List of figures xi
List of tables xix
List of symbols xx
1 Introduction 1
1.1 Motivation 1
1.2 Background 2
1.3 Problem statement 4
1.4 Objectives 4
1.5 Scope of research 5
1.6 Research methodology 6
2 A Review of Vibration Issues in Deviated Wellbores 9
2.1 Deviated drilling technology 9
2.2 Review of deviated drilling dynamic failures 13
3 A Lumped Segment Based Modeling Approach for Axial and Torsional Motions of Vertical Drillstring 25
3.1 Introduction 25
3.1.1 Vertical wells and the increasingly important role of stick-slip 25
3.1.2 Review of drillstring torsional vibration and coupled axial-torsional vibration models 27
3.1.3 Chapter outline 32
3.2 Bond graph overview 33
3.2.1 Bond graph modeling formalism 34
3.3 Modeling of top drive motor dynamics 37

3.4 Modeling of drillstring axial dynamics 45
3.5 Modeling of drillstring torsional dynamics 51
3.6 Bit-rock interaction model 54
3.7 A demonstration of vertical well 57
4 A Model of Quasi Static Wellbore Friction – Application to Horizontal Oilwell Drilling Simulation 74
4.1 Introduction 74
4.1.1 Torque and drag issues in deviated wells 74
4.1.2 Review on work with wellbore friction models 75
4.1.3 Chapter outline 85
4.2 Modeling of stick-slip friction phenomena 86
4.2.1 Validation with finite element friction model 91
4.3 Normal contact force for wellbore friction 95
4.3.1 Horizontal section of drillstring 98
4.4 Modeling of drillstring segment motions 99
4.5 Modified bit-rock interaction model 105
4.6 Tuning of friction factor 107
4.6.1 Horizontal well field data 107
4.6.2 Selection of friction factor 112
4.7 Experimental characterization of downhole tool 116
4.8 Simulation of horizontal drillstring with downhole tool 122
5 A 3D Multibody System Approach for Horizontal Oilwell BHA Vibration Modeling 131
5.1 Introduction 131
5.2 Effectiveness of three-dimensional multi-body modeling approach for shaft dynamic modeling 134
5.2.1 Multi-body bond graph model description 135
5.2.2 Case study – pipe deflection 140
5.2.3 Case study – pipe rotor dynamics 143
5.3 Modeling drillstring-wellbore contact-friction 147
5.3.1 Case study – contact force 150
5.3.2 Case study – rolling motion 153
5.4 Multi-body bond graph simulation of buckling of pipes inside wellbore 155

5.5 Demonstration of complete horizontal model 160
5.5.1 Simulation results 162
6 Conclusions and Further Work 177
6.1 Thesis summary 177
6.2 Summary of main results 179
6.3 Future work 181
6.3.1 Experimentally determine parameters for bit-rock interaction models 181
6.3.2 Experimentally validation of drillstring buckling model in curved/horizontal wellbore 182
6.3.3 Experimentally determination of pipe-borehole friction factor in horizontal drilling with a bed of cuttings 184
6.3.4 Extension of the horizontal drillstring model to predict the fatigue in horizontal wells 185
6.3.5 Experimentally determine parameters for downhole mud motor model 185
6.3.6 Extension of vertical drillstring model to include the effect of riser buckling on offshore drilling dynamics. 186
6.3.7 Experimentally determine parameters for axial excitation tool model 187
6.3.8 Validate the complete horizontal drilling dynamic simulator with MWD field data 187
6.4 Application for this work 188
6.5 Final word 188
References 190
Appendix A: Well information 200
Appendix B: Simulation data 202
Appendix C: 20Sim® model programming codes 203
Appendix D: LS-DYNA® model programming codes 222

List of figures

Figure 2.1: Wytch Farm ERD well (http://frackland.blogspot.ca/2014/01/extended-reach drilling.html). 10

Figure 2.2: Modern multilateral well application (https://www.slb.com/resources). 10

Figure 2.3: Sketch of mud motor assembly (http://primehorizontal.com/drilling-tools). 12

Figure 2.4: Sketch of (a) simple power pack steerable assembly and (b) power drive RSS (Downton et al., 2000). 12

Figure 2.5: Sketch of directional drilling with mud motor (red trajectory) and RSS (black trajectory) (Downton et al., 2000). 13

Figure 2.6: Sketch of (a) modes of drillstring vibration (www.bakerhughes.com) and (b) two modes of lateral vibration (Bailey et al., 2008). 14

Figure 2.7: Cracked drillpipe tool joints (Amro, 2000). 16

Figure 2.8: Photo of fatigue failures (Bert et al., 2007). 17

Figure 2.9: Photo of drill bit and tool failures (Akinniranye et al., 2009). 19

Figure 2.10: Fracture of the drillpipe twistoff (Raap et al., 2012). 19

Figure 2.11: Initial and final placement of each DDDR sensor from start of the run (at 9258 ft) to end of the run (at 10524 ft) (D'Ambrosio et al., 2012). 21

Figure 2.12: Stick-slip vibration comparison (Jerz and Tilley, 2014). 22

Figure 2.13: Photos of damaged and worn out drill bits, stabilizers (Wright et al., 2014). 23

Figure 3.1: Sketch of Kharaib reservoir layer in Qatar's Idd El Shargi field. (www.slb.com/~ /media/Files/resources). 26

Figure 3.2: Sketch of vertical oilwell drilling system (Leine et al., 2002). 27

Figure 3.3: Schematic used by Yigit and Christoforou (2006) 29

Figure 3.4: (a) Simplified model used by Richard et al. (2004), (b) simplified model used by Zamanian et al. (2007). 31

Figure 3.5: A physical sketch of three phase induction motor (http://www.learningelectronics.net) 37

Figure 3.6: Equivalent circuit of an induction motor in (a) α axis and (b) β axis 38

Figure 3.7: A sketch of induction motor different coordinate systems 38

Figure 3.8: I-field Relations and causalities for the rotor and the stator in the α-β axis 39

Figure 3. 9: Gyrator structure for torque and induced voltages 40

Figure 3.10: Bond graph model of an Induction motor 41

Figure 3.11: Phase lags between the three phase input voltage. 42

Figure 3.12: Input voltage V_a plot 42

Figure 3.13: Input voltage V_b plot 42

Figure 3.14: Input voltage V_c plot 42

Figure 3.15: Current i_a of the induction motor 43

Figure 3.16: Current i_b of the induction motor 43

Figure 3.17: Current i_c of the induction motor. 43

Figure 3.18: Electromagnetic torque of the induction motor at no load. 43

Figure 3.19: Run-up response of the induction motor at no load. 44

Figure 3.20: Torque of the induction motor at no load. 44

Figure 3.21: Schematic of drillstring used in rotary drilling modeling and simulation 48

Figure 3.22: Schematic of kelly axial segment 48

Figure 3.23: Bond graph axial model segment of kelly 49

Figure 3.24: Schematic of drill pipe/collar lumped segment model showing drilling fluid flow. 49

Figure 3.25: Schematic of drill pipe/collar axial segment model. 50

Figure 3.26: Bond graph axial model segment of drill pipe/collar 50

Figure 3.27: Schematic of kelly torsional segment 52

Figure 3.28: Bond graph torsional model segment of kelly 53

Figure 3.29: Schematic of drill pipe/collar torsional segment 53

Figure 3.30: Bond graph torsional model segment of drill pipe/collar 53

Figure 3.31: sketches show (a) a lobe pattern of formation surface elevation (courtesy of A. Scovil Murray), (b) bit and rock spring-damper representation when x < s and (c) bit contacts with rock when x > s and rock spring and damper under compression and generates a applied upward force to drillstring. 55

Figure 3.32: Bond graph model for vertical section of CNRL HZ Septimus C9-21-81-19 well.. 61

Figure 3.33: Simulation plots of top drive speed, mud motor speed and weight on bit. 62

Figure 3.34: Simulation plots of bit speed, surface torque and mud flow rate. 63

Figure 3.35: Zoom in plot of mud flow rate. 63

Figure 3.36: Axial force distribution plots in DP segments from one to four at 6.28 rad/sec top drive speed with 8.48 rad/sec downhole mud motor speed and 100kN applied WOB. 64

Figure 3.37: Axial force distribution plots in DP segments from four to eight at 6.28 rad/sec top drive speed with 8.48 rad/sec downhole mud motor speed and 100kN applied WOB. 65

Figure 3.38: Axial force distribution plots in DP segments from nine to ten and HWDP segments from one to two at 6.28 rad/sec top drive speed with 8.48 rad/sec downhole mud motor speed and 100kN applied WOB. 66

Figure 3.39: Axial force distribution plots in HWDP segments from three to six at 6.28 rad/sec top drive speed with 8.48 rad/sec downhole mud motor speed and 100kN applied WOB.... 67

Figure 3.40: Axial force distribution plots in HWDP segments from seven to ten at 6.28 rad/sec top drive speed with 8.48 rad/sec downhole mud motor speed and 100kN applied WOB.... 68

Figure 3.41: Simulation plots of bit speed and surface torque for different bit cutting coefficients at 6.28 rad/sec top drive speed with 8.48 rad/sec downhole mud motor speed and 100kN applied WOB. 69

Figure 3.42: High stick-slip vibrations at 6.28 rad/sec top drive speed without using downhole mud motor and 100 kN applied WOB. 70

Figure 3.43: Stick-slip eliminated by increasing the top drive speed to 14 rad/sec at 100 kN applied WOB without using downhole mud motor. 71

Figure 3.44: Stick-slip eliminated by lowering the applied WOB to 50kN at 6.28 rad/sec top drive speed without using downhole mud motor. 72

Figure 4.1: Sketch of force balance on the drillstring curved element illustrating sources of normal force (left side) and forces acting on drillstring curved element during pickup (Johansick et al., 1984). 76

Figure 4.2: Physical schematic of stick-phase. 88

Figure 4.3: Physical schematic of slip-phase. 89

Figure 4.4: (a) sketch of the system and (b) Bond graph model of the friction-element with system 89

Figure 4.5: Simulation results for the mass-surface system, F(t) = 35sin(50t) N. 90

Figure 4.6: Simulation results for the mass-surface system, F(t) = 25sin(50t) N. 90

Figure 4.7: Simulation results for the mass-surface system, F(t) = 40sin(50t) N. 90

Figure 4.8: Physical geometry of the LS-DYNA® model. 92

Figure 4.9: Transition from static to dynamic friction (adapted from LS-DYNA® manual). 93

Figure 4.10: Solid cube velocity at 35Sin(50t) N applied force. 93

Figure 4.11: Acting friction force at 35Sin(50t) N applied force. 93

Figure 4.12: Solid cube velocity at higher amplitude applied forces. 94

Figure 4.13: Physical sketch (left) and normal contact forces (right) of drillstring segments in the build section. 96

Figure 4.14: (a) Physical sketch of drillstring contact with wellbore and (b) Free body diagram of curved drillstring segment when tension dominates weight. 96

Figure 4.15: (a) Physical sketch of drillstring contact with wellbore and (b) Free body diagram of curved drillstring segment when weight dominates tension. 97

Figure 4.16: (a) Physical sketch of drillstring contact with wellbore and (b) Free body diagram of curved drillstring segment when segment under compression. 97

Figure 4.17: Schematic of (a) drillpipes axial lumped segment model showing drilling fluid flow and (b) free body diagram of axial segment of build (curved) section of drillstring. 102

Figure 4.18: Schematic of (a) drillpipe contact force when drillpipe touches upper portion of wellbore and (b) free body diagram of torsional segment of build (curved) section of drillstring. 102

Figure 4.19: Bond graph segment model for (a) longitudinal (or axial) and (b) torsional motions of build (curved) section of drillstring. 103

Figure 4.20: Schematic of (a) drillpipes axial lumped segment model showing drilling fluid flow and (b) free body diagram of axial segment of horizontal section of drillstring. 103

Figure 4.21: Schematic of (a) drillpipe contact force and (b) free body diagram of torsional segment of horizontal section of drillstring. 104

Figure 4.22: Bond graph segment model for (a) longitudinal (or axial) and (b) torsional motions of horizontal section of drillstring. 104

Figure 4.23: sketches show (a) a lobe pattern of formation surface elevation, and (b) bit and rock spring-damper representation when x < p and (c) bit contact with rock when x >= p rock sping and damper under compression. 106

Figure 4.24: Bond graph model of bit-rock motion 106

Figure 4.25: Measured depth vs. drilling day of CNRL HZ Septimus C9-21-81-19 well. 109

Figure 4.26: Average ROP vs. drilling day of CNRL HZ Septimus C9-21-81-19 well. 109

Figure 4.27: Static weight vs. depth of CNRL HZ Septimus C9-21-81-19 well. 110

Figure 4.28: Drag force vs. depth of CNRL HZ Septimus C9-21-81-19 well..... 110

Figure 4.29: Off-bottom torque vs. depth of CNRL HZ Septimus C9-21-81-19 well. 111

Figure 4. 30: On- bottom torque vs. depth of CNRL HZ Septimus C9-21-81-19 well..... 111

Figure 4. 31: Static weight vs. depth of the model of CNRL HZ Septimus C9-21-81-19 well.. 114

Figure 4.32: Upward motion drag force vs. depth of the model of CNRL HZ Septimus C9-21-81-19 well. 114

Figure 4.33: Downward motion drag force vs. depth of the model of CNRL HZ Septimus C9-21-81-19 well. 115

Figure 4.34: Off-bottom torque vs. depth of the model of CNRL HZ Septimus C9-21-81-19 well. 115

Figure 4.35: Testing frame and associated pumping facility in Advanced Drilling Laboratory at MUN..... 117

Figure 4.36: (a) load cells, (b) upstream pressure sensor and (c) downstream pressure sensor used in testing frame in Advanced Drilling Laboratory at MUN..... 118

Figure 4.37: Mobile DAQ system in Advanced Drilling Laboratory at MUN..... 118

Figure 4.38: Inlet pressure fluctuation at 70 gpm flow rate. 119

Figure 4.39: Outlet pressure fluctuation at 70 gpm flow rate..... 119

Figure 4.40: Axial force profile generated from Agitator® tool at 70 gpm flow rate..... 120

Figure 4.41: Spectrum of tool generated force at 70 gpm flow rate. 120

Figure 4.42: Frequency vs. flow rate of Agitator® tool..... 121

Figure 4.43: Pressure drop vs. flow rate of Agitator® tool. 121

Figure 4.44: The top drive speed, mud motor speed and WOB for the case of without and with axial excitation source (AES) 124

Figure 4.45: The surface torque, bit speed and ROP for the case of without and with AES..... 125

Figure 4.46: The axial excitation force, displacements at different locations for the case of without and with AES. 126

Figure 4.47: Axial forces at different locations for the case of without and with AES. 127

Figure 4.48: The AES segment displacements for different amplitudes and frequencies of applied forces..... 127

Figure 4.49: The displacements of 950 m behind bit segment for different amplitudes and frequencies of applied forces. 128

Figure 4.50: The displacements of 350 m behind bit segment for different amplitudes and frequencies of applied forces. 128

Figure 4.51: WOB results for different amplitudes and frequencies of applied forces. 129

Figure 4.52: ROP results for different amplitudes and frequencies of applied forces. 129

Figure 5.1: Successive multibody segments 136

Figure 5.2: Body i bond graph (Rideout et al., 2013) 139

Figure 5.3: Joint i bond graph (Rideout et al., 2013) 140

Figure 5.4: Sketch of pipe geometry 141

Figure 5.5: Load-deflection comparison between LS-DYNA® and 20Sim®. 143

Figure 5.6: A rotating pipe model with an eccentric mass in LS-DYNA®. 144

Figure 5.7: Eccentric mass bond graph modeling. 145

Figure 5.8: The x-displacement of disk center. 145

Figure 5.9: The disk center whirling orbit. 146

Figure 5.10: The disk center state-space (displacement vs. velocity). 146

Figure 5.11: Physical schematic of contact and friction. 148

Figure 5.12: Bond graph model for drillstring-wellbore contact and friction.. 149

Figure 5.13: Sketch of LS-DYNA® contact model geometry. 150

Figure 5.14: Contact forces results. 151

Figure 5.15: Errors in 20Sim® results compared to LS-DYNA® model. 152

Figure 5.16: Sketch of LS-DYNA® contact model geometry. 153

Figure 5.17: The shaft center whirling orbit for different applied torque. 154

Figure 5.18: Sketch of the buckling test case. 156

Figure 5.19: Pipe inside wellbore model in LS-DYNA®. 156

Figure 5.20: Sinusoidal buckling (snaking motion) animation. 157

Figure 5.21: Helical buckling (whirling motion) animation. 157

Figure 5.22: The x-displacement of pipe center at 50 m length distance when 150 kN applied load and 16 rad/sec rotation speed. 158

Figure 5.23: The trajectory of pipe center at 50 m length distance when 150 kN applied load and 16 rad/sec rotation speed. 158

Figure 5.24: The x-displacement of pipe center at 50 m length distance when 200 kN applied load and 16 rad/sec rotation speed. 158

Figure 5.25: The trajectory of pipe center at 50 m length distance when 200 kN applied load and 16 rad/sec rotation speed. 159

Figure 5.26: Schematic of the horizontal drillstring for simulation. 162

Figure 5.27: Simulation plots of top drive speed, mud motor speed and dynamic WOB. 163

Figure 5.28: Simulation plots of bit speed, surface torque and instantaneous ROP. 164

Figure 5.29: The trajectory of drill bit center 165

Figure 5.30: The trajectory of motor HS center at 4 m behind bit. 165

Figure 5.31: The trajectory of collar center at 17 m behind bit. 166

Figure 5.32: The trajectory of collar center at 28 m behind bit. 166

Figure 5.33: Whirl speed at bit, 4 m behind bit (motor HS), 17 m and 28 m behind bit (collar). 167

Figure 5.34: Contact force at bit, 4 m behind bit (motor HS), 17 m and 28 m behind bit (collar). 167

Figure 5.35: Animation plot of BHA in 20Sim®. 168

Figure 5.36: Top drive speed, mud motor speed and WOB for the case of without and with AES, 100sin(125t) kN. 170

Figure 5.37: Surface torque, bit speed and ROP for the case of without and with AES, 100sin(125t) kN. 170

Figure 5.38: WOB, surface torque and ROP for different amplitudes and frequencies of AES force. 171

Figure 5.39: Axial force at 17 m and 28 m behind bit segments for the case of without and with AES. 171

Figure 5.40: The trajectory of bit center for different amplitudes and frequencies of AES force. 172

Figure 5.41: The trajectory of mud motor center at 4 m behind bit for different amplitudes and frequencies of AES force. 172

Figure 5.42: The trajectory of collar center at 17 m behind bit for different amplitudes and frequencies of AES force. 173

Figure 5.43: The trajectory of collar center at 28 m behind bit for different amplitudes and frequencies of AES force. 173

Figure 5.44: Contact force at bit for different amplitudes and frequencies of AES force. 174

Figure 5.45: Contact force at 4 m behind bit (motor HS) for different amplitudes and frequencies of AES force. 174

Figure 5.46: Contact force at 17 m behind bit (collar) for different amplitudes and frequencies of AES force. 175

Figure 5.47: Contact force at 28 m behind bit (collar) for different amplitudes and frequencies of AES force. 175

Figure A.1: Sketch of well profile 200

Figure A.2: Drillstring configurations in different depths. 201

List of tables

Table 3.1: Generalized bond graph quantities (Rideout et al. 2008)..... 35

Table 3.2: Bond graph elements (Rideout et al. 2008)..... 36

Table 3.3: Section of cutting coefficient (6.28 rad/s top drive speed, 8.48 rad/s downhole mud motor speed and 100 kN applied WOB) 59

Table 5.1: Natural frequencies comparison chart 142

Table 5.2: Summary of the lumped segments for section one 161

Table 5.3: Summary of the multibody segments for section two..... 161

Table A.1: Drillstring configuration chart 201

Table B.1: Data used in vertical rotary drilling simulation. 202

List of symbols

A = Cross sectional area, m^2

b = bit factor

C_d = Frictional damping, N-s/m

C_i = Segment i compliance, m/N

C_{i-1} = Segment i-1 compliance, m/N

dx = DP or DC segment length, m

DC = Decay constant

E = Elastic modulus, N/m^2

f = Frequency, Hz

F_A = The drag force on the drillstring due to flow in the annulus, N

F_c = Compressive force acting in the curved segment, N

F_f = Friction force acting in the curved segment, N

F_i = Segment i force, N

F_{i-1} = Segment i-1 force, N

F_n = Normal force, N

F_P = The drag force on the drillstring due to flow in the DP, N

F_t = Tension force acting in the curved segment, N

ΔF_t = Increment of tension force, N

F_w = Contact force matrix, N

I = Area moment of inertia, m^4

$I_{s\alpha}$ = The α-axis stator current, amp

$I_{s\beta}$ = The β-axis stator current, amp

$I_{r\alpha}$ = The α-axis rotor current, amp

$I_{r\beta}$ = The β-axis rotor current, amp

J_i = Segment i mass inertia, kg-m^2

J_{i-1} = Segment i-1 mass inertia, kg-m^2

J_m = Motor rotor inertia, kg-m^2

k_c = Formation contact stiffness, N/m

k_s = Frictional spring, N/m

L_{ls} = The per phase stator leakage inductance, H

L_{lr} = The per phase rotor leakage inductance, H

L_m = α-β axis magnetizing inductance, H

p = Number of pole

q_i = Segment i displacement (or angular displacement), m (or rad)

q_{i-1} = Segment i-1 displacement (or angular displacement), m (or rad)

M_i = Segment i mass, kg

M_{i-1} = Segment i-1 mass, kg

ΔM = Increase in torsion over length of element, N-m

p_i = Segment i momentum, kg-m/s (or kg-m^2-rad/s)

p_{i-1} = Segment i-1 momentum, kg-m/s (or kg-m^2-rad/s)

Q = volume rate of flow of drilling mud, m^3/s

r = Characteristic radius of drillstring element, N

r_b = Drill bit radius, m

r_i = internal radius of DP or DC, m

r_o = External radius of DP or DC, m

r_w = wellbore radius of DP or DC, m

R_i = Segment i material damping, N-s/m (or N-m-s/rad)

R_{i-1} = Segment i-1 material damping, N-s/m (or N-m-s/rad)

R_s = Stator resistance, ohms

R_r = Rotor resistance, ohms

R_m = Motor rotor damping, N-m-s

$R_{viscous}$ = Viscous damping per unit length, N-m-s/rad

s = Bottom-hole surface profile, m

s_o = Bottom-hole surface profile amplitude, m

T_e = Electromagnetic torque, N-m

T_i = Segment i torque, N

T_{i-1} = Segment i-1 torque, N

T_R = Resistive torque per unit length due to viscous damping, N-m

V_a = Voltage in the three phase system a-axis, volts

V_b = Voltage in the three phase system b-axis, volts

V_c = Voltage in the three phase system c-axis, volts

V_P = Drilling mud velocity inside the drillpipe, m/s

V_A = Drilling mud velocity inside the annulus, m/s

V_i = Segment i moving velocity, m/s

V_{i-1} = Segment i-1 moving velocity, m/s

$V_{s\alpha}$ = The α-axis stator voltage, volts

$V_{s\beta}$ = The β-axis stator voltage, volts

$V_{r\alpha}$ = The α-axis rotor voltage, volts

$V_{r\beta}$ = The β-axis rotor voltage, volts

W = Buoyed weight of drillstring element, N

W_{fs} = Threshold weight-on-bit, N

α_a = Weisbach friction factor; outside DP or DC

α_p = Weisbach friction factor; inside DP or DC

$\Delta\alpha$ = Increase in azimuth angle over length of element, degree, rad

ω_i = Segment i angular velocity, rad/s

ω_{i-1} = Segment i-1 angular velocity, rad/s

$\lambda_{s\alpha}$ = The α-axis stator flux linkage, amp-H

$\lambda_{s\beta}$ = The β-axis stator flux linkage, amp-H

$\lambda_{r\alpha}$ = The α-axis rotor flux linkage, amp-H

$\lambda_{r\beta}$ = The β-axis rotor flux linkage, amp-H

ρ_m= drilling mud density, kg/m^3

μ_e = Equivalent viscosity for fluid resistance to rotation, N-s/(m-rad)

θ = rotation about body fixed y-axis, rad

$\bar{\theta}$= Average inclination angle of element, degree, rad

$\Delta\theta$ = Increase in inclination angle over length of element, degree, rad

φ = Rotational displacement of the bit, rad

ψ = rotation about body fixed z-axis, rad

ϕ = rotation about body fixed x-axis, rad

μ_o = Bit-rock frictional factor

δ_c = Depth of cut per revolution, m

μ = Sliding friction coefficient between drillstring and wellbore

μ_k = Kinetic friction coefficient

μ_s = Static friction coefficient

κ = Parameter accounting for non-uniform shear across a cross section

Ω = Whirl speed, rad/s

1 Introduction

1.1 Motivation

Excessive vibration in the drillstring, bottom-hole-assembly (BHA) and related drilling components is a common scenario during deviated well drilling. It is a serious concern in the oil and gas industry and a key cause of deteriorating drilling performance. Field experience suggests that drillstring vibrations and related failures can account for approximately 2% to 10% of well costs (Jardine *et al.*, 1994). Therefore, the oil and gas industry is highly motivated to focus on controlling drillstring vibrations. Even though drillstring vibration control is one of the most important topics in the oil and gas industry, very few steps have been taken to build a deviated drilling dynamic simulator.

A key issue in designing and planning a deviated well, choosing drilling parameters, and selecting BHA tools, etc. for a successful drilling operation is the development of the best drilling simulator. Because of the complexity and huge cost associated with directional drilling experiment, research is increasing into numerical drilling simulator for well planning, vibration prediction, and vibration mitigation.

This research work presents a demonstration of deviated wellbore model for predicting the vibrations and shows the effect of drilling downhole tool on these vibrations.

1.2 Background

Oil and natural gas are non-renewable natural resources vital to the maintenance of our day-to-day life, as well as being essential to industry. The discovery and cost-effective production of these hydrocarbons depends heavily on an efficient drilling process. Interest in using directional drilling technology to extract oil and gas is increasing as it has the ability to direct the well path in order to drill multiple wells from the same rig, avoid hard-to-drill rock formations such as salt domes, drill beneath obstacles, or improve the drainage by maximizing the intersection of the well with the reservoir.

Currently, directional drilling is a multibillion dollar a year industry with hundreds of contractors and thousands of drilling rigs operating on five continents (Allouche *et al.*, 2000). Drilling operations represent approximately 40% of all exploration and production costs (Lopez, 2010). Drilling engineers wishing to improve drilling efficiency, avoid potential drillstring failures, control well trajectory, and optimize BHA tool life need a detailed understanding of drillstring dynamic behavior and how these affect drilling operations in each well.

There is considerable literature that analyzes the dynamics of a vertical drillstring. Each author uses a different approach to model the drillstring dynamics: cosserat theory (Tucker and Wang, 1999), one mode approximation (Yigit and Cristoforou, 2006), beam modes together with finite element method (Khulief *et al.*, 2007), discretized systems with two degrees of freedom (Richard *et al.*, 2007), lumped segments approach (Sarker *et al.*, 2012a), and multibody segments approach (Rideout *et al.*, 2013).

There are comparatively few papers treating the dynamic modeling of deviated drillstrings. In almost all the models described in (Millheim and Apostal, 1981; Burgess *et al.*, 1987) only the BHA up to the so-called point of tangency is taken into account by the dynamic analysis, whereas the model in (Dunayevsky *et al.*, 1985) includes continuous wall contact and the main focus was on the parametric excitation of lateral vibrations due to fluctuating weight on bit (WOB). Recently an analytical solution for the threshold rotary speed, after which the drillstring starts to snack, is derived and presented in (Heisig and Neubert, 2000). Also the analytical results are verified using a versatile finite element formulation to model the drillstring in greater detail.

Existing research work shows that no complete dynamic model for a directional oilwell drillstring, capturing axial, lateral, and torsional vibrations, has been developed. Therefore, development of a dynamic model of a directional oilwell drillstring that shows the mutual dependence of axial, torsional and lateral vibrations, which arise due to interactions of drill bit with the formation and drillstring with the borehole wall, has been focused in this research work.

Outcomes of this research work will benefit the world oil and gas industries by further developing a technology that could predict and control drillstring vibrations, reduce vibration-related drillstring failures, aid in well planning, increase the efficiency of drilling, and reduce drilling cost.

1.3 Problem statement

Since the early twentieth century there are very few published field case studies that have reported problem free directional drilling operations. Field experience shows that mud motor, drill bit, measurement while drilling (MWD), and BHA component failures are very common during directional drilling operations. Especially during extended-reach lateral wells drilling that maximizes reservoir contact, which are much more complex than standard horizontal wells, the failures cause time-consuming and costly trips out of the hole. Downhole data shows that vibration in the BHA is one of the main reason for these failures.

To overcome the failures, identifying the sources of the vibrations and adjusting the drilling parameters to eliminate the vibrations are required for successful drilling operations. Thus, it is imperative to conduct a research on understanding the dynamic behavior of drillstring, and to develop a numerical drilling simulator to predict and mitigate vibrations.

1.4 Objectives

This study will develop a numerical drilling simulator that has been one of the main demands in the oil and gas industry to evaluate the effect of downhole tools parameters on overall drilling performance. The main objectives of this research are:

a. To generate a deviated wellbore model capturing axial and torsional vibrations

- extend an existing model for vertical wells in Sarker (2012) by adding wellbore friction term specific to deviated wells.

- validate the extended model using field data already acquired from an industry collaborator, Ryan Energy Technologies of Calgary, AB.

b. To develop the three phase induction motor model for capturing the top drive motor dynamics.

c. To extend the simulation model to include lateral dynamics by using multi-body simulation to represent the final portion of the drillstring as a series of connected segments that can move in three dimensions.

d. To develop friction model suitable for stick-slip vibration, for predicting drag torque and whirl accurately.

e. To analyze the sensitivity of lateral vibration to the presence of downhole tools such as agitators.

1.5 Scope of research

The overall purpose of this research project is to develop an efficient yet accurate deviated oilwell drillstring dynamic model. The simulation results will help us assess the relationships between drilling parameters (WOB, top drive speed, drilling fluid flow rate and density, mud pump pulsation frequency, and drillstring geometry, etc.), bit geometry, formation types, downhole vibration tools and severity of unwanted vibrations (stick-slip, bit-bounce, and whirl, etc.). More specifically, the thesis will address the following research questions:

- What is the sensitivity of unwanted vibration modes such as stick-slip, bit-bounce, and whirl to drilling parameters?

- What is the effect of the presence of downhole tool on drilling performance?

Outcomes:

- A model that can assist with well trajectory planning, and predict relationships between WOB, rotary speed, bit-bounce, and stick-slip.
- A model to assist industry partners and the industry in general, with predicting loads on downhole tools. Such a model would allow drillers to choose drilling parameters and tool locations to minimize the chances of failure.

1.6 Research methodology

The bond graph method using 20Sim® (software for modeling dynamic systems) is applied throughout the modeling and simulation. The simulation time is very fast compared to high order finite-and discrete-element models, making the model suitable as a tool for design and sensitivity analysis. An advanced general-purpose multiphysics simulation software called LS-DYNA® is used for validating the multibody segment approach that is used to simplify modeling of 3D shaft vibration. Mathematical methods for the derivation of viscous damping, hydrodynamic damping, whirling motion and friction phenomena etc. are also applied in this dissertation.

This thesis is devoted pre-dominantly to the understanding and prediction of sensitivity of unwanted vibration modes such as stick-slip and whirl to drilling parameters while drilling in deviated wellbores. To frame the problem, a review of vibration issues in

deviated wellbores is presented (Chapter 2). It is found that the overall drilling cost arises due to vibration related problems, such as lost time while pulling out of hole and fishing, reduce ROP, poor wellbore quality, and increased service cost because of the need for ruggedized equipment. Predicting the expected coupling between WOB, bit speed, and rock-bit interface condition; and their effect on stick-slip, a bond graph model of a vertical drillstring is developed by having lumped segment axial and torsional models with no drillstring wellbore wall contact, an empirical treatment of rock-bit interaction, and top drive motor dynamics (Chapter 3). To address the excessive torque and drag issue in deviated wellbore which arises due to drillstring contact with wellbore wall while drilling in inclination and long lateral section, a quasi-static torque and drag model for deviated wellbores is developed (Chapter 4). The model has been simulated with downhole tools such as the Agitator®. To address the role of lateral vibration in the BHA, a 3D multibody segment approach for BHA modeling is described and validated with LS-DYNA finite element analysis (Chapter 5). Finally, demonstration of a complete horizontal wellbore model by having nonlinear 3D multibody segments with lateral vibration in the final horizontal section (i.e. BHA) ending at the bit, and having simpler axial and torsional lumped segments for the vertical, curved build section and initial horizontal portions is presented. It includes a bit-rock interaction submodel, friction and contact of the drillstring with the wellbore wall, hydrodynamic damping due to drilling mud within the drillstring, and viscous damping. The friction model includes stick-slip phenomena which allows either sliding, or rolling without slip, during contact between the wellbore and an arbitrary segment. The effect of downhole tool parameters on drillstring lateral vibration has been

analyzed. The dissertation work has a good potential to use as a directional drilling dynamic simulator for the oil and gas industry to improve drilling efficiency. Finally, effectiveness and limitations of the model, and corresponding future works on the model are described (chapter 6).

2 A Review of Vibration Issues in Deviated Wellbores

2.1 Deviated drilling technology

The earliest oil and natural gas wells in modern times were drilled percussively, by hammering a cable tool into the earth. Soon after, cable tools were replaced with rotary drilling, which could drill boreholes to much greater depths and in less time. Until the 1970s, most oil and natural wells were vertical, although lithological and mechanical imperfections cause most wells to deviate at least slightly from true vertical. Nowadays the oil and gas industry relies heavily on directional drilling to develop offshore reserves, facilitate development in environmentally sensitive areas, and provide a capability that is essential to the oil industry. The initial practice of directional drilling was in the 1920s, when basic wellbore surveying methods were introduced. By the 1930s, a controlled directional well was drilled in Huntington Beach, California, USA, from an onshore location to target offshore oil sands (Mantle, K., 2014). Special applications of directional drilling such as extended-reach drilling (ERD), multilateral drilling and short-radius drilling are very common in oil and gas industry. Usually ERD is used to access offshore reservoirs from land locations, sometimes eliminating the need for a platform. Fig. 2.1 shows a sketch of Wytch Farm ERD well into Sherwood sandstone. And in the year 2013, the world longest ERD well (12,345 m) was drilled from Sakhalin Island, Russia, to the offshore Odoptu field (Mantle, K., 2014). Multilateral drilling application increases

wellbore contact with hydrocarbon producing zones by branching multiple extensions off a single borehole. A sketch of modern multilateral application is shown in Fig. 2.2.

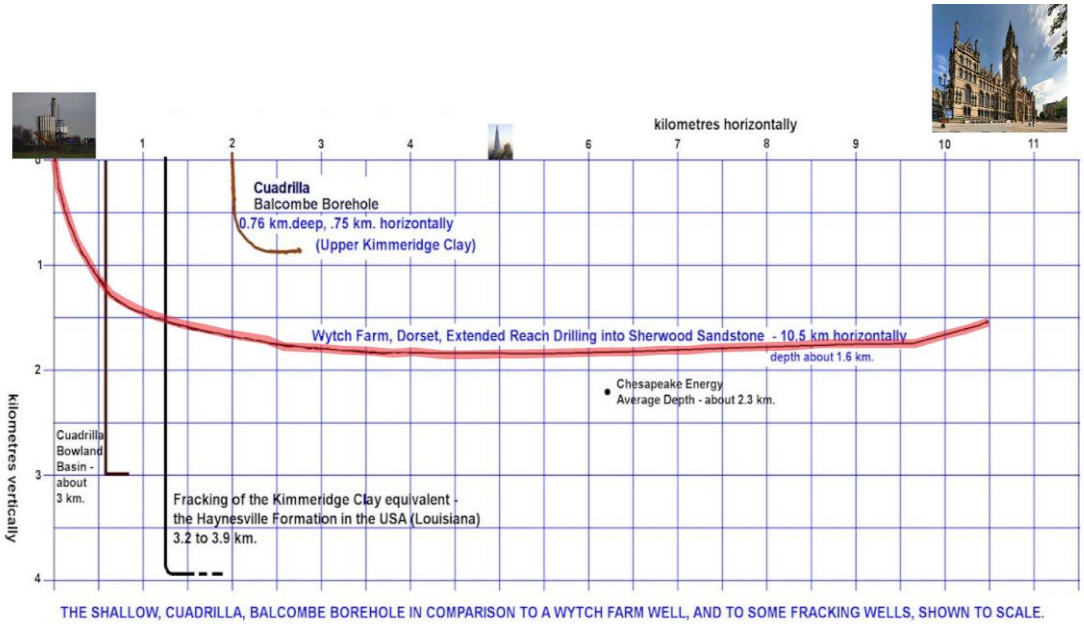

Figure 2.1: Wytch Farm ERD well (http://frackland.blogspot.ca/2014/01/extended-reach drilling.html).

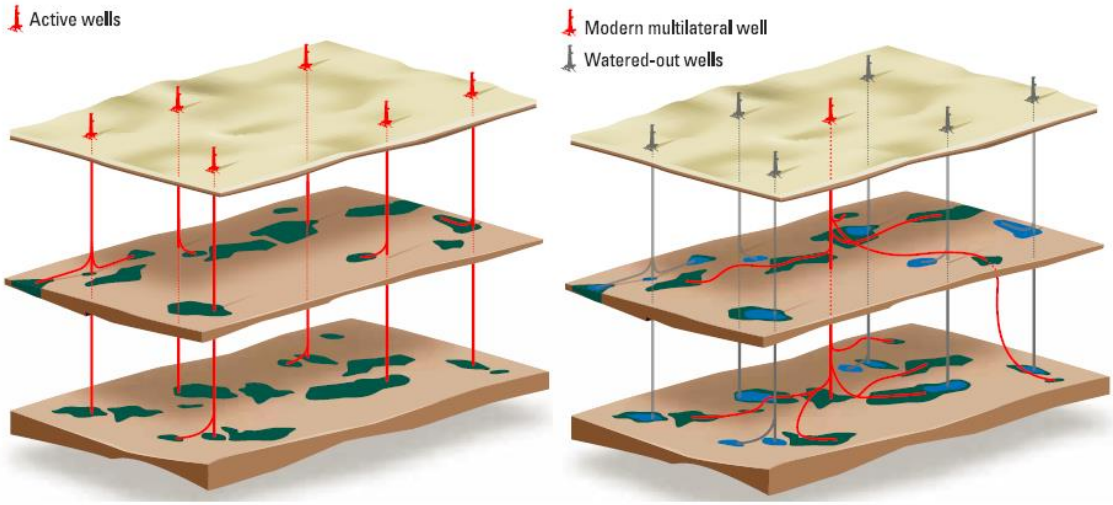

Figure 2.2: Modern multilateral well application (https://www.slb.com/resources).

Early directional drilling involved the use of deflection devices such as whipstocks and simple rotary assemblies to reach the desired target. This time-consuming approach offered limited control and frequently resulted in missing targets. The introduction of reliable mud motors offered steering capability and with it, directional control, and provided an important advance in directional drilling technology. Wellbore direction is controlled by using a bent motor housing, which was oriented to point the drill bit in the desired direction. Mud motors use the mud pumped through a rotor and stator assembly to turn the bit without rotating the drillstring from the surface. A sketch of mud motor assembly is shown in Fig. 2.3. By controlling the amount of hole drilled in the sliding versus the rotating modes. By alternating intervals of rotating mode and sliding mode, the directional driller controls the wellbore trajectory and steers it in the desired direction. In rotating mode, the rotary table or top drive rotates the entire drillstring to transmit power to the bit. By contrast, in sliding mode, the bend and bit are first oriented in the desired direction, then the downhole mud motor alone powers the bit, with no rotation of the drillstring above the bit. While motors drill very quickly in rotating mode, sliding can be problematic. Frictional effects cripple ROP, dropping penetration rate to as little as one-third of rotational rates (Mantle, K., 2014). Orientating the motor for correct directional drilling is tedious and time-consuming; the deeper the well, the greater the penetration time. Proper orientation is complicated at depth by reactive torques swinging the bit to the left. The development of rotary steerable technology eliminated these issues by providing the benefit of simultaneously rotating and steering in a discrete direction. Fig. 2.4 shows a sketch of rotary steerable system (RSS) assembly. Continuous rotation transfers weight to

the bit more efficiently, which increases the ROP. RSS improves direction control in three dimensions (Fig. 2.5), provides smoother, cleaner and longer wellbore, and drills more quickly with fewer problems.

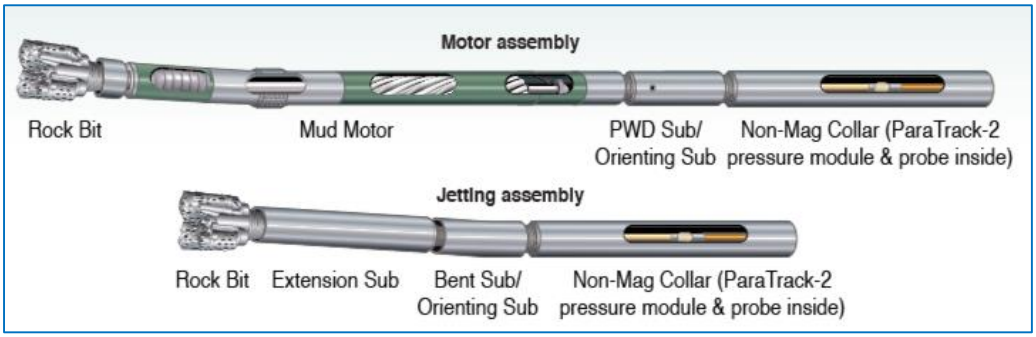

Figure 2.3: Sketch of mud motor assembly (http://primehorizontal.com/drilling-tools).

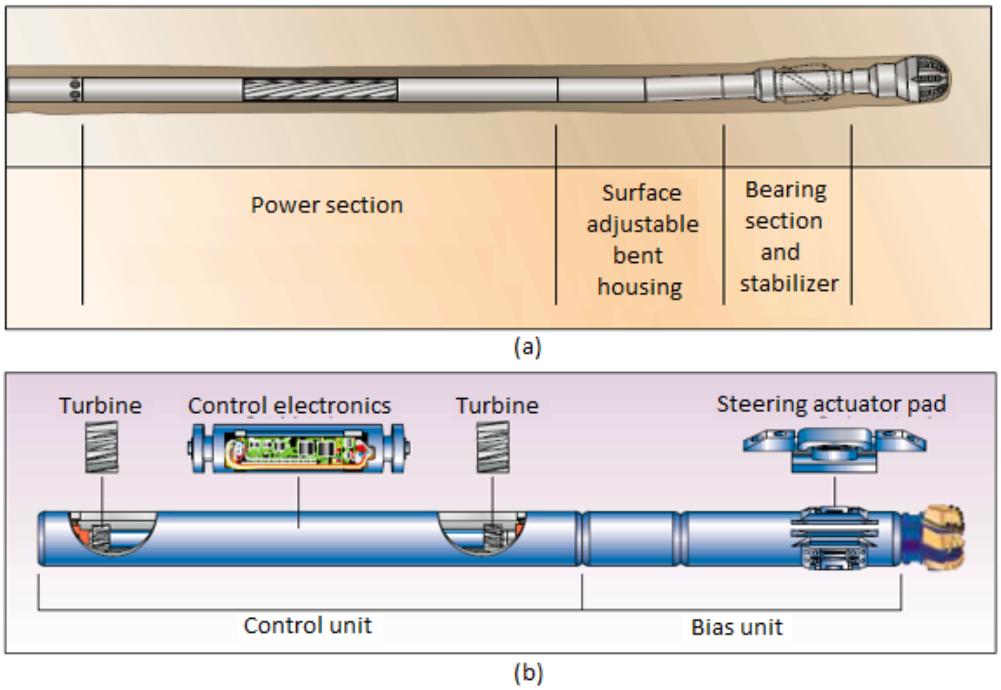

Figure 2.4: Sketch of (a) simple power pack steerable assembly and (b) power drive RSS (Downton et al., 2000).

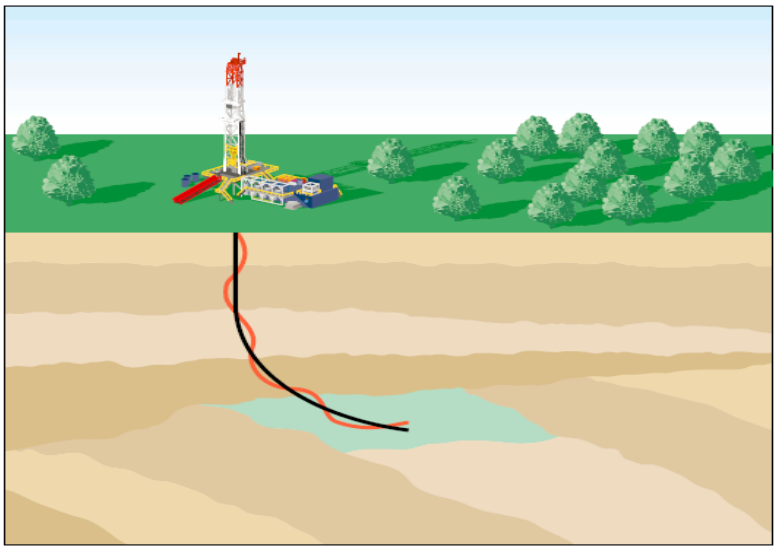

Figure 2.5: Sketch of directional drilling with mud motor (red trajectory) and RSS (black trajectory) (Downton et al., 2000).

2.2 Review of deviated drilling dynamic failures

Field vibration detection has revealed that vibrations are always present to some degree, but can be especially bad in difficult drilling environments (e.g. hard formations, steep angle wells). Vibration can affect WOB, ROP, and drilling direction and can also severely damage drilling tools such as BHA, MWD tools, cutters, and bearings. The drillstring undergoes various types of vibration during drilling. The most severe manifestations of these are, respectively,

- bit-bounce where the bit repeatedly loses contact with the hole bottom.
- stick-slip where the torsional vibration of the drillstring is characterized by alternating stops and intervals of large velocity of the bit.

- severe lateral forward and backward whirl with wellbore contact. In forward whirl, the spin angular velocity is in the same direction as the lateral deflection. During backward whirl, the shaft rolls without slip around the enclosure such that spin speed is opposite the whirl direction.

Different modes of drillstring vibration are shown in Fig. 2.6. These vibrations are to some degree coupled. Bit whirl can be triggered by high bit speeds during stick-slip motion. Stick-slip can generate lateral vibration of the BHA as the bit accelerates during the slip phase. Large lateral vibration of the BHA into the wellbore can cause bit-bounce due to axial shortening. Induced axial vibrations at the bit can lead to lateral vibrations in the BHA, and axial and torsional vibrations observed at the rig floor may actually be related to severe lateral vibrations downhole near the bit.

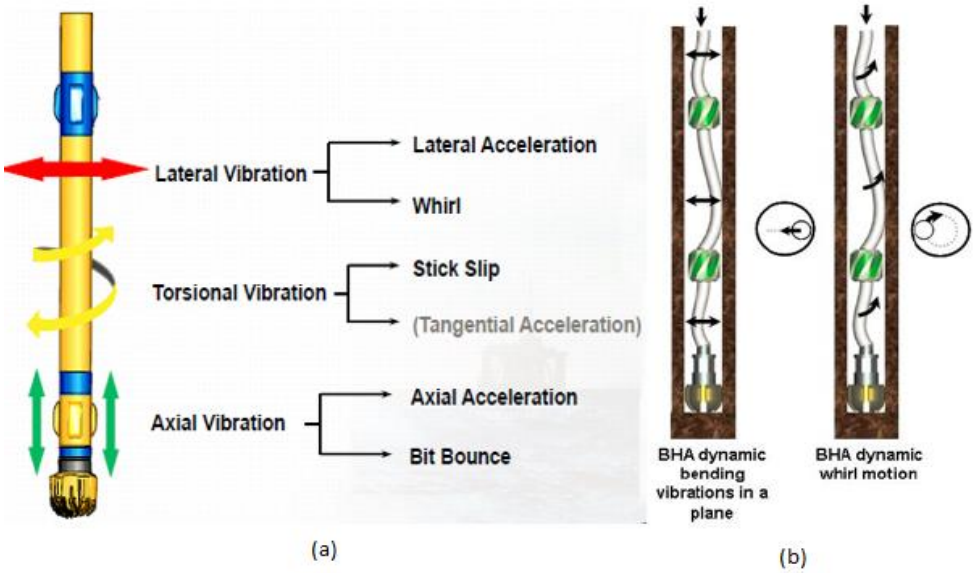

Figure 2.6: Sketch of (a) modes of drillstring vibration (www.bakerhughes.com) and (b) two modes of lateral vibration (Bailey *et al.*, 2008).

Cook *et al.* (1989) developed a drilling mechanics sub for the first time to measure the downhole real time vibrations in direction drilling operations in the Gulf of Mexico. Higher transverse accelerations have been identified while rotating in the build section. The higher curvature couples the rotation of the drillstring strongly to the transverse motion (e.g., backward whirling), and the stabilizer or collar interaction with the borehole wall increases the level of shocks to the assembly. Axial and torsional acceleration were much lower than the transverse accelerations and typically did not exceed 0.5 g. Perreau *et al.* (1998) tested a developed estimator of the downhole vibrations and one of the tests was carried out in Qatar in a deviated well at a depth of 3300 m. The signal of estimated rotation speed of the bit computed in real time showed very clearly that there was a stick-slip and the estimated speed of rotation oscillated between 0 and 250 rpm. Also the variations were very regular and at the frequency of the stick-slip phenomena. Amro (2000) presented a field case study of drillstring failure during drilling of medium radius horizontal wells. Several cracks were found in the drillpipe tool joints which are shown in Fig. 2.7. A cyclic or alternating bending stress, which was caused by the rotation of the drillstring in the high build section, were the main reason for the failure. A case study on two directional wells with aggressive PDC bits and a new downhole dynamic tool has been conducted in Hood *et al.* (2001). Drilling in soft formation with rotary speeds between 150-170 RPM and low weight on bit (WOB) between 2-5 klbf at rates of penetration (ROP) up to 60 m/hr the diagnosis system reported a backward whirl event together with an increase in lateral acceleration. In case of harder formation drilling the required higher WOB and lower rotary speeds led to torsional vibrations which several times developed into full stick-slip. After a few minutes

of stick-slip the rotary speed was usually increased and the WOB decreased again. Forward whirl occurred a few times while drilling through the harder formation, but it was eliminated through decreasing the rotary speed.

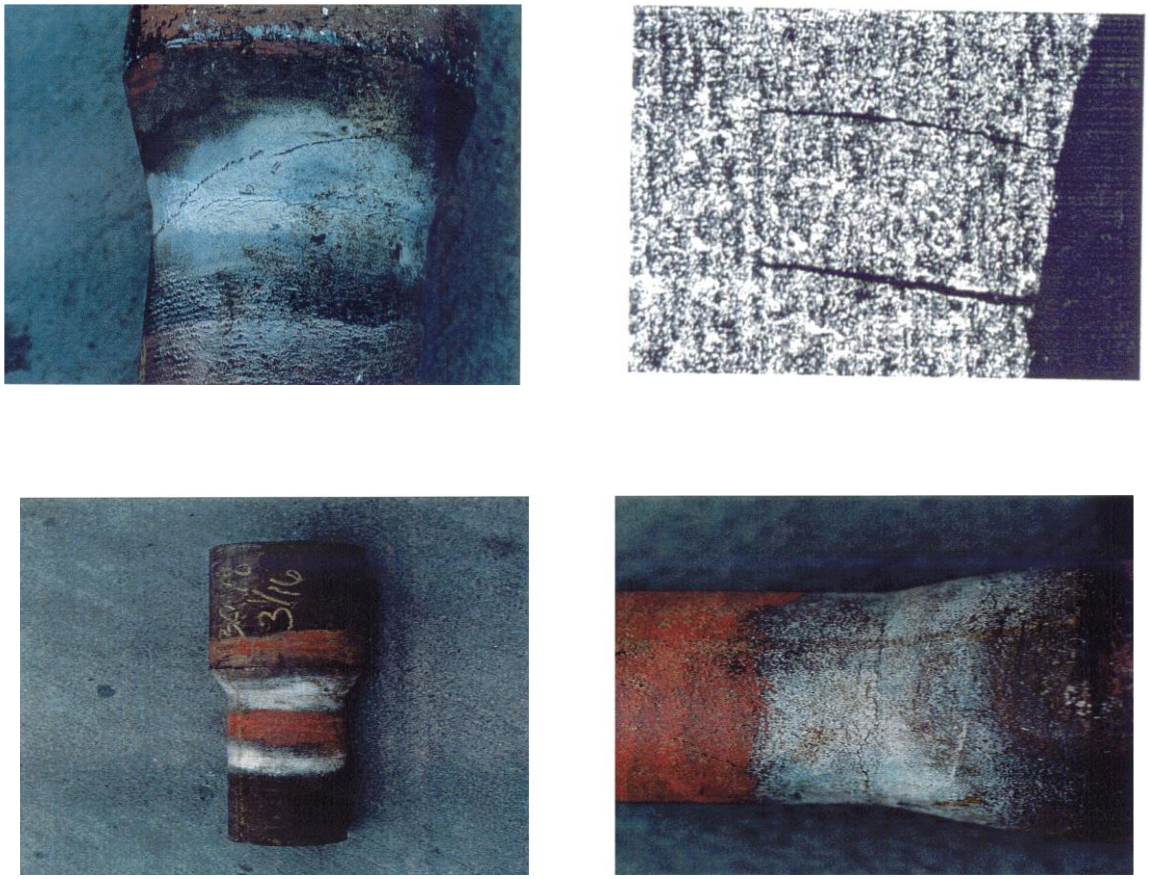

Figure 2.7: Cracked drillpipe tool joints (Amro, 2000).

Lenamond *et al.* (2005) showed that the BHA suffered high levels of stick-slip throughout most of the directional drilling section, especially while drilling through shale and interbedded formations. Lateral shocks have been found while drilling through intercalated formations and coincides with the increment of stick-slip. These excessive

vibrations at the BHA lead to rotary steerable system (RSS) failures mentioned in Lenamond *et al.* (2005). Compared to vertical section drilling curved and lateral sections required more times due to high torque and drag along with low penetration rates (Janwadkar *et al.*, 2006). Drillstring buckling while drilling curved and lateral sections generated stick-slip and bit whirl that damaged the bit and reduced the ROP.

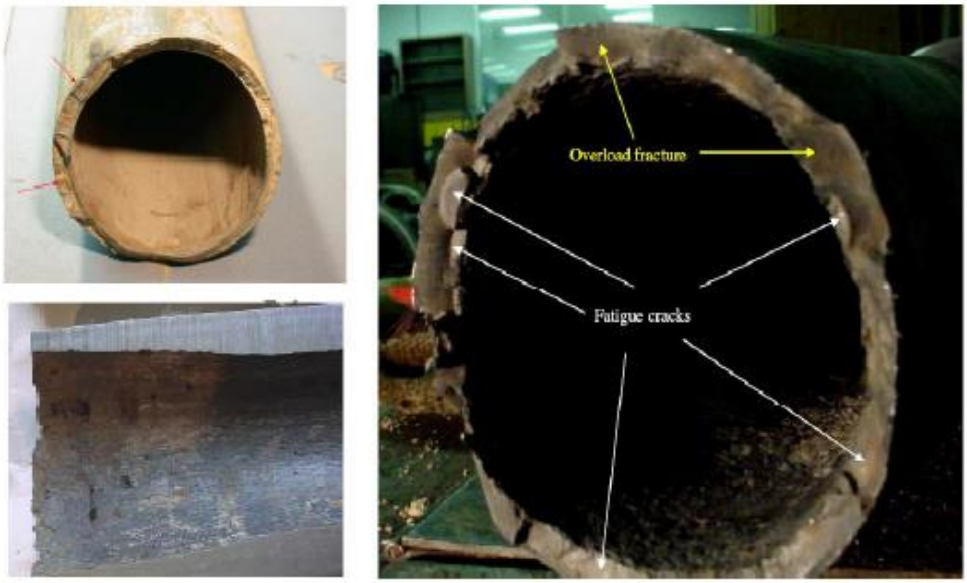

Figure 2.8: Photo of fatigue failures (Bert et al., 2007).

Sugiura and Jones (2007) mentioned that stick-slip becomes increasingly problematic with smaller diameter and longer drillstrings while drilling extended-reach and horizontal wells. Based on three directional wells drilling operations, the real-time stick-slip and vibration detection system revealed that excessive stick-slip hindered ROP on these wells. Very little lateral and axial vibrations were observed in the real-time data. Bert *et al.* (2007) conducted a case study on three drillstring fatigue failures (Fig. 2.8) that occurred while

drilling two deep wells in the USA midcontinent region. All the failures occurred across 2°/100 ft to 3°/100 ft dogleg severity. Higher transverse accelerations due to off-bottom rotation and lower WOB were the main reason for these failures. Jaggi *et al.* (2007) conducted a field study on PDC/RSS vibration management while drilling a main horizontal and two lateral wells in Panna Field Gulf of Combay, India. Drilling dynamics data log showed that drill bit experienced severe stick-slip. From the downhole data measurements, it was apparent that the BHA was going into complete torsional oscillation and was coming to complete halt before starting again. This was resulting the expensive BHA elements to severe impact damage.

Barton and Lockley (2008) reviewed the field performance of a number of drill bits within Canadian Rockies on directional assemblies which included downhole dynamics data analysis. The downhole dynamic data recorder recorded quite severe stick-slip with downhole RPM ranging between 0 to 385 and significant amount of lateral vibrations, which had a negative effect on drilling performance and caused mechanical damage to the bit. Bacarreza *et al.* (2008) presented a knowledge based study on extended reach drilling wells in the north of the Brunei offshore sector for future well construction. The vibrations induced while drilling the hard stringers were monitored by the applied drilling technology center and excessive lateral vibrations were creating complicated situations while drilling. Akinniranye *et al.* (2009) presented shock and vibration data while drilling two deep-water wells in the Gulf of Mexico. There was severe stick-slip and a significant amount of lateral shock in the plots. The problems identified were twist-offs and tool lost in hole, tool damage and component failures (Fig. 2.9) and loss of directional control. Sonowal *et al.*

(2009) reviewed the history, challenges and planning, leading through to the successful drilling of the BD-04A well in offshore Qatar which was claimed as world longest horizontal well at that time. They found that drilling torque friction factor started relatively high when drilling out of the casing shoe, however, it stabilized between friction factor of 0.20-0.25. Stick-slip varied between 30 to 290 peak to peak RPM difference.

Figure 2.9: Photo of drill bit and tool failures (Akinniranye *et al.*, 2009)

Figure 2.10: Fracture of the drillpipe twistoff (Raap *et al.*, 2012).

Sanuel and Yao (2010) presented a case study on three wells and two of the wells were horizontal. The horizontal section of the well experienced severe stick-slip. Lateral vibrations (whirl) were present while drilling the build section. Lesso *et al.* (2011) conducted a test at the Schlumberger directional drilling test facility near Cameron, Texas. Drilling mechanics module data predicted severe stick slip and most destructive backward whirl with stick-slip. Sack, J. (2011) conducted a case study on extended-reach laterals in the Denver-Julesburg Basin. One of the biggest challenges in longer laterals was excessive torque and drag of the drillpipe caused by wellbore friction. Excessive stick-slip was very common while drilling in long lateral sections and stick-slip reduction was one of the main concern during drilling plan. Raap *et al.* (2012) discussed the dynamic behavior of drillstrings in lateral wells and high frequency data were recorded by use of downhole dynamic recorders. Despite the rotational speed and WOB being kept constant, alternating periods of lateral or torsional vibrations were observed. During periods of several torsional vibrations, the downhole dynamic recorder in the lower BHA recorded minimum downhole rotations of 0 rev/min and maximum values as high as 240 rev/min. This ultimately resulted in the pipe failing in tension with a 45^0 fracture plane (Fig. 2.10). D'Ambrosio *et al.* (2012) evaluated and analyzed the acquired vibration data by use of downhole dynamic data recorders (DDDR) along the drillstring on a horizontal well in Oklahama Woodford Shale. Fig. 2.11 illustrates the trajectory path each individual DDDR sensor traverses during the drilling operations. DDDR sensor near the bit showed maximum lateral acceleration was found from near the bit DDDR sensor data whereas average torsional vibrations were lower. Rajnauth and Jagai (2012) analyzed the downhole tool (motor, bit and MWD) failures

while drilling lateral wells in Trinidad. Most section of the lateral wells have been drilled without real time downhole vibration measurement tools used with MWD tools because of high cost associated with using the downhole vibration measurement tools. The collected data clearly showed that there were significant levels of torsional vibration that adversely affected downhole motor, bit and MWD failures.

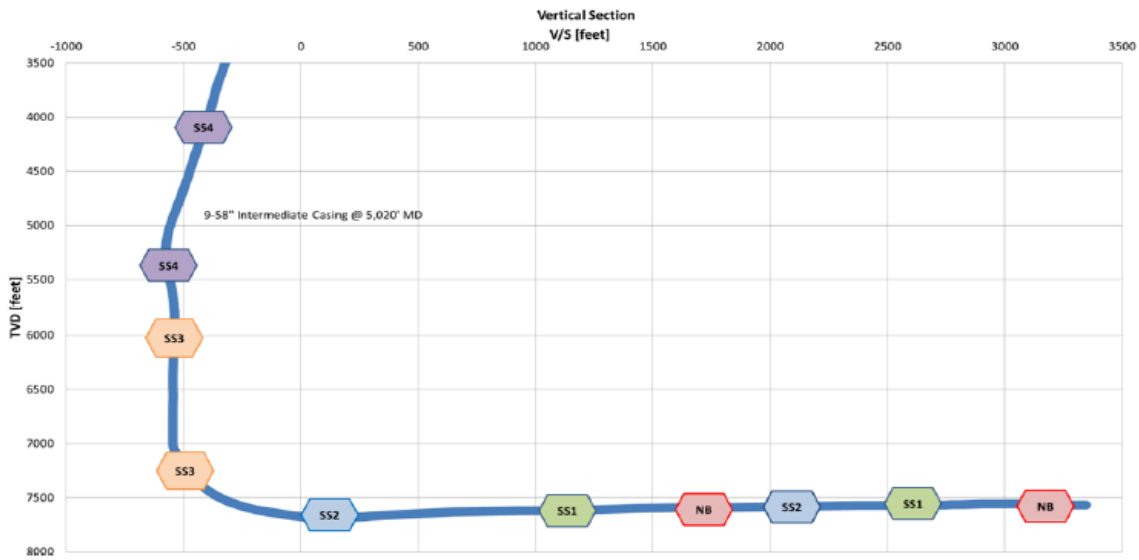

Figure 2.11: Initial and final placement of each DDDR sensor from start of the run (at 9258 ft) to end of the run (at 10524 ft) (D'Ambrosio *et al.*, 2012).

Chrisman *et al.* (2012) discussed the challenges encountered while drilling the long lateral sections in the Williston Basin and the advantages of using real-time downhole dynamics information on lateral drilling performance. Controlling stick-slip and lateral vibration in order to enhance the life of the bit, motor, MWD and BHA were one of the main challenge. It was discussed that downhole motor rotation speed was creating lateral vibration and it was controlled by changing the mud flow rate. Whenever the drillstring

rotary speed was decreasing stick-slip was becoming severe. Jerz and Tilley (2014) conducted a total of four case studies (offshore deepwater UK, continental Europe exploratory campaign, Middle East hard formation, and Unconventional play) to show the advancements in power rotary steerable technologies results in record breaking runs. The results show the improvement of ROP by using the power rotary steerable technology because of less stick-slip compared to mud motor technology (Fig. 2.12).

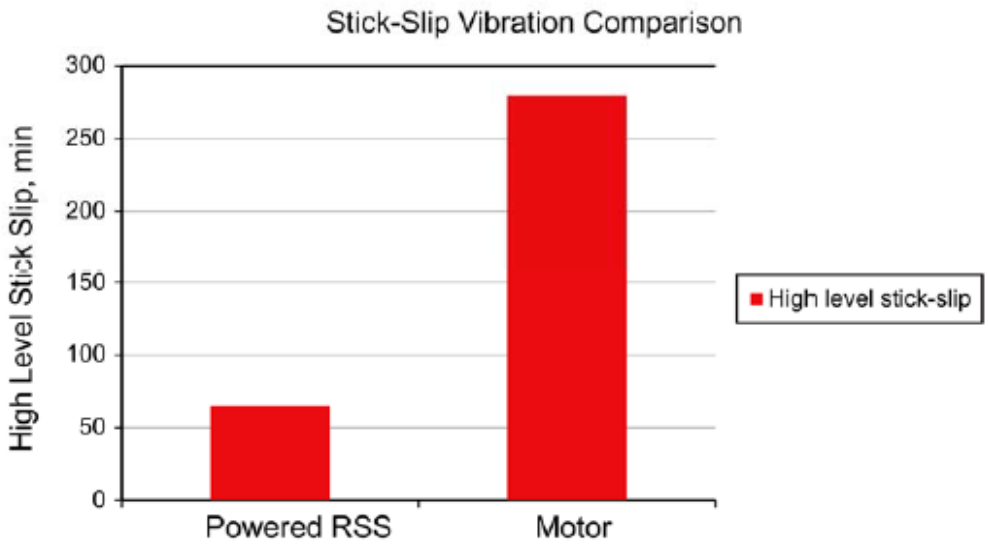

Figure 2.12: Stick-slip vibration comparison (Jerz and Tilley, 2014).

Wright *et al.* (2014) presented downhole tool failures due to excessive vibrations while drilling Nikaitchup wells in Beaufort Sea within the North Slope region of Norther Alaska. The 12 feet and 1/4-inch intermediate section of the Nikaitchup wells were drilled with a RSS 1at high inclination prior to landing ne

4ar-horizontal in the reservoir. The intermediate hole section passed through a very abrasive sand with an unconfined compressive strength (UCS) of approximately 22 ksi called the Lower Ugnu. Due to the abrasive nature of the Lower Ugnu combined with

interbedded soft sand the driller drilled the 12 feet and ¼-inch intermediate section with two to three bit runs consisting of various PDC and tri-cone designs. It was found that high stick-slip and lateral vibrations were the main phenomena damaging the bit/BHA. The photos of bit/BHA damage are shown in Fig. 2.13.

Figure 2.13: Photos of damaged and worn out drill bits, stabilizers (Wright *et al.*, 2014).

Efland *et al.* (2014) placed the high-speed downhole dynamics sensors in multiple locations along the drillstring. Stick-slip was playing a significant role inhibiting drilling performance in the Eagle Ford Shale play, particularly while drilling the lateral sections. Stick-slip generated excessive cycle downhole rotational speed variations with high peaks that induced extreme lateral shocks and accelerations.

The field case studies show that mud motor, drill bit, MWD, and BHA component failures are very common while drilling deviated oilwell. The downhole data shows that excessive vibrations, especially lateral shocks, in the drillstring, BHA, and related drilling components is the main cause of the failures. In the next chapter, a lumped segment based modeling approach will be presented for modeling the oilwell drillstring dynamics.

3 A Lumped Segment Based Modeling Approach for Axial and Torsional Motions of Vertical Drillstring

3.1 Introduction

3.1.1 Vertical wells and the increasingly important role of stick-slip

Most directional wells begin as vertical wellbores. At a designated depth the directional driller deflects the well path by increasing well inclination to begin the build section. During horizontal well drilling the vertical section usually goes at deeper depth ranges up to several thousand meters (Fig. 3.1). Vertical wells are typically drilled by means of a rock cutting tool (drill bit), which is attached at the end of a long drillstring consisting of drill pipes and the BHA screwed together by tool joints, and driven by a speed controlled electric or hydraulic drive rotary system (Fig. 3.2). Due to large lengths and small cross sections of the drilling pipes, low tool inertia, and rock-bit friction, the overall drillstring is often subjected to poorly damped torsional vibrations including stick-slip behavior. Stick-slip vibration has received considerable attention in recent years with increasing use of polycrystalline diamond compact (PDC) bits, and has become an important risk element to evaluate in the planning of oil and gas drilling. Stick-slip may also excite severe axial and lateral vibrations in the BHA, causing damaged bit, failure of BHA, over torqued tool joints, torsional fatigue of drillstring, and failure of downhole equipment. Drilling with optimum parameters such as WOB, surface RPM, torque on bit

(TOB) and bit hydraulic horsepower is required from an economic point of view. Although MWD tools provide downhole data and help toward real-time adjustment of the drilling parameters to avoid severe downhole vibrations, their failure due to successive stick-slip in conjunction with their high cost has led drilling companies to develop sophisticated drillstring vibration models for pre-drilling analysis.

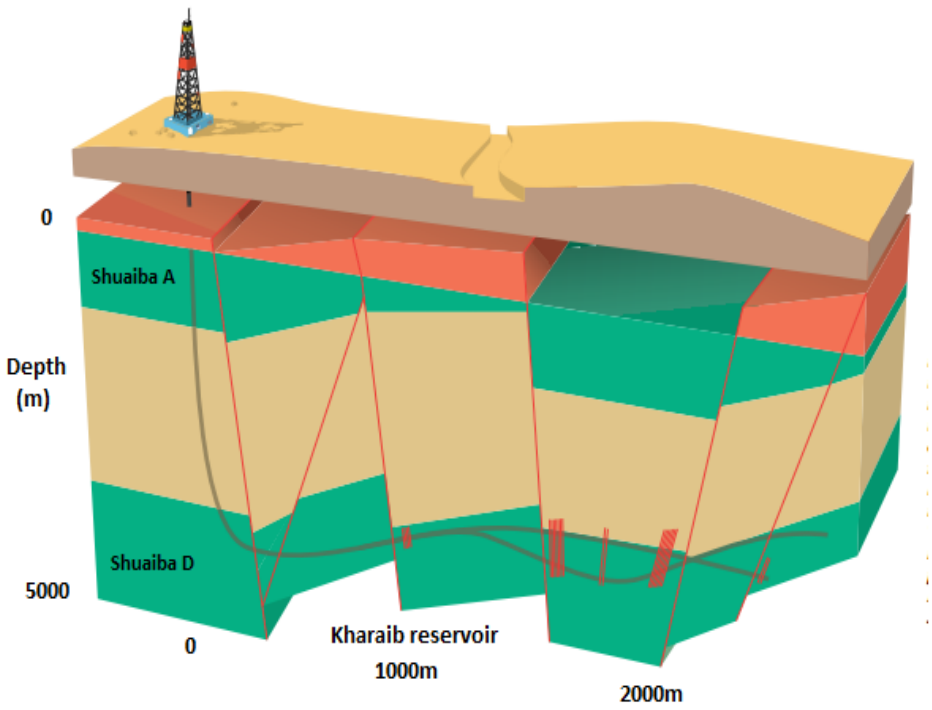

Figure 3.1: Sketch of Kharaib reservoir layer in Qatar's Idd El Shargi field. (www.slb.com/~/media/Files/resources).

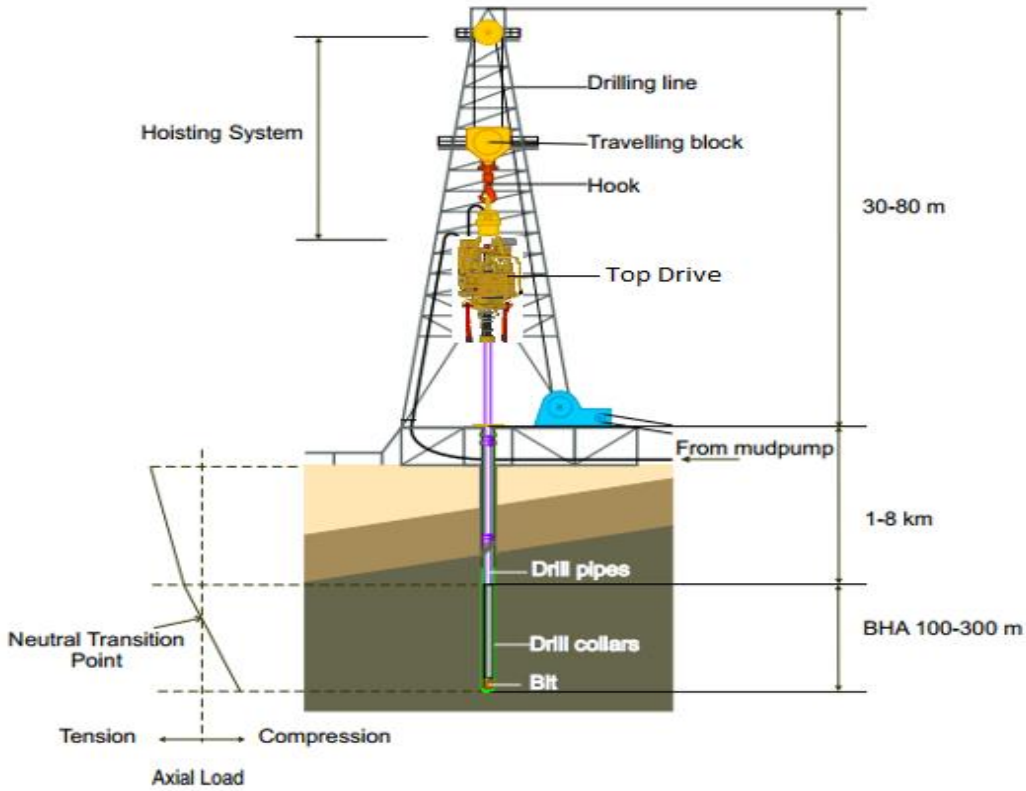

Figure 3.2: Sketch of vertical oilwell drilling system (Leine *et al.*, 2002).

3.1.2 Review of drillstring torsional vibration and coupled axial-torsional vibration models

Several dynamic formulations of drillstring vibrational behavior have been reported for analyzing torsional vibrations and coupled axial-torsional vibrations. One of the earliest drillstring dynamic model which discussed about the coupling between axial and torsional vibration were presented by Bailey and Finnie (1960) which consisted drill pipe and collars, and boundary conditions at the ends of the string. For longitudinal motion, a spring-mass system at the top of the string was taken as a boundary condition and for torsional

motion, the top boundary condition was taken as a fixed end. At the bottom of the string, a fixed boundary condition was taken for longitudinal motion and free boundary condition was taken for torsional motion. Only longitudinal and torsional vibrations of the string were considered in the analysis. Lateral motions of the string (due to bending, buckling, whirling, whipping, and so on) were neglected, and it was assumed that the torsional and longitudinal motions considered were independent. Dareing and Livesay (1968) developed computer programs based on the theory for analyzing longitudinal and angular drillstring vibration. Forces act at the top of the drillstring and were, therefore, considered part of the drillstring boundary conditions. Cable spring and mass for the kelly, swivel and traveling block were assumed at the top of the drillstring. The source that excites the drillstring was assumed to act at the bit. A three cone RC bit was used in the study. The motion of the bit was assumed to be sinusoidal and the influence of the rock in contact with the bit was ignored. For the sake of simplicity, the effect of different types of friction such as fluid, rubbing and material, which act along the string, was approximated by viscous friction. Kyllingstad and Halsey (1988) presented a mathematical model of stick-slip motion which included parameters describing downhole friction effects and a simplified description of the drillstring. The limitation of the model is that it does not predict whether stick-slip motion will or will not occur under a given set of conditions. The model also does not provide any information about a rock-bit interaction law. Jansen and Steen (1995) presented a simplified model of torsional vibrations and assumed that the drillstring behaves as a torsional pendulum in which drill pipes and collars were represented as a torsional spring and rigid body respectively. A simple dc motor dynamic was assumed in

drive system modeling. The TOB function was assumed as a nonlinear behavior. Challamel *et al.* (2000) also presented a similar type of torsional modeling approach. The drilling structure is considered as a beam in torsion. A lumped inertia is chosen to represent the BHA and a damping coefficient is taken into account along the structure. A constant rotary speed was assumed as a top boundary condition and torque on bit was taken as a bottom boundary condition for drillstring. Yigit and Christoforou (2006) used a simple dynamic model to simulate the effects of varying operating conditions on stick-slip and bit bounce interactions. Fig. 3.3 was considered as a necessary geometry for modeling the system. The equations of motion of such a system were developed by using a simplified lumped parameter model with only one compliance. One assumption in their model was that the rotary table is driven by an armature controlled DC motor through a gearbox (Fig. 3.3). This model did not account for the effect of higher modes, the flow inside and outside the drillpipe and collars, or complicated cutting and friction conditions at the bit/formation interface.

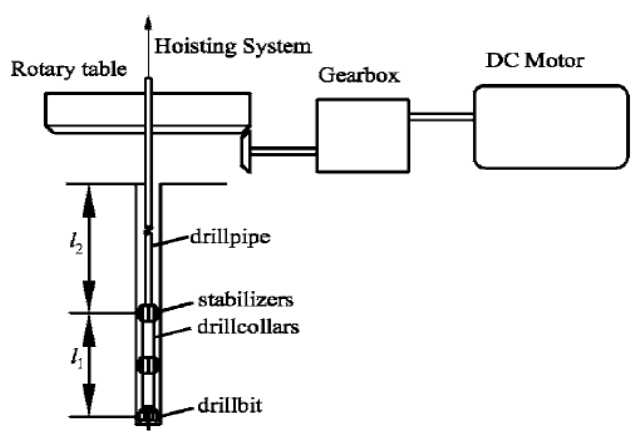

Figure 3.3: Schematic used by Yigit and Christoforou (2006)

Sampaio *et al.* (2007) presented a geometrically non-linear model to study the coupling of axial and torsional vibrations on a drill string, which is described as a vertical slender beam under axial rotation. The geometrical stiffening is analyzed using a non-linear finite element approximation, in which large rotations and non-linear strain displacements are taken into account. The effect of structural damping and a non-linear bit torque are considered in the model. Navarro-Lopez and Cortes (2007) presented a lumped-parameter segment model of the torsional behavior of the drillstring including the bit–rock interaction. Friction between the pipes and the borehole is neglected which means both are assumed as a vertical and straight. The lateral bit motion was neglected in the bit-rock interaction model. The drilling mud was simplified by a viscous-type friction element at the bit. The motor dynamics was not considered in surface rotary system modeling. Richard *et al.* (2004) studied axial and torsional coupling vibration by using an interaction law between the rock and drag bit. A lumped inertia moment was considered for BHA and the effect of rotary table moment was not considered, and the damping of drilling mud and active damping systems is neglected. Fig. 3.4(a) shows the simplified model of a drilling system used by Richard *et al.* (2004), where Ω_0, Ω, H_0, k, M, J_B, T and W are the steady-state angular velocity, bit angular velocity, hook load, torsional stiffness of the drillpipe, mass of BHA, moment of inertia of BHA, TOB, and WOB. The cutting process introduced a delay in the equations of motion which was ultimately responsible for the existence of self-excited vibrations, exhibiting stick-slip oscillations under certain conditions. One of the limitations of the model is that the simulation stops when the bit lifts off and loses bit-rock contact. Furthermore, the model reduced the drillstring to a two degree of freedom system.

Zamanian *et al.* (2007) presented a discrete model of the drillstring which includes a rotary table at the top with torsional degrees of freedom, a BHA with torsional and axial degrees of freedom and an interaction law between the rock and drag bit. In more details, it was assumed that drill collar and bit behave as a rigid body and the moment of inertia of the drill pipe was ignored in comparing with the moment of inertia of the rotary table and BHA. The simplified model is shown in Fig. 3.4(b).

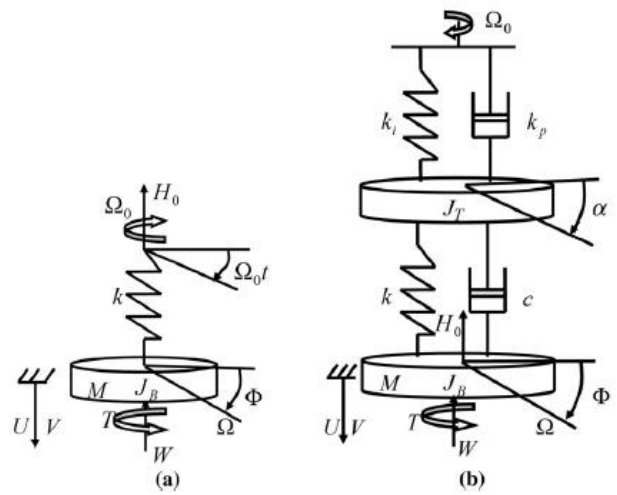

Figure 3.4: (a) Simplified model used by Richard *et al.* (2004), (b) simplified model used by Zamanian *et al.* (2007)

At present, some models are available for analyzing drillstring vibrations, but none of them reflect the actual downhole conditions in drilling operations. A more relevant model should be developed to consider the combined effect of at least axial and torsional vibration modes. Much previous work on drillstring stick-slip was based on a single degree of freedom torsional pendulum, wherein a rigid body with constant mass and moment of inertia was used to model the BHA, and a linear spring to model the drillstring. Although

some previous models provided limited insight into stick-slip and bit-bounce phenomena, the continuum nature of the drillstring has been ignored.

3.1.3 Chapter outline

Several dynamic models related to vertical drillstring vibration modeling have been proposed in the past, however, the majority were developed low order drillstring model and simple rock-bit model. Sarker (2012) introduced a suitable approach for modeling, simulation and control of stick-slip and bit-bounce vibration in a vertical oilwell drillstring where a lumped segment approach was used to develop the drillstring dynamics model. In the lumped segment approach, the system is divided into a number of rigid elements, interconnected with springs. The accuracy of the model depends on the number of elements considered, however, analytical mode shapes and natural frequencies need not be determined. The proposed dynamic model included the mutual dependence of axial and torsional vibrations, and coupling between axial and torsional vibration due to bit-rock interaction. The top drive motor dynamics assumed a DC motor, the developed model accounted for the effect of higher modes, the flow inside and outside the drillpipe and collars, and complicated cutting and friction conditions at the bit/formation interface.

This chapter work will present a 3 phase induction motor dynamic for top drive modeling which is in common use in the drilling industry. A dynamic model for vertical section of a horizontal drilling (well name: CNRL HZ Septimus C9-21-81-19) will be developed in this chapter. The well information is shown in Appx. A. A validation work

with field data will be conducted during building the model. Finally, a demonstration of vertical section drilling bond graph model will be presented.

3.2 Bond graph overview

Bond graphs are an explicit graphical tool for capturing the common energy structure of systems and can increase one's insight into system behavior. In the vector form, they give concise description of complex systems. Moreover, the notation of causality provides a tool not only for formulation of system equations, but also for intuition – based discussion of system behavior, viz. controllability, observability, fault diagnosis, etc. (Samantaray, 2006).

Bond graphs were introduced by Henry M. Paynter, professor at MIT & UT Austin, who, with introduction of the junctions in April 1959, concluded a period of about a decade in which most of the underlying concepts were formed and put together into a conceptual framework and corresponding notation. In the 1960's the notation was further elaborated by his students, in particular Dean C. Karnopp, later professor at UC Davis, and Ronald C. Rosenberg, later professor at Michigan State University who also designed the first computer tool (ENPORT) that supported simulation of bond graph models. Jan J. van Dixhoorn, professor at the University of Twente, NL and Jean U. Thoma (1975) professor at the University of Waterloo, Ont. were the first to introduce bond graphs in Europe (Breedveld, 2003).

These pioneers in the field and their students have been spreading these ideas worldwide. Jan van Dixhoorn realized that an early prototype of the block-diagram-based software TUTSIM could be used to input simple casual bond graphs, which, about a decade later, resulting in a PC-based tool. This laid the basis for the development of the truly port-based computer tool 20-sim at the University of Twente (*www.20sim.com*). He also initiated research in modeling more complex physical systems, in particular thermo-fluid systems.

In the last three decades bond graphs either have been a topic of research or are being used in research at many universities worldwide and are part of (engineering) curricula at a growing number of universities.

3.2.1 Bond graph modeling formalism

In bond graphs (Karnopp *et al.*, 1990), generalized inertias and capacitance store energy as a function of the system state variables, sources provide inputs from the environment, and generalized resistors remove energy from the system. The state variables are generalized momentum and displacement for inertias and capacitances, respectively. The time derivatives of generalized momentum p and displacement q are generalized effort e and flow f. Table 3.1 expresses the generalized power (effort and flow) variables and energy (momentum and displacement) variables in the terminology of common engineering disciplines. Power-conserving elements allow changes of state to take place. Such elements include power-continuous generalized transformer (TF) and gyrator (GY)

elements that algebraically relate elements of the effort and flow vectors into and out of the element. In certain cases, such as large motion of rigid bodies in which coordinate transformations are functions of the geometric state, the constitutive laws of these power-conserving elements can be state modulated. Dynamic force equilibrium and velocity summations in rigid body systems are represented by power-conserving elements called 1 and 0 junctions, respectively.

Table 3.1: Generalized bond graph quantities (Rideout *et al.* 2008)

Variable	General	Translation	Rotation
Effort	$e(t)$	Force	Torque
Flow	$f(t)$	Velocity	Angular Velocity
Momentum	$p = \int e\,dt$	Linear momentum	Angular momentum
Displacement	$q = \int f\,dt$	Displacement	Angular displacement
Energy	$E(p) = \int^{p} f\,dp$ $E(q) = \int^{q} e\,dq$	Kinetic potential	Kinetic Potential

Sources represent ports through which the system interacts with its environment. The power-conserving bond graph elements - TF, GY, 1 junctions, 0 junctions, and the bonds that connect them - are collectively referred to as “junction structure”. Table 3.2 defines the symbols and constitutive laws of sources, storage and dissipative elements, and power-conserving elements in scalar form. Bond graphs may also be constructed with the constitutive laws and junction structure in matrix-vector form, in which case the bond is indicated by a double line.

Table 3.2: Bond graph elements (Rideout *et al.* 2008)

Variable	Symbol	Constitutive law (Linear)	Causality Constraints
		Sources	
Flow	Sf	$f = f(t)$	Fixed flow out
Effort	Se	$e = e(t)$	Fixed effort out
		Energetic elements	
Inertia	I	$f = \frac{1}{I}\int e\,dt$	Preferred integral
	I	$e = I\frac{df}{dt}$	
Capacitor	C	$e = \frac{1}{C}\int f\,dt$	Preferred integral
	C	$f = C\frac{de}{dt}$	
Resistor	R	$e = Rf$	None
	R	$f = \frac{1}{R}e$	
		Port elements	
Transformer	1 TF 2, n	$e_2 = ne_1$ $f_1 = nf_2$	Effort in-effort out or Flow in-flow out
Modulated transformer	θ, MTF, n(θ)	$e_2 = n(\theta)e_1$ $f_1 = n(\theta)f_2$	
Gyrator	1 GY 2, n	$e_2 = nf_1$ $e_1 = nf_2$	Flow in-effort out or Effort in-flow out
Modulated Gyrator	θ, MGY, n(θ)	$e_2 = n(\theta)f_1$ $e_1 = n(\theta)f_2$	
		Constraint nodes	
1 junction	1 2, 3	$e_2 = e_1 - e_3$ $f_1 = f_2 = f_3$	One flow input
0 junction	1 0 2, 3	$f_2 = f_1 - f_3$ $e_1 = e_2 = e_3$	One effort input

Power bonds contain a half-arrow that indicates the direction of algebraically positive power flow, and a causal stroke normal to the bond that indicates whether the effort or flow variable is the input or output from the constitutive law of the connected elements. The constitutive laws in Table 3.2 are consistent with the placement of the causal strokes. Full

arrows are reserved for modulating signals that represent powerless information flow such as orientation angles that determine the transformation matrix between a body-fixed and inertia reference frame.

3.3 Modeling of top drive motor dynamics

Usually the top drive consists of one or more motors (electric and hydraulic) connected with appropriate gearing to a short section of pipe, which in turn may be screwed into the drillstring. In this research work a bond graph model for AC induction motor has been presented to simulate the top drive system. A physical schematic of three phase induction motor is shown in Fig. 3.5.

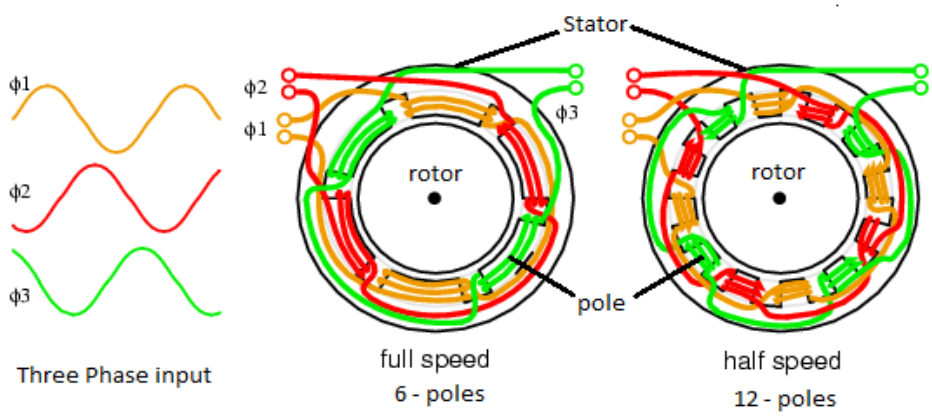

Figure 3.5: A physical sketch of three phase induction motor (http://www.learningelectronics.net)

The bond graph model of an induction motor is developed using the equivalent circuits depicted in Fig. 3.6. The inductive coupling between the stator and rotor are considered in the α-β fixed reference frame (Fig. 3.7) attached to the stator. The linear relationships

between the stator flux linkages and currents, and rotor flux linkages and currents are represented in terms of self and mutual inductance parameters and these relationships are implemented using generalized inertia (*I*) fields in the bond graph (Karnopp, 2003). Fig. 3.8 shows the coupling between the stator and rotor state variables.

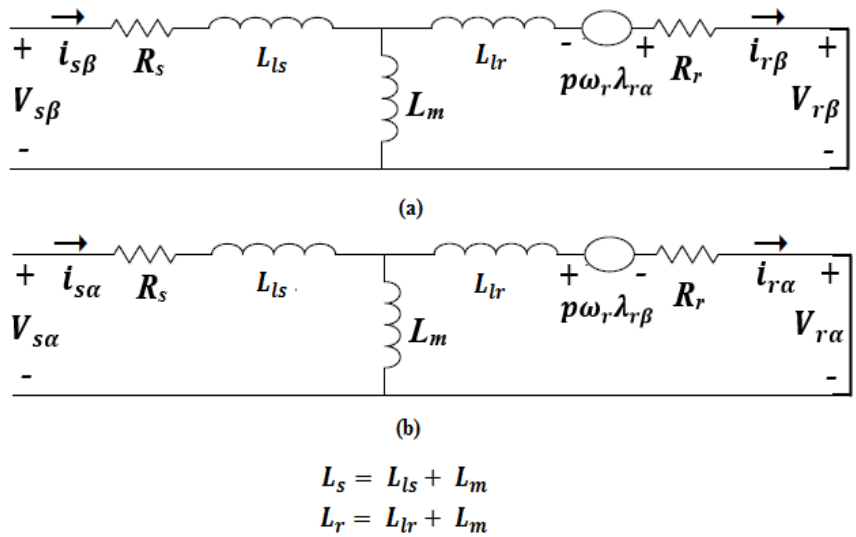

$$L_s = L_{ls} + L_m$$
$$L_r = L_{lr} + L_m$$

Figure 3.6: Equivalent circuit of an induction motor in (a) α axis and (b) β axis

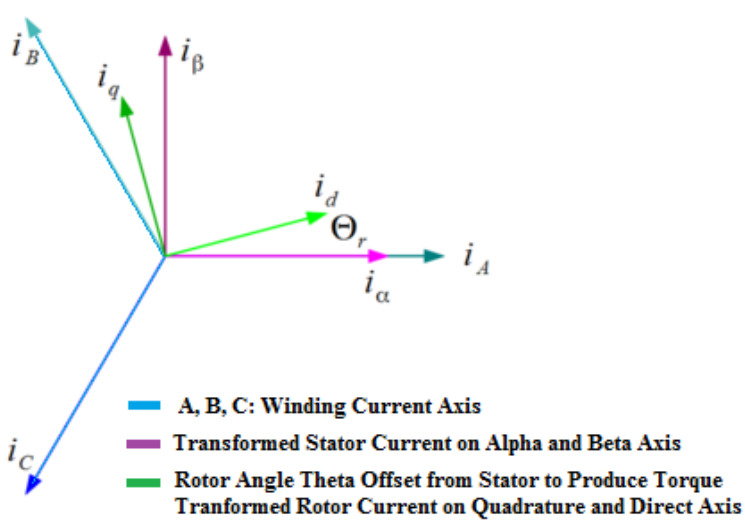

Figure 3.7: A sketch of induction motor different coordinate systems

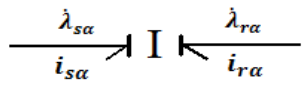

$$\begin{bmatrix} i_{s\alpha} \\ i_{r\alpha} \end{bmatrix} = \left(\frac{1}{L_r * L_s - L_m{}^2}\right) \begin{bmatrix} L_r & -L_m \\ L_m & L_s \end{bmatrix} \begin{bmatrix} \lambda_{s\alpha} \\ \lambda_{r\alpha} \end{bmatrix}$$

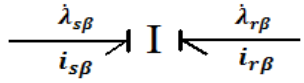

$$\begin{bmatrix} i_{s\beta} \\ i_{r\beta} \end{bmatrix} = \left(\frac{1}{L_r * L_s - L_m{}^2}\right) \begin{bmatrix} L_r & -L_m \\ L_m & L_s \end{bmatrix} \begin{bmatrix} \lambda_{s\beta} \\ \lambda_{r\beta} \end{bmatrix}$$

Figure 3.8: I-field Relations and causalities for the rotor and the stator in the α-β axis

The electromagnetic torque and the induced voltages are calculated using Eqs. 3.1-3.11 which are derived from the equivalent circuits (Karnopp, 2003; Ozpineci and Tolbert, 2003).

$$\begin{bmatrix} V_a \\ V_b \\ V_c \end{bmatrix} = \sqrt{\frac{2}{3}} \begin{bmatrix} \sin(2\pi ft) \\ \sin\left(2\pi ft - \frac{2\pi}{3}\right) \\ \sin\left(2\pi ft + \frac{2\pi}{3}\right) \end{bmatrix} \tag{3.1}$$

$$\begin{bmatrix} V_{s\alpha} \\ V_{s\beta} \end{bmatrix} = \sqrt{\frac{2}{3}} \begin{bmatrix} 1 & -\frac{1}{2} & -\frac{1}{2} \\ 0 & -\frac{\sqrt{3}}{2} & \frac{\sqrt{3}}{2} \end{bmatrix} \tag{3.2}$$

$$V_{s\beta} = R_s I_{s\beta} + \frac{\mathrm{d}\lambda_{s\beta}}{\mathrm{dt}} \tag{3.3}$$

$$V_{s\alpha} = R_s I_{s\alpha} + \frac{\mathrm{d}\lambda_{s\alpha}}{\mathrm{dt}} \tag{3.4}$$

$$V_{r\beta} = 0 = R_r I_{r\beta} + \frac{\mathrm{d}\lambda_{r\beta}}{\mathrm{dt}} - \mathrm{p}\omega_r \lambda_{r\alpha} \tag{3.5}$$

$$V_{dr} = 0 = R_r I_{dr} + \frac{\mathrm{d}\lambda_{dr}}{\mathrm{dt}} + \mathrm{p}\omega_r \lambda_{r\beta} \tag{3.6}$$

$$\lambda_{s\beta} = I_{s\beta} L_s + I_{r\beta} L_m \tag{3.7}$$

$$\lambda_{s\alpha} = I_{s\alpha} L_s + I_{r\alpha} L_m \tag{3.8}$$

$$\lambda_{r\beta} = I_{r\beta} L_r + I_{s\alpha} L_m \tag{3.9}$$

$$\lambda_{r\alpha} = I_{r\alpha} L_r + I_{s\beta} L_m \tag{3.10}$$

$$T_e = p\left(\lambda_{r\alpha} I_{s\beta} - \lambda_{r\beta} I_{r\alpha}\right) \tag{3.11}$$

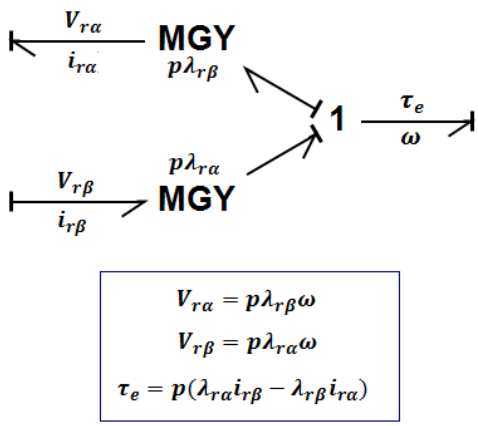

Figure 3. 9: Gyrator structure for torque and induced voltages

The electromagnetic torque Eq. 3.11 contains the flux and current terms. A gyrator structure for the torque and induced voltages is illustrated in Fig. 3.9. The modulated gyrator enforces the relations between the electromagnetic torque τ_e and the α-β axis

currents ($i_{r\alpha}$ and $i_{r\beta}$) as well as the relation between the induced voltages ($V_{r\alpha}$ and $V_{r\beta}$) and the rotor angular speed ω_r.

Fig. 3.10 presents the complete bond graph model of an induction motor based on its electrical equivalent circuit Eqs. 3.10-3.11. Four fluxes ($\lambda_{s\alpha}$, $\lambda_{r\alpha}$, $\lambda_{s\beta}$ and $\lambda_{r\beta}$) and the angular momentum of the rotor are used as the state variables. Commercial bond graph software is used to automate the generation of state equations (Karnopp *et al.* 1999). The proposed induction motor model has been driven by a three phase fixed frequency balanced ac supply. Modulated transformers MTF: m_1, MTF: m_2, MTF: m_3, MTF: m_4, MTF: m_5 with moduli $m_1 = \sqrt{2/3}$, $m_2 = -\sqrt{1/6}$, $m_3 = -\sqrt{1/6}$, $m_4 = -\sqrt{1/2}$, $m_5 = \sqrt{1/2}$ have been employed to implement the mathematical transform of Eq. 3.2. Effort sources Se: V_a, Se: V_b, and Se: V_c having sinusoidal voltages with equal amplitude but with corresponding phase angles of 0, -2π/3, 2π/3 phase angles, respectively, have been used to excite the system. Figs. 3.11-3.14 show the plot of the input voltages V_a, V_b and V_c.

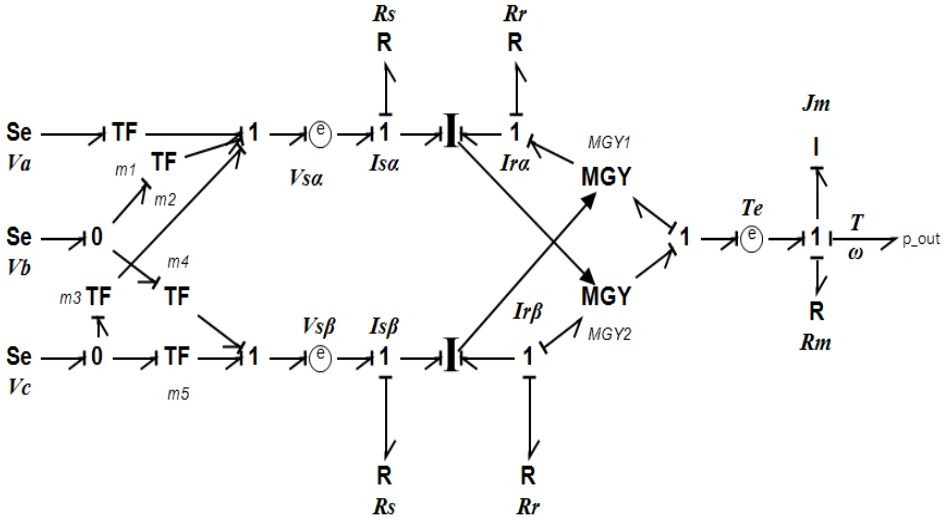

Figure 3.10: Bond graph model of an Induction motor

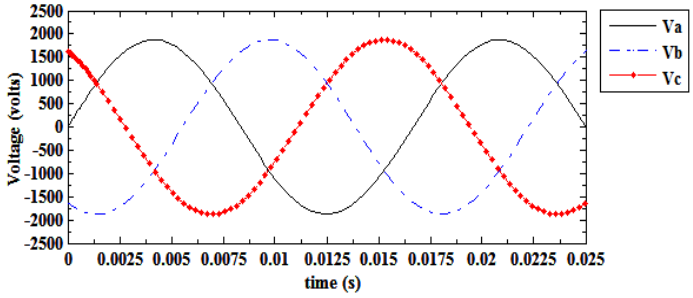

Figure 3.11: Phase lags between the three phase input voltage.

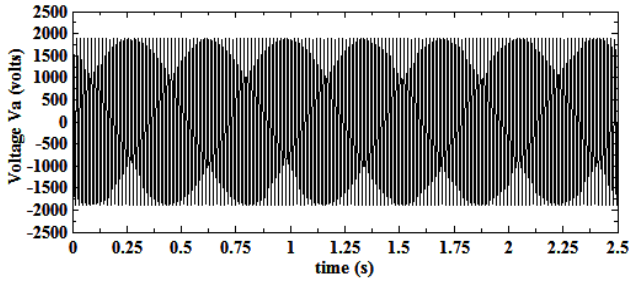

Figure 3.12: Input voltage V_a plot

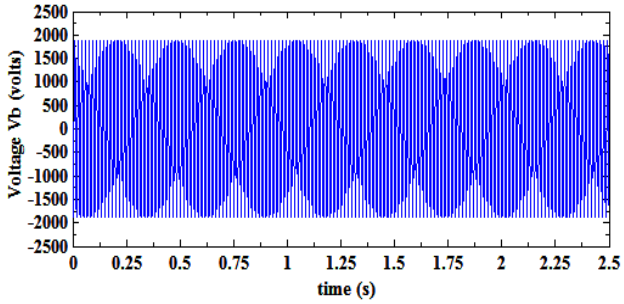

Figure 3.13: Input voltage V_b plot

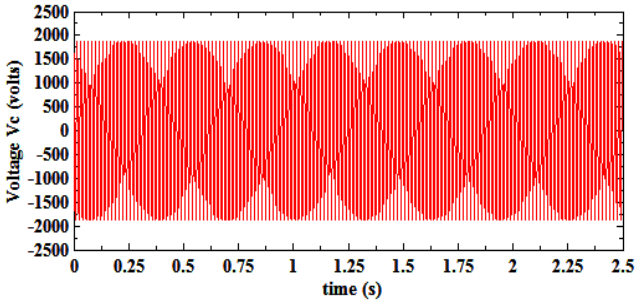

Figure 3.14: Input voltage V_c plot

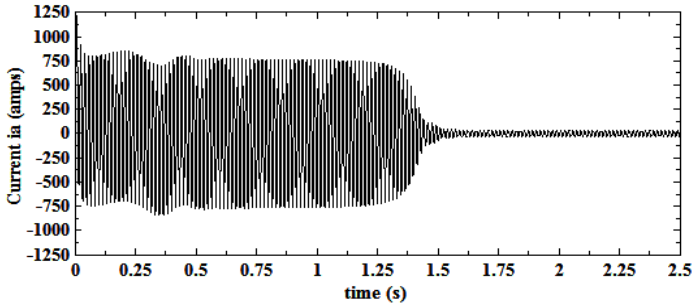

Figure 3.15: Current i_a of the induction motor

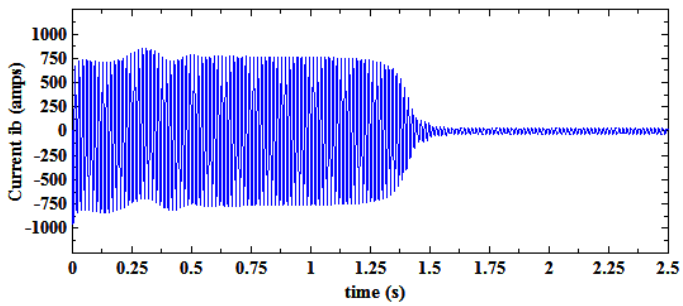

Figure 3.16: Current i_b of the induction motor

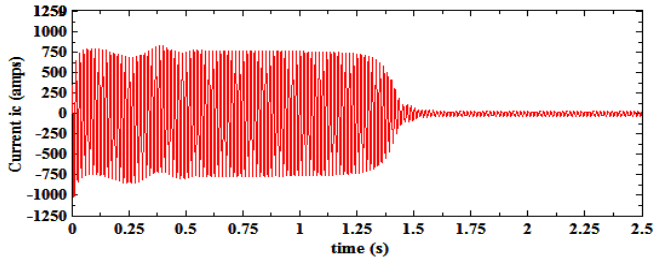

Figure 3.17: Current i_c of the induction motor.

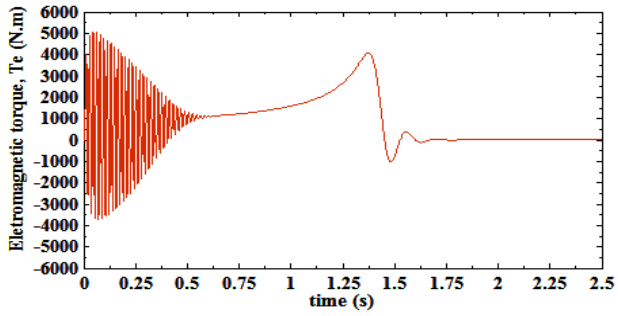

Figure 3.18: Electromagnetic torque of the induction motor at no load.

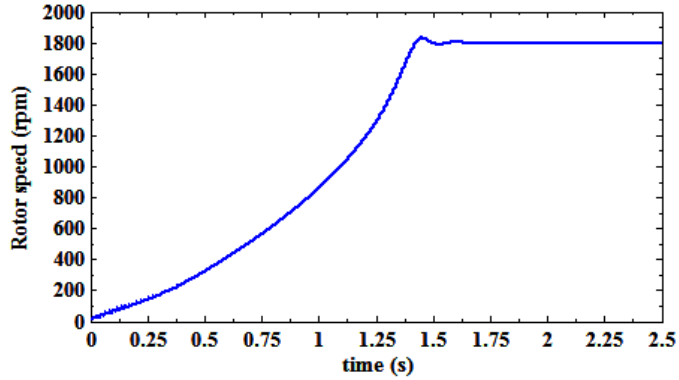

Figure 3.19: Run-up response of the induction motor at no load.

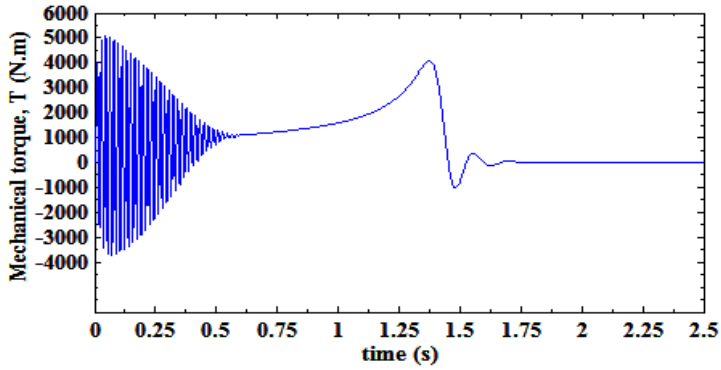

Figure 3.20: Torque of the induction motor at no load.

Figs. 3.15-3.20 present the no-load responses from the bond graph model of a 500 hp induction motor (3-phase, 4 pole, 2300 V). The simulation data of induction motor is shown in table B.1. Figs. 3.18 and 3.19 illustrate electromagnetic torque and the run-up response of the induction motor respectively. The fluctuation in the electromagnetic torque curve shown in Fig. 3.18 has been identified at the beginning of the simulation during the transient period. Also the transient has been verified from the motor current plot shown in Figs. 3.15-3.17. The simulation results show that the proposed bond graph model of ac induction motor provides acceptable accuracy to capture the motor dynamics. In the next section, the modeling of drillstring axial and torsional dynamics will be presented.

3.4 Modeling of drillstring axial dynamics

The main elements in a horizontal drilling vertical section drillstring that are considered in this model are shown in Fig. 3.21. From the figure, several kinds of elements are distinguished: cable and derrick modeled as a lumped spring; swivel and traveling block modeled as lumped mass; kelly pipe (Fig. 3.22), drill pipe (DP); and heavy weight drill pipe (HWDP) or drill collar (Fig. 3.24) modeled as rigid inertias and linear springs of longitudinal stiffness and longitudinal damping; and the bit. Fig. 3.21 shows the drilling mud flow in the drilling system; the mud flow inside the drillstring is downward and for the annulus the flow is upward. The terms V_P and V_a in Fig. 3.21 indicate drilling mud velocity inside the drill pipe and the annulus, respectively. For the drill collar modeling the values of V_P and V_a will be different, because they depend on the drill pipe/collar and wellbore geometry. Fig. 3.25 shows the schematic of a drill pipe/collar axial segment model and the FBD of a drill pipe/collar axial segment. A drill pipe/collar bond graph model segment is shown in Fig. 3.26. Buoyancy, which is a surface force acting on a body in the opposite direction of the gravitational force, has been included in the drillstring segment to capture the effect of drilling mud density. Hydrodynamic damping due to drilling fluid circulation in the drill pipe and the annular space is considered in the drill pipe and collar model instead of viscous damping (Eronini, 1978).

Nonlaminar newtonian flow formulations are used in calculation of fluid drag force/damping for the axial model. These result in simple expressions which may also approximate laminar flow conditions provided appropriate values of the pertinent variables are used. Fig. 3.21 shows the drilling mud flow in a conventional vertical drillstring.

Ignoring any eccentric location of the drill string in the wellbore, the pressure drop in the annulus between the borehole and a stationary drill pipe can be written as (Eronini, 1978)

$$\Delta P = \frac{\alpha_a \, \rho_m \, Q^2 \, dx}{4 \, \pi^2 \left(r_w - r_0\right) \left(r_w^2 - r_0^2\right)^2} \tag{3.12}$$

Where α_a = Weisbach friction factor; outside drill pipe or collar

ρ_m = drilling mud density

Q = volume rate of flow of drilling mud

dx = drill pipe or collar segment length

r_w = wellbore radius

r_o = external radius of drillpipe or collar

The resulting longitudinal force, F_A (positive down) exerted on the drillstring segment which is moving with velocity V_n can be written as below (Eronini, 1978)

$$F_A = -\left\{\frac{\alpha_a \, \rho_m \, \pi \left(r_w + r_0\right) \, dx}{4}\right\} \left|\left[\frac{Q}{\pi \left(r_w^2 - r_0^2\right)}\right] + V_n\right| \left\{\left[\frac{Q}{\pi \left(r_w^2 - r_0^2\right)}\right] + V_n\right\} \tag{3.13}$$

and the drag force on the drillstring due to flow in the drillpipe is given by (Eronini, 1978)

$$F_p = -\left\{\frac{\alpha_p \, \rho_m \, \pi \, r_i \, dx}{4}\right\} \left|\frac{Q}{\pi \, r_i^2} - V_n\right| \left\{\frac{Q}{\pi \, r_i^2} - V_n\right\} \tag{3.14}$$

Where α_p = Weisbach friction factor; inside drill pipe or collar

r_i = internal radius of drillpipe or collar

Eqs. 3.13 and 3.14 are applied to the axial model (Fig. 3.23) for adding the effect of drilling fluid (mud) on the drillstring dynamic response. From Fig. 3.25, when segment i moves with a velocity V_i downward then the inertia force $M_i\dot{V}_i$ will be upward, the drag forces F_A and F_P ($V_p > V_i$) will be upward and downward respectively, and the weight M_i g will be always downward.

The bond graph segment model shown in Fig. 3.26 can be written in term of "Cauchy" form ordinary differential equations (ODE) for analysis and simulation. And the set of equations are written as below.

$$\dot{p}_i = M_i\dot{V}_i = F_{i-1} - F_i + M_i g + F_p - F_A \tag{3.15}$$

$$\dot{q}_i = V_{i+1} - V_i \tag{3.16}$$

$$V_i = \frac{1}{M_i} p_i \tag{3.17}$$

$$F_i = \frac{1}{C_i} q_i + R_i \left(V_{i+1} - \frac{1}{M_i} p_i \right) \tag{3.18}$$

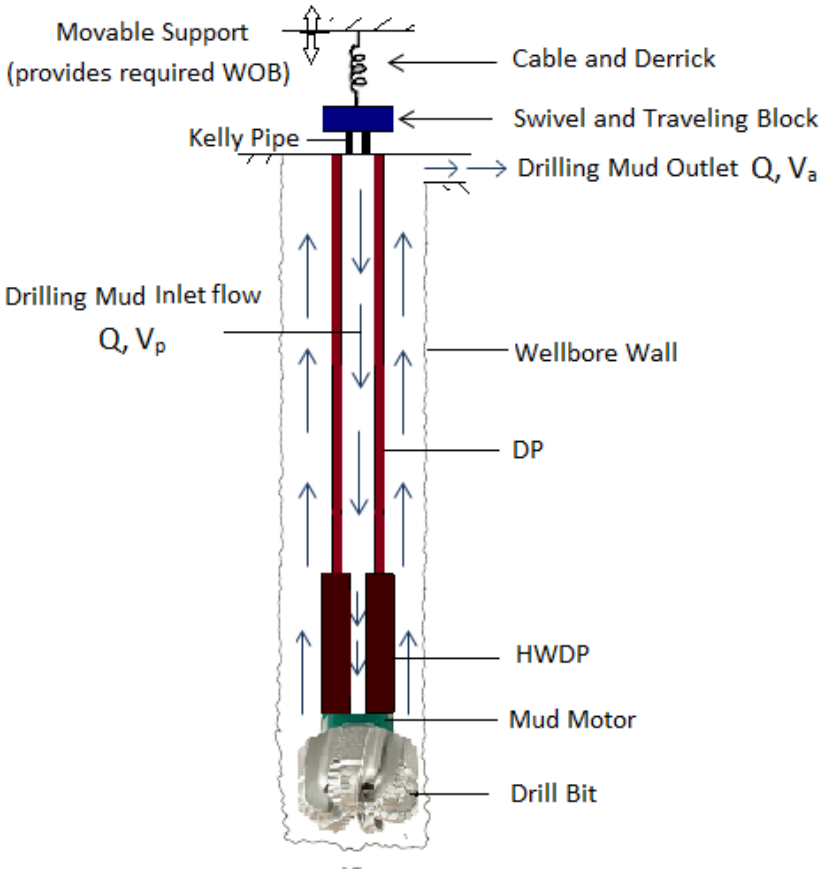

Figure 3.21: Schematic of drillstring used in rotary drilling modeling and simulation

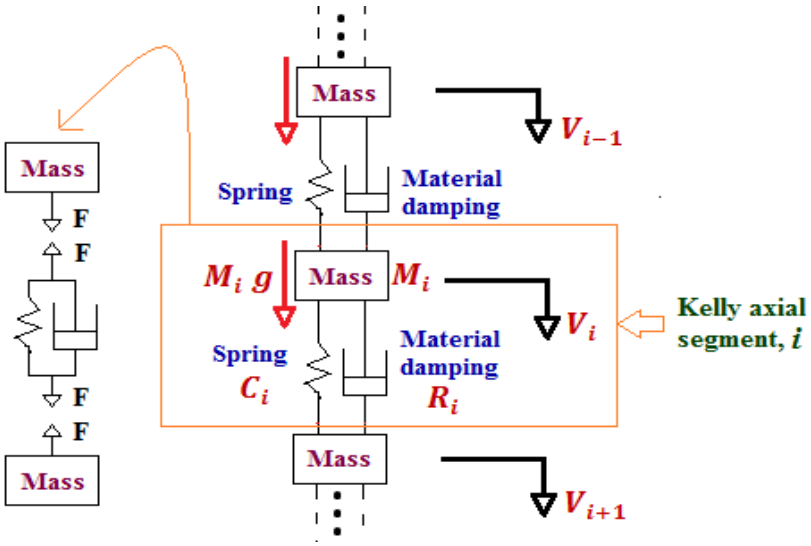

Figure 3.22: Schematic of kelly axial segment

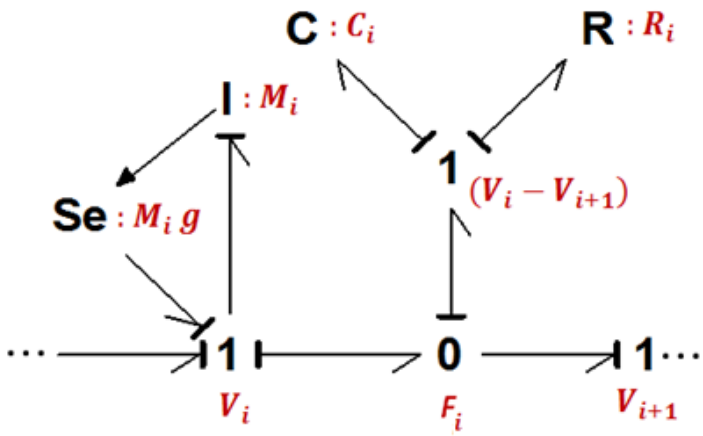

Figure 3.23: Bond graph axial model segment of kelly

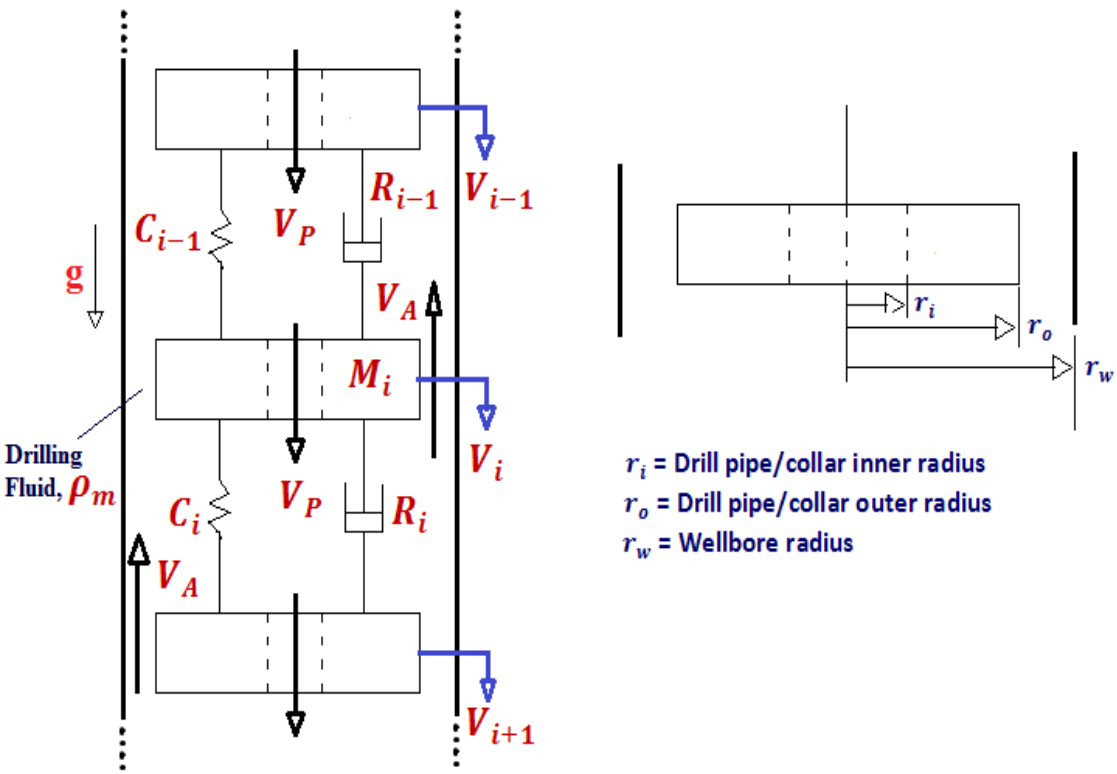

Figure 3.24: Schematic of drill pipe/collar lumped segment model showing drilling fluid flow.

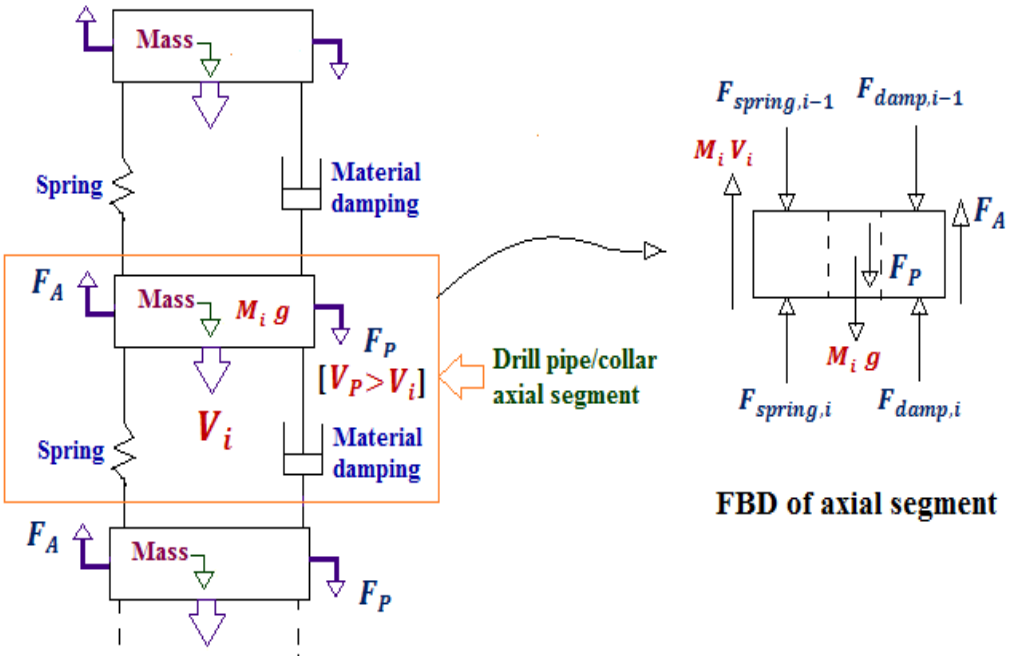

Figure 3.25: Schematic of drill pipe/collar axial segment model.

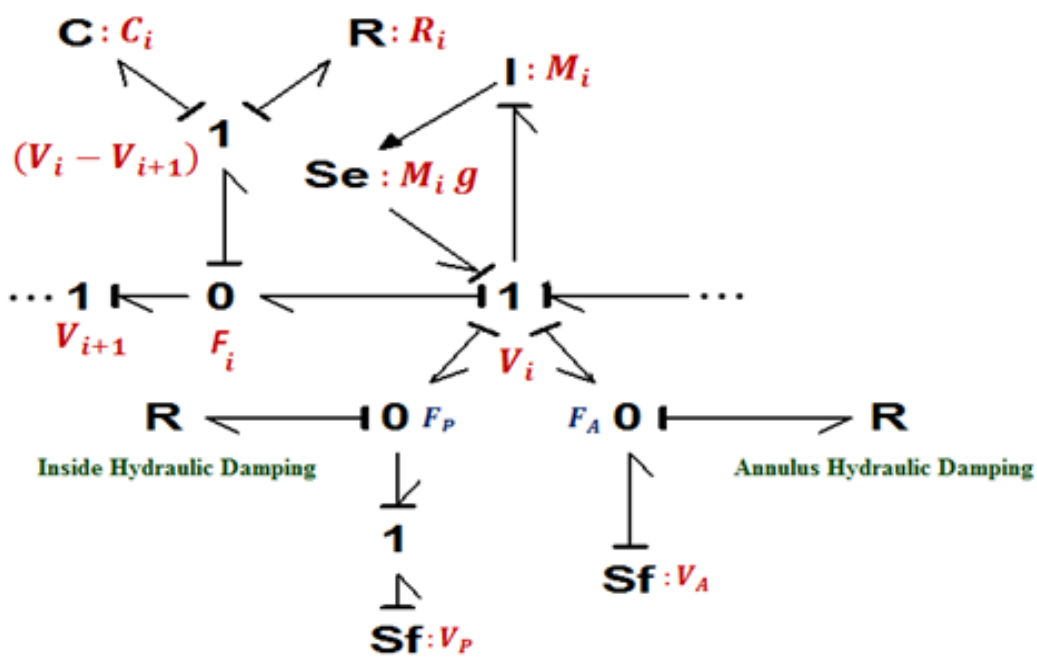

Figure 3.26: Bond graph axial model segment of drill pipe/collar

3.5 Modeling of drillstring torsional dynamics

The kelly pipe, drill pipe (DP), heavy weight drill pipe (HWDP) and drill collar are modeled as rigid inertias and linear springs of torsional stiffness and torsional damping. The schematics of kelly and drill pipe/collar torsional segments are shown in Figs. 3.27 and 3.29, respectively. Figs. 3.28 and 3.30 depicts torsional dynamic submodels for kelly and drill pipe/collar segments. The drill pipe and drill collar dynamic models consider viscous damping which results from the contact between drillstring surfaces and the drilling fluid (Eronini, 1978). With the exception of the details of fluid friction, the torsional model and bond graphs are rotational analogs of the axial models.

The schematic of rotational fluid friction resistance/viscous damping is shown in Fig. 4.29. Again, ignoring any nonconcentric drillpipe location in the borehole, a simple expression for the fluid torque is given by Eronini (1978) and Yigit and Christoforou (2006)

$$T_{R_n} = \left(R_{Viscous}\right)_n dx_n \, \omega_n \tag{3.19}$$

where $R_{Viscous}$ indicates viscous damping per unit length of drillpipe/collar and it can be written as,

$$R_{Viscous} = \frac{2\pi \mu_e r_0^3}{r_w - r_0} \tag{3.20}$$

where μ_e = equivalent viscosity for fluid resistance to rotation.

The bond graph segment model shown in Fig. 3.30 can be written in term of "Cauchy" form ODE for analysis and simulation and are written as below.

$$\dot{p}_i = J_i \dot{\omega}_i = T_{i-1} - T_i - T_{R_i} \tag{3.21}$$

$$\dot{q}_i = \omega_{i+1} - \omega_i \tag{3.22}$$

$$\omega_i = \frac{1}{J_i} p_i \tag{3.23}$$

$$T_i = \frac{1}{C_i} q_i + R_i \left(\omega_{i+1} - \frac{1}{J_i} p_i \right) \tag{3.24}$$

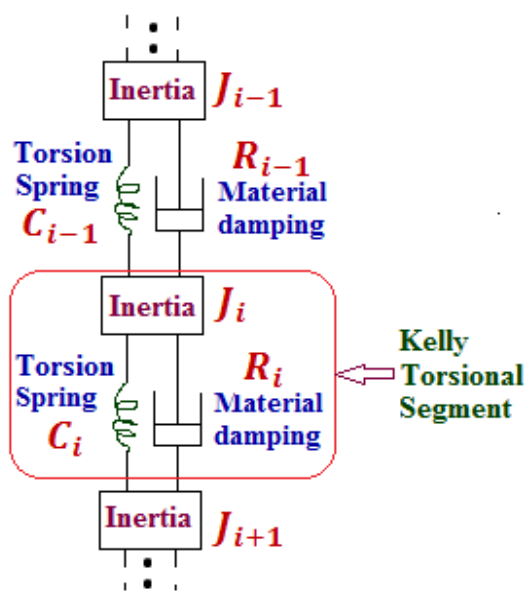

Figure 3.27: Schematic of kelly torsional segment

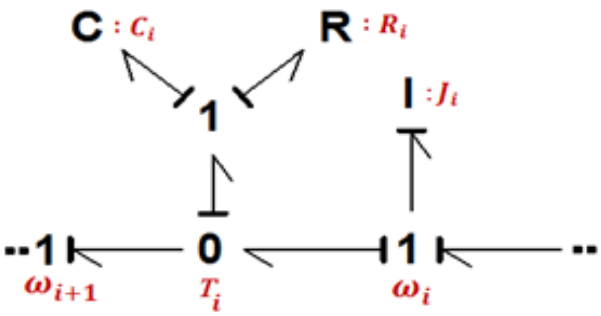

Figure 3.28: Bond graph torsional model segment of kelly

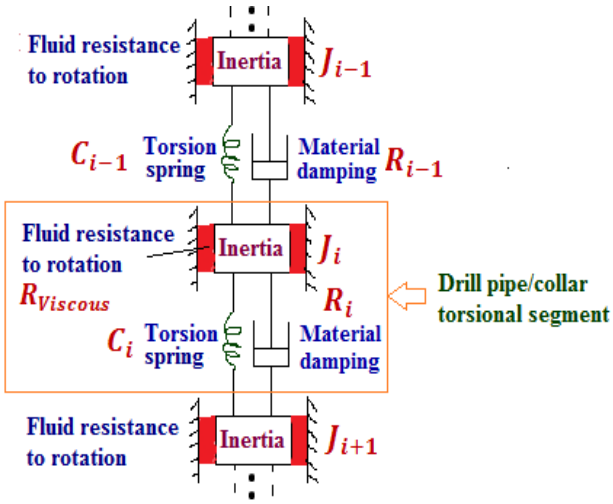

Figure 3.29: Schematic of drill pipe/collar torsional segment

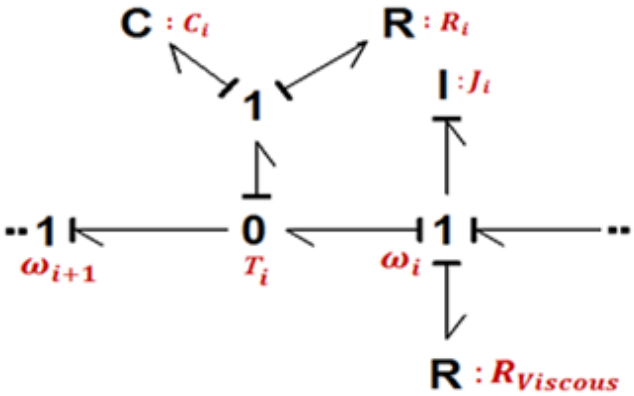

Figure 3.30: Bond graph torsional model segment of drill pipe/collar

3.6 Bit-rock interaction model

The bit-rock interaction provides coupling between axial and torsional drillstring dynamics. In this present work, a quasi-static rock-bit model is used instead of a computationally intensive and difficult-to-parameterize complete dynamic representation. Yigit and Christoforou (2006) have developed a static bit-rock interaction model in a drillstring represented using only two inertias and one compliance for both axial and torsional vibration. Their model is modified as described below and as given graphically in Fig. 3.31. The original model in (Yigit and Christoforou, 2006) assumed both friction and cutting torque regardless of whether or not the dynamic weight on the bit was sufficient to create penetration and cuttings. Depth of cut was a function of average rather than instantaneous rotation speed, along with rate of penetration (ROP). ROP was a function of average rotation speed and a constant applied WOB, rather than dynamic WOB. The current model incorporates threshold force and the effect of instantaneous WOB and bit rotation speed on cutting torque on bit (TOB). Below a threshold force W_{fs}, the drill tool does not penetrate into the rock, leaving only friction as a source of TOB. The model equations are presented in two parts. First, the dynamic WOB, which is the axial force applied at the bit under dynamic conditions is given as Yigit and Christoforou (2006).

$$\mathrm{WOB} = \begin{cases} \mathrm{k_c}\left(x - s\right) & \text{if } x \geq s \\ 0 & \text{if } x < s \end{cases} \tag{3.25}$$

Where k_c and s indicate formation contact stiffness and bottom-hole surface profile. Surface profile is given as Yigit and Christoforou (2006)

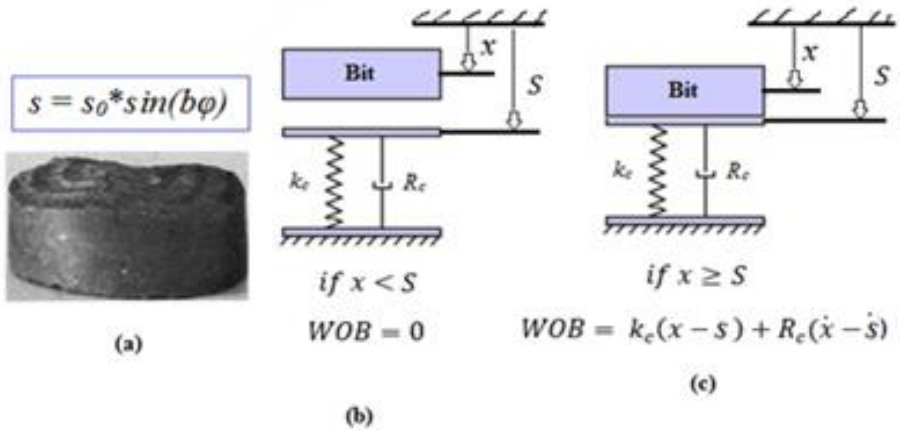

Figure 3.31: sketches show (a) a lobe pattern of formation surface elevation (courtesy of A. Scovil Murray), (b) bit and rock spring-damper representation when x < s and (c) bit contacts with rock when x > s and rock spring and damper under compression and generates an applied upward force to drillstring.

$$s = s_0 \, f(\varphi) \tag{3.26}$$

The formation elevation function $f(\varphi)$ is chosen to be sinusoidal as in Yigit and Christoforou (2006), $f(\varphi) = sin(b\varphi)$, where b indicates bit factor which depends on the bit type. The term φ indicates rotational displacement of the bit. The total torque on bit (TOB) is related to frictional and cutting conditions, and dynamic WOB. When bit rotary speed is in the positive direction then TOB can be written as

$$\mathrm{TOB} = \begin{cases} \mathrm{TOB}_f + \mathrm{TOB}_C & WOB > \mathrm{W}_{fs} \\ \mathrm{TOB}_f & WOB \le \mathrm{W}_{fs} \end{cases} \tag{3.27}$$

In the case of zero bit rotary speed,

$$\mathrm{TOB} = \begin{cases} \mathrm{TOB}_C & WOB > \mathrm{W}_{fs} \\ 0 & WOB \le \mathrm{W}_{fs} \end{cases} \tag{3.28}$$

Finally, for negative bit rotary speed,

$$\mathrm{TOB} = \mathrm{TOB}_f \tag{3.29}$$

Where TOB_f and TOB_c represent frictional and cutting torque on bit and both are calculated as below,

$$\mathrm{TOB}_f = (\mathrm{WOB}) r_b \mu(\dot{\varphi}) \tag{3.30}$$

$$\mathrm{TOB}_C = (\mathrm{WOB}) r_b \xi \sqrt{\frac{\delta_C}{r_b}} \tag{3.31}$$

The term $\dot{\varphi}$ indicates instantaneous bit rotary speed, and the function $\mu(\dot{\varphi})$ characterizes the friction process at the bit and it is given as Yigit and Christoforou (2006)

$$\mu(\dot{\varphi}) = \mu_0 \left(\tanh \dot{\varphi} + \frac{\alpha \dot{\varphi}}{\left(1 + \beta \dot{\varphi}^{2\gamma}\right)} + \nu \dot{\varphi} \right) \tag{3.32}$$

Where μ_o, α, β, γ, and ν are the experimentally-determined parameters of the frictional model. In equation (3.31) the terms r_b and δ_c indicate bit radius and depth of cut per revolution, the latter given as

$$\delta_C = \frac{2\pi \mathrm{ROP}}{\dot{\varphi}} \tag{3.33}$$

The instantaneous ROP is a function of dynamic WOB, instantaneous bit speed $\dot{\varphi}$, and rock/bit characteristics. The modified ROP equation from Yigit and Christoforou (2006) can be written as

$$\mathrm{ROP} = C_1 \mathrm{WOB} \sqrt{\dot{\varphi}} + C_2 \tag{3.34}$$

Where ζ, C_1 and C_2 characterize the cutting action at the bit and depend on the type of the bit and formation.

3.7 A demonstration of vertical well

The bond graph model of the vertical rotary drilling system in Fig. 3.32 has been developed in the commercial bond graph modeling software 20-sim® (*http://www.20sim.com/*). With 20-sim®, models can be entered as equations, block diagrams, bond graphs and physical components. 20-sim is widely used for modeling complex multi-domain systems and the development of control systems. The developed bond graph model for simulation has been three main parts: axial dynamic model, torsional dynamic model and bit-rock model. The input (flow excitation) of the torsional model depends on the WOB of the axial model. A total of 21 segments are used in the drillstring dynamic model and the selection of the number of segments has been discussed in Sarker (2012). One segment is used for the relatively short kelly, and for both drill pipe and collar, 10 segments are used in the model. Appx. B summarizes all relevant data that is used in the current simulation.

The main objective of this simulation is to show the ability of the proposed model in capturing the axial and torsional vibrations, and more importantly in predicting the effect

of drilling parameters (such as top drive speed, downhole mud motor speed, applied WOB etc.) on stick-slip vibrations which is the excessive form of torsional vibrations. The stick-slip vibration of the drillstring is characterized by alternating stops (during which the bit sticks to the rock) and intervals of large angular speed of the bit. Figs. 3.33-3.44 comprises the overall simulation results under different drilling case studies provided by Ryan Directional Services (2012) including drilling at high WOB using a top drive and mud motor and drilling in the absence of downhole mud motor at higher top drive speed and at lower applied WOB conditions. The proposed bond graph model has the capability to pull and push the drillstring from the top boundary condition of the drillstring (similarly the hoisting system) for providing a desired applied WOB to the bit. Fig. 3.33-3.40 presents the simulation results for drilling using a top drive and mud motor based on Ryan Directional Services (2012) drilling data at 1720 m total drilled depth. Simulation results in Fig. 3.34 shows that drill bit rotates smoothly with 14.76 rad/sec or 141 rpm angular speed, which is the combined speeds of top drive and mud motor shown in Fig. 3.33, after experiencing some certain speed fluctuations at the start of drilling. This bit speed fluctuation phenomena can also be verified through surface torque fluctuations shown in Fig. 3.34. Dynamic WOB plotted in Fig. 3.33 also shows higher fluctuations with 100 kN average WOB at the bit rotating speed fluctuation zone and less fluctuation at steady-state bit rotation. The dynamic forces distribution along drillstring segments shown in Figs. 3.36-3.40 show the dynamic forces distribution along the drillstring segments. HWDP segments eight to ten, which are the lower portions of the drillstring, are under compression, whereas the whole DP and HWDP segments one to seven are under tension.

Overall simulation results will be sensitive to the bit cutting coefficient C_1 in equation 3.34 which depends on the bit type. Thus the chosen bit cutting coefficient C_1 requires a validation with field data. Table 3.3 shows that by choosing bit cutting coefficient value C_1 = 4e-8 provides similar on bottom rotary torque to what industry personnel reported in drilling (Ryan Directional Services, 2012).

Fig. 3.42 shows the full model simulation results in the case without a mud motor when the desired top drive rotary speed is 6.28 rad/sec with 100 kN applied WOB. Although the top drive motor appears to maintain the rotary speed as desired, the bit experiences large speed fluctuations evolving into limit cycles. As mentioned earlier, this behavior is known as stick-slip. Also at the same time the torque at surface experiences large fluctuations consistent with stick-slip. In contrast, Fig. 3.34 shows the absence of stick-slip phenomena in bit rotation speed because of using mud motor just behind the bit which increases overall bit rotary speed and increses the frequency of coupled axial-torsional inputs from the rock.

Table 3.3: Section of cutting coefficient (6.28 rad/s top drive speed, 8.48 rad/s downhole mud motor speed and 100 kN applied WOB)

Sources of on-bottom rotary torque	On Bottom Torque (N-m)
Field Data (Ryan Directional Services, 2012)	3000
Simulation (Cutting coefficient C_1 = 1e-8)	1850
Simulation (Cutting coefficient C_1 = 2e-8)	2360
Simulation (Cutting coefficient C_1 = 3e-8)	2750
Simulation (Cutting coefficient C_1 = 4e-8)	3000

Fig. 3.43 shows stick-slip completely eliminated by increasing top drive speed to 14 rad/sec in the case without mud motor. A nearly constant steady-state bit rotation is attained. This is due to the positive slope of the friction behavior curve explained in Yigit and Christoforou (2006). At very low speed, the transition from static to kinetic friction coefficient causes a drop in the frictional torque and the negative slop causes instability in torsional motion. At high speed, the slope of friction torque is found to be positive and suppresses torsional instability.

Fig. 3.44 shows the simulation results in the case without a mud motor when the applied WOB is 50 kN at 6.28 rad/sec top drive speed. Stick-slip vibration is reduced due to decreasing the applied WOB. Equations 3.30 and 3.31 represents the applied TOB which is decreased by lowering the applied WOB. From simulation results it is found that by decreasing applied WOB, increasing desired top drive speed beyond a threshold and using downhole mud motor it may possible to eliminate stick-slip. The results obtained are in excellent agreement with the actual drilling optimization workflow (*http://www.slb.com/*) in the field.

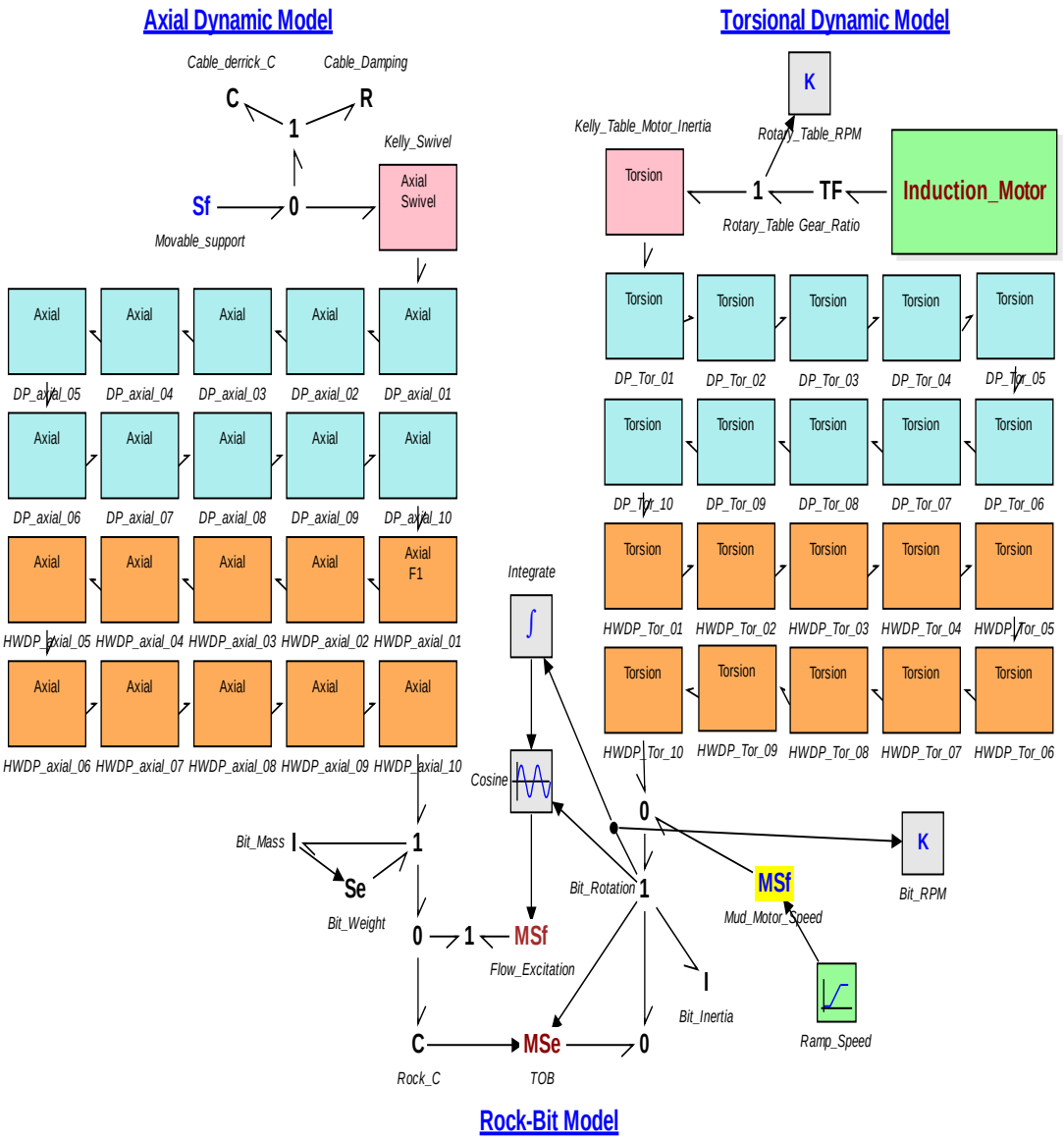

Figure 3.32: Bond graph model for vertical section of CNRL HZ Septimus C9-21-81-19 well.

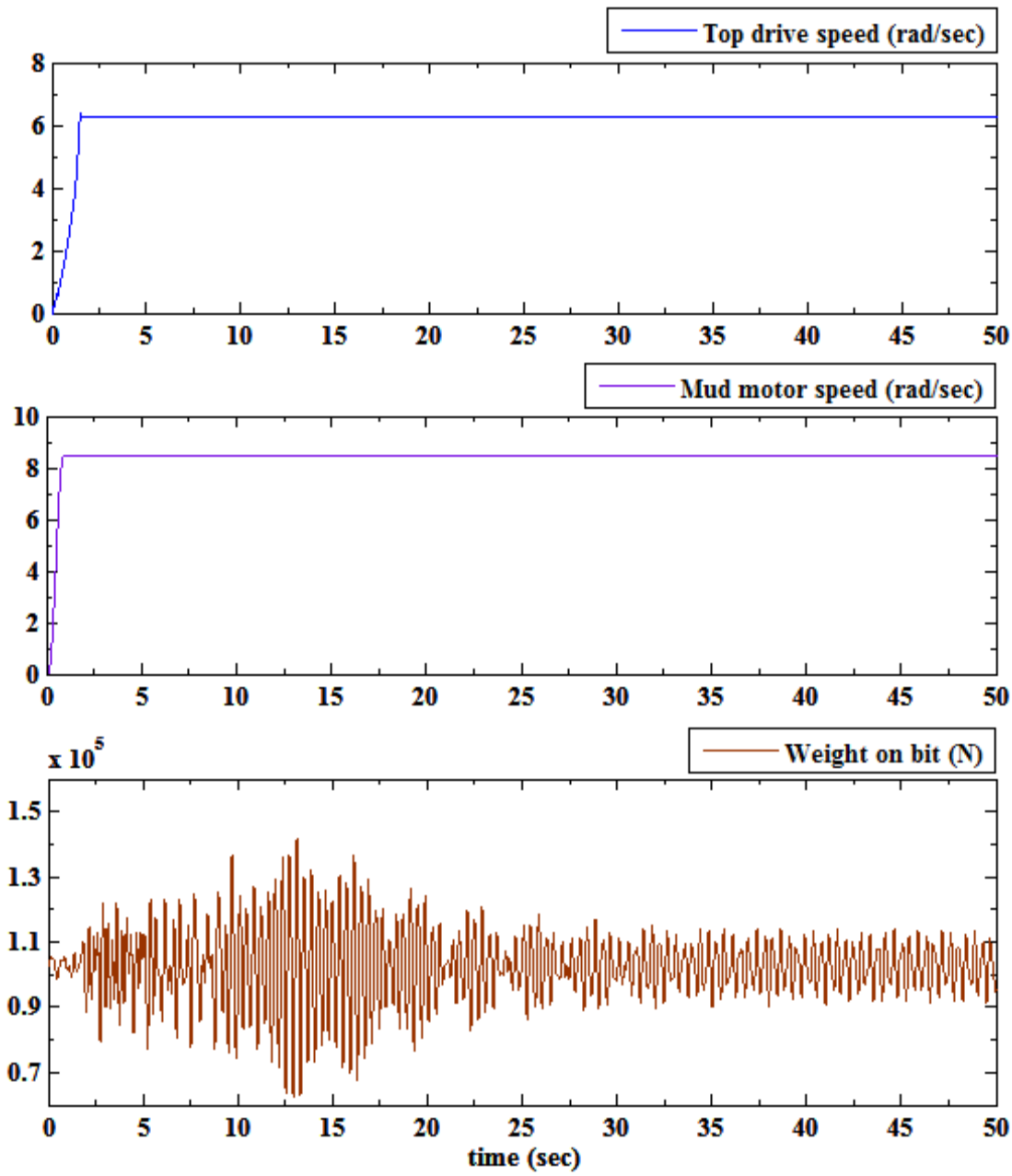

Figure 3.33: Simulation plots of top drive speed, mud motor speed and weight on bit.

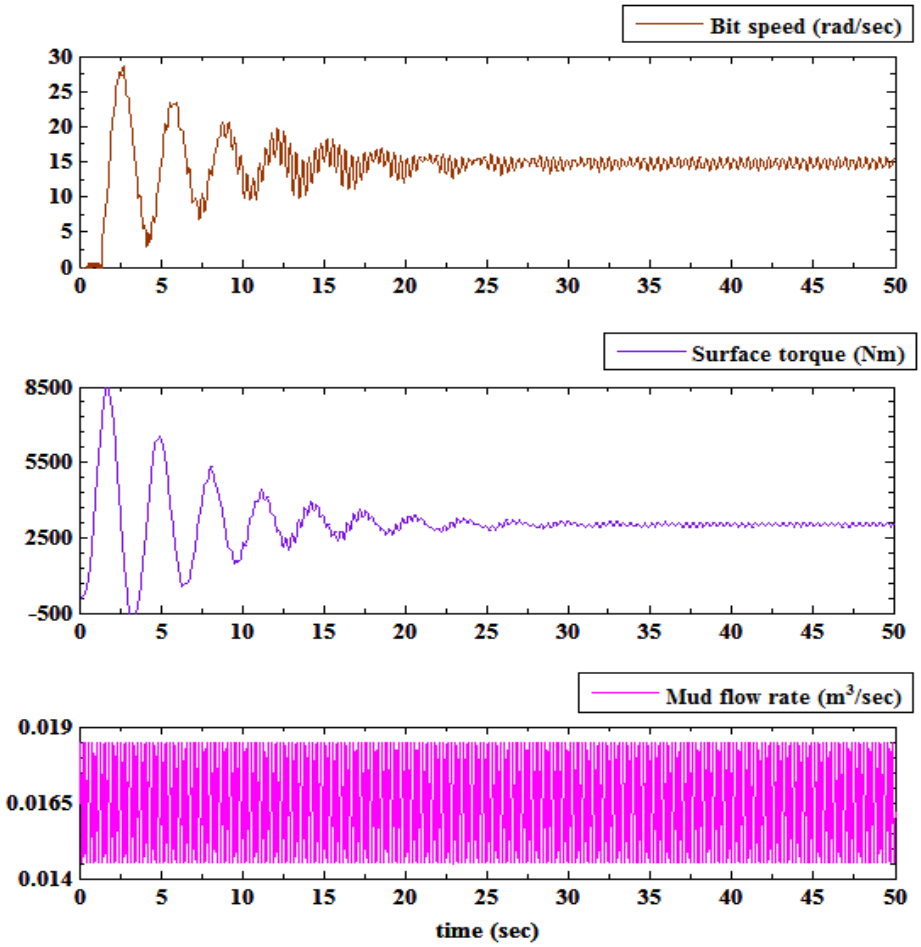

Figure 3.34: Simulation plots of bit speed, surface torque and mud flow rate.

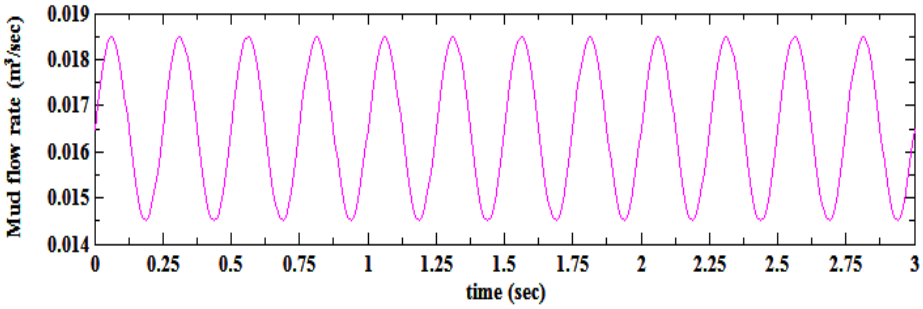

Figure 3.35: Zoom in plot of mud flow rate.

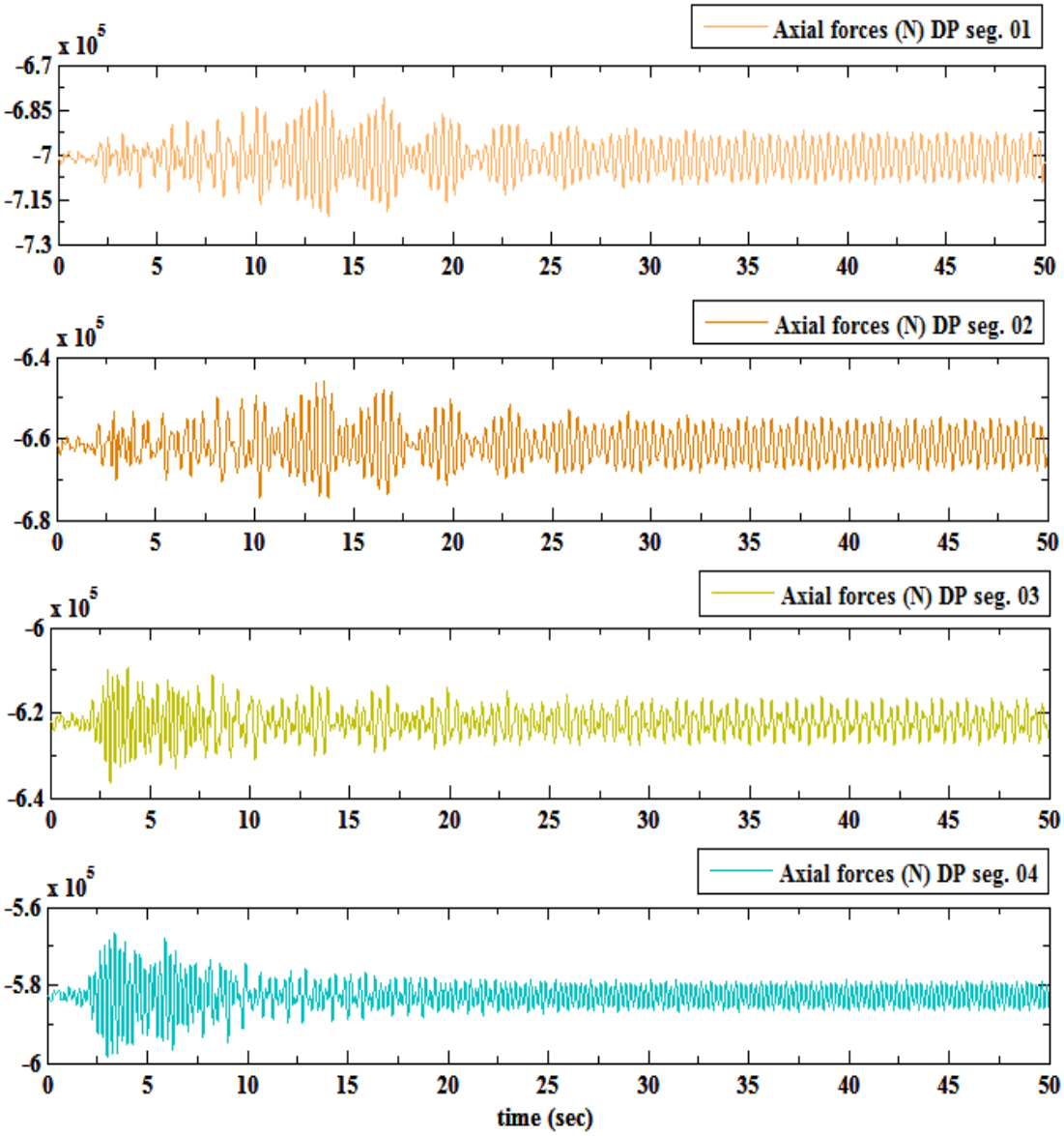

Figure 3.36: Axial force distribution plots in DP segments from one to four at 6.28 rad/sec top drive speed with 8.48 rad/sec downhole mud motor speed and 100kN applied WOB.

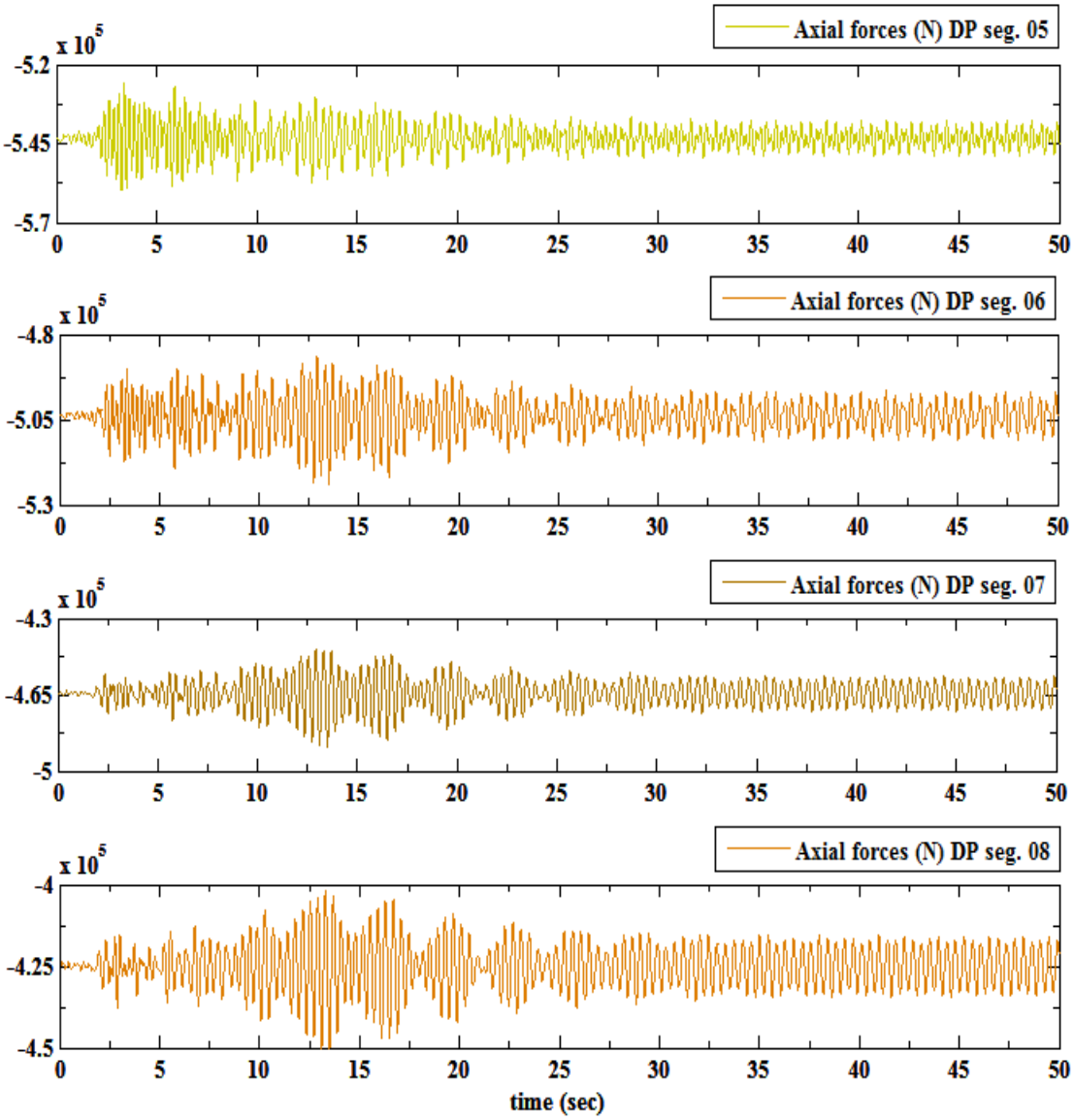

Figure 3.37: Axial force distribution plots in DP segments from four to eight at 6.28 rad/sec top drive speed with 8.48 rad/sec downhole mud motor speed and 100kN applied WOB.

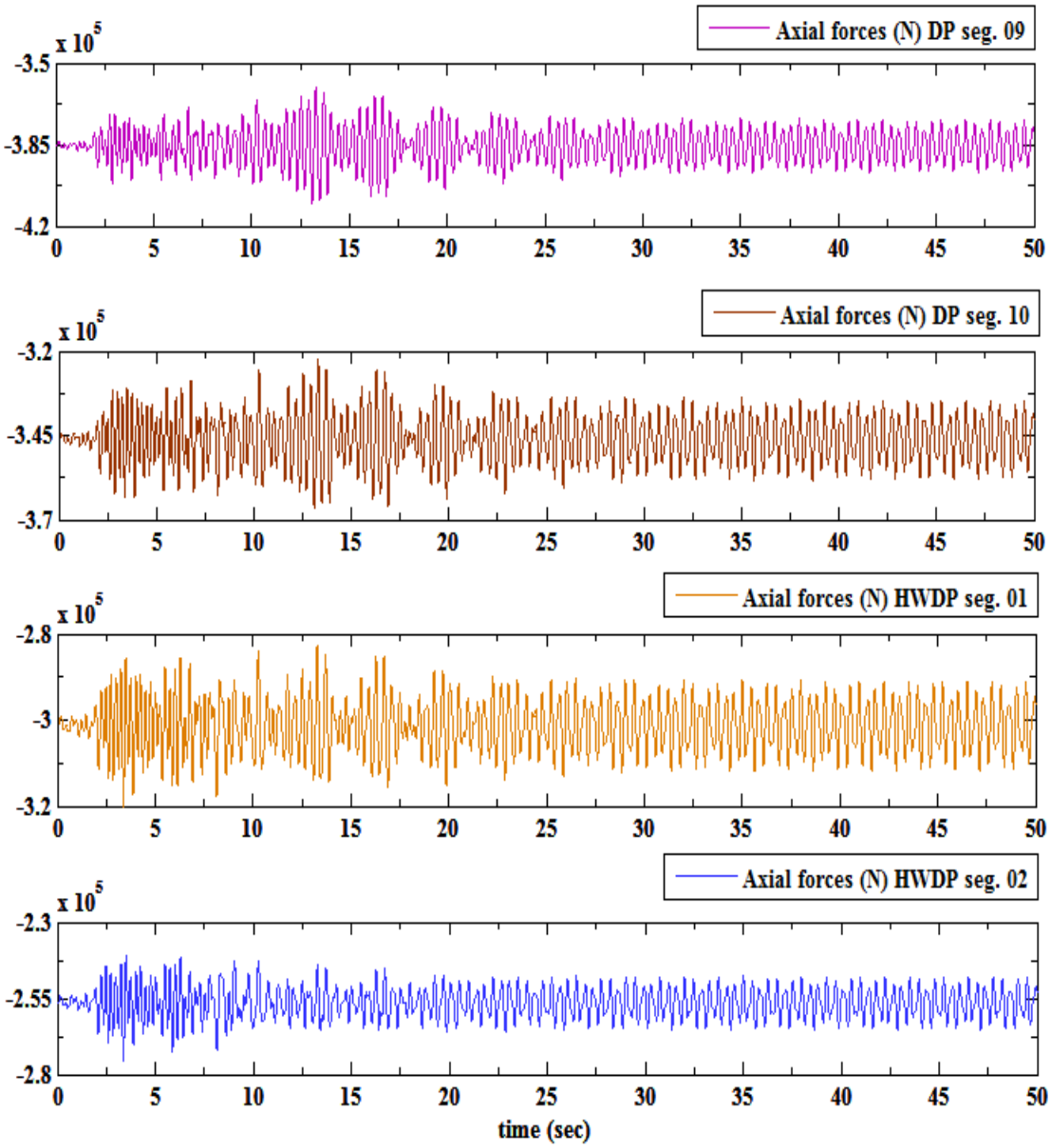

Figure 3.38: Axial force distribution plots in DP segments from nine to ten and HWDP segments from one to two at 6.28 rad/sec top drive speed with 8.48 rad/sec downhole mud motor speed and 100kN applied WOB.

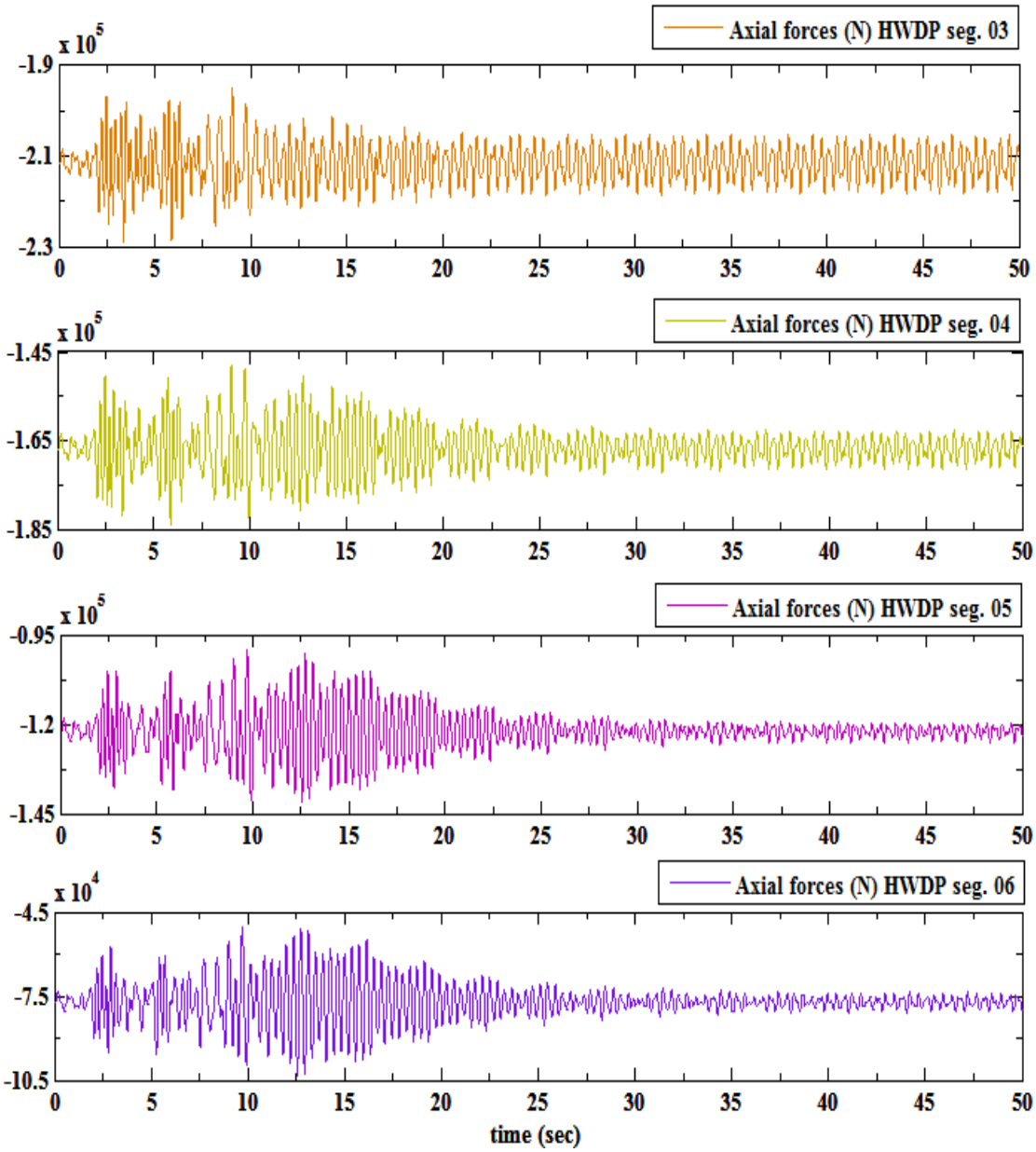

Figure 3.39: Axial force distribution plots in HWDP segments from three to six at 6.28 rad/sec top drive speed with 8.48 rad/sec downhole mud motor speed and 100kN applied WOB.

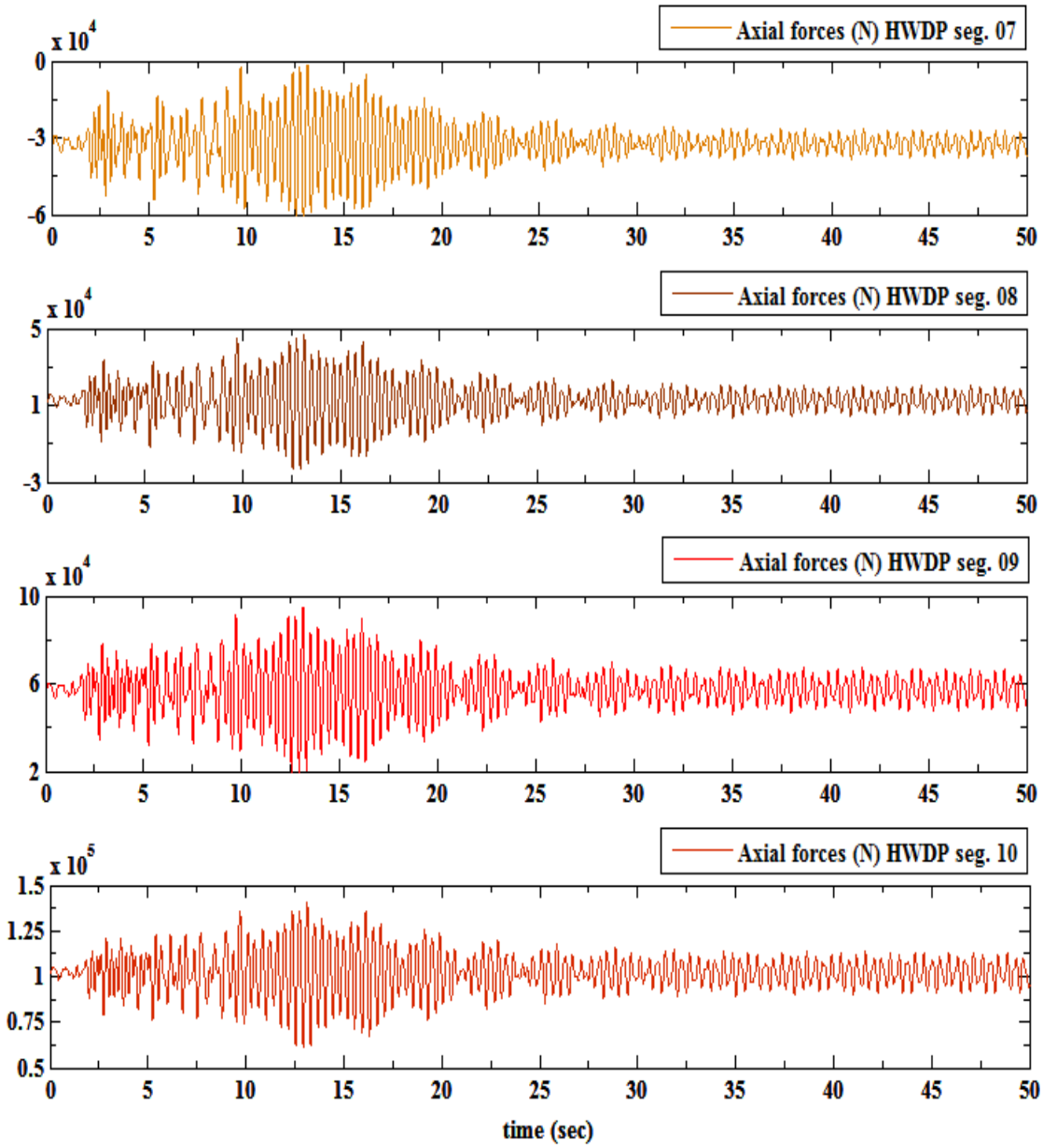

Figure 3.40: Axial force distribution plots in HWDP segments from seven to ten at 6.28 rad/sec top drive speed with 8.48 rad/sec downhole mud motor speed and 100kN applied WOB.

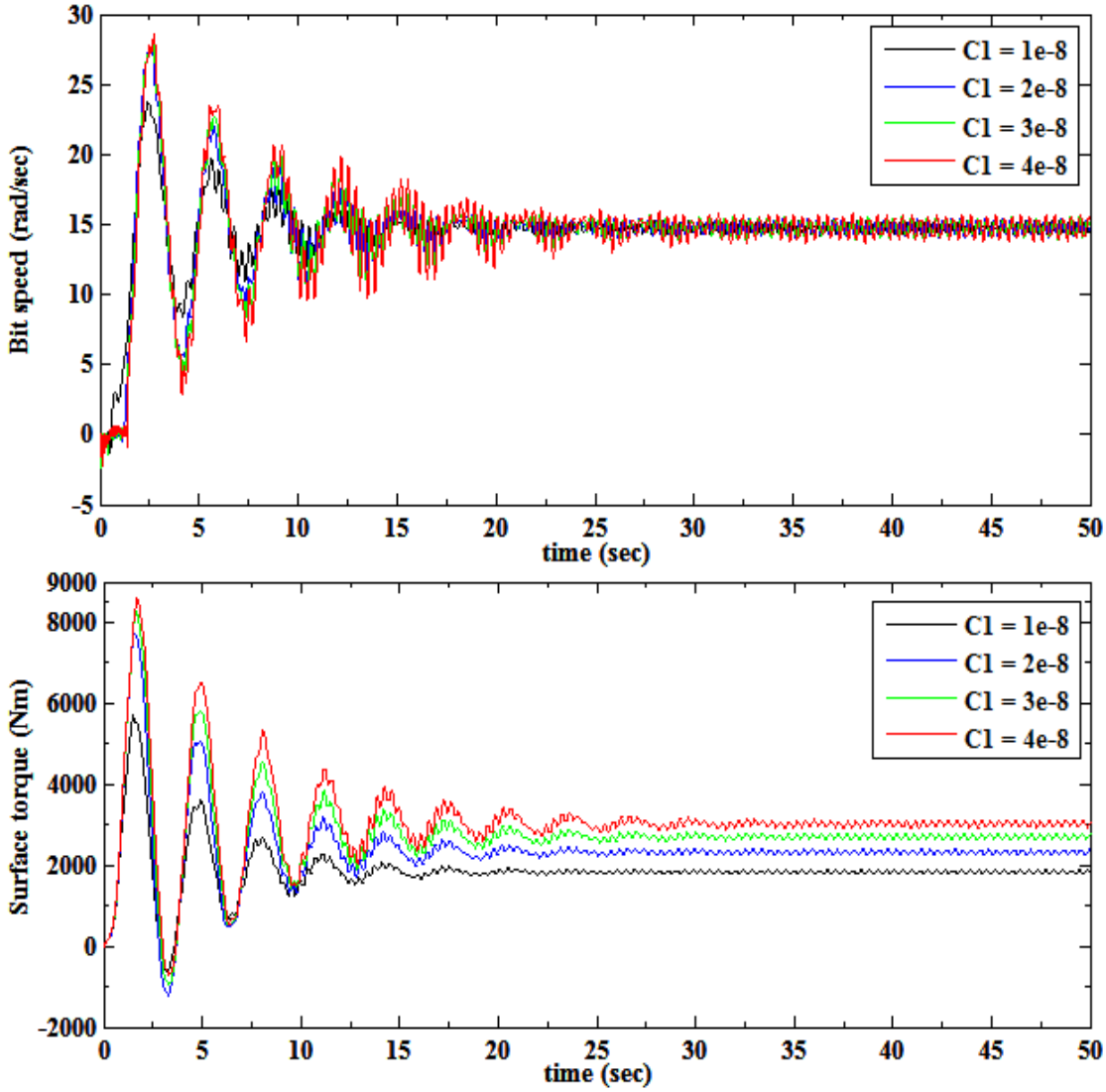

Figure 3.41: Simulation plots of bit speed and surface torque for different bit cutting coefficients at 6.28 rad/sec top drive speed with 8.48 rad/sec downhole mud motor speed and 100kN applied WOB.

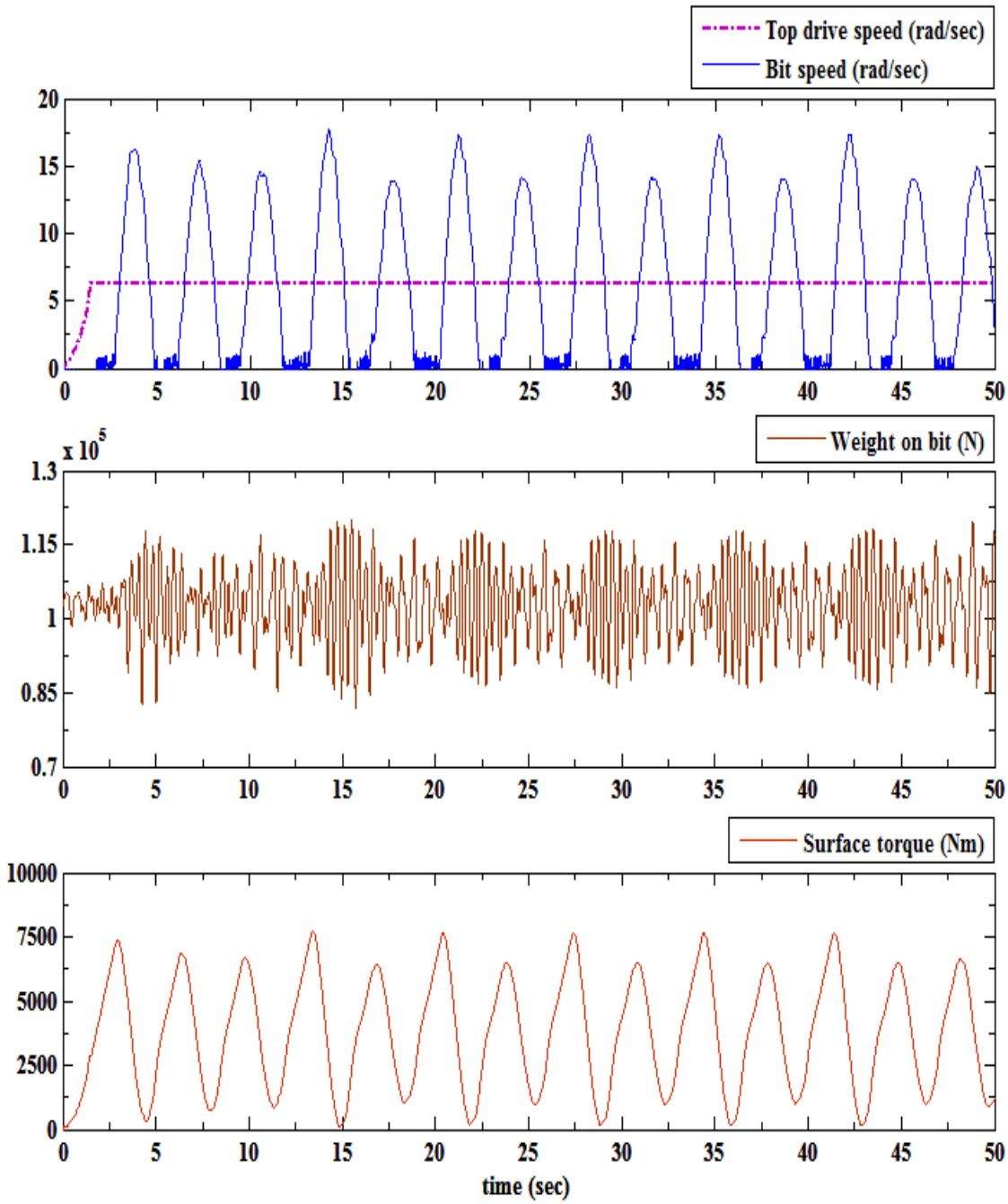

Figure 3.42: High stick-slip vibrations at 6.28 rad/sec top drive speed without using downhole mud motor and 100 kN applied WOB.

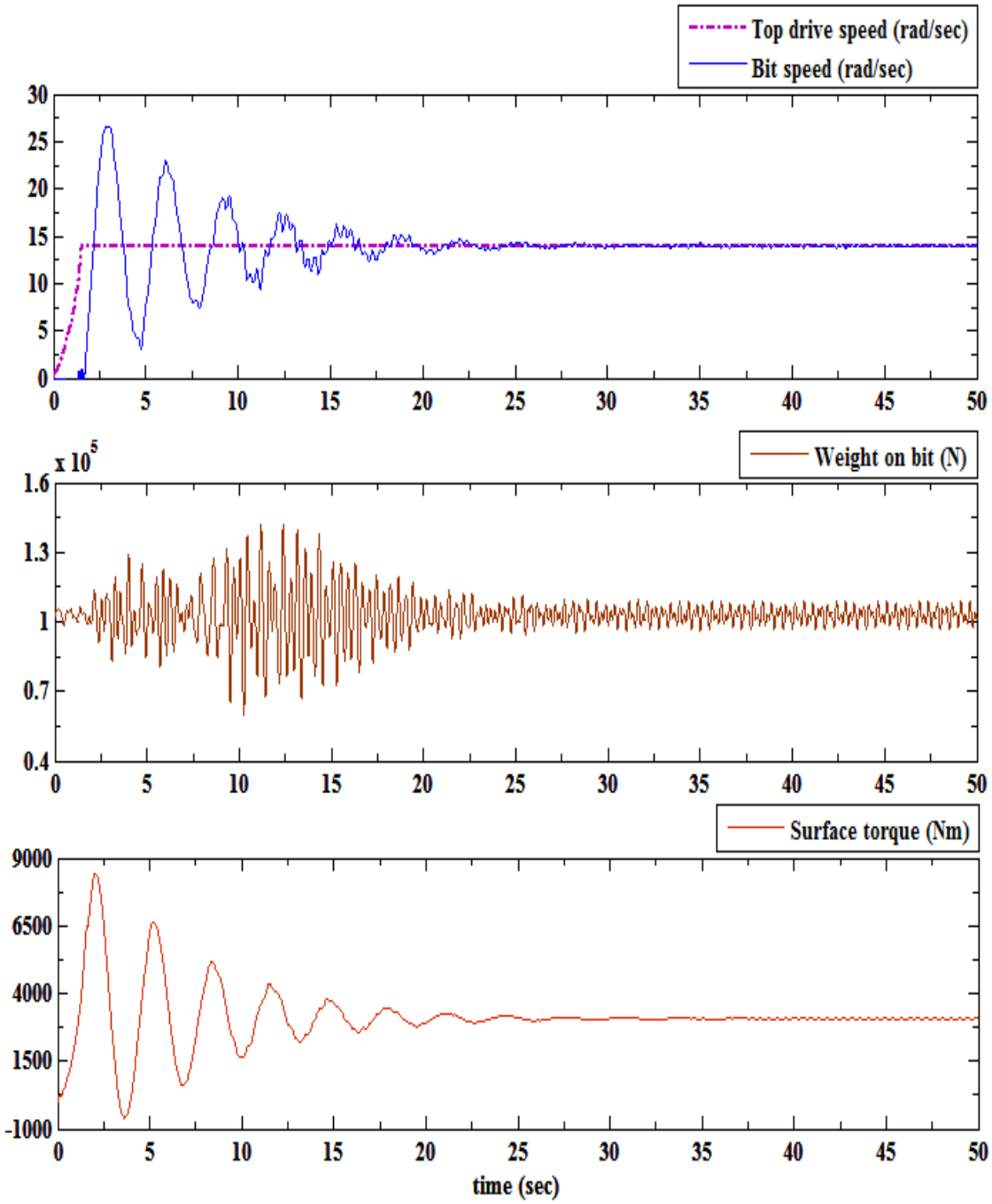

Figure 3.43: Stick-slip eliminated by increasing the top drive speed to 14 rad/sec at 100 kN applied WOB without using downhole mud motor.

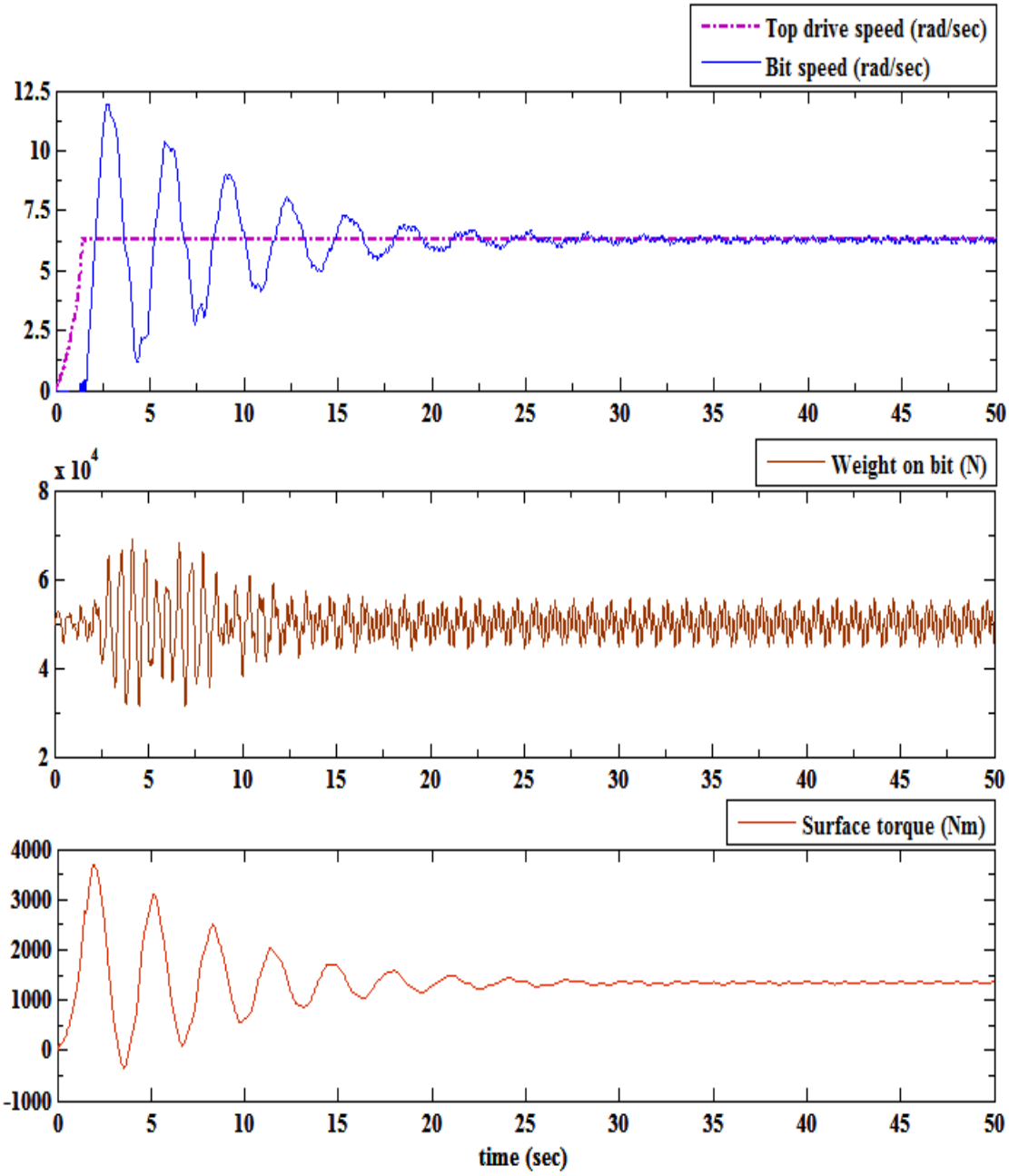

Figure 3.44: Stick-slip eliminated by lowering the applied WOB to 50kN at 6.28 rad/sec top drive speed without using downhole mud motor.

This chapter introduced a suitable approach for modeling and simulation of stick-slip vibrations in a vertical oilwell drilling section. Development and application of a bond graph model of a drillstring using a lumped segment approach has been presented. Simulation results show the same qualitative trends as field observations regarding stick-slip oscillations and their relationship to top drive rotary speed and weight on bit. This chapter study is limited to vertical drilling systems, however, our main goal in this dissertation work is to focus on developing a model for deviated drillstring dynamics and including frictional torque and drag effects. A model of quasi static torque and drag with the application to horizontal oilwell drilling vibrations simulation will be presented in the next chapter.

4 A Model of Quasi Static Wellbore Friction – Application to Horizontal Oilwell Drilling Simulation

4.1 Introduction

4.1.1 Torque and drag issues in deviated wells

Torque and drag issues, which are the results of friction caused by moving pipe in the wellbore, are particularly prominent in drilling horizontal or extended-reach wells (Sheppard *et al.*, 1987). Dynamic frictional forces are assumed to oppose the direction of motion and dependent upon coefficient of friction (friction factor which depends on the type of surfaces in contact) and contact loads (wall force) between the two surfaces. Drag occurs while moving the pipe along the wellbore, and torque occurs while rotating the pipe. Sliding drag and torque can increase dramatically in horizontal and extended-reach wells, and may become the limiting factors in determining the horizontal length or extended-reach of a well, and may need minimization. Analyzing torque and drag is an important evaluation process for assessing drilling feasibility of horizontal or extended-reach wells, minimizing the occurrence of catastrophic drillstring failures and avoiding premature termination of the drilling operation before reaching planned target depth (Adewuya *et al.*, 1998). Deep extended-reach-drilling wells face issues arising from high string tension, such as high over pulls, high torque, tubular strength problems, severe casing wear, and high

contact loads. And for shallow high-step out profiles, the issues center on relatively high compressive forces, high sliding drags, and potential buckling problems (Aston *et al.*, 1998). One of the biggest challenges in longer laterals is excessive torque and drag of the drillpipe caused by wellbore friction (Halliburton, 2011). The additional torque and drag will lead to lower rate of penetration, poor tool face control, induced torsional vibration, instable drilling operation and higher rates of nonproductive rig time (Altamimi *et al.*, 2015). Unplanned extreme torque and drag is a primary limiter to reach of horizontal and extended-reach wells. Surface torque and hook loads are familiar to the driller and important factors in the decision-making process to determine if certain wells can be drilled or not. Surface values are useful but do not always provide the true value of forces within the string that are virtually invisible on the rig floor (McCormick and Lie, 2012). Therefore, the accurate prediction of torque and drag are very important if the well is to be successfully and economically drilled and completed.

4.1.2 Review on work with wellbore friction models

Several methods and techniques have been reported for analyzing the torque and drag issues in drilling wells. The earliest contributions to understanding of well friction was Johansick *et al.* (1984) who established the basic equations for friction in deviated wellbores. It was assumed that both torque and drag are caused by sliding friction which is defined by multiplying the sidewall contact force by a friction coefficient. The force balanced for an element of the pipe is shown in Fig. 4.1 where it is assumed that the normal component of the tensile force acts on the element contributing to the normal force. This assumption is considered for the calculation of torque and drag in curved section (build

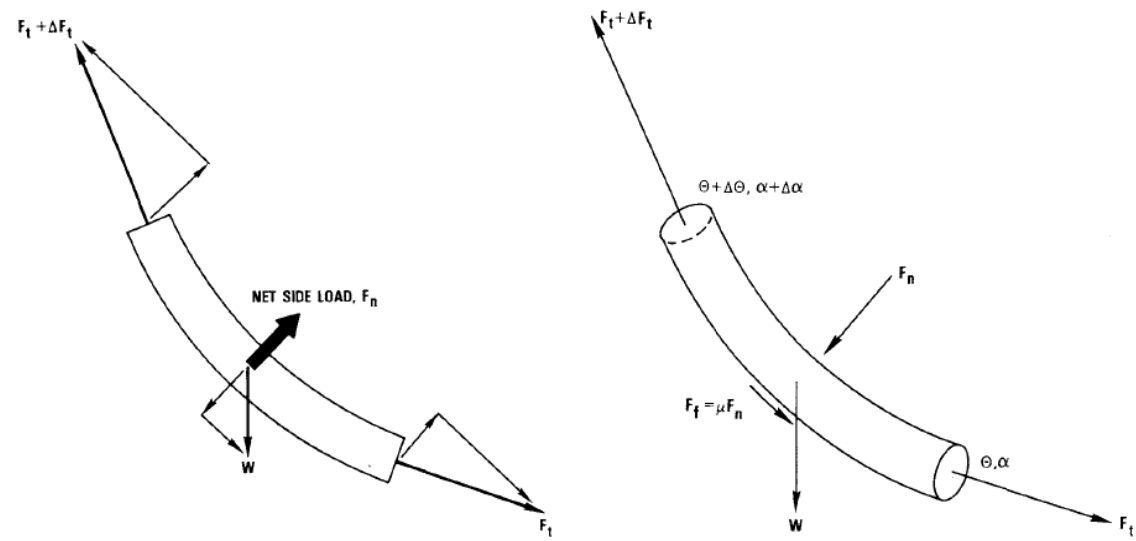

Figure 4.1: Sketch of force balance on the drillstring curved element illustrating sources of normal force (left side) and forces acting on drillstring curved element during pickup (Johansick *et al.*, 1984).

and drop sections). But in the case of straight section, especially in hold section, only normal component of weight acts on the element contributing to the normal force.

The net normal force, F_n shown in Fig. 4.1 is the negative vector sum of normal components from the weight, W and from the two tension forces, Ft and $F_t + \Delta F_t$. The magnitude of the normal force presented by Johansick *et al.* (1984) is written as below.

$$F_n = [(F_t * \Delta\propto * sin\bar{\theta})^2 + (F_t * \Delta\theta + W * sin\bar{\theta})^2]^{1/2} \quad (4.1)$$

Where Δα = increase in azimuth angle over length of element, degree [rad]

Δθ = increase in inclination angle over length of element, degree [rad]

W = buoyed weight of drillstring element, lbf [N]

$\bar{\theta}$ = average inclination angle of element, degree [rad]

And the tension and torsion increment presented by Johansick *et al.* (1984) is written as below.

$$\Delta F_t = W * cos\bar{\theta} \pm \mu * F_n \tag{4.2}$$

$$\Delta M = \mu * F_n * r \tag{4.3}$$

Where μ = sliding friction coefficient between drillstring and wellbore

r = characteristic radius of drillstring element, lbf [N]

ΔM = increase in torsion over length of element, ft-lbf (Nm)

The plus or minus signs in equation 4.1 are for pipe upward motion where friction adds to the axial load and downward motion where the opposite in the case. Johansick *et al.* (1984) calibrated the proposed computer model with field measurement of torque and drag, and calculated friction coefficient for the model. The model was tested in three directional wells with a significant length of the cased hole section (70%, 83%, and 99%). No distinction was made between cased hole friction and the open borehole friction. Also, the hydrodynamic effects were not considered which might have been an adequate simplification. Because of the simplicity and being user friendly, well friction model in Johansick *et al.* (1984) has been extensively used in the drilling industry and is very popular in the measurement of torque and drag.

Sheppard *et al.* (1987) proposed a wellbore friction model in standard differential form considering the inclusion of the mud pressure which was neglected by Johansick *et al.* (1984). It was mentioned that the effective tension as the sum of the true tension and mud

pressure. One of the main assumptions in the friction model was that the drag force on the drillstring at any location is proportional to the side force acting there. A brief investigation on the advantages of planning for an undersection trajectory (steady buildup) has been conducted to reduce torque and drag. In the one field case studied, the friction factor has been identified as 0.36.

Maidla and Wojtanowicz (1987a) presented a method to evaluate an overall friction coefficient between borehole and casing. The friction factor coefficient has been computed by matching the hook load data, which is recorded in the field, with the calculated hook load. The equations for predicting surface hook loads are derived from the respective governing differential equations. Friction between the borehole and casing were looked at in a macroscopic scenario, where its overall average value is relatively constant along a borehole which is similar to that approach undertaken in Johansick *et al.* (1984) on the drillstring borehole friction. The effects of lithology stratification, the compressive and shear strength of the rock, rock and casing hardness, and the ever changing borehole diameter have been ignored in order to simplify the model. It has been commented that the relative error in the friction factor coefficient is smaller for deeper depths. A new procedure for wellbore drag prediction based on the borehole friction factor concept has been presented in Maidla and Wojtanowicz (1987b). The procedures employed iteration over the directional survey stations and mathematical models of the axial loads within a moving pipe in the borehole. The effects of hydrodynamic viscous drag, contact surface and the bearing angle component of dogleg severity have been incorporated in the model. It has been commented that the borehole friction factor appeared fairly insensitive to measured

depth, various well trajectories, size of pipe and its surface. The borehole friction factor values, for most cases were 0.21-0.30 for pulling conditions, and 0.27-0.43 for running conditions.

Ho (1988) presented an improved modeling program that combines a bottom-hole-assembly (BHA) analysis in the stiff collar section, coupled with an improved soft-string model for the remainder of the drillstring. It is an improvement of previous soft-string models presented in Johansick *et al.* (1984), Sheppard *et al.* (1987) and Maidla and Wojtanowicz (1987a and 1978b). It has been discussed that the soft string model violates fundamental equilibrium of the drillstring. It was recommended that the very deep vertical wells should be handled as directional wells.

Lesage *et al.* (1988) defined two kind of friction coefficients such as the rotating friction coefficient for conventional drilling or wiper trips and the sliding friction coefficient for downhole motor drilling or tripping in/out without rotation, and presented an estimation process of these two friction coefficients on a foot-by-foot basis at the wellsite with both measurement-while-drilling (MWD) and surface values of weight on bit (WOB) and torque. It has been suggested that the rotating friction coefficient can be used to evaluate the transfer of torque between the surface and the MWD tool. The sliding friction coefficient can be used to evaluate the transfer of WOB between the surface and the MWD tool.

Brett *et al.* (1989) presented a borehole friction model which is similar to the models presented in Johansick *et al.* (1984) and Sheppard *et al.* (1987). The model is capable of

predicting drags, torques, normal forces and buckling behavior. The effect of drillstring stiffness has been ignored in the model. Finally, a brief comparison between field data and model predictions has been presented for a wide range of different inclinations to prescribe several remedial measures for directional wells. On the basis of real-time tension/torque analysis, operations have been changed by modifying mud properties, conducting wiper trips, circulating off bottom while reciprocating the pipe to clean the well, reaming areas where key-seat formation was likely, adding wall scratchers to casing because reciprocation was deemed possible.

A technique, which is based on an analysis of expected drillstring side-forces using field derived friction data, for predicting the total torque losses in drilling directional wells has been demonstrated in Lesso *et al.* (1989). Simulation of survey data with variations on inclination and azimuth that are matched to the corrections and dog-leg severity found in the wells has been conducted in the proposed method.

Aarrestad (1990) presented a case study of the effect of steerable BHA on drag and torque in wells. It has been identified that excessive use of directional control method (or steerable BHA) may results in problems with high drag and torque in the wells and in some cases target point may not be reached due to large doglegs in building parts of the well. The difference between a planned smooth well and a rather extreme uneven well has been identified based on the torque calculations. The various aspects of torque and drag problems encountered in drilling extended-reach-drilling wells have been addressed in

Aarrestad (1994). Application of catenary well profile in a well in North Sea that has been introduced by Sheppard *et al*. (1987) has been discussed.

Wilson and Yalcin (1992) used a torque and drag model from Sheppard *et al.* (1987) for planning and drilling of two double azimuth-double "S"-shaped wells. Both wells have been drilled with water based mud, steel drill pipe and conventional rotary drive, and completed as gravel packed duals. It has been identified that double azimuth-double "S" well paths can successfully hit multiple targets to reduce dry hole risk. It is recommended that although the torque and drag models are useful for planning if simulated doglegs are included in the model, but should be updated frequently with the actual surveys.

Luke and Juvkam-Wold (1993) presented the calculation of true hook load and line tension under dynamic conditions. It has been identified through theoretical and experimental studies that true hook load depends on sheave friction, direction of block movement, and previous movement history. In some cases, actual hook load has been observed to be up to 19% higher than the load predicted by the previous developed method.

Alfsen *et al.* (1993) performed a field case study on torque and drag analysis with the model in Johancsik *et al.* (1986). The drilled well 33/9-C2 with its horizontal reach of 7290 m was a world record in extended reach drilling. A low coefficient of friction mud system, well profile that minimized drillpipe to wall contact and drilling procedures that provide good borehole cleaning can reduce wellbore friction.

He et al. (1995) presented a theoretical model for the effects of torque on helical buckling, normal contact force, and pitch of helix in the curved wellbore. The effects of

helical buckling and the post buckling contact forces on torque and drag in a drilling operation have been modelled. Finally, the proposed models have been used for realistic simulations for both conventional drilling and coiled tubing applications. It has been recommended that the buckling effects should be considered for extended reach and horizontal drilling.

Payne and Abbassian (1996) presented a brief overview on the issues related to torque and drag prediction, monitoring, and management in extended reach directional wells. The importance of drilling data in calibrating torque/drag models has been addressed in order to capture the continual changes in drilling parameters and operating conditions. A number of field case studies have been presented where analyses have been conducted to directly assist drilling operations. It has been recommended that string torque/drag should be analyzed based on examination of distinct friction factors for the cased-hole and open-hole and friction factors should be derived from field data for each hole section as it can vary significantly from defaults. It has been identified that drag prediction is dependent on accurate diagnosis of frictional drag in the well and the extent of buckling in the string.

Adewuya and Pham (1998) presented a robust torque and drag analysis approach, which is based on the logical representation of the system states as functions of interval objectives at the modeling stage, providing solutions for extremely complex interplay of variables without necessarily simplifying the system model, for well planning and drillstring design. The proposed approach uses available theoretical foundations and analyses, combined with the extensions to conservative criterion offered by practice to

arrive quickly at feasible parameters for hole dogleg severity, optimum tubular properties, and scope of drilling feasibility.

Reiber *et al.* (1999) presented a technique, which is an enhancement of Lesage *et al.* (1988) model with a stiff string model where the bending stiffness of the string elements is taken into account in the algorithms, for evaluating torque and drag effects in real time and for interpreting the effectiveness of actions taken. The proposed techniques operate in four operational modes: drilling, rotating off bottom, picking-up and slacking-off. In drilling operations without rotation, a sliding friction factor has been calculated. While operating with rotation the torque-method has been applied which stops the friction factor iteration if the measured surface torque matches the calculated one. It has been identified that the proposed analysis can provide information on the current buckling status as well as the yield and fatigue stresses along the string.

Aadnoy and Anderson (1998, 2001) presented a brief derivation of analytical expressions for build, drop, hold and side profiles, and also a new modified catenary profile where using equations, which are based on the assumption of soft string model, a friction analysis can be carried out without requiring a simulator. Application of low weight drillpipes in drilling ultra-long wells have been recommended as it reduces tension and increases buoyancy, leading to less friction and less casing wear. Analytical solutions to calculate wellbore friction for different well geometries has been developed. Explicit analytical equations have been derived to model drill string tension for hoisting or lowering of the drill string. Also both constant curvature models and a new modified catenary model,

which is developed for arbitrary entry and exit inclinations, are derived. The necessary equations to determine well friction in three-dimensional well profiles have been presented. In addition, expressions for torque and drag have been developed based on the tension equations. Equations for combined motion and drilling with a motor are also given. An analysis and design of ultra-long wells using a catenary well profile has been presented in Aadnoy *et al.* (2006). A comparison between standard build profile and catenary profile has been studied. It has been shown that the catenary is not as favorable as expected due to friction in the entrance to the catenary, except that friction reduction measures can be applied over a small area. It has been recommended that the catenary concept has a high potential but it requires detailed analysis and follow-up to be successful. A new generalized friction model, which consists only two equations: one for rotating friction (torque) and one for pulling friction (drag) that is valid for all well geometries, has been presented in Aadnoy and Djurhuus (2008). The generalized friction model, which is valid for tubular both in tension and compression, covers vertical sections, build-up bends, drop-off bends and straight sections. A three dimensional analytical model for wellbore friction has been presented in Aadnoy *et al.* (2010). In high tension the string weight is assumed negligible as compare to the tension. The friction in a bend has been formulated in terms of three dimensional dogleg. A new assumption, which is weightless pipe that means the pipe is always tensile forces are considered to be dominant over weight of the pipe, in new three dimensional model has been introduced in Mirhaj *et al.* (2011). It was not applicable for the heavy sections of the drillstring.

All models discussed above are soft-string models and the stick-slip phenomena in the friction model has been ignored. A computationally efficient yet predictive wellbore friction model remains an open research problem. To the best of the author's knowledge, no complete dynamic model for a horizontal oilwell drillstring has been developed.

4.1.3 Chapter outline

This chapter is organized as follows. Section 4.2 develops, implements and validates a stick-slip friction model that will allow the simulation to accurately capture an important source of energy loss during drilling and tripping. In Section 4.3, dynamic normal forces for the friction submodel are calculated based on a modification of an existing static treatment. A lumped-segment drillstring model, with coupled axial and torsional vibratory motions, is presented in Section 4.4, followed by a bit-rock interaction model in Section 4.5 that allows the drillstring and bit to advance in the borehole. Field data is used in Section 4.6 to tune the friction factor. Given that the authors and their industry partners are motivated to predict the vibrations on and induced by downhole tools, Section 4.7 summarizes an experimental program by which an axially-vibrating tool (Agitator®) was characterized for use in the simulation. In Section 4.8, the complete horizontal drillstring model is used to show the effect of downhole tool output on WOB, ROP, and vibration levels at multiple locations. The model is a potentially valuable tool in the design of drillstrings with optimized top drive speeds, stabilizer and downhole tool locations, mud motor speeds, and trajectories.

4.2 Modeling of stick-slip friction phenomena

The stick-slip nature of friction is very common when the relative velocity between sliding surfaces approaches zero and the surfaces become 'stuck', requiring a force larger than the sliding friction force to break the surface loose. The most basic friction models contain Coulomb friction and linear viscous damping which describe the friction forces well for steady state velocities. When velocity crosses zero, most models present numerical problems. To overcome these problems during simulations, Karnopp (1985) proposed a friction model to set the friction force equal to the external forces acting on the object, for a small neighborhood around zero velocity, outside of which friction is function of velocity. The model has the advantage of generating ordinary differential equations but can still experience numerical instabilities in the stick phase. A switch model proposed in (Leine, 2000) consists of three different sets of ordinary differential equations for the stick, slip and the transition phases. At each time step the state vector is inspected to determine whether the system is in the slip mode, in the stick mode or the transition mode. The corresponding time derivative of the state vector is then chosen. A region of small velocity is defined for the stick band and the system is considered to be in the slip mode if the relative velocity lies outside this narrow stick band. In one state the velocity is prescribed and the force is determined, and in other state, the force is prescribed and the velocity is determined. Such causal inversions create formulation and computational problems, and these problems can be quite prohibitive if many switches are part of the model.

A modification of the Karnopp's model is presented by Margolis (2004) that allows the stick-slip friction element to be self-contained, which is represented as a combination

of dissipative and elastic elements in a bond graph. The elements require a velocity input from the attached system and output the friction force similarly to Karnopp's model. The difference can be identified during the 'stuck' phase where the friction force continues to be calculated internally to the element and does not require any information from the attached system. The model is self-contained because the tests of the 'stuck' and 'unstuck' states have no dependence on the overall systems to which the friction generated elements are attached.

The stick-slip friction model proposed in this research work takes a similar modeling approach to Margolis. A bond graph C-element (compliance with some logical modification of build-in codes) simulates the stick-slip phenomena. The output of the C-element is the friction force. The input velocity, which is the relative motion between the contact surfaces, allows determination of the 'stuck' and 'unstuck' states. The necessary logical information is shown in Figs. 4.2-4.3. In the 'stick' phase, the friction force is generated by the small but finite deformation of a high stiff spring-damper system which represents deformation of contact surface asperities. When the force exerted by the spring-damper on the system mass becomes equal to the maximum static friction force and the relative motion is still in the stick band, then the spring state (deflection) is set at a constant value in order to create a constant static friction force output. During the 'slip' phase the output from the C-element is simply the kinetic friction force. The model from Figs. 4.2-4.3 are simulated in 20Sim® bond graph software using the proposed self-contained friction model. The bond graph model of the mass-surface system (Fig. 4.4(a)) is shown in Fig. 4.4(b). As described in Section 3.2, elements bonded to the 1-junction have a common

generalized flow (velocity), and their generalized efforts (forces) sum to zero. Therefore, the 1-junction captures the fact that the applied force source moves with the mass, and simultaneously enforces Newton's Second Law. Elements bonded to the 0-junction have a common force, and their velocities sum to zero in accordance with the power bond half-arrow directions, which indicate the direction of algebraically positive power flow. In Fig. 4.4(b), all elements bonded to the 0-junction are subjected to the friction force F_f. The velocity input to the generalized compliance (C-element), is therefore the relative velocity (V_{rel}) between the mass and its sliding surface. The short strokes normal to the bond indicate the input-output structure of the constitutive laws of the bonded elements. These "causal strokes" give a visual indication of causal conflicts when submodels of a complex system such as an oilwell drillstring are assembled. Table 4.1 summarizes all relevant data that is used in the mass-block system simulation.

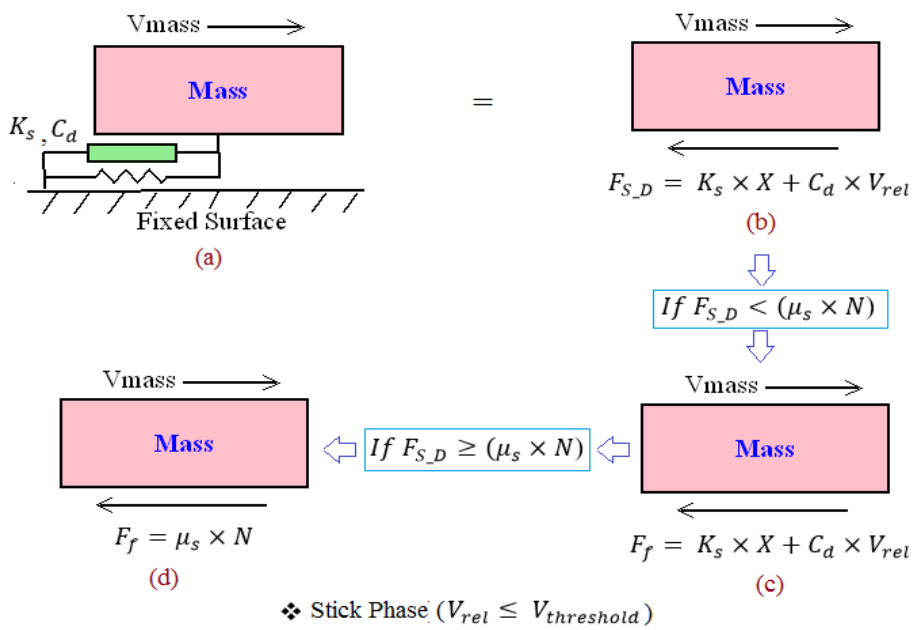

Figure 4.2: Physical schematic of stick-phase.

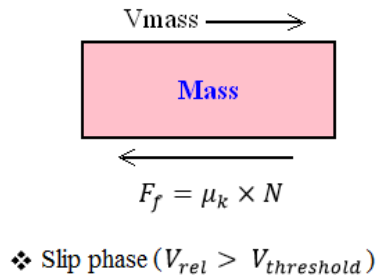

Figure 4.3: Physical schematic of slip-phase

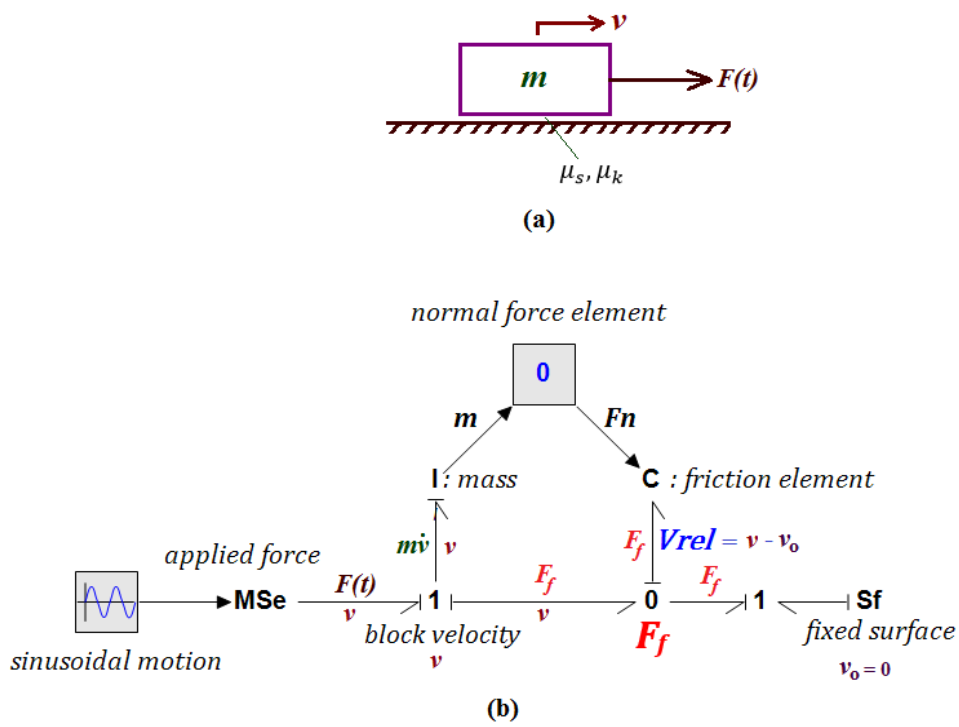

Figure 4.4: (a) sketch of the system and (b) Bond graph model of the friction-element with system

Table 4.1: Data used in mass-block system simulation

Parameters	Value
Mass, m	10 kg
k_s, C_d	10^7 N/m, 10^5 N-s/m
μ_s, μ_k, $V_{threshold}$	0.3, 0.2, 0.0005 m/s

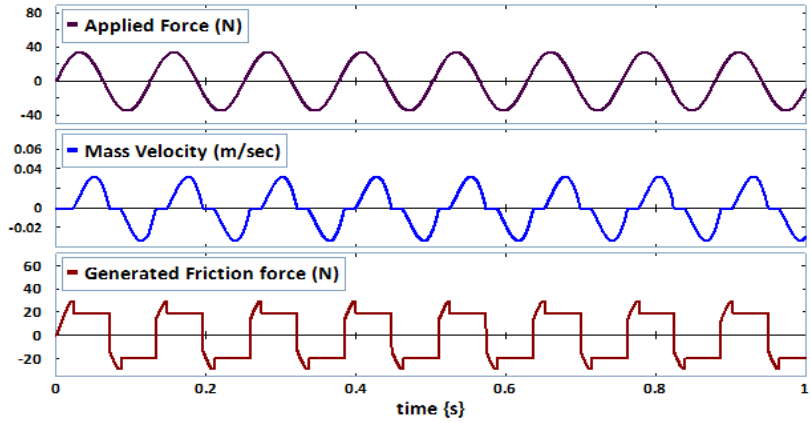

Figure 4.5: Simulation results for the mass-surface system, F(t) = 35sin(50t) N.

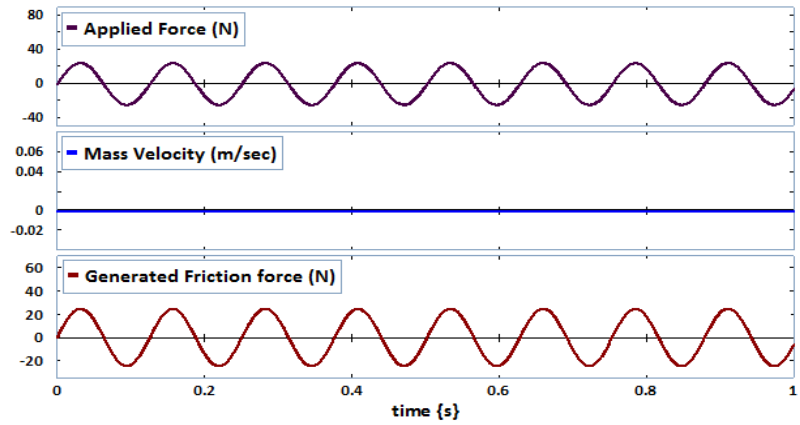

Figure 4.6: Simulation results for the mass-surface system, F(t) = 25sin(50t) N.

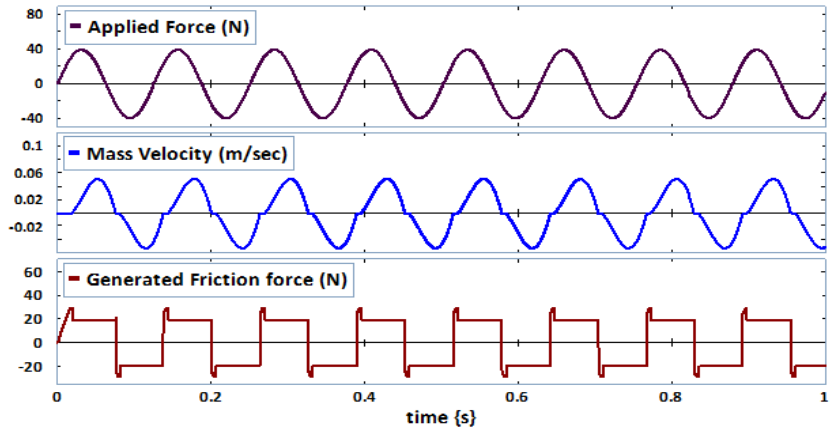

Figure 4.7: Simulation results for the mass-surface system, F(t) = 40sin(50t) N.

Fig. 4.5 shows the simulation results of the mass-surface system when the amplitude and frequency of the applied sinusoidal force are 35 N and 50 rad/s, respectively. At the start of the simulation, the mass is in the stick zone, the force output of the C-element is equal to the applied force (Fig. 4.6) and the C-element starts to act as an ideal compliance element with parallel damping. The initial positive slope from the friction force plot is due to deformation of spring element. The flat portion at the tip of the slope indicates that the model is limiting the friction force at the stick phase by constraining the deflection of the C-element to be constant. The block starts to slip when the applied force overcomes the maximum allowable static friction force and the output of the C-element becomes a constant kinetic friction force. The block velocity plot shows repeating stick-slip phenomena. Another set of simulation results are shown in Fig. 4.7 by increasing the applied force amplitude to 40 N keeping the same frequency. The mass velocity plot shows less stick time as compared to Fig. 4.5 which validates the performance of the proposed friction model.

4.2.1 Validation with finite element friction model

A 10 kg solid cube contacting a shell plate model has been constructed in LS-DYNA® to validate the friction model (Fig. 4.8). Fixed boundary conditions have been applied to the shell plate. The materials for solid cube and shell plate have been modeled as *MAT_ELASTIC and *MAT_RIGID, respectively. The contact model between the solid cube and shell plate in LS-DYNA® is the source of the friction force. There are several contact-related parameters available in LS-DYNA® which can be used to modify or improve contact model behavior. A non-automatic contact type *CONTACT_SURFACE_

TO_SURFACE has been chosen for building the model. By default, LS-DYNA® considers only a static friction coefficient (FS). In reality, sliding friction is usually less than the maximum static friction. The transition from static to dynamic friction is modeled using an exponentially decaying function as below.

$$\mu = FD + (FS - FD)e^{(-DC \times |v_{rel}|)} \tag{4.4}$$

Where FD is dynamic friction coefficient, DC is decay constant, v_{rel} is the instantaneous relative velocity between the sliding node and the corresponding master segment. The cube has been assigned as the slave segment and the shell plate as the master segment. The transition curve from static to dynamic friction is shown in Fig. 4.9. The inputs of FS and FD values are chosen similar to the 20Sim® model which are 0.3 and 0.2. The direction of the sinusoidal force, which is applied to the cube, is in the x-direction in Fig. 4.8. In order to preload the system to a steady state prior to dynamic loading for the explicit transient analysis a keyword *CONTROL_ DYNAMIC_RELAXATION step has been selected for the LS-DYNA® simulation. Figs. 4.10-4.12 summarizes the simulation results from LS-DYNA®.

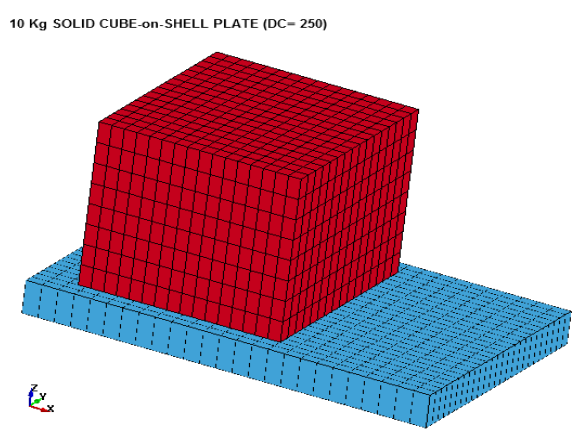

Figure 4.8: Physical geometry of the LS-DYNA® model.

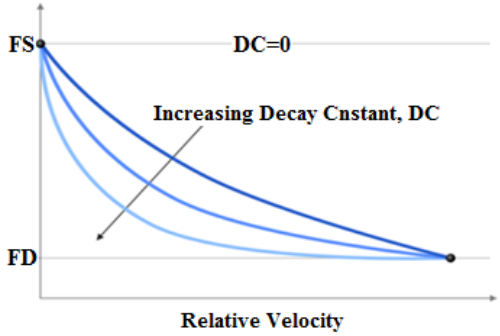

Figure 4.9: Transition from static to dynamic friction (adapted from LS-DYNA® manual).

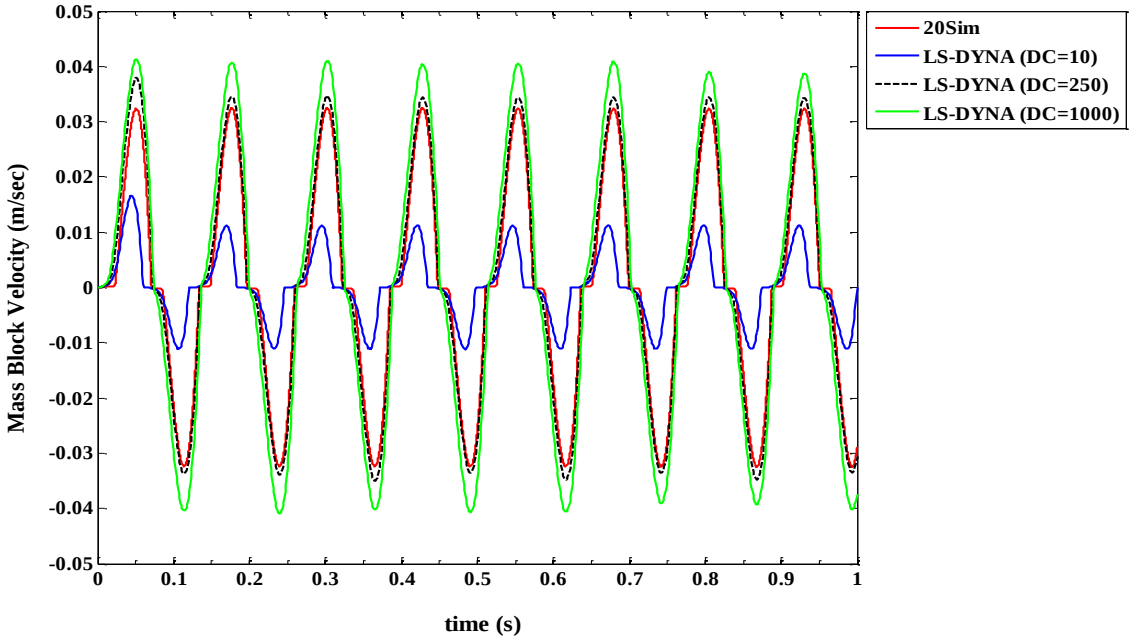

Figure 4.10: Solid cube velocity at 35Sin(50t) N applied force.

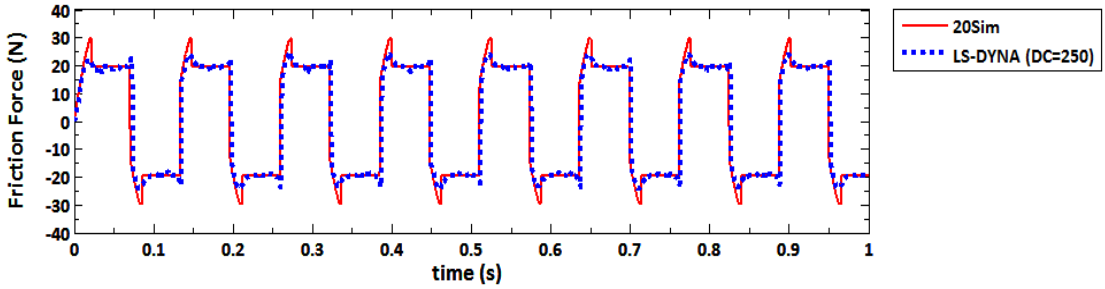

Figure 4.11: Acting friction force at 35Sin(50t) N applied force.

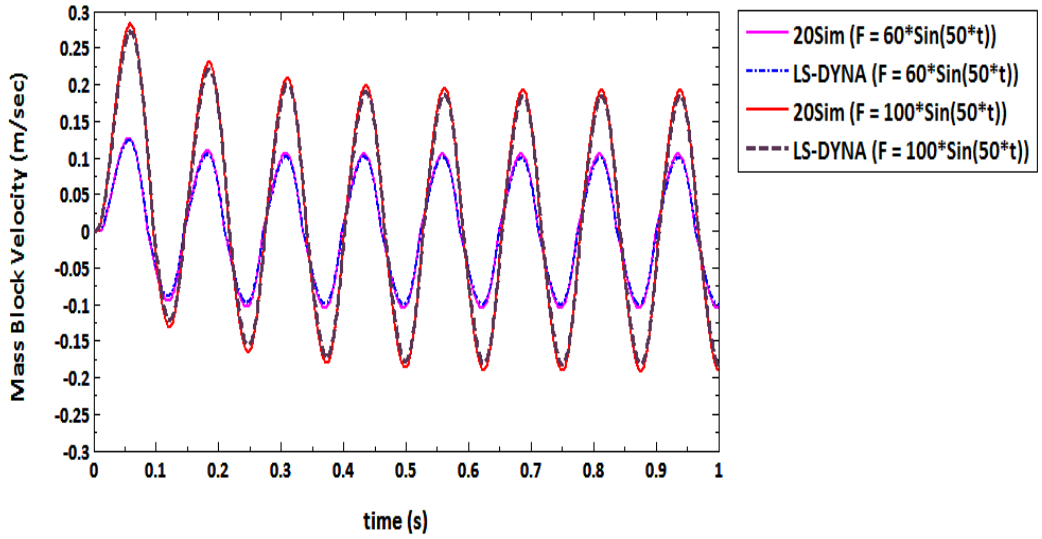

Figure 4.12: Solid cube velocity at higher amplitude applied forces.

Fig. 4.10 shows the cube motion for different decay constants. The stick period increases in the cube motion plots with decreasing of the decay constant which is in agreement with Fig.4.9. Simulation results show that the decay constant value of 250 in LS-DYNA® provides quite similar results to the 20Sim® model. Also friction forces in both models are found to be quite similar as shown in Fig. 4.11. Fig. 4.12 compared the results from model in LS-DYNA®, when the decay constant value is 250, with the 20Sim® model at higher amplitude applied forces. Again, these results indicate that the cube motions are almost the same between the two models.

4.3 Normal contact force for wellbore friction

Early analytical wellbore friction models discussed in (Johancsik *et al.*, 1984; Sheppard *et al.*, 1987; Aadnoy, 1998) are most suitable for the case of drillstring pulling in/out operations, in which drillstring rotation is negligible compared to axial motion. In this research work, the analytical model presented in (Johancsik *et al.*, 1984), which is still very popular in the drilling industry because of its simplicity, has been modified for drilling operations with string rotation. One of the main modifications has been the addition of stick-slip friction phenomena instead of sliding friction. In this research work, horizontal wellbore friction has been included. Friction in the vertical section of the drillstring has been neglected. A sketch of the build section of the horizontal drillstring segments is shown in Fig. 4.13. The section is divided into curve elements. It has been assumed that the drillstring contacts at the upper face of the wellbore when drillstring segments are under tension. A free body diagram of a curve element is shown in Fig. 4.14 when the drillstring is moving in the downward direction and the normal force can be written as below,

$$F_n = F_t \, \Delta\theta - W \sin\bar{\theta} \tag{4.5}$$

where F_t = tension force acting in the curved segment

$\Delta\theta$ = increment of inclination angle

W = segment buoyancy weight

$\bar{\theta}$ = average inclination angle of the segment

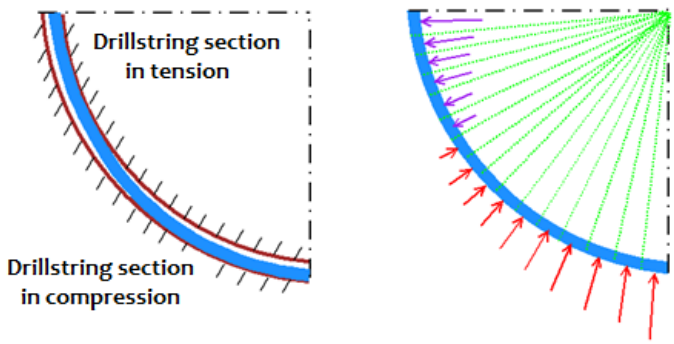

Figure 4.13: Physical sketch (left) and normal contact forces (right) of drillstring segments in the build section.

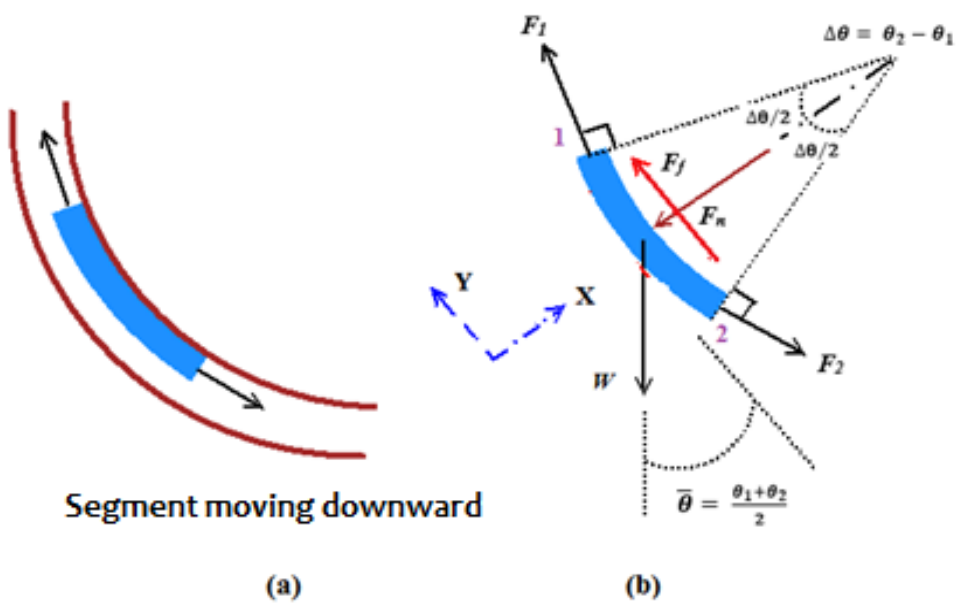

Figure 4.14: (a) Physical sketch of drillstring contact with wellbore and (b) Free body diagram of curved drillstring segment when tension dominates weight.

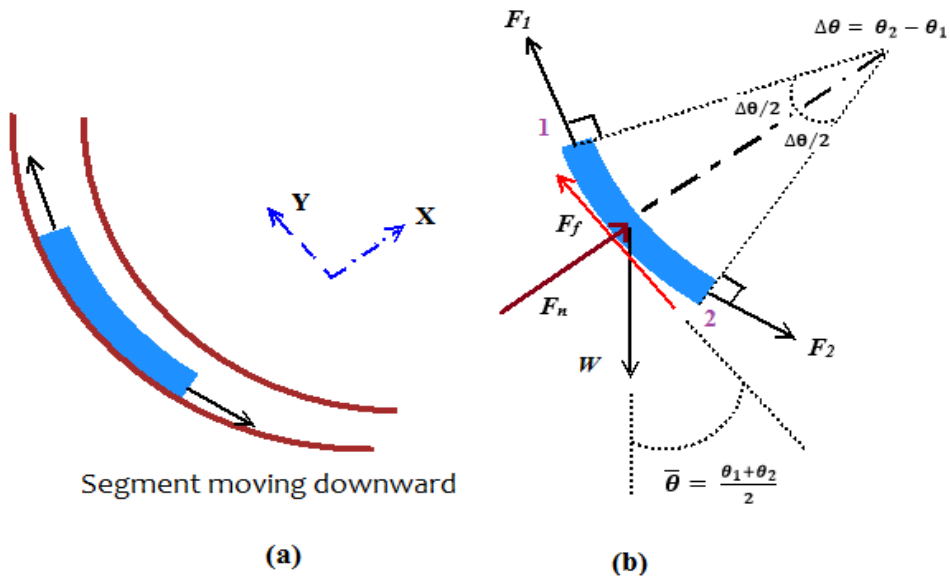

Figure 4.15: (a) Physical sketch of drillstring contact with wellbore and (b) Free body diagram of curved drillstring segment when weight dominates tension.

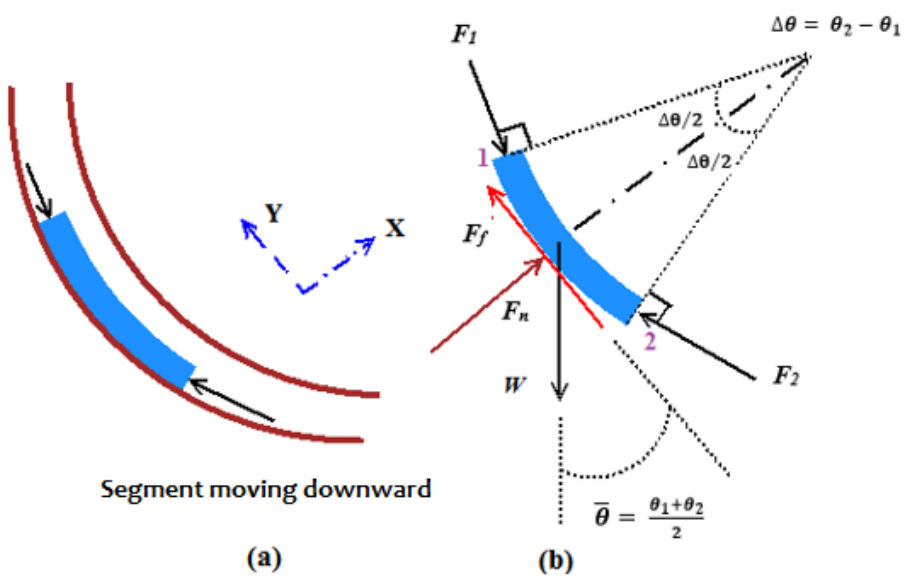

Figure 4.16: (a) Physical sketch of drillstring contact with wellbore and (b) Free body diagram of curved drillstring segment when segment under compression.

There will be a neutral point where the upper portion of the drillstring experiences tension force and lower portion is in compression. In the upper portion, close to the neutral point, the term $F_t\,\Delta\theta$ becomes less than the term $W\sin\bar{\theta}$ in Eq. (2). The situation is depicted in Fig. 4.15 and the drillstring segment contacts at the bottom of the drillstring. Thus the normal contact force equation from the free body diagram of curve segment in Fig. 4.15 can be written as

$$F_n = W\sin\bar{\theta} - F_t\,\Delta\theta \tag{4.6}$$

Finally, the normal contact force for the case of curved segment under compressive force, which is shown in Fig. 4.16, can be written as

$$F_n = W\sin\bar{\theta} + F_c\,\Delta\theta \tag{4.7}$$

where F_c = compressive force acting in the curved segment.

4.3.1 Horizontal section of drillstring

In this research work, it has been assumed that the drillstring segments contact the wellbore at the bottom side and thus the normal forces have been assumed as equal to the buoyancy weight W of the drillstring segments.

4.4 Modeling of drillstring segment motions

A vertical drillstring dynamics model discussed in Chapter 3 has been extended for modeling the build and horizontal sections of the horizontal drillstring. A lumped-segment approach is used in the longitudinal and torsional motion models. The model accounts for the effect of drilling fluid circulation in the drillstring and the annular space between the drillstring and the wellbore on drillstring motions. The drilling fluid was characterized by the flow rate developed by the mud pumps. Nonlaminar Newtonian flow formulations are used in calculation of fluid drag force/damping for the longitudinal motion. Hydrodynamic damping due to drilling fluid circulation in the drillstring and the annular space was considered in the longitudinal direction instead of viscous damping. In the case of torsional motion, the viscous damping which results from the contact between drillstring surfaces and the drilling fluid was considered. In addition, the model considered the self-weight effect and buoyancy effect due to drilling fluid. Figs. 4.17 and 4.18 show the schematic of drillpipe axial segment model with the FBD of axial segment and the FBD of torsional segment of build (curved) section of drillstring. A bond graph model for longitudinal and torsional motions of a build (curved) drillstring segment is shown in Fig. 4.19. The buoyancy weight of the drillstring segment acts in the longitudinal direction for the case of vertical drilling. It is not the same while drilling the build (or curve) section where a portion of buoyancy weight acts in the longitudinal direction, and is shown in Fig. 4.19 as an effective weight. For the case of horizontal section drilling, there will be no contribution of buoyancy weight in the longitudinal direction (Figs. 4.20). Fig. 4.21 shows the FBD of torsional segment of horizontal section of drillstring. The axial segment bond graph in Fig.

4.19 shows a mass (I element) and effective weight force source (Se element) associated with segment velocity *v*. Hydrodynamic dissipative forces (R elements) also contribute to Newton's Second Law of the mass, with the flow sources (Sf) and 0-junctions calculating relative fluid flow velocities inside and outside the pipe. The dissipative forces are functions of these relative velocities. Axial compliance and material damping of the segment of the segment are modeled by parallel compliance (C) and dissipative elements, the forces of which are functions of the relative velocity (calculated by the 0-junction) of the segment with respect to the adjoining segment. The curve and horizontal drillstring segment models have the friction terms (Figs. 4.19 and 4.22), whereas friction loss has been neglected in the vertical sections. The friction elements (C elements) in the bond graph model shown in Figs. 4.19 and 4.22 provide the drag force for longitudinal motion and transverse frictional force which multiplies with drillstring radius to provide frictional torque for torsional motion.

The bond graph segment model shown in Fig. 4.19 can be written in term of "Cauchy" form ordinary differential equations (DOE) for analysis and simulation. And the set of equations are written as below.

$$\dot{p}_i = M_i \dot{V}_i = F_{i-1} - F_i + M_i g \cos\bar{\theta} + F_p - F_A - F_f \tag{4.8}$$

$$\dot{q}_i = V_{i+1} - V_i \tag{4.9}$$

$$V_i = \frac{1}{M_i} p_i \tag{4.10}$$

$$F_i = \frac{1}{C_i} q_i + R_i \left(V_{i+1} - \frac{1}{M_i} p_i \right) \tag{4.11}$$

$$\dot{p}_i = M_i \dot{\omega}_i = T_{i-1} - T_i - T_{R_i} - T_f \tag{4.12}$$

$$\dot{q}_i = \omega_{i+1} - \omega_i \tag{4.13}$$

$$\omega_i = \frac{1}{J_i} p_i \tag{4.18}$$

$$T_i = \frac{1}{C_i} q_i + R_i \left(\omega_{i+1} - \frac{1}{J_i} p_i \right) \tag{4.19}$$

The bond graph segment model shown in Fig. 4.22 can be written in term of "Cauchy" form ODE for analysis and simulation and are written as below.

$$\dot{p}_i = M_i \dot{V}_i = F_{i-1} - F_i + F_p - F_A - F_f \tag{4.20}$$

$$\dot{q}_i = V_{i+1} - V_i \tag{4.21}$$

$$V_i = \frac{1}{M_i} p_i \tag{4.22}$$

$$F_i = \frac{1}{C_i} q_i + R_i \left(V_{i+1} - \frac{1}{M_i} p_i \right) \tag{4.23}$$

$$\dot{p}_i = M_i \dot{\omega}_i = T_{i-1} - T_i - T_{R_i} - T_f \tag{4.24}$$

$$\dot{q}_i = \omega_{i+1} - \omega_i \tag{4.25}$$

$$\omega_i = \frac{1}{J_i} p_i \tag{4.26}$$

$$T_i = \frac{1}{C_i} q_i + R_i \left(\omega_{i+1} - \frac{1}{J_i} p_i \right) \tag{4.27}$$

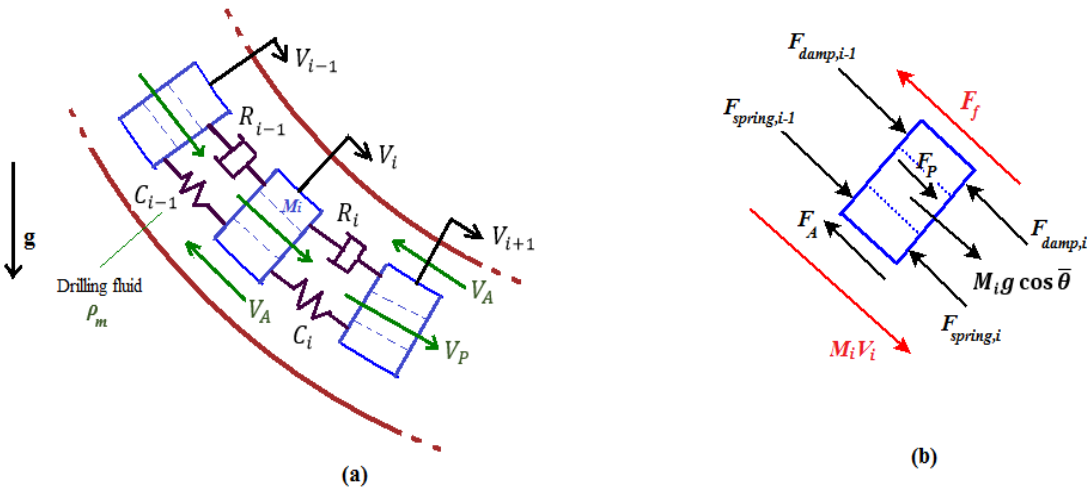

Figure 4.17: Schematic of (a) drillpipes axial lumped segment model showing drilling fluid flow and (b) free body diagram of axial segment of build (curved) section of drillstring.

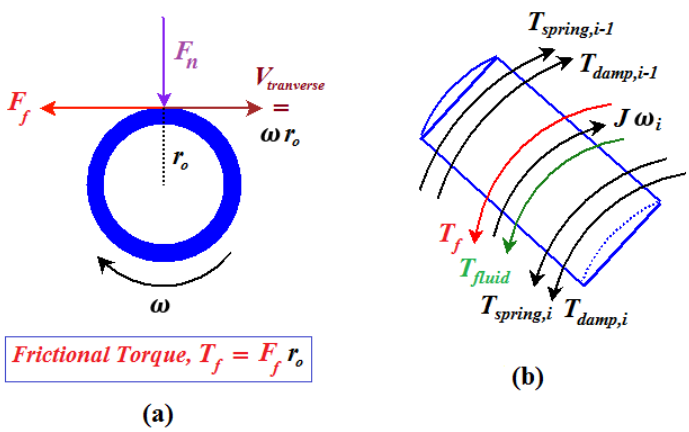

Figure 4.18: Schematic of (a) drillpipe contact force when drillpipe touches upper portion of wellbore and (b) free body diagram of torsional segment of build (curved) section of drillstring.

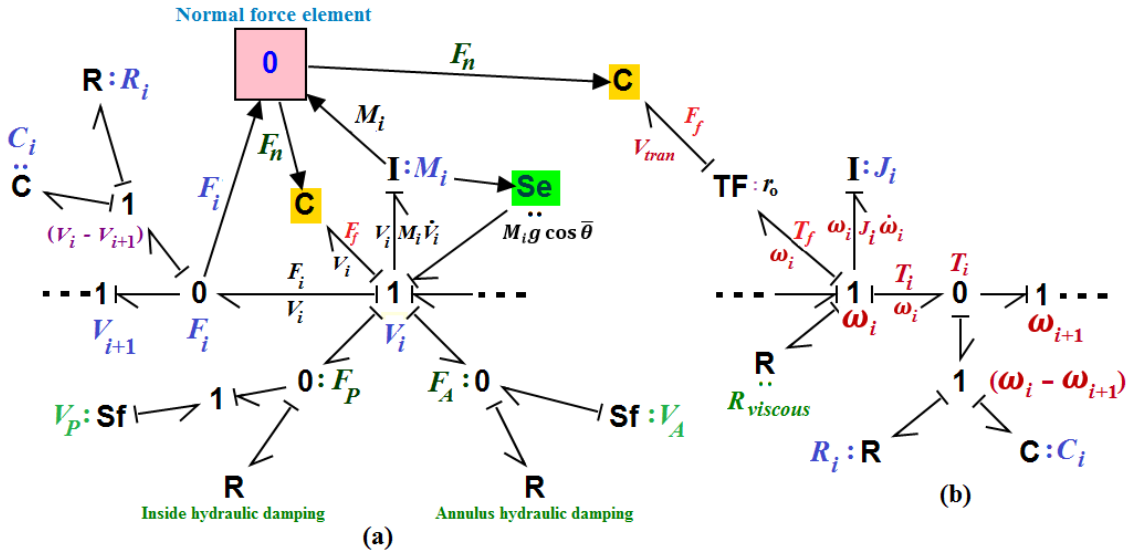

Figure 4.19: Bond graph segment model for (a) longitudinal (or axial) and (b) torsional motions of build (curved) section of drillstring.

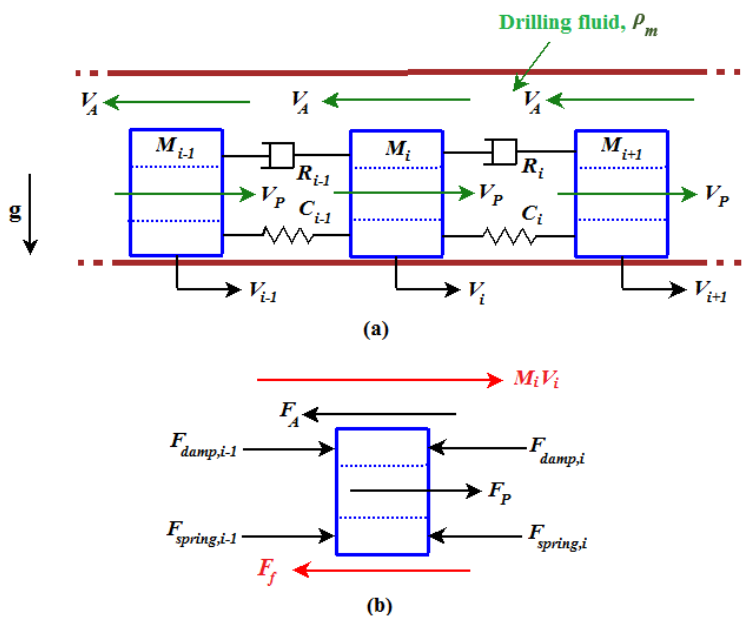

Figure 4.20: Schematic of (a) drillpipes axial lumped segment model showing drilling fluid flow and (b) free body diagram of axial segment of horizontal section of drillstring.

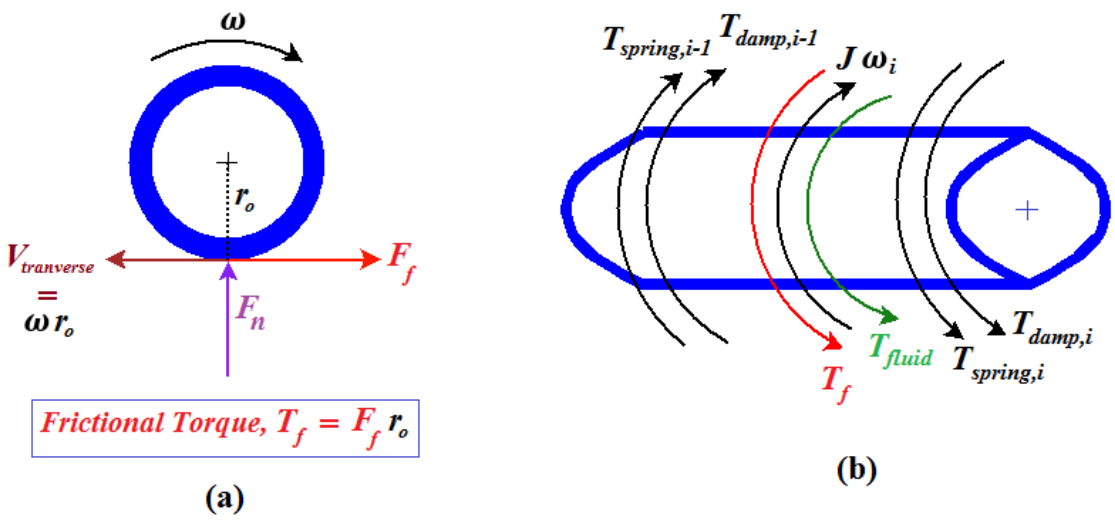

Figure 4.21: Schematic of (a) drillpipe contact force and (b) free body diagram of torsional segment of horizontal section of drillstring.

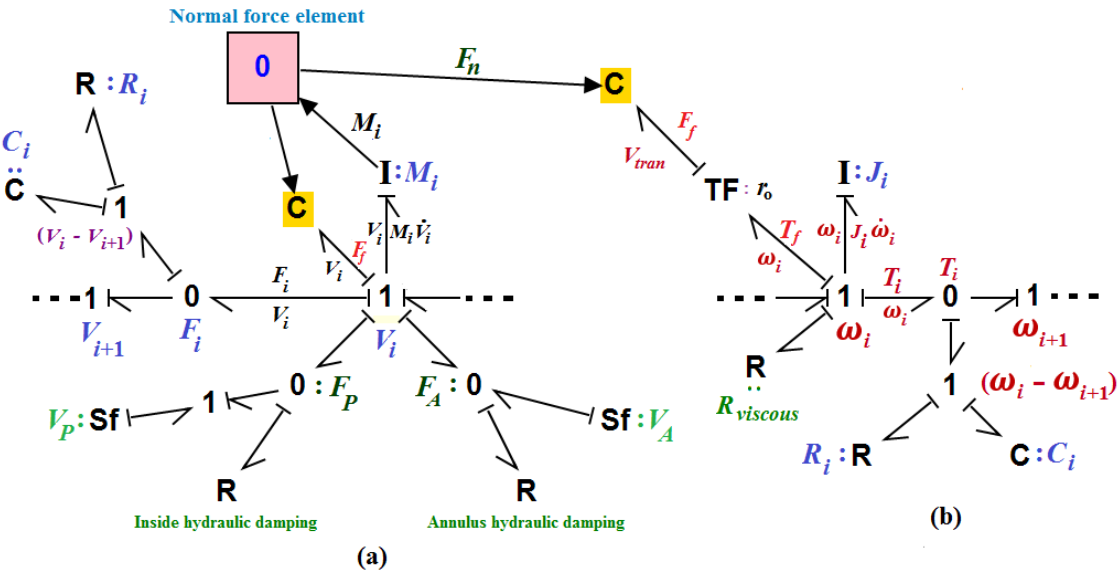

Figure 4.22: Bond graph segment model for (a) longitudinal (or axial) and (b) torsional motions of horizontal section of drillstring.

4.5 Modified bit-rock interaction model

The bit-rock interaction model discussed in Chapter 3, which provides coupling between longitudinal and torsional drillstring motions, has been modified in this chapter work for simulating the friction phenomena while drilling the horizontal oilwell. The model incorporated threshold force and the effect of instantaneous WOB and bit rotation speed on the cutting TOB. Below a threshold force, the drill bit does not penetrate into the rock, leaving only friction as a source of TOB. One of the major limitations in the Chapter 3 bit-rock interaction model is that the drill bit could not move longitudinally as the drill bit cut the rock formation. Thus, the bit-rock model has been modified accordingly. This has the important benefit of allowing prediction of ROP. The dynamic WOB equation has been modified as follows:

$$\mathrm{WOB} = \begin{cases} \mathrm{k_c}\left(x - s - \int ROP\right) & if\ x \geq (s + \int ROP) \\ 0 & if\ x < (s + \int ROP) \end{cases} \tag{4.28}$$

where k_c, s and ROP indicate formation contact stiffness, bottom-hole surface profile and rate of penetration. The physical sketch of the contact between drill bit and rock formation is shown in Fig. 4.23, and the bond graph model is shown in Fig. 4.24. The reader is referred to Chapter 3 for the equations of the bit-rock interaction model.

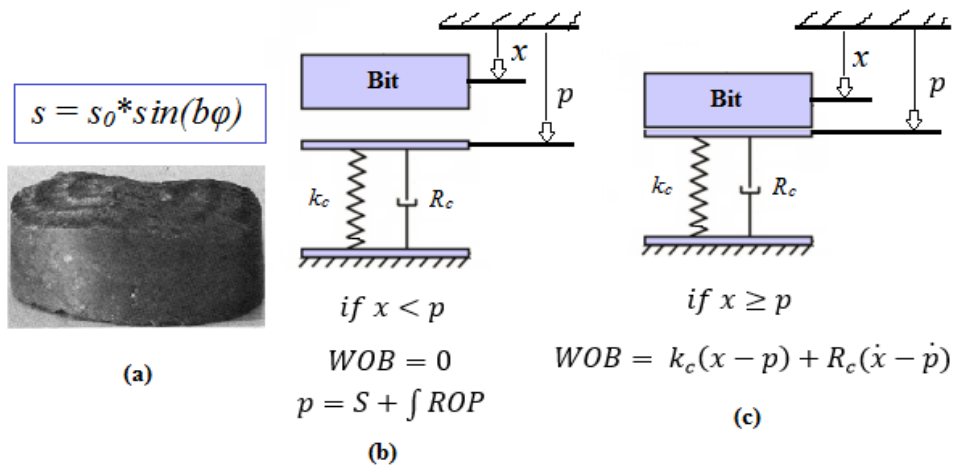

Figure 4.23: sketches show (a) a lobe pattern of formation surface elevation, and (b) bit and rock spring-damper representation when x < p and (c) bit contact with rock when x >= p rock sping and damper under compression.

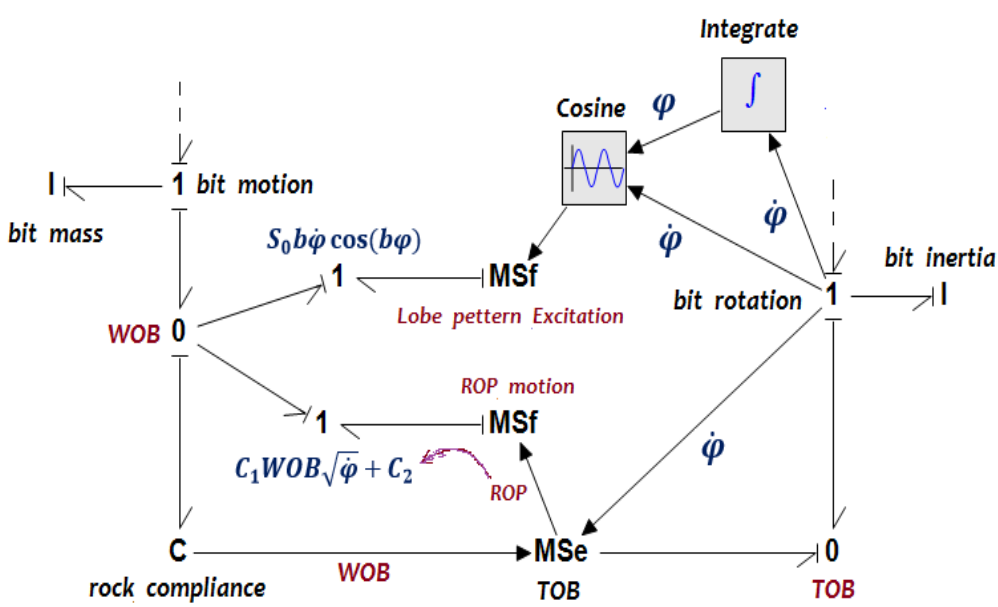

Figure 4.24: Bond graph model of bit-rock motion

4.6 Tuning of friction factor

Overall simulation results will be sensitive to the friction factor between drillstring and wellbore contact surfaces. Researchers from both academia and industry (Aadnoy *et al.*, 2001; 2010; Tveitdal, 2011) have recommended friction factors between 0.1 to 0.4. The friction factor should be tuned with field data.

4.6.1 Horizontal well field data

Friction factor is tuned using data from a horizontal well in the Septimus field in British Columbia (BC), Canada. The total measured depth (MD) of this well is 4340 m and true vertical depth (TVD) of this well is 2014 m. This well has been designed to be a single build section after kick-off point followed by a long horizontal section. The kick-off point of this well is 1720 m MD and the build section is from this depth to 2182 m MD and from this point forward until the target, which is 4340 m MD, is the long horizontal section. The radius of the build section of this well is 294 m, a medium range radius type well. The well trajectory is shown in Appx. A, Fig. A1. Sketches of drillstring configurations for different depths are shown in Fig. A2. Table A.1 summarizes drillstring configuration as a function of length. The time-depth plot shown in Fig. 4.25 shows that the drilling rate was high in the vertical section compared to build section. This can be verified with the time-ROP plot shown in Fig. 4.26. For the horizontal section, the average drilling rate is better compared to the build section shown in Fig. 4.26. The drillstring static weights for different depths are shown in Fig. 4.27. The static weight decreases after passing the build section because of removing the heavy weight drill pipe (HWDP) from the drillstring configuration which can be identified in the drillstring configuration chart in Appx. A. Figs. 4.28 shows the drag

forces due to friction between the drillstring and wellbore during pulling the drillstring up and pushing the drillstring down. Negligible drag forces are encountered in the vertical section and a significant amount can be noted in the build section but the drag increases significantly in the horizontal section. Also, the drag forces during pulling the drillstring up from the well are larger than the drag forces during pushing the drillstring down. Figs. 4.29 and 4.30 show the surface torques which are required for rotating the drillstring during the off-bottom and on-bottom conditions, respectively. Off-bottom torque is caused by the friction between drillstring and wellbore, whereas the on-bottom torque (drilling torque) is the summation of the torque required to overcome the friction and the torque required to cut the rock formation. A significant amount of off-bottom torque in the vertical section indicates contacts between the drillsting and wellbore. The increasing off-bottom torque in the build and horizontal sections is due to the expected higher contact area between the drillstring and wellbore. The on-bottom torque plot in Fig. 4.30 shows a constant torque in the vertical section which can be assumed as a torque required for cutting the rock formation. In the build section, the increasing on-bottom torque with depth proves the importance of torque due to contact-friction and the necessity of capturing this in the simulation model. Even higher on-bottom torque while drilling the horizontal section verified the presence of high frictional torque due to large contact area between the drillstring and wellbore.

From the field results it is clear that the analysis of wellbore friction is an important factor in drilling and well design.

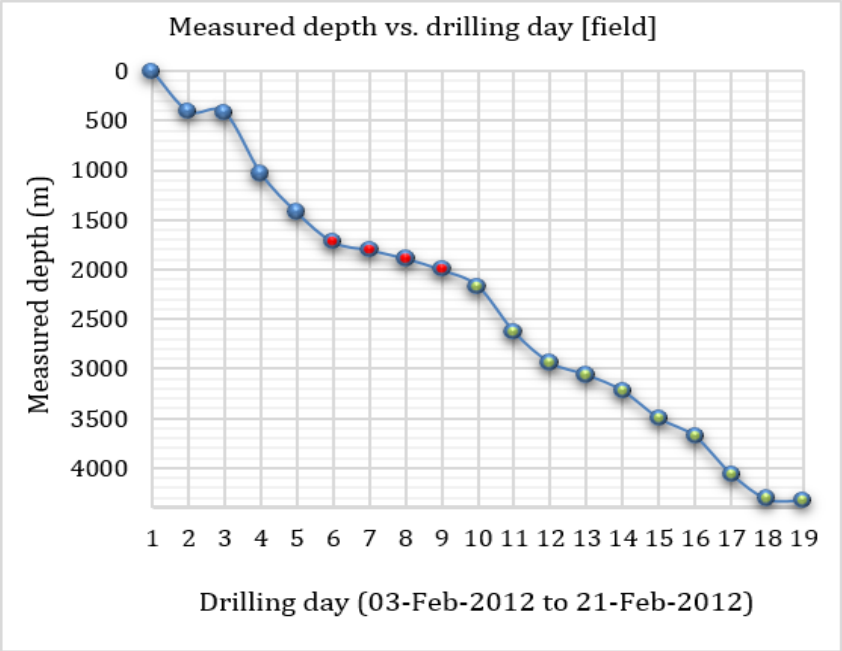

Figure 4.25: Measured depth vs. drilling day of CNRL HZ Septimus C9-21-81-19 well.

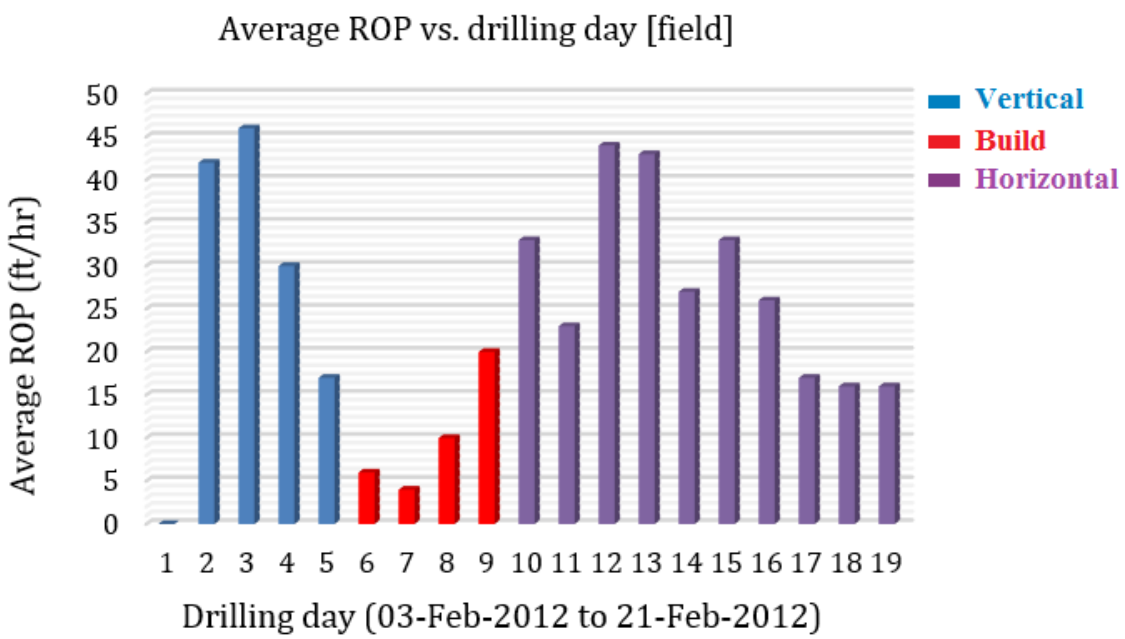

Figure 4.26: Average ROP vs. drilling day of CNRL HZ Septimus C9-21-81-19 well.

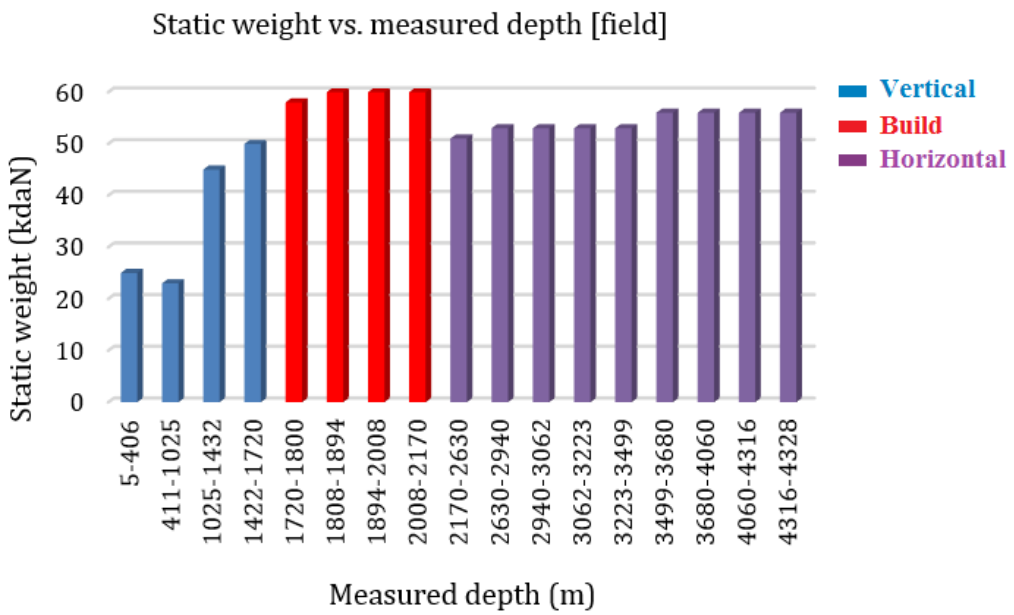

Figure 4.27: Static weight vs. depth of CNRL HZ Septimus C9-21-81-19 well.

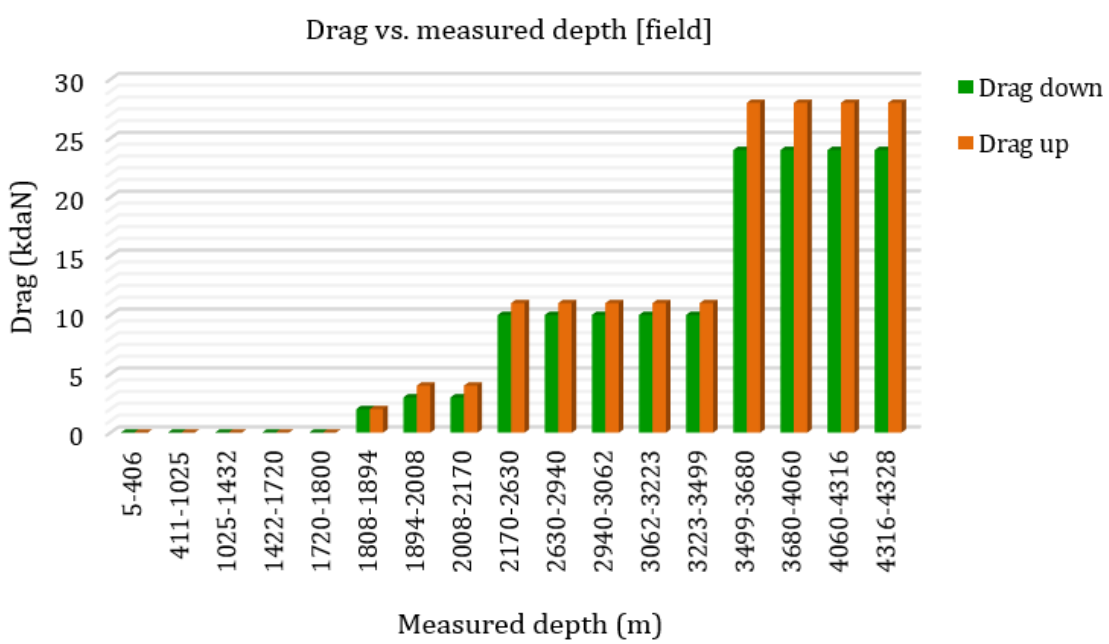

Figure 4.28: Drag force vs. depth of CNRL HZ Septimus C9-21-81-19 well.

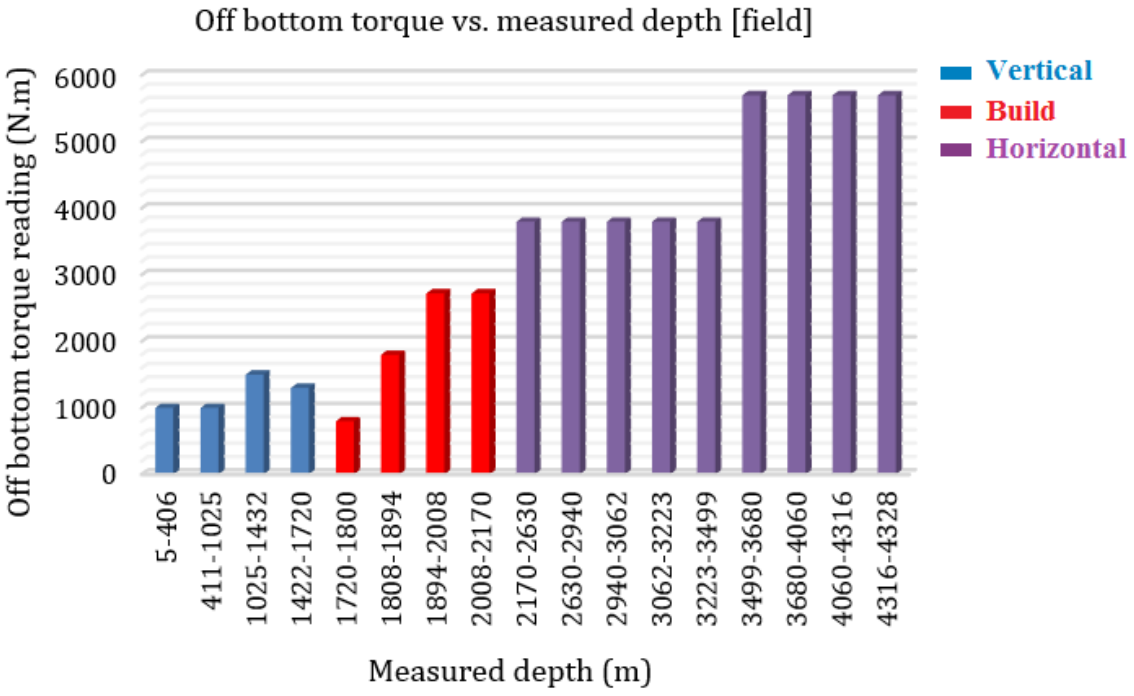

Figure 4.29: Off-bottom torque vs. depth of CNRL HZ Septimus C9-21-81-19 well.

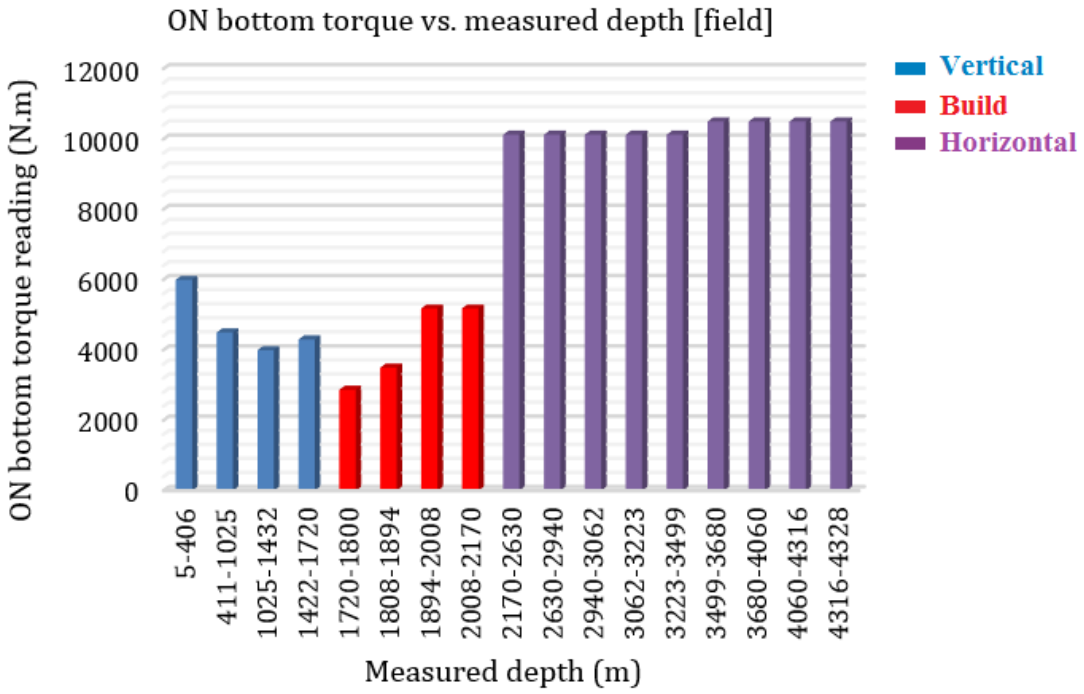

Figure 4. 30: On- bottom torque vs. depth of CNRL HZ Septimus C9-21-81-19 well.

4.6.2 Selection of friction factor

The bond graph model of the horizontal oilwell drillstring motions has been implemented in the commercial bond graph modeling software 20Sim®. The drillstring model has three main parts: longitudinal motion submodel, torsional motion submodel and bit rock submodel. The top of the drillstring is subject to a tension force (or hook load). Rotary motion is applied by an ac motor, through a gear box, to the drillstring. Here an induction motor model has been used to simulate the top drive motor dynamics. The reader is referred to the previous chapter for the bond graph modeling of a three phase induction motor which is adopted in this chapter work. The lumped segment approach, which is used in the modeling of continuous shafts, beams and rods, gives the flexibility to specify the segment length independently of the number of segments in the whole model. Here, a total of 10 segments has been used for the vertical section. The curved portion of the drillstring has been divided into 20 segments, and 25 segments have been chosen for the horizontal portion of the drillstring. Thus the whole model consists of a total of 10 segments in the simulation of vertical section which is up to a 1720 m MD in the well chart (Appx. A) and when the drillstring exceeds the KOP and goes to the curve section then the whole model consists a total of 30 segments. Finally, a total of 55 segments have been used to simulate the complete drillstring, including the horizontal portion.

Figs 4.31-4.34 present the results obtained from the drillstring lumped segment model. Static weights of the drillstring configurations based on the chart in Appx. A at different measuring depths are shown in Fig. 4.31. The static weight of the drillstring at 2550 m MD is lower than the static weight at 2160 m MD which is consistent with the field result

shown in Fig. 4.27. As mentioned earlier, the reason is the absence of HWDPs in the drillstring configuration at 2550 m MD. The static weight of the drillstring is increased again in the horizontal section because of addition of heavy weight drill pipes. In order to tune the friction factor between the drillstring and wellbore, the tripping in and out operations have been conducted in the model and the results of drag force required to overcome the friction are shown in Figs. 4.32 and 4.33, respectively. Discrepancies compared to the field results shown in Fig. 4.28 are attributed to low resolution of the field data logging. From a qualitative comparison between model results and field data, the dynamic and static friction coefficients are recommended as 0.35 and 0.4, respectively. Another validation of friction factor has been conducted through rotating the drilltring in off bottom condition and the torques required to overcome the friction at different depths are shown in Fig. 4.34. Dynamic and static frictions coefficients of 0.2 and 0.25 give the best match with field data as shown in Fig. 4.29. Thus, rotating friction coefficients (static and dynamic) for drillstring rotational motion differ from longitudinal friction coefficient (static and dynamic). This assumption has a good agreement with the work presented in (Lesage et al., 1988). The negative effect of friction on drilling performance can be mitigated through axially-vibrating downhole tools. Such a tool will be incorporated into the simulation, and results generated in Section 4.8. In the next section, the experimental characterization of such a tool by the author's research group is presented.

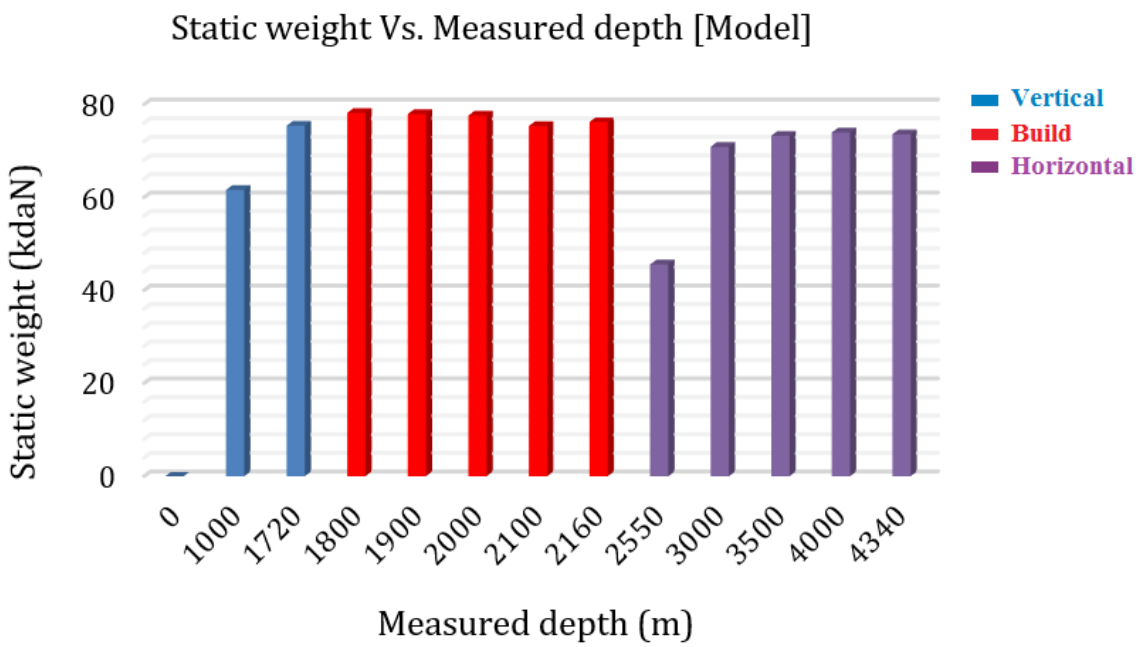

Figure 4. 31: Static weight vs. depth of the model of CNRL HZ Septimus C9-21-81-19 well.

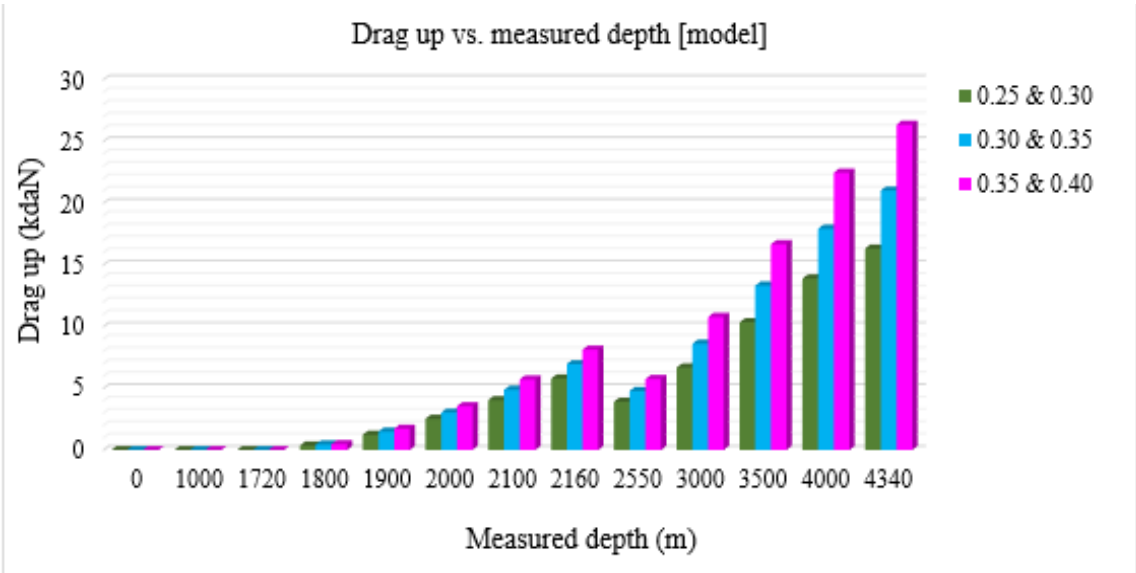

Figure 4.32: Upward motion drag force vs. depth of the model of CNRL HZ Septimus C9-21-81-19 well.

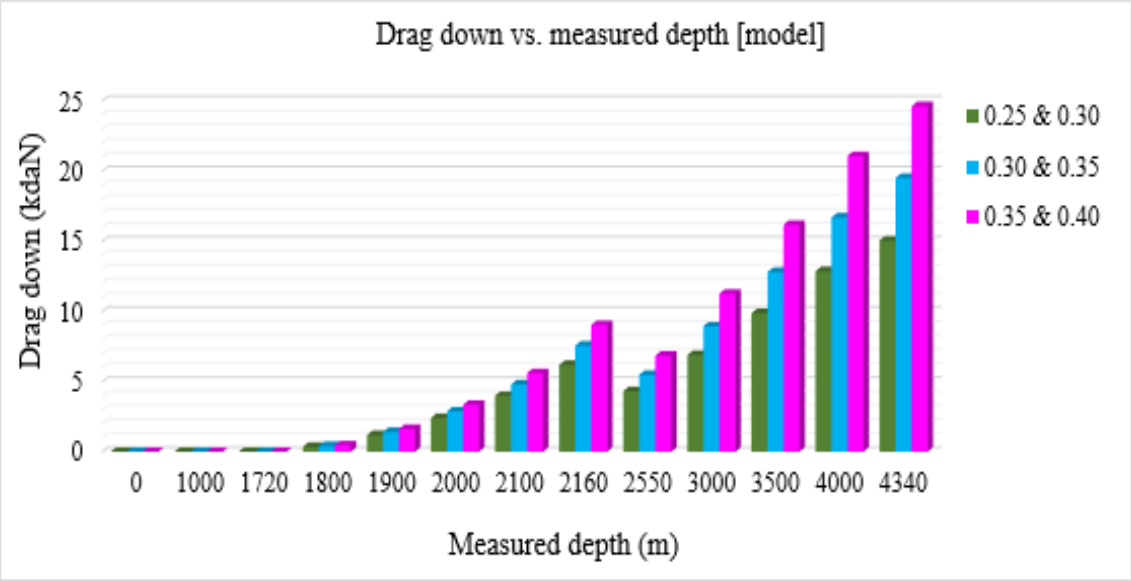

Figure 4.33: Downward motion drag force vs. depth of the model of CNRL HZ Septimus C9-21-81-19 well.

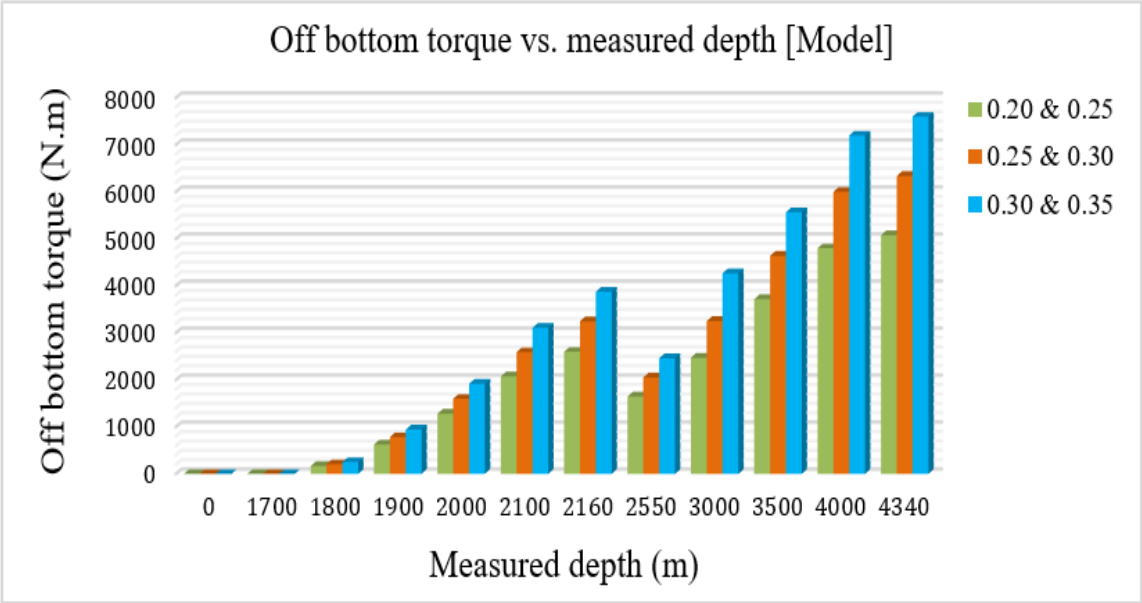

Figure 4.34: Off-bottom torque vs. depth of the model of CNRL HZ Septimus C9-21-81-19 well.

4.7 Experimental characterization of downhole tool

In order to reduce the friction energy loss, National Oilwell Varco (NOV) has developed and manufactured the Agitator® tool which is capable of producing axial oscillations down-hole. It has been proved to be an effective method to convert friction from static to dynamic and reduce the overall energy loss. A 25% friction reduction can be achieved by using the Agitator® tool (Skyles *et al.*, 2012). To determine the pressure, flow, and force characteristics of the tool, a testing frame has been built in the Advanced Drilling Laboratory (ADL) at Memorial University of Newfoundland (MUN) that is capable of measuring upstream and downstream pressures and resulting axial force. The testing frame for the Agitator® tool experiment is shown in Fig. 4.35. Three load cells (Fig. 4.36), each with a capacity of 5000 lb, have been installed underneath each corner of the triangular plate. The Agitator® tool has been installed at the middle of the triangular plate and fixed laterally from bottom to top using three sets of constraints. Sensors (Fig. 4.36) record the upstream and downstream pressures. The upstream and downstream pressure transducers have the ranges of 0 to 4000 psi and 0 to 1500 psi, respectively, and temperature range from (-20) to (+80) degrees Celsius. High pressure hose has been attached at the top of the tool that allows the tool to vibrate axially. A flow meter has been installed at the outlet of the pipe to measure the flow rate. Three ball valves have been put in the set up that can be operated manually in order to isolate the Agitator® unit from the main stream line. The input flow is supplied through the mobile pumping unit shown in Fig. 4.35. The unit can deliver a flow rate up to 70 gallons per minute (gpm) with maximum pressure of 2500 psi. A sophisticated 16-channel portable data acquisition (DAQ) system, designed to work in

harsh environments, has been used to read the data from sensors. The DAQ has a NI9188 chassis and a NI9237 for acquiring the data. The power supply system of the DAQ system shown in Fig. 4.37 has been designed to be safe from water during operation. The power system uses a custom cable to plug into the main supply line (110 V) and the system provides three different voltage outputs (5 V, 9-12 V and 24 V).

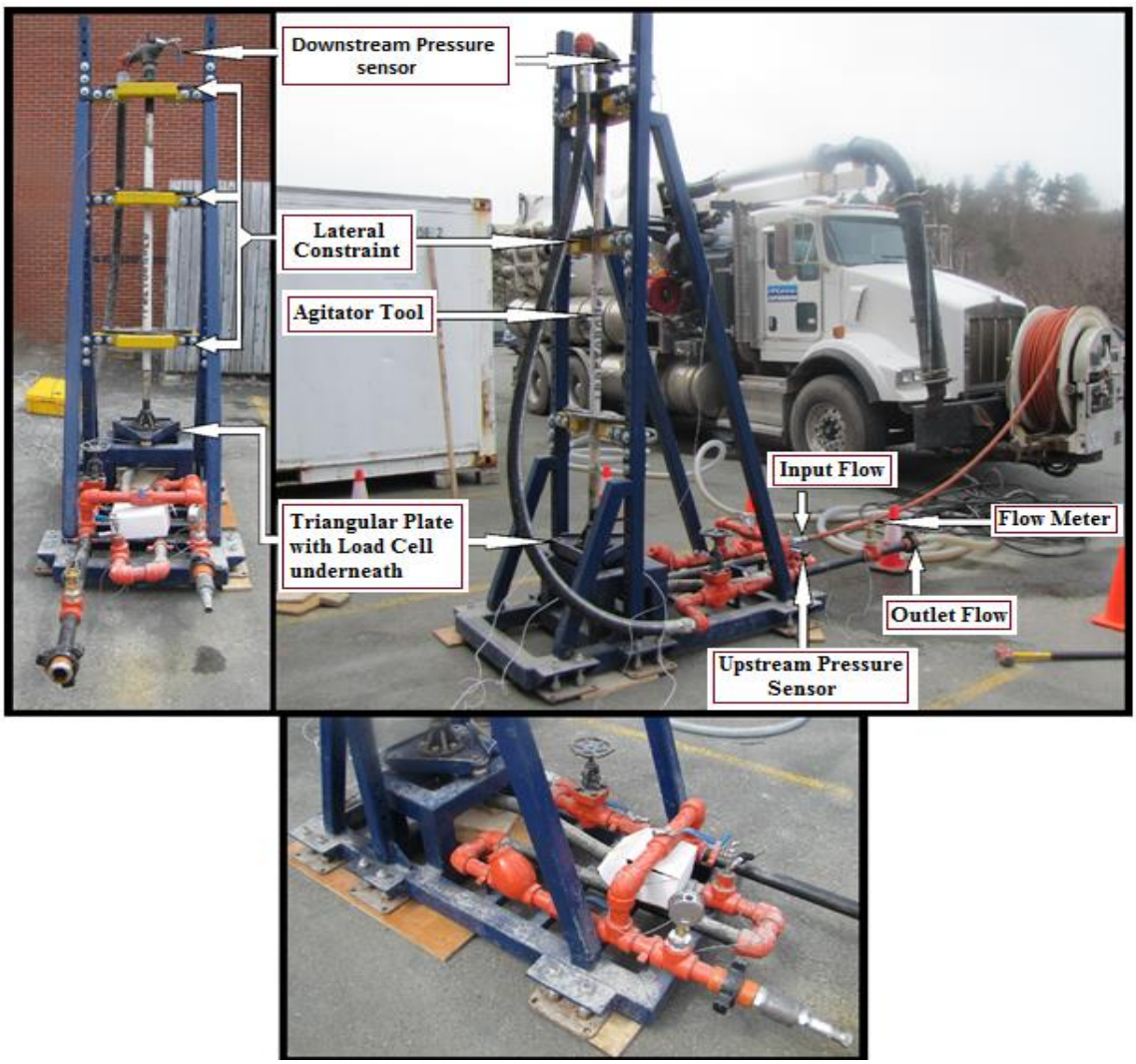

Figure 4.35: Testing frame and associated pumping facility in Advanced Drilling Laboratory at MUN.

Figure 4.36: (a) load cells, (b) upstream pressure sensor and (c) downstream pressure sensor used in testing frame in Advanced Drilling Laboratory at MUN.

Figure 4.37: Mobile DAQ system in Advanced Drilling Laboratory at MUN.

Figs 4.38-4.43 show the experimental results found from the Agitator® tool. All tests have been done at atmospheric pressure. The inlet and outlet pressure fluctuations at 70 gpm flow rate are shown in Figs. 4.38 and 4.39, respectively. A pressure fluctuation of 570 psi was measured. The generated force from the Agitator® tool at 70 gpm flow rate is shown in Fig. 4.40. An oscillation of 400 lbs was observed. The dominant frequency was found to be 20 Hz as seen in frequency spectrum of the force oscillation shown in Fig. 4.41. The oscillating frequency increases with flow rate. The plot of oscillation frequencies at different flow rates is shown in Fig. 4.42. The pressure drop across the agitator tool also depends on the flow rate, as shown in Fig. 4.43.

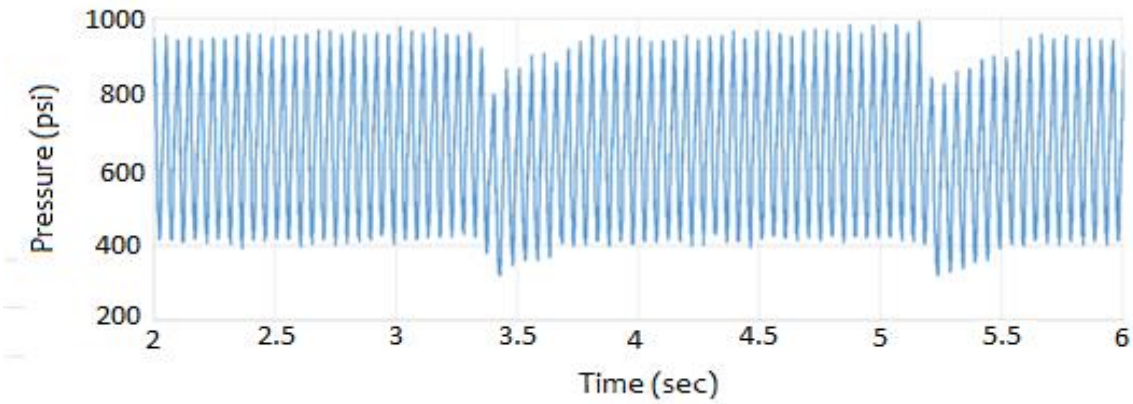

Figure 4.38: Inlet pressure fluctuation at 70 gpm flow rate.

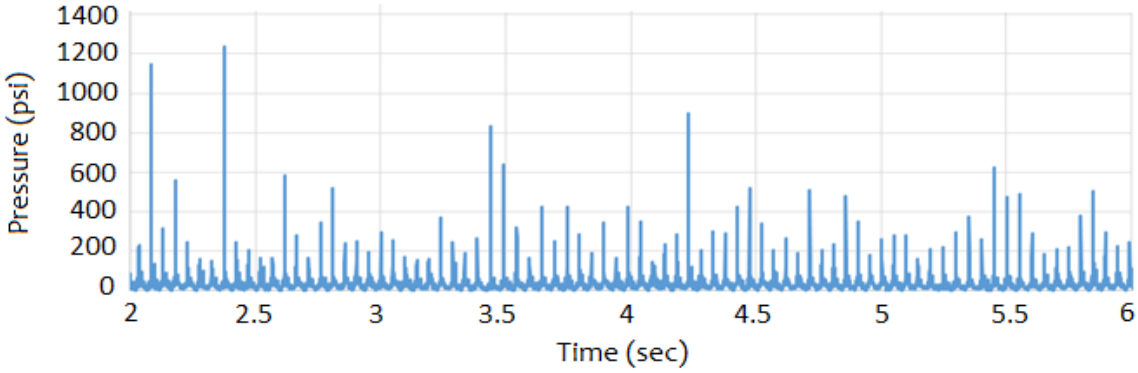

Figure 4.39: Outlet pressure fluctuation at 70 gpm flow rate.

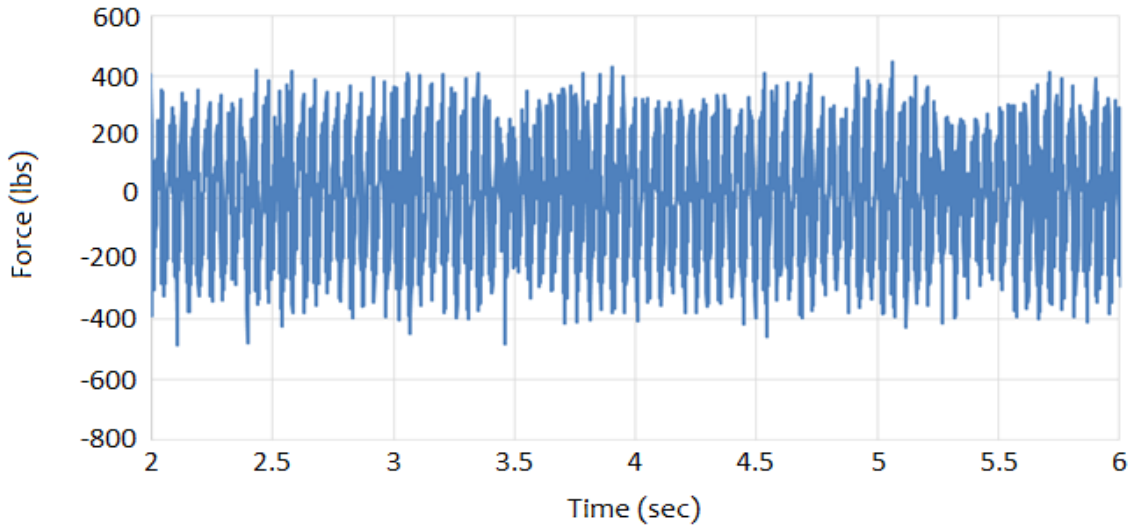

Figure 4.40: Axial force profile generated from Agitator® tool at 70 gpm flow rate.

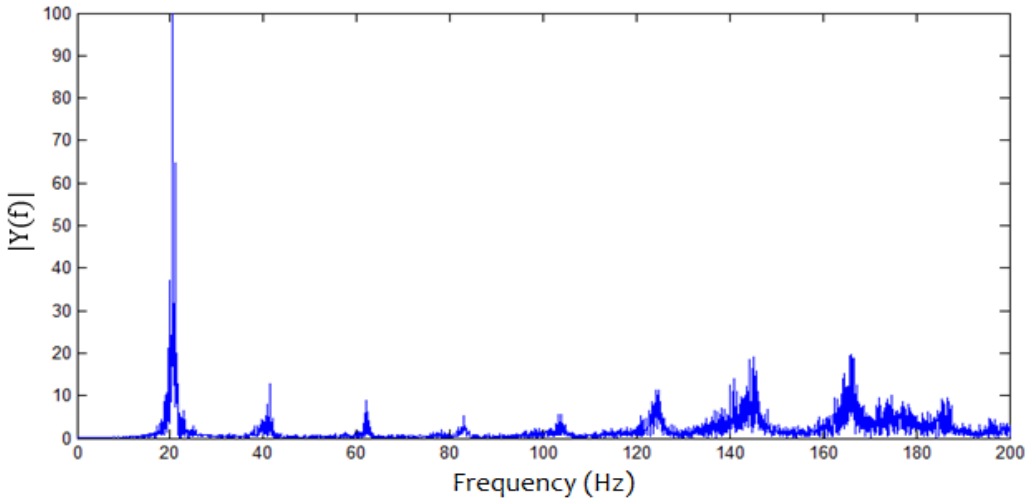

Figure 4.41: Spectrum of tool generated force at 70 gpm flow rate.

The direct measurement of force generation has been done at atmospheric pressure, which differs greatly from downhole conditions. In order to predict the actual force generation down-hole, back pressure has to be applied during experiment. The axial oscillation generator tool discussed in (Ali *et al.*, 2011) provides a very high pressure drop

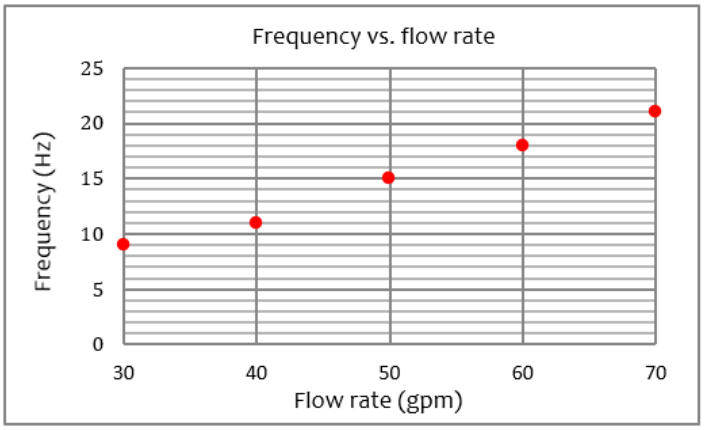

Figure 4.42: Frequency vs. flow rate of Agitator® tool.

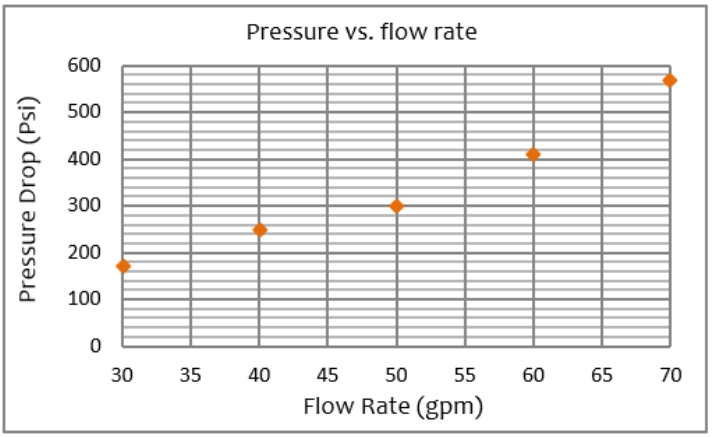

Figure 4.43: Pressure drop vs. flow rate of Agitator® tool.

(700 psi at 485 gpm and 10 lb/gal mud). The pressure drop for these tools ranges from 200 psi to over 700 psi, depending on setup, and typically is in the 450-600 psi range (Gee *et al.*, 2015). Gee *et al.* (2015) modeled the excitation as an oscillating mass in the simulation, in the form of a sine wave. The magnitude and frequency of the excitations were 26 klbs (115.65 kN) and 20 Hz. Currently, an experimental facility is under development in the ADL at MUN that will be able to do this. The simulation of horizontal drillstring with downhole tool will be presented in the next section.

4.8 Simulation of horizontal drillstring with downhole tool

The main objective of this simulation is to show the ability of the proposed model to capture the longitudinal and torsional motions of a horizontal drillstring including predicting the effect of an axial excitation tool on the motions of the drillstring. The model has the capability to advance the bit and predict ROP. The simulation results for drilling using a top drive and mud motor at 4340 m MD are shown in Figs 4.44-4.52. The top of the drillstring was rotated at 5.2 rad/s (or 50 rpm) while the mud motor was rotated at 13.7 rad/s (or 131 rpm). The string was pushed down until it touched the rock and the WOB built up to 100 kN. Then, rotary motion was applied to drillstring. At the beginning of the simulation, the bit does not rotate due to the high cutting torque and wellbore friction torque. The bit does not move forward, friction drag throughout the string decreases and WOB increases as shown in Fig. 4.44. As soon as the drill bit rotates the bit starts to move forward (Fig. 4.45), friction drag is increased, and WOB is decreased to 100 kN (Fig. 4.44). The surface torque required to overcome the cutting torque at the bit and frictional torque throughout the drillstring is shown in Fig. 4.45. The absence of fluctuation in the surface torque indicates the constant rotation at the bit (Fig. 4.45). The constant WOB and bit speed provide a constant ROP that can be verified from the ROP plot in Fig. 4.45.

An axial excitation source (AES), which is a sinusoidal force, has been placed at 650 m behind the bit according to the chart in Appx. A and the comparison with the conventional drilling (without AES) is shown in Figs. 4.44-4.47. The amplitude and frequency of the force have been chosen as 200 kN and 125 rad/s (20 hz) for the simulation results in Figs. 4.44-4.47. The WOB plot in Fig. 4.44 shows the 32.5% increment in WOB

compared to drilling without AES. The bit speed comes down from 18.9 rad/s due to the higher TOB, which is shown in Fig. 4.45, caused by higher WOB. Again the drill bit reaches a constant speed of 18.9 rad/s when the top drive provides the extra torque to overcome the cutting torque. The increase in surface torque can be seen in Fig. 4.45. The 30.7% increment in ROP due to higher WOB introduced by the AES is shown in Fig. 4.45. The axial displacements and forces in the drillstring segments generated from the AES have been shown in Figs. 4.46 and 4.47, respectively. The displacements at 350 m and 650 m behind bit show less than 1.0 mm oscillation amplitude, which is a good indication that the vibrations from the AES are not transferred to the drill bit where they could cause damage. There exist optimum values of amplitude and frequency for the AES force to achieve higher WOB, higher ROP and less oscillation at the BHA and the bit.

A comparison study for different amplitudes and frequencies of AES force on the drillstring motions has been conducted to show how the model could be used to optimize the ROP. The displacements generated at the AES segment for different applied forces are shown in Fig. 4.48. The higher amplitude force generated higher amplitude displacement at the AES segment. Also, a higher amplitude is found when higher frequency AES force is applied. The simulation results in Figs. 4.49 and 4.50 show that the displacement oscillation throughout the drillstring is very sensitive to the AES force frequency. Higher displacement throughout the drillstring can be achieved by applying a low frequency AES force that increase significantly WOB (Fig. 4.51) and ROP (Fig. 4.52). On the other hand, a very low frequency of AES force can provide a higher oscillation to the bit that can damage the bit. Thus a very high amplitude and very low frequency AES force should be

avoided in order to protect the BHA and drill bit. A very low amplitude and a very high frequency AES force is also not a good choice as it does not increase the WOB and ROP. The horizontal drillstring model described herein is effective at predicting the effect of downhole tool parameters on drilling performance and vibration throughout the string.

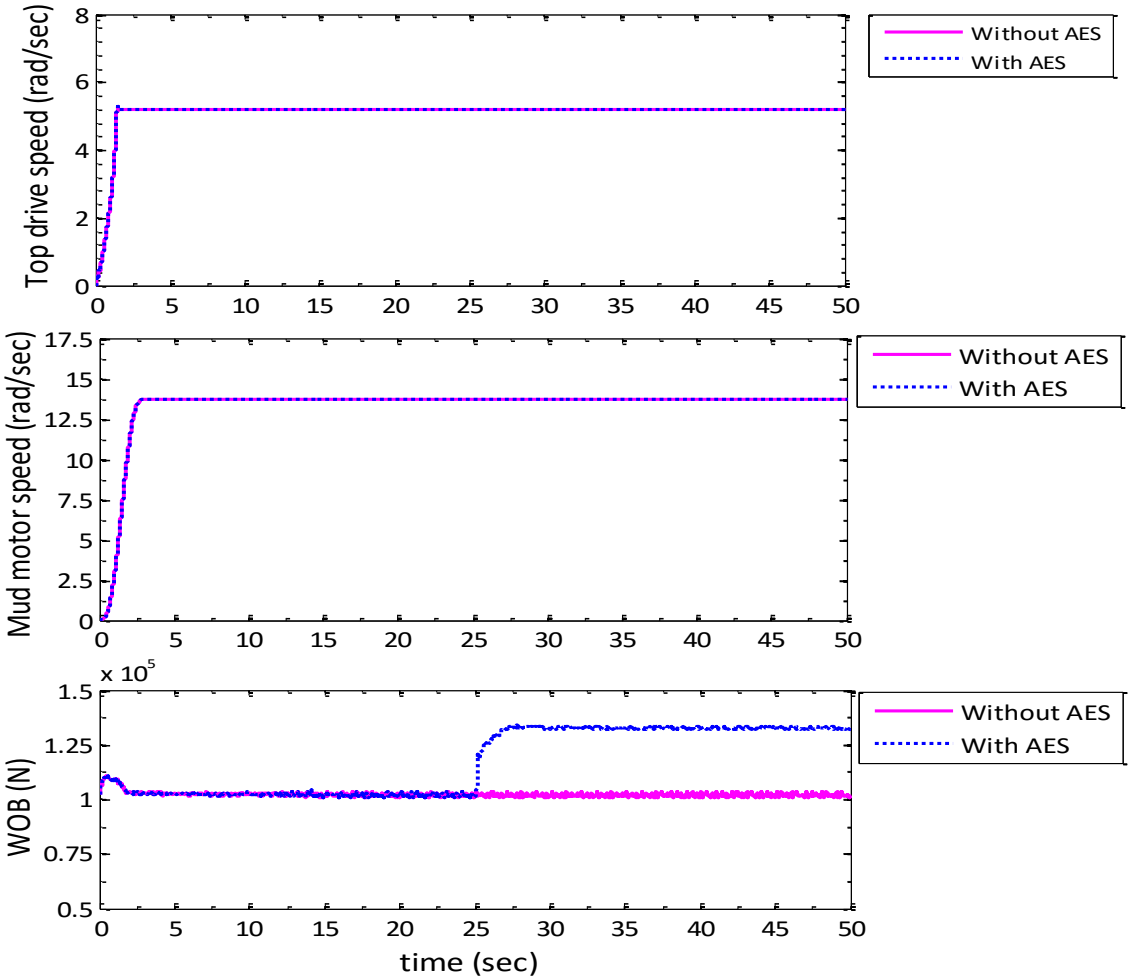

Figure 4.44: The top drive speed, mud motor speed and WOB for the case of without and with axial excitation source (AES)

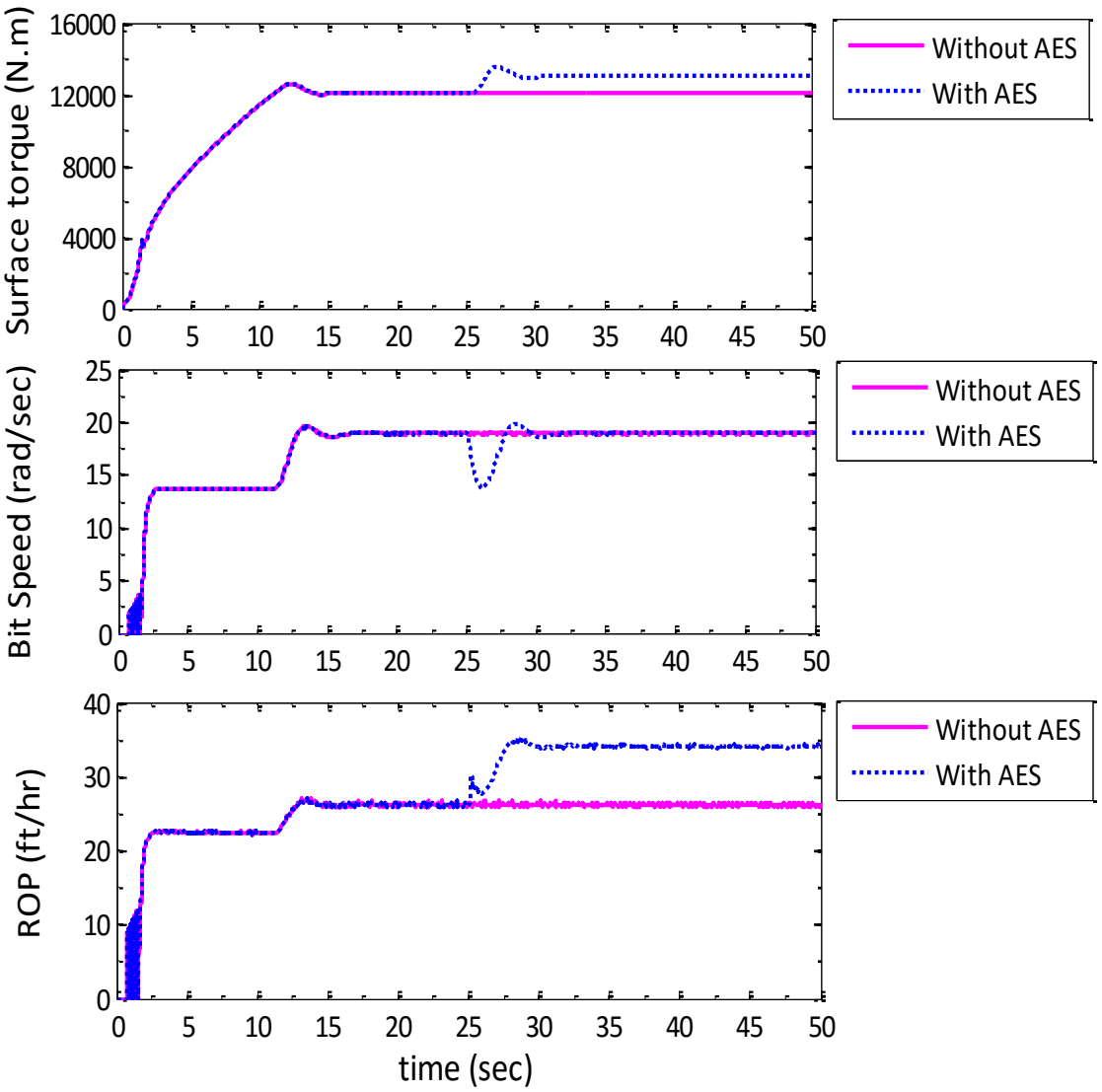

Figure 4.45: The surface torque, bit speed and ROP for the case of without and with AES.

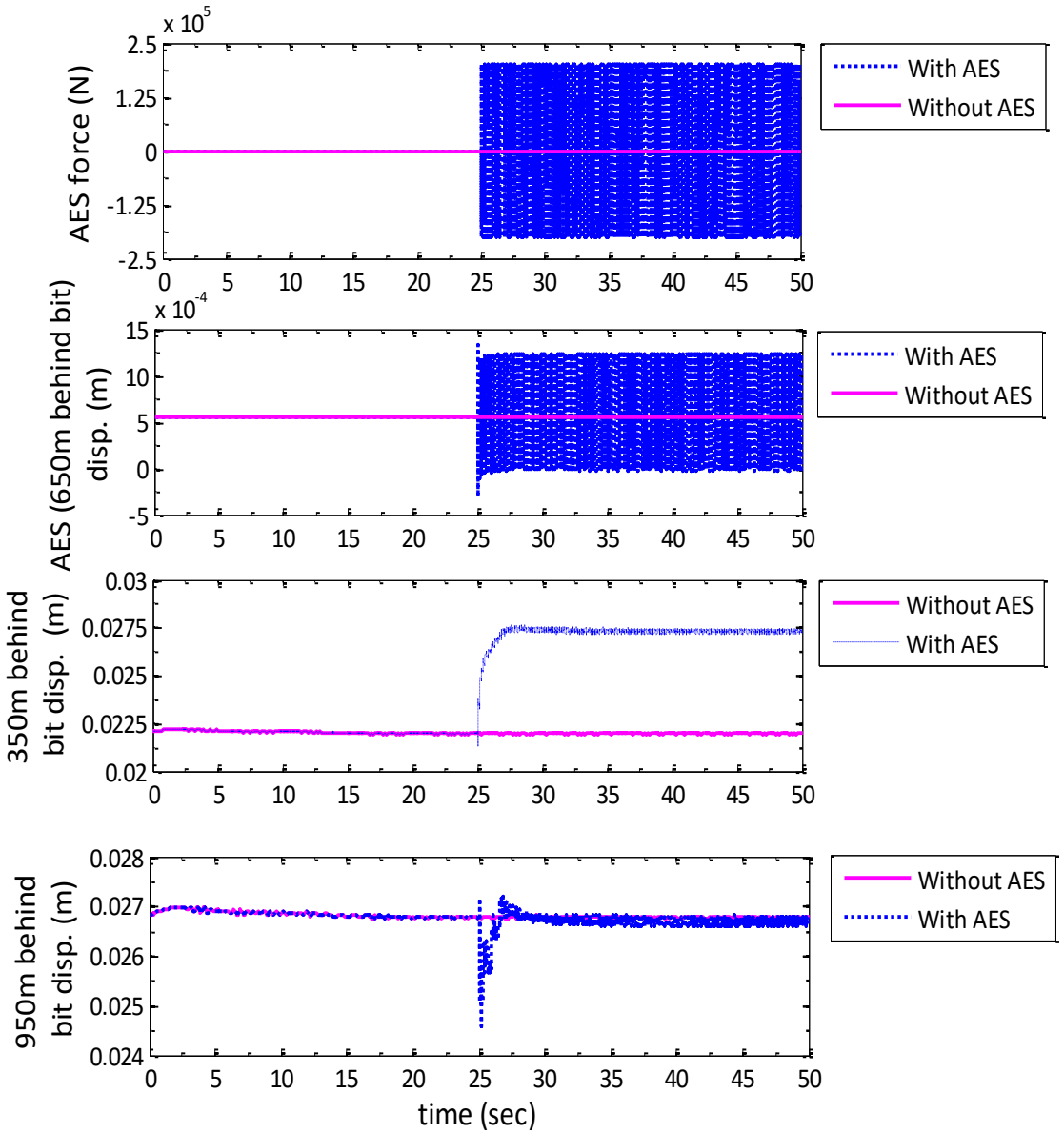

Figure 4.46: The axial excitation force, displacements at different locations for the case of without and with AES.

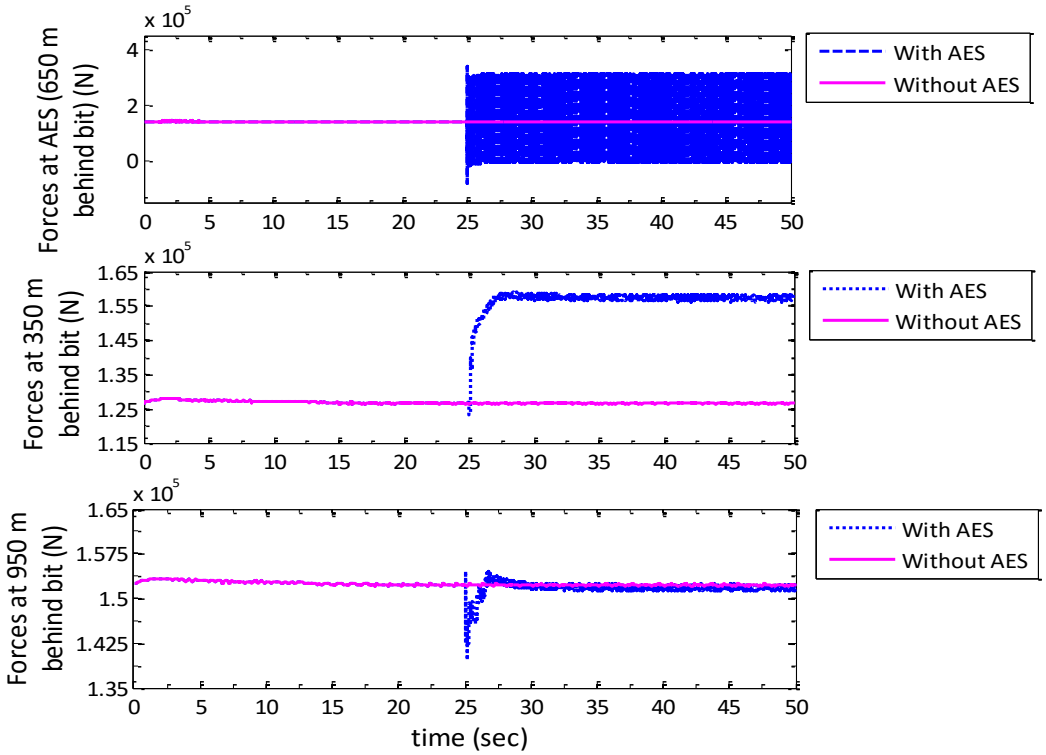

Figure 4.47: Axial forces at different locations for the case of without and with AES.

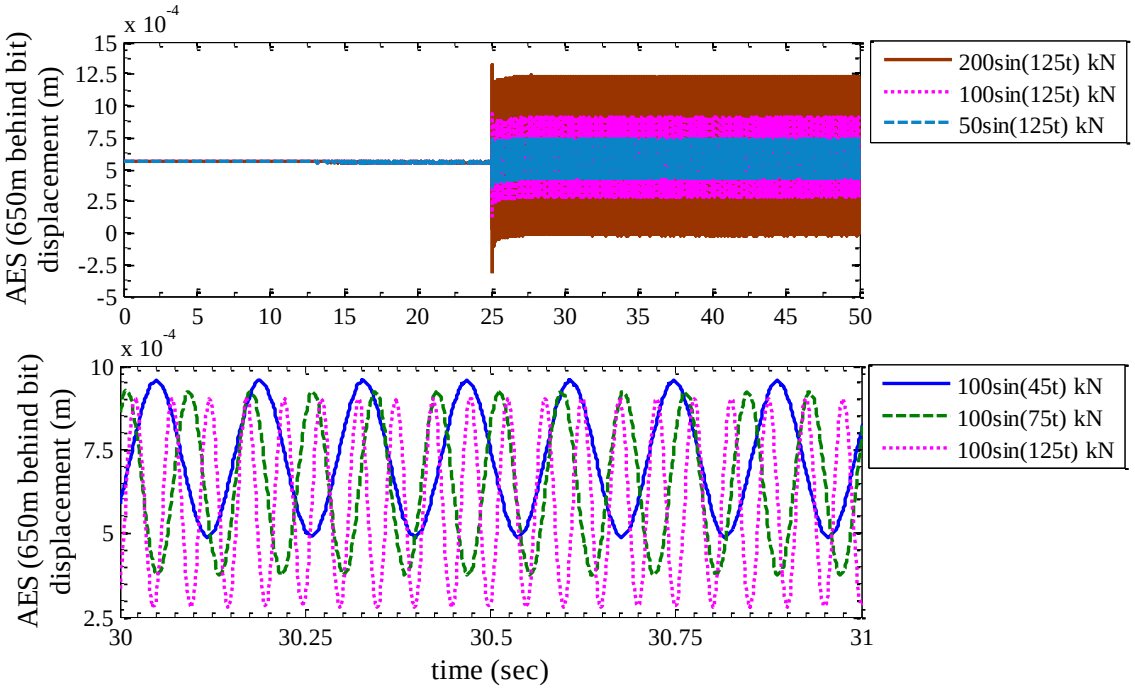

Figure 4.48: The AES segment displacements for different amplitudes and frequencies of applied forces.

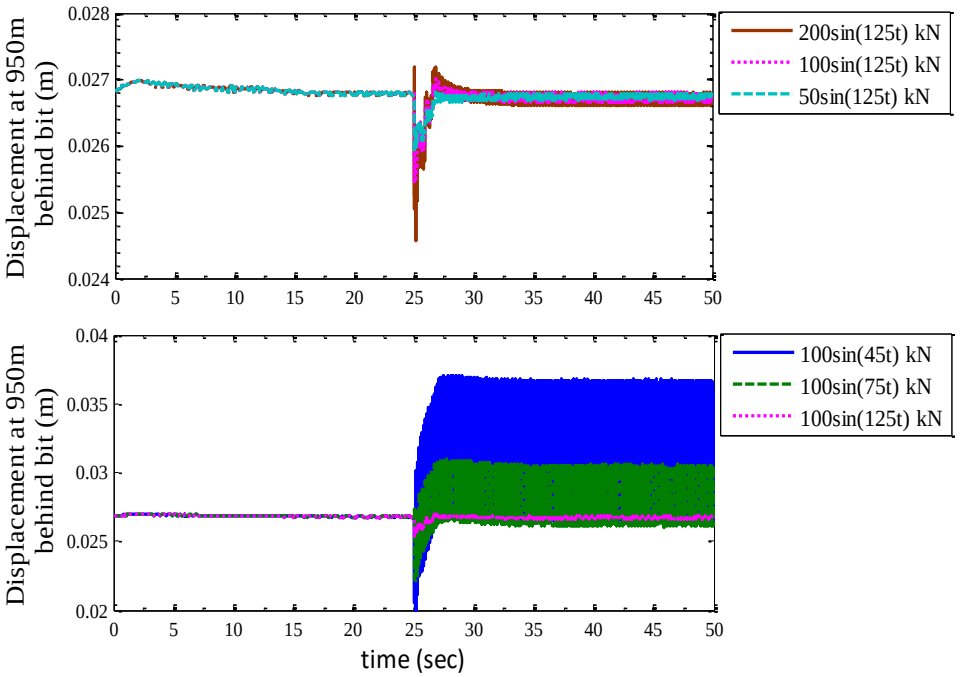

Figure 4.49: The displacements of 950 m behind bit segment for different amplitudes and frequencies of applied forces.

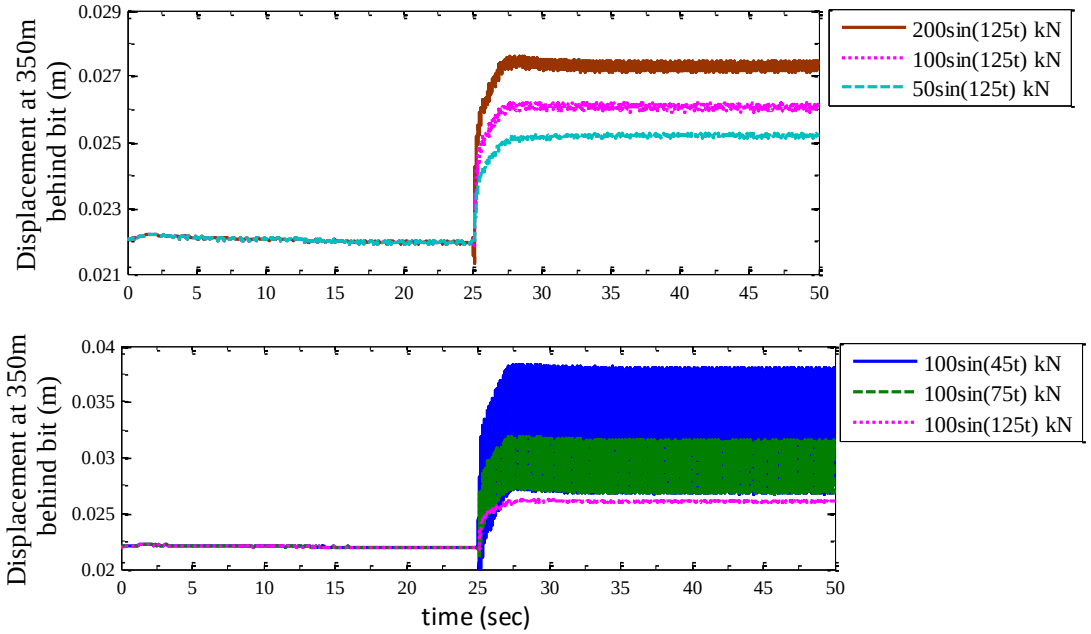

Figure 4.50: The displacements of 350 m behind bit segment for different amplitudes and frequencies of applied forces.

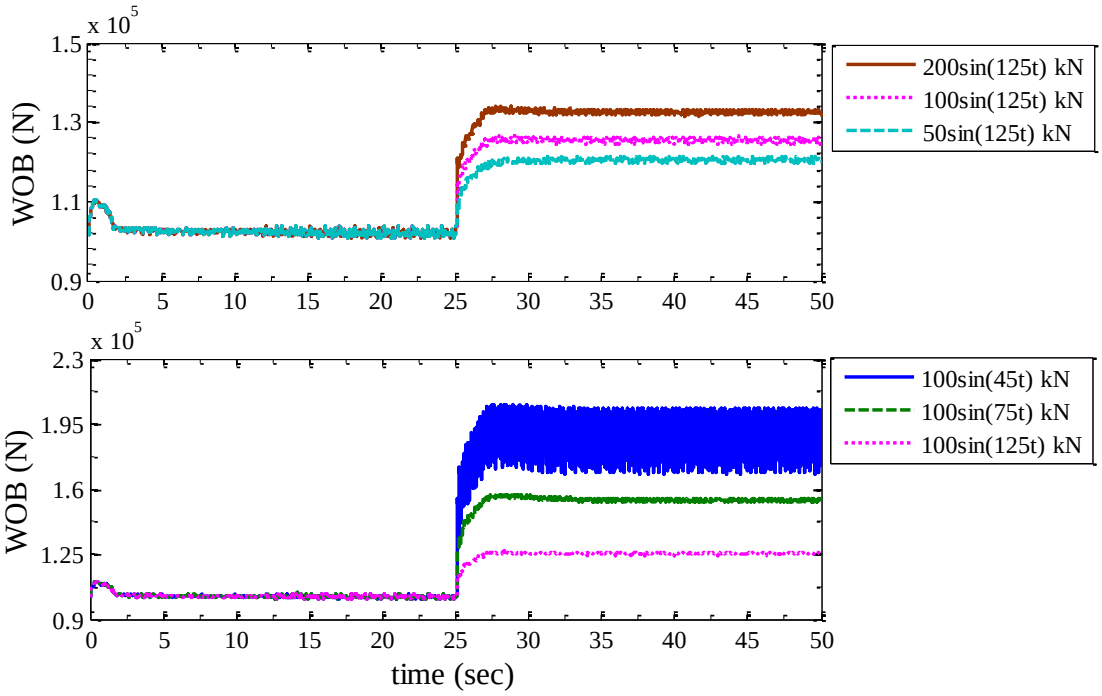

Figure 4.51: WOB results for different amplitudes and frequencies of applied forces.

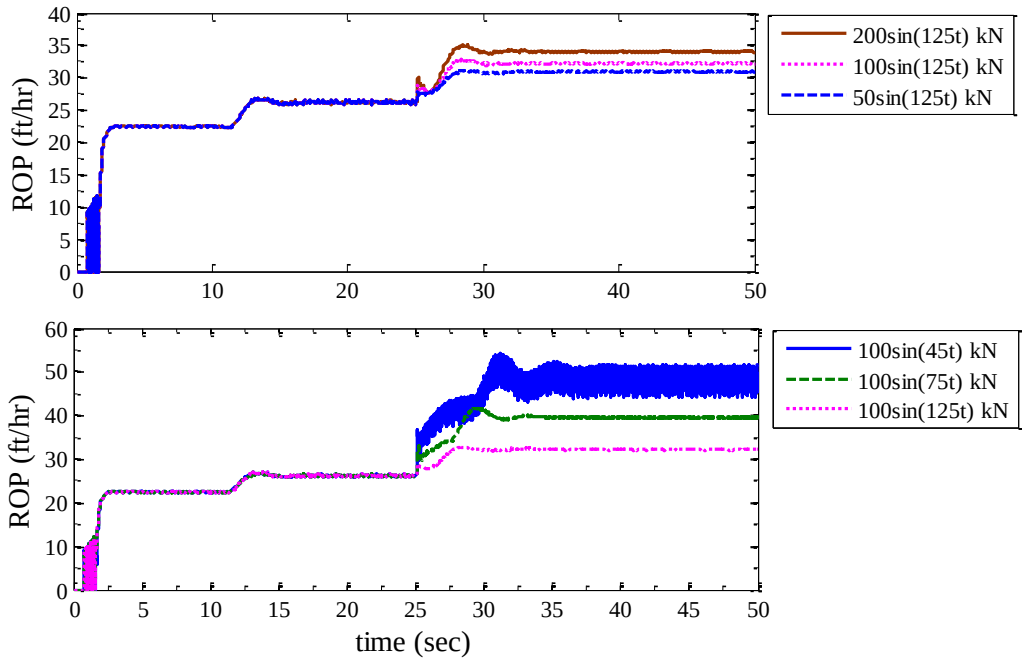

Figure 4.52: ROP results for different amplitudes and frequencies of applied forces.

Development of a bond graph model of a horizontal oilwell drillstring, capturing longitudinal and torsional motions, using a lumped segment approach has been presented. The dynamic model accounts for wellbore stick-slip friction. The model incorporates a modified bit-rock interaction model that allows the drill bit to move forward for prediction of the ROP. The proposed stick-slip friction model is in good agreement with an LS-DYNA® friction model. The torque and drag obtained from the proposed model is in qualitative agreement with field data. Lab experiments show that an Agitator® tool can be represented as a sinusoidal force. The application of high amplitude and low frequency of axial excitation force in the horizontal portion of the drillstring can provide better weight transfer to the bit and increase ROP. A trade-off between WOB transfer and vibration amplitude must be managed in order to protect the BHA and drill bit. The proposed model can be used as a tool for predrilling analysis. The ability to predict segment forces throughout the string allows for prediction of dynamic stresses. While not the focus of the simulation exercise in this research work, stress analysis for fatigue design of components, or forensic analysis of failed components, are other potential uses of the model. Finally, the proposed model is limited to the longitudinal and torsional motions of drillstring. In the next chapter, the model will be extended to include lateral motions of the drillstring.

5 A 3D Multibody System Approach for Horizontal Oilwell BHA Vibration Modeling

5.1 Introduction

Downhole data shows that excessive vibration in drillstring, bottom-hole-assembly (BHA) and related drilling components is a common scenario that presents a serious concern to the oil and gas industry. Lateral drillstring vibrations can cause severe problems such as: twist-offs due to accelerated fatigue in threaded connections, premature bit failure due to bit whirl, and failure of measurement-while-drilling (MWD) tools due to high shock loads during impacts of the bottom-hole-assembly (BHA) against the borehole wall. Stick-slip can put excessive wear and tear on the BHA and reduce the life of the drill bit. These vibrations are to some degree coupled. Bit whirl can be triggered by high bit speeds during stick-slip motion. Stick-slip can generate lateral vibration of the BHA as the bit accelerates during the slip phase. Large lateral vibration of the BHA into the wellbore can cause bit-bounce due to axial shortening. Induced axial vibrations at the bit can lead to lateral vibrations in the BHA, and axial and torsional vibrations observed at the rig floor may actually be related to severe lateral vibrations downhole near the bit. More information regarding vibrations in oilwell drillstring can be found in (Spanos *et al.*, 2003). Because of the complexity and huge cost associated with drilling experiment, research is increasing into numerical modeling of drillstring for vibration prediction and mitigation. Also,

dynamic models are the first essential step toward developing control strategies for a faster and efficient drilling without premature component failures.

There is considerable literature that analyzes aspects of the fully coupled vibrations in the BHA. One of the early studies on BHA dynamics was conducted by Tucker and Wang (1999). The cosserat theory approach (Rubin, 2000) was used to model the drillstring dynamics. The model is expressed in terms of six continuous independent degrees of freedom. The model is used to discuss the stability of axisymmetric drillstring configurations in vertical boreholes under coupled axial, torsional and lateral vibrations. Leine *et al.* (2002) introduced a simple model for the whirling motion of a BHA with wellbore contact-friction. A finite element method (FEM) dynamic model of the drillstring including the BHA has been formulated in (Khulief and Al-Naser, 2005). The model accounted for gyroscopic effects, torsional-bending inertia coupling, inertia-axial stiffening coupling and gravity. The dynamic effects resulting from drillstring-wellbore contact and stick-slip at the bit were neglected. Zare *et al.* (2011) presented a FEM model using ANSYS® software to investigate lateral vibrations in slightly deviated wells. The modeling was developed in the presence of mud, friction and nonlinear contact between the drillstring and wellbore wall. The effects of drilling mud, drillstring length, well inclination and weight-on-bit (WOB) were also considered. Ghasemloonia *et al.* (2013) presented a dynamic FEM model of a vertical drillstring assuming a multispan BHA. The model incorporates the effects of mud damping, driving torque, multispan contact and spatially varying axial load. A detailed review of drillstring vibration modeling can be

found in (Ghasemloonia *et al.*, 2015). The main purpose of most of the models is to analyze the vertical or slightly deviated drillstring BHA dynamics.

There are comparatively few papers treating the dynamic modeling of horizontal drillstring BHA's. When the drillstring inside a horizontal wellbore is subjected to increasing compressive loads, it will undergo at first sinusoidal buckling or "snaking" where the string assumes a two-dimensional waveform shape resembling a sine wave, winding back and forth along the sides of the wellbore. With increased compressive forces, the second stage of helical buckling or "whirling" occurs. The earliest work on modeling the drillstring BHA dynamics for extended-reach well was conducted by Heisig and Neubert (2000). The analytical model was able to analyze the bending vibrations of the BHA lying on the low side of the horizontal borehole. The model results showed that a drillstring in a horizontal borehole can vibrate in a snaking or in a whirling mode. Another analytical model for simulating the snaking and whirling mode of drillstring is presented by Pororelov *et al.* (2012). The rigid-flexible multi-body system approach was used in the modeling. The contact interaction between the drillstring and wellbore was modeled discretely with circle-cylinder force elements. Sliding Coulomb friction was implemented instead stick-slip. The nonlinear model of Wilson and Heisig (2015) accounts for arbitrary three-dimensional well profiles, complex tool geometry, drillstring contact with the wellbore, hydrodynamic effects from the drilling fluid, and the complete elastic coupling of the drillstring. Although some existing modeling approaches are able to capture coupled BHA dynamics for horizontal wells, there remains a need for a complete simulation that

incorporates the top drive, hydrodynamic effect due to drilling fluid flow, bit-rock interaction and bit advancement, and stick-slip.

A bond graph method with low simulation time compared to high-order FEM models was introduced by Rideout *et al.* (2013) for modeling three-dimensional drillstring dynamics. The model used a multi-body approach and was implemented in the 20Sim® multi-domain modeling and controller simulation environment. The contact friction model has been modified in this research work to include stick-slip whirl. Refinement and validation of the multibody BHA model with stick-slip friction and integration with other drillstring system models comprise the primary scope of this research work.

This chapter is organized as follows. Section 5.2 discusses and validates the three-dimensional multibody shaft dynamics model. Section 5.3 develops and validates the coupled stick-slip and whirl phenomena for a horizontal shaft rolling inside a wellbore. Prediction and validation of snaking and whirling motions are presented in Section 5.4. A complete drillstring model that allows visualization of the three-dimensional BHA motions follows in Section 5.5.

5.2 Effectiveness of three-dimensional multi-body modeling approach for shaft dynamic modeling

The shaft model applies multi-body theory through the multiband or vector bond graph technique. Rigid lumped segments with six degrees of freedom are connected by axial, torsional, shear, and bending springs to approximate continuous system response. Accuracy increases with the number of lumped segments used. However, increasing the

number of segments leads to larger simulation times and also there is no closed-form relation between the number of segments in a model and accuracy of the natural frequencies or total response. The model formulation has been presented in the next section. Also a comparison study with the LS-DYNA® finite element (FE) model has been performed to show the effectiveness of the multi-body formulation.

5.2.1 Multi-body bond graph model description

Bond graphs are an explicit graphical tool for capturing the common energy structure of systems and can in-crease one's insight into system behavior. In the vector form, they give concise description of complex systems. Moreover, the shaft is represented as a sequence of cylindrical rigid bodies joined by spherical joints with three translational and rotational compliances, as shown in Fig. 5.1. Springs 'k_{bend}' are rotary springs about the body-fixed x and y axes of body i+1, 'k_{tors}' is a rotary spring about body-fixed z, 'k_{axial}' is a translational spring in body-fixed z and 'k_{shear}' are translational springs in the body-fixed x and y. The torsional and bending springs are shown separately in the right portion of the figure, and one shear spring is omitted for clarity; however, all springs exist at the joint between point B on body i and point A on body i+1. The springs are assumed to have zero free length.

Stiffness values are computed for a segment length $\Delta x = L/n$ of a string of length L with n segments, using basic solid mechanics theory, as follows (Karnoop *et al.*, 2006):

$$k_{axial} = {}^{EA}/_{\Delta z} \tag{5.1}$$

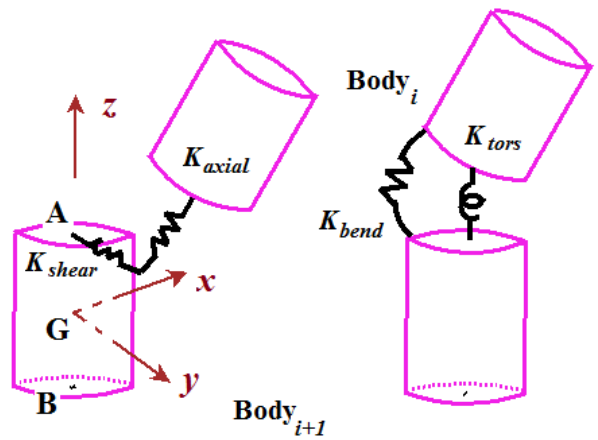

Figure 5.1: Successive multibody segments

$$k_{torsion} = {}^{GJ}/_{\Delta z} \tag{5.2}$$

$$k_{bend} = {}^{EI}/_{\Delta z} \tag{5.3}$$

$$k_{shear} = {}^{\kappa AG}/_{\Delta z} \tag{5.4}$$

where E is elastic modulus, A and I are cross-sectional area and area moment, G is modulus of rigidity, J is polar moment of area, and κ is a parameter accounting for non-uniform shear across a cross section. The shear coefficient for a cylindrical tube cross section is obtained from (Hutchinson, 2001):

$$\kappa = \frac{6\left(a^2+b^2\right)(1+v)^2}{7a^4+34a^2b^2+7b^4+v\left(12a^4+48a^2b^2+12b^4\right)++v^2\left(4a^4+16a^2b^2+4b^4\right)} \tag{5.5}$$

where v is poisson's ratio, and a and b are inner and outer radii respectively.

5.2.1.1 Bond graph of segments and joints

The Euler junction structure is used, representing the following equations governing the dynamics of bodies undergoing large motions (Karnoop *et al.*, 2006):

$$\sum {}^{0}\vec{F} = {}^{d}/_{dt}(\vec{m}\ {}^{0}\vec{v}_{Gi}) = \vec{m}\ {}^{0}\dot{\vec{v}}_{Gi} \tag{5.6}$$

$$\sum {}^{i}\vec{M} = {}^{d}/_{dt}(\vec{J}\ {}^{i}\vec{\omega}_{i}) = \vec{J}\ {}^{i}\dot{\vec{\omega}}_{i} + {}^{i}\vec{\omega}_{i} \times \vec{J}\ {}^{i}\vec{\omega}_{i} \tag{5.7}$$

where G is the mass center, left superscript 0 indicates vectors resolved into inertial frame components, and i indicates vectors (in this case, absolute velocities) resolved along body-fixed frame i. The translational equations are expressed in frame 0 to facilitate application of the gravity vector. The first term on the right hand side of the rotational equation is an inertial term, and the second term gyrational. The hinge point A velocity is defined as follows (B is defined similarly):

$${}^{1}\vec{v}_{Ai} = {}^{1}\vec{v}_{Gi} + {}^{1}\vec{v}_{Ai/Gi} \tag{5.8}$$

$${}^{1}\vec{v}_{Ai/Gi} = {}^{i}\vec{\omega}_{i} \times {}^{i}\vec{r}_{Ai/Gi} = {}^{i}\tilde{r}_{Ai/Gi}\ {}^{i}\vec{\omega}_{i} \tag{5.9}$$

where ${}^{i}\vec{r}_{Ai/Gi}$ is the position vector from G to A, and ${}^{i}\tilde{r}_{Ai/Gi}$ is a skew-symmetric matrix containing the relative position vector components.

Fig. 5.2 is a top-level vector bond graph (Breedveld, 1985) representation of the above equations. The right-hand side of translation Eq. (5.6) is represented by the 'mass matrix' multiport I element, the velocity ${}^{0}\vec{v}_{Gi}$ of which is the body-fixed center of mass velocity ${}^{i}\vec{v}_{Gi}$ multiplied by the rotation matrix R_i^0. This transformation of velocities is accomplished by the vector MTF in the lower part of Fig. 5.2. The four vector bonds into

the ${}^{0}\vec{v}_{Gi}$ 1-junction represent the force summation on the left-hand side of Eq. (5.6). To define the velocity of Body-*i* point A with respect to G, the 0-junction in Fig. 5.2 adds ${}^{0}\vec{v}_{Gi}$ and the relative velocity cross-product on the right-hand side of Eq. (5.9). Note the modulated transformer (MTF) representation of the cross-product. Cardan orientation angle (rotations "ψ, θ, ϕ" about body fixed *z*, *y*, *x*) rates are calculated, integrated, and used to create rotation matrices between body-fixed and inertial coordinate frames according to the following equations:

$$\dot{\theta} = \cos\phi\,\omega_y - \sin\phi\,\omega_z \tag{5.10}$$

$$\dot{\psi} = \frac{\sin\phi}{\cos\theta}\omega_y + \frac{\cos\phi}{\cos\theta}\omega_z \tag{5.11}$$

$$\dot{\phi} = \omega_x + \sin\phi\,\frac{\sin\theta}{\cos\theta}\omega_y + \cos\phi\,\frac{\sin\theta}{\cos\theta}\omega_z \tag{5.12}$$

Orthogonal rotation matrices transform vector components as follows:

$${}^{0}\vec{v} = R_i^0\ {}^{i}\vec{v}, \quad {}^{i}\vec{v} = R_0^i\ {}^{0}\vec{v}, \quad R_0^i = \left[R_i^0\right]^T \tag{5.13}$$

The rotation matrix, as a function of cardan angles, is:

$$R_i^0 = \begin{bmatrix} c_\theta c_\psi & -c_\theta s_\psi & s_\theta \\ c_\theta s_\psi + s_\phi s_\theta c_\psi & c_\phi c_\psi - s_\phi s_\theta s_\psi & -s_\phi c_\theta \\ s_\phi s_\psi - c_\phi s_\theta c_\psi & s_\phi c_\psi + c_\phi s_\theta s_\psi & c_\phi c_\theta \end{bmatrix} \tag{5.14}$$

where '*c*' and '*s*' represent cos and sin respectively. The rotational dynamics of a body, Eq. (5.7), require a vector 1-junction ${}^{i}\vec{\omega}_i$ for angular velocity, to which are bonded external moments from bodies *i* - 1 and *i* + 1 via joints, inertial effects via the I element,

the Euler's equation inner product terms [final term in Eq. (5.7)] via the modulated gyrator *MGY*, and moments from forces at the hinge point A. Only one hinge point is shown; however, an arbitrary number can be similarly defined.

Fig. 5.3 shows a joint submodel in which the relative velocity between points B and A on successive bodies is calculated in the Body i+1-fixed frame. The multiport C and R elements have a diagonal stiffness matrix to model the stiffness described in Eq. (5.1) to (5.4), and a viscous material damping matrix tuned to give a realistic damping ratio in the first mode. The 0-junctions in Fig. 5.3 enforce velocity constraints that define the relative velocity of the parallel spring/damper elements for angular velocity and shear/axial velocity. From the bond graph half-arrow directions, relative velocity is defined as $({}^{i+1}\vec{v}_{A(i+1)} - {}^{i+1}\vec{v}_{Bi})$. Positive axial spring displacement thus occurs if axial velocity of point A on top of the lower body exceeds the velocity of point B on the bottom surface of the

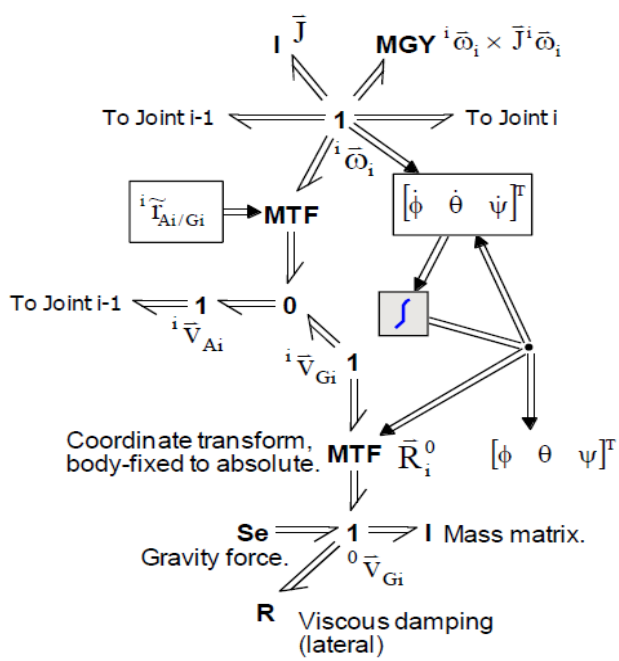

Figure 5.2: Body i bond graph (Rideout *et al.*, 2013)

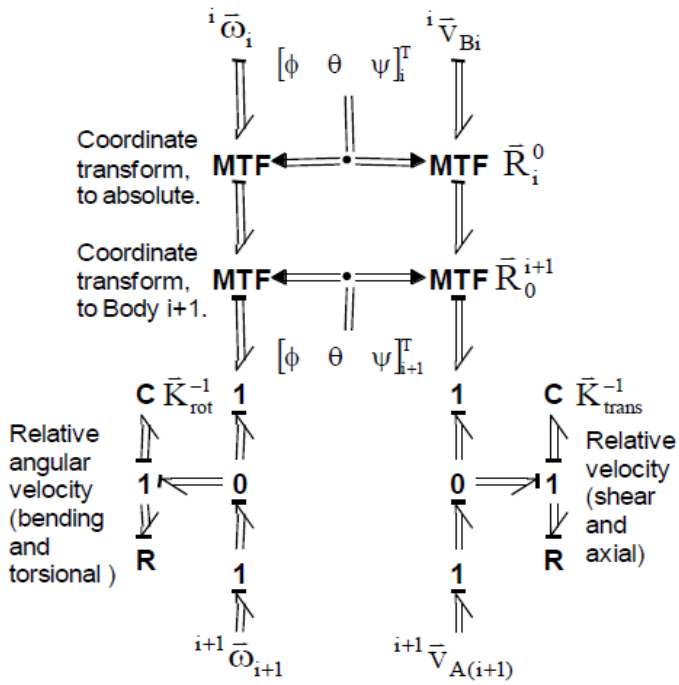

Figure 5.3: Joint i bond graph (Rideout *et al.*, 2013)

upper body. In other words, positive axial spring displacement occurs during compression. The two successive *MTF* elements in Fig. 5.3 use Cardan angles from bodies *i* and *i*+1 to transform velocity vectors into a common frame (Rideout *et al.*, 2013).

5.2.2 Case study – pipe deflection

A 10 m pipe section with fixed boundary condition subject to a static transverse load, as shown in Fig. 5.4, has been constructed both in 20Sim® using multibody bond graphs and in LS-DYNA® using beam elements for the comparison study. A total of 25 segments and 200 beam elements were used in 20Sim® and LS-DYNA®, respectively. The effect of gravity has been included in the models. The gravity load is applied in LS-DYNA® via the

*LOAD_BODY_Z command. The material of the shaft is chosen as steel and modeled as *MAT_PLASTIC_KINEMATIC. Material damping is applied through the *DAMPING_GLOBAL command. The Belytschko-Schwer tubular beam with cross-section integration and 2×2 Gaussian quadrature has been chosen through *SECTION_BEAM command to define the element formulation and quadrature rule, respectively. A modal analysis has been conducted by using the implicit method analysis. The *CONTROL_IMPLICIT_GENERAL command is used to activate the implicit method and initial time step has been chosen as 5.0×10^{-4}. The keyword command *CONTROL_IMPLICIT_EIGENVALUE is used to extract the eigenmodes. The natural frequencies of the pipe obtained with LS-DYNA® match reasonably well with the theoretical and 20Sim® results (see Table 5.1).

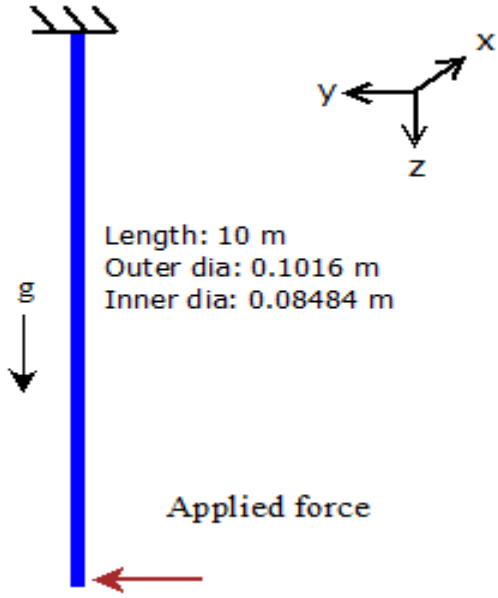

Figure 5.4: Sketch of pipe geometry

In Fig. 5.5 the deflection results from 20Sim® and from LS-DYNA® computation are compared with the theoretical results. The direction of the static load, which is applied to the free end of the pipe, is in the y-direction. In order to preload the system to a steady state prior to dynamic loading for the explicit transient analysis a dynamic relexation step has been selected for the LS-DYNA® simulation. It is found that 20Sim® results have an excellent agreement with the theoretical value. Whereas the LS-DYNA® results match reasonably well with the theoretical, especially at lower applied load and the discrepancy between the results increases with the higher applied load.

Table 5.1: Natural frequencies comparison chart

	Natural Frequencies (Rad/Sec)					
	Theoretical		**20Sim** 3D multibody bond graph method Segments: 25		**LS-DYNA** Beam Element ELFORM=5 (Belytschko-Schwer tubular beam with cross-section integration) Nodes: 401 Elements: 200	
Mode	*Lateral*	*Axial*	*Lateral*	*Axial*	*Lateral*	*Axial*
1	6.01	812.44	6.12	828.4	6.01	812.44
2	37.71	2437.34	39.50	2482	37.77	2437.28
3	105.57	4062.24	109.80	4125	105.50	4061.97
4	206.92	5687.13	214.90	5752	206.92	5686.40
5	342.06	7312.03	354.70	7355	342.02	7310.49
6	510.99	8936.93	528.50	8927	510.90	8934.13
7	713.68	10561.8	735.60	10460	713.56	10557.2
8	950.17	12186.7	975.10	11940	949.97	12179.6

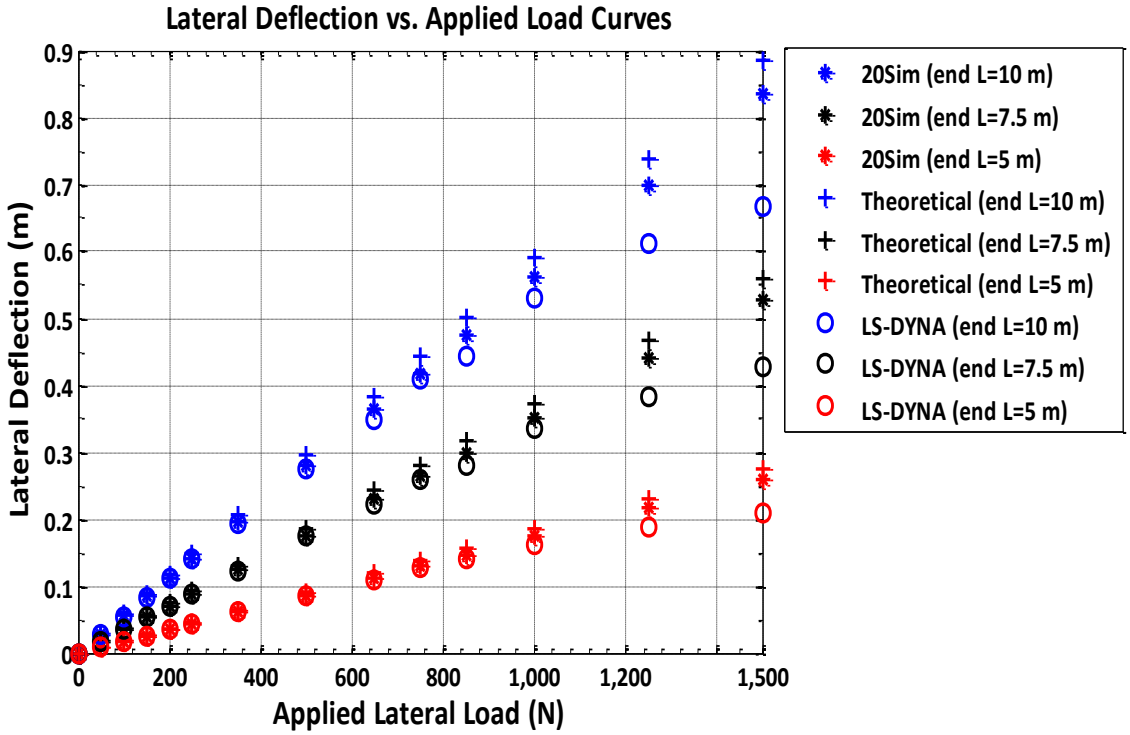

Figure 5.5: Load-deflection comparison between LS-DYNA® and 20Sim®.

5.2.3 Case study – pipe rotational dynamics

A 10 m pipe section with rotating boundary condition subject to an eccentric mass, as shown in Fig. 5.6, has been constructed both in 20Sim® and LS-DYNA® for comparing the rotor dynamic responses. At the top, the pipe is constrained both in the axial and lateral directions, and a rotation is applied. Diameter and thickness of the disk shown in Fig. 5.6 are 1.0 m and 0.01 m, respectively. The eccentricity of the 200 kg cube (0.2 m length) center of gravity from the pipe center line is 0.3 m. For the 20Sim® model, a point mass is assumed for the cube and the bond graph model of the eccentric mass in the disk segment is shown in Fig. 5.7. Figs. 5.8-5.10 present the results obtained from the models when the

pipe rotates with z-axis at 10 rad/sec. The x-displacement of the disk center obtained from LS-DYNA® and 20Sim® are shown in Fig. 5.8. The displacements are not exactly the same for the two simulations but the response frequencies are almost the same. The disk center whirling orbits are shown in Fig. 5.9. The whirling center is very close for the two simulations. The disk movements are not exactly similar but the pattern of movements are very similar. The disk center state-spaces, which are displacement vs. velocity, in the x-axis direction is shown in Fig. 5.10. Again, the pattern of movements of the disk center are almost the same.

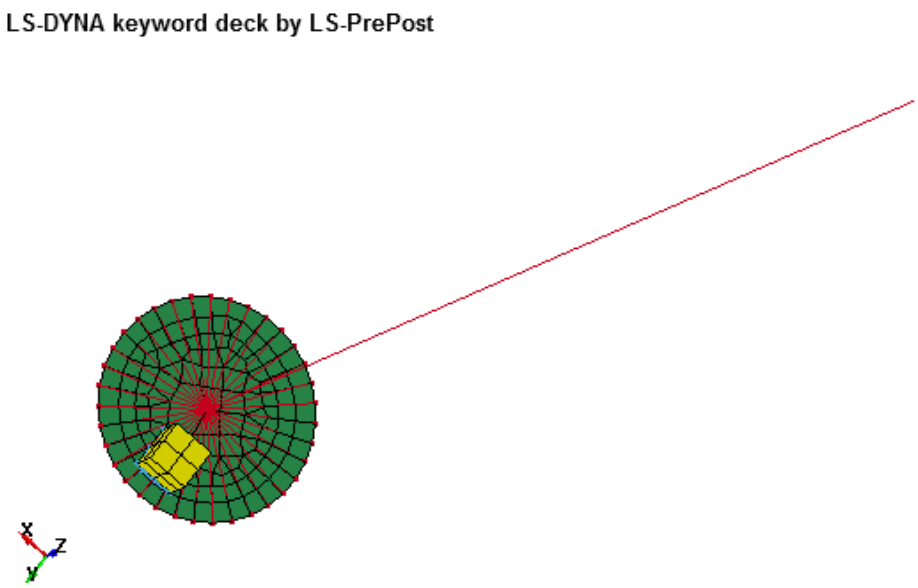

Figure 5.6: A rotating pipe model with an eccentric mass in LS-DYNA®.

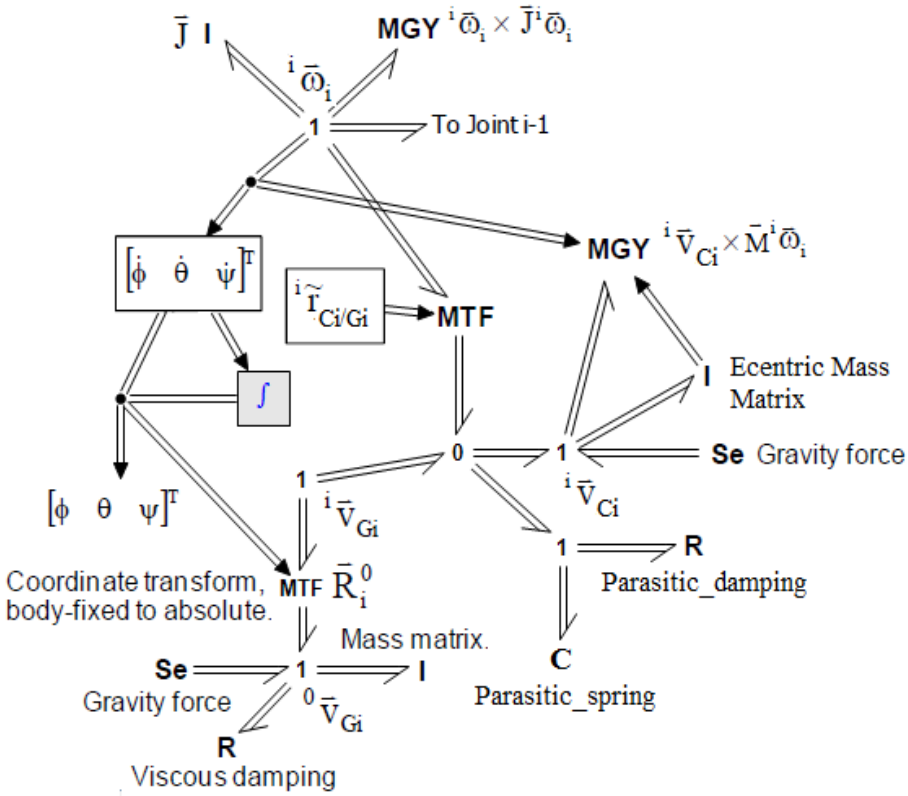

Figure 5.7: Eccentric mass bond graph modeling.

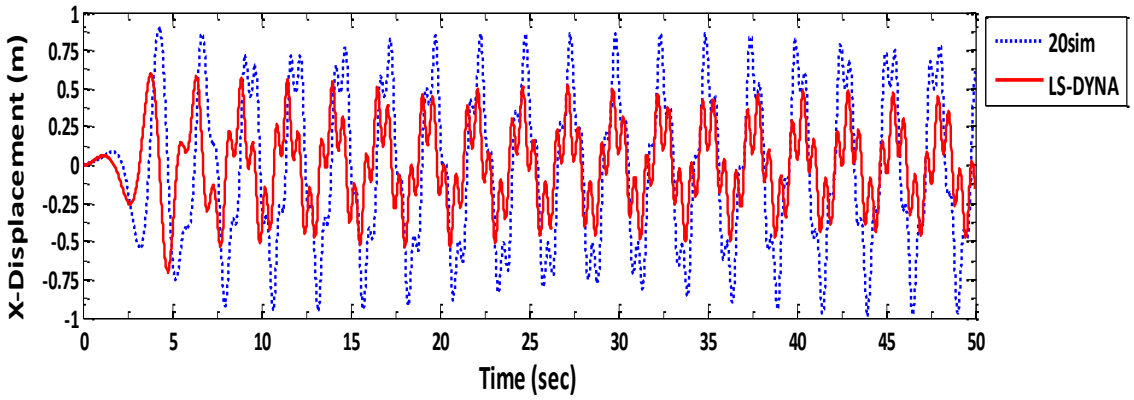

Figure 5.8: The x-displacement of disk center.

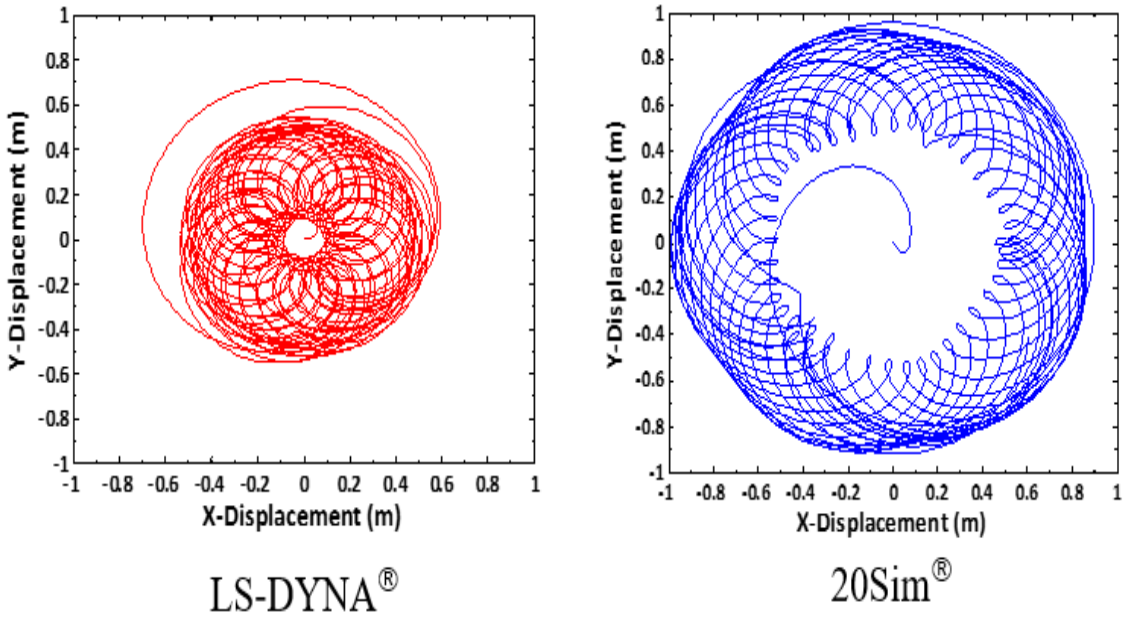

Figure 5.9: The disk center whirling orbit.

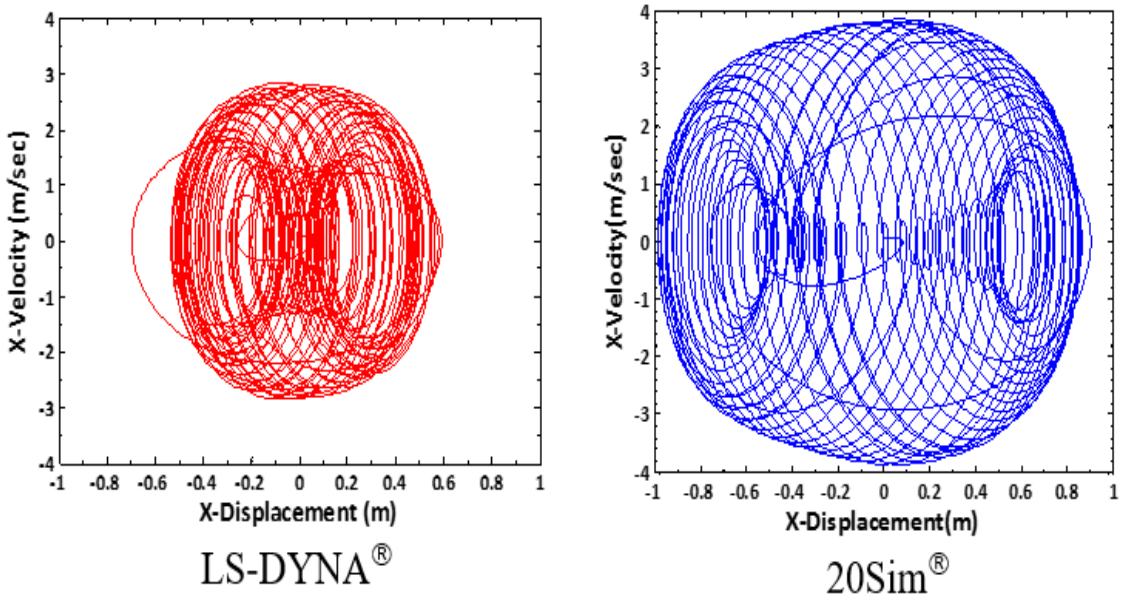

Figure 5.10: The disk center state-space (displacement vs. velocity).

5.3 Modeling drillstring-wellbore contact-friction

One of the key factors in simulation of vibration of shafts within enclosures, such as oilwell drillstrings within a wellbore, is to have an accurate but efficient treatment of the contact forces that affect lateral vibrations. An especially challenging aspect of contact force modeling is the treatment of friction. A rotating drillstring can undergo lateral vibrations characterized by brief impacts with the wellbore, or can undergo whirl. "Backward whirl" refers to rolling-without-slip of the shaft around the wellbore, with whirl angular velocity being opposite to spin angular velocity. "Forward whirl" occurs when whirl and spin angular velocities are in the same direction, and there is sliding between the shaft and wellbore. The multibody bond graph model simplifies the inclusion of contact interaction between the drillstring and wellbore. Drillstring contact with the wellbore wall, which can occur continuously over a line of contact for horizontal drillstrings, generates normal forces using a user-definable stiff spring constitutive law. Tangential contact forces due to friction between the drillstring and wellbore wall must be generated in order to whirl to occur. The potential for backward whirl, as seen in drilling applications, requires the transition from pipe-wellbore sliding motion to a motion where the pipe rolls without slip around the wellbore surface. The model computes the relative velocity between sliding surfaces when contact occurs, and enforces a rolling-without-slip constraint as the velocity approaches zero. The physical schematic of drillstring contact and friction with wellbore wall is shown in Fig. 5.11. The wellbore wall induces normal and tangential forces (Fig. 5.11(b)) on the pipe if the radial displacement becomes larger than the radial clearance δ_o.

Detection of wellbore contact and computation of force and angle are done using the following equations.

$$\delta = \sqrt{x^2 + y^2} \tag{5.15}$$

$$\phi = \tan^{-1}(y/x) \tag{5.16}$$

$$F = k_s(\delta - \delta_o) + C_s(\dot{\delta} - \dot{\delta}_o) \tag{5.17}$$

$$F_x = F\cos\phi, \qquad F_y = F\sin\phi \tag{5.18}$$

where δ is radial deflection, δ_o is initial clearance, x and y are coordinates of pipe center; F, k_s and C_s are contact force, spring stiffness and damping, and ϕ is angle between the line OA and the inertial x axis.

The bond graph model to capture the pure rolling and rolling with sliding is shown in Fig 5.12. The orientation angles are used to transform velocities to the inertial frame. The modulated transformer (MTF) elements in Fig. 5.12 enforce the velocity constraints of the

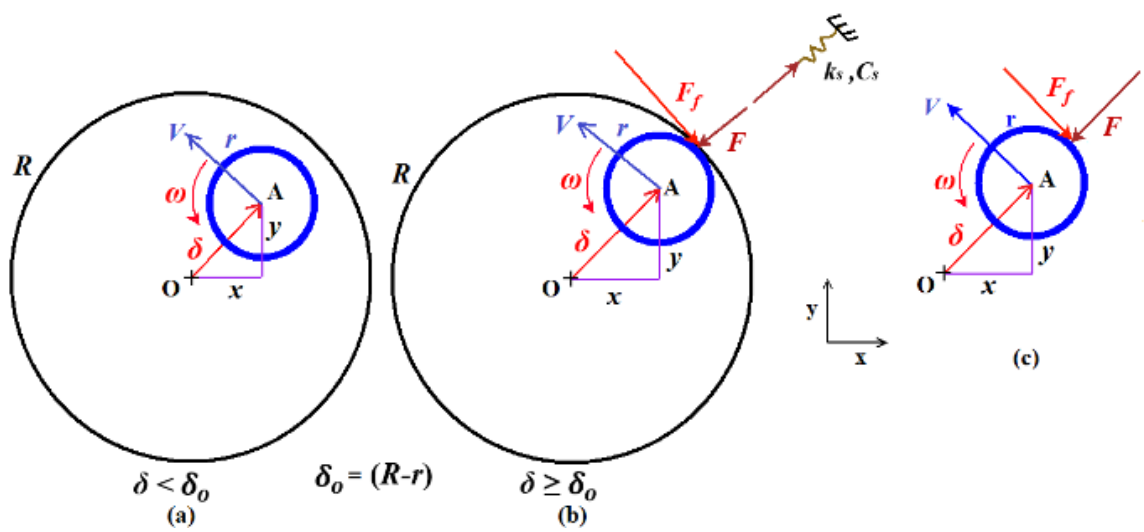

Figure 5.11: Physical schematic of contact and friction.

'whirl speed' equation in Fig. 5.12. The transformer (TF: radius, r) converts pipe spin speed into tangential velocity. The (small) difference between tangential and whirl velocities is the velocity with which a virtual stiff spring (C) deforms during the stick phase. When the spring force exceeds the maximum available static friction force, the spring releases to allow slip. The "Mse: F_w" element computes and applies a normal contact force from the spring in Fig. 5.11 during a collision. The reader is referred to Chapter 3 for the modeling of stick-slip friction force using bond graph C-elements. The model results will be sensitive to the contact spring stiffness and damping constant. Thus a validation study has been performed with LS-DYNA® contact-friction model.

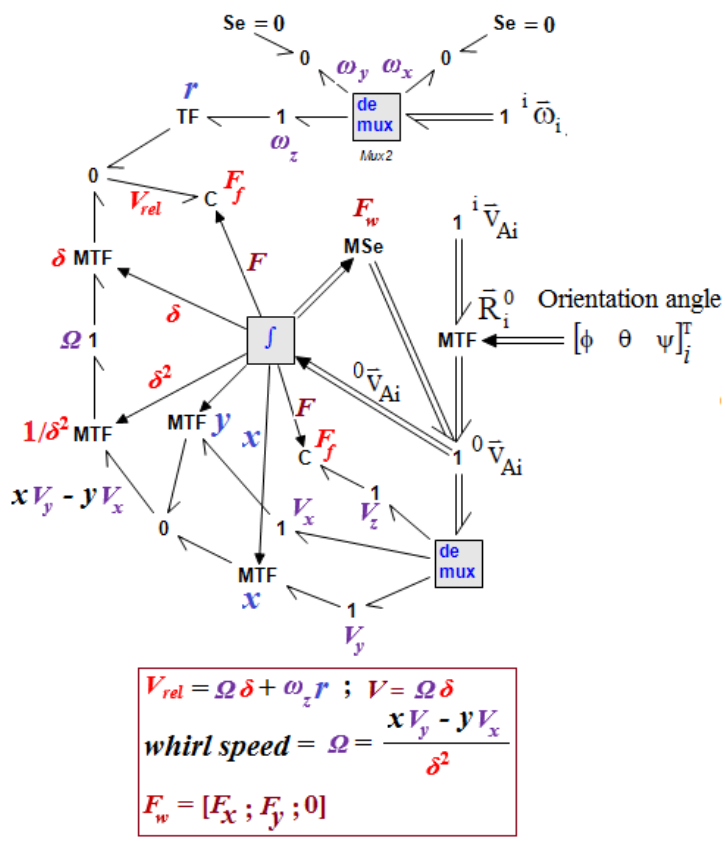

Figure 5.12: Bond graph model for drillstring-wellbore contact and friction.

5.3.1 Case study – contact force

A 101.6 mm diameter heavy solid shaft falling from inside of a 180 mm diameter cylindrical wall has been modeled in LS-DYNA® software. The position of the 100 mm length shaft at time zero is shown in Fig. 5.13. Elastic material with 8.0×10^4 kg/m^3 density is used for modeling the solid shaft. The wall has been chosen as a rigid material. Fixed boundary conditions have been applied to the wall. A single body segment has been used to model the shaft in 20Sim®. There are several contact-related parameters available in LS-DYNA® which can be used to modify or improve contact behavior. A non-automatic *CONTACT_SURFACE_TO_SURFACE command has been chosen for building the model. By default, LS-DYNA® considers only a static friction coefficient (FS). In reality, the friction is dependent on relative velocity less than the static friction value. To model this behavior, two parameters, dynamic friction coefficient (FD) and decay constant, have been included. The inputs of FS, FD and decay constant values are chosen 0.6, 0.5 and 250, respectively. Fig. 5.14 shows computed shaft-cylindrical wall contact forces. The result

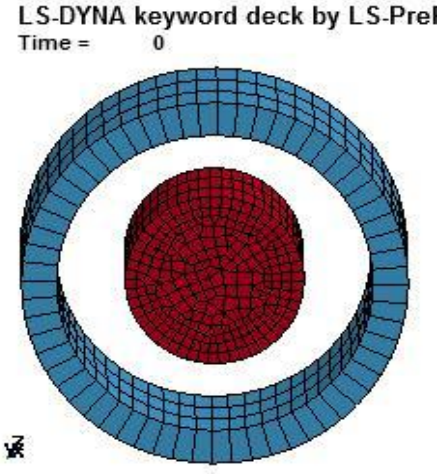

Figure 5.13: Sketch of LS-DYNA® contact model geometry.

shows that contact force in 20Sim® is sensitive to the chosen spring-damper combination. The computed errors compared to the LS-DYNA® model is shown in Fig. 5.15. Almost the same contact forces are found when the values of spring and damping constants are chosen as 1.3×10^8 N/m and 2.0×10^3 N-s/m, respectively.

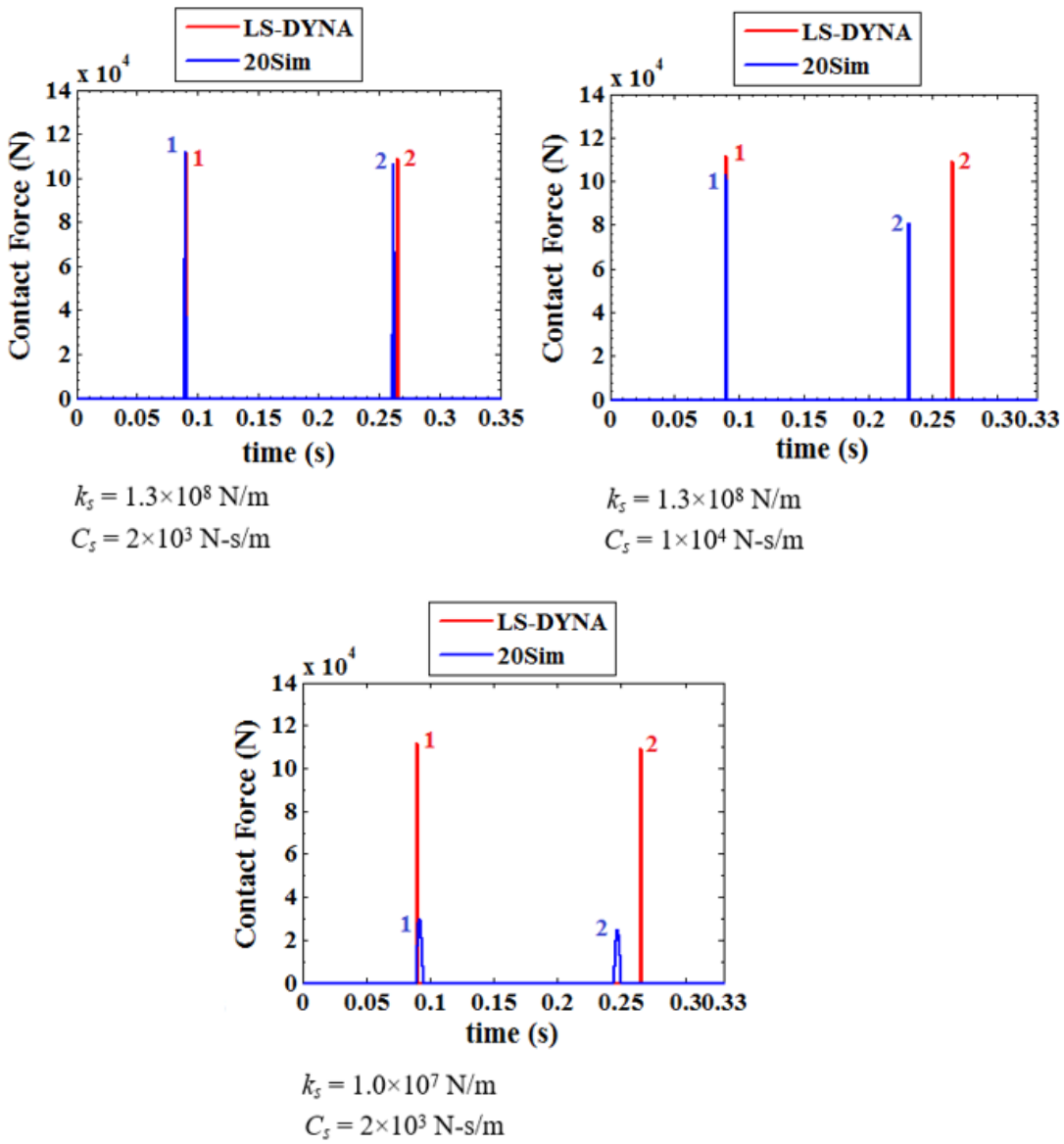

Figure 5.14: Contact forces results.

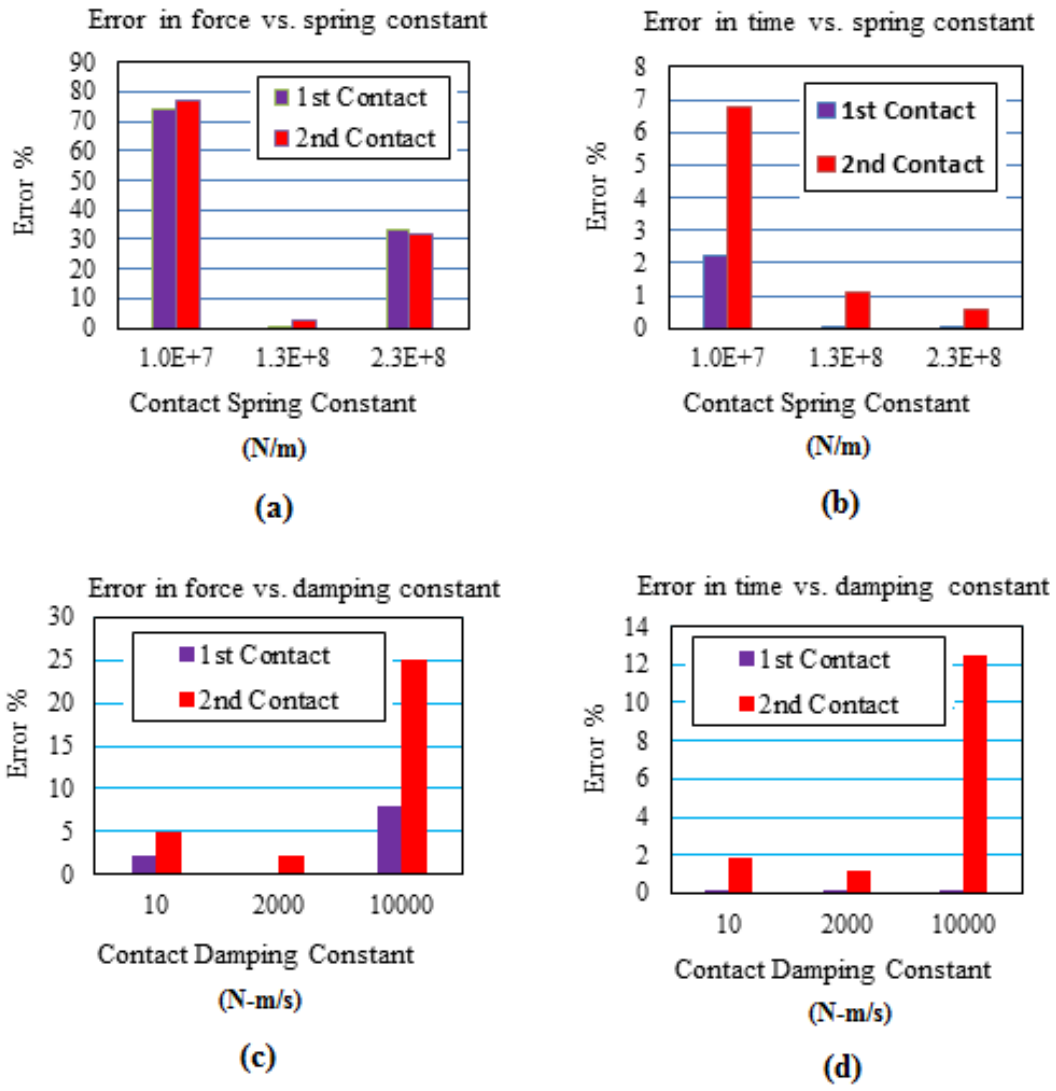

Figure 5.15: Errors in 20Sim® results compared to LS-DYNA® model.

5.3.2 Case study – rolling motion

A similar shaft and wall geometry have been considered for the rolling motion validation. The position of the 100 mm length shaft at time zero is shown in Fig. 5.16. The sinusoidal torque is applied at the shaft through the center line. The inputs of 20Sim® contact spring stiffness and damping constant are chosen to be 1.3×10^{8} N/m and 2.0×10^{3} N-s/m, respectively. The shaft center whirling orbits from LS-DYNA® and 20Sim® due to torque values (20sin(5t), 30sin(5t) and 40sin(5t) N-m) are shown in Fig. 5.17. The shaft movements are very similar. As the torque amplitude increases the shaft rolling distance path increases. Fig. 4.17(c) depicts the shaft rolling over the complete wall circumference when the torque amplitude is 40 N-m. Overall simulation results show the ability of the proposed model to capture the rolling motion.

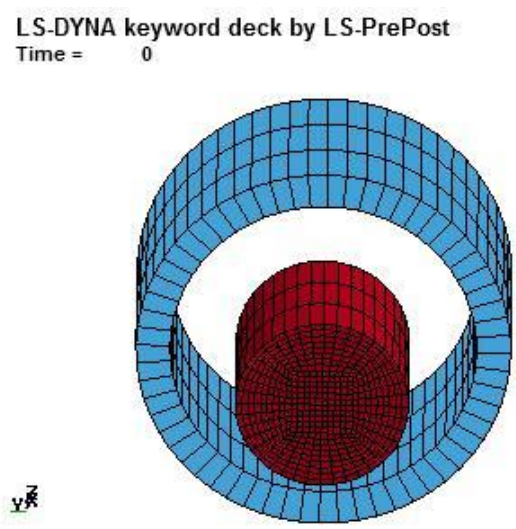

Figure 5.16: Sketch of LS-DYNA® contact model geometry.

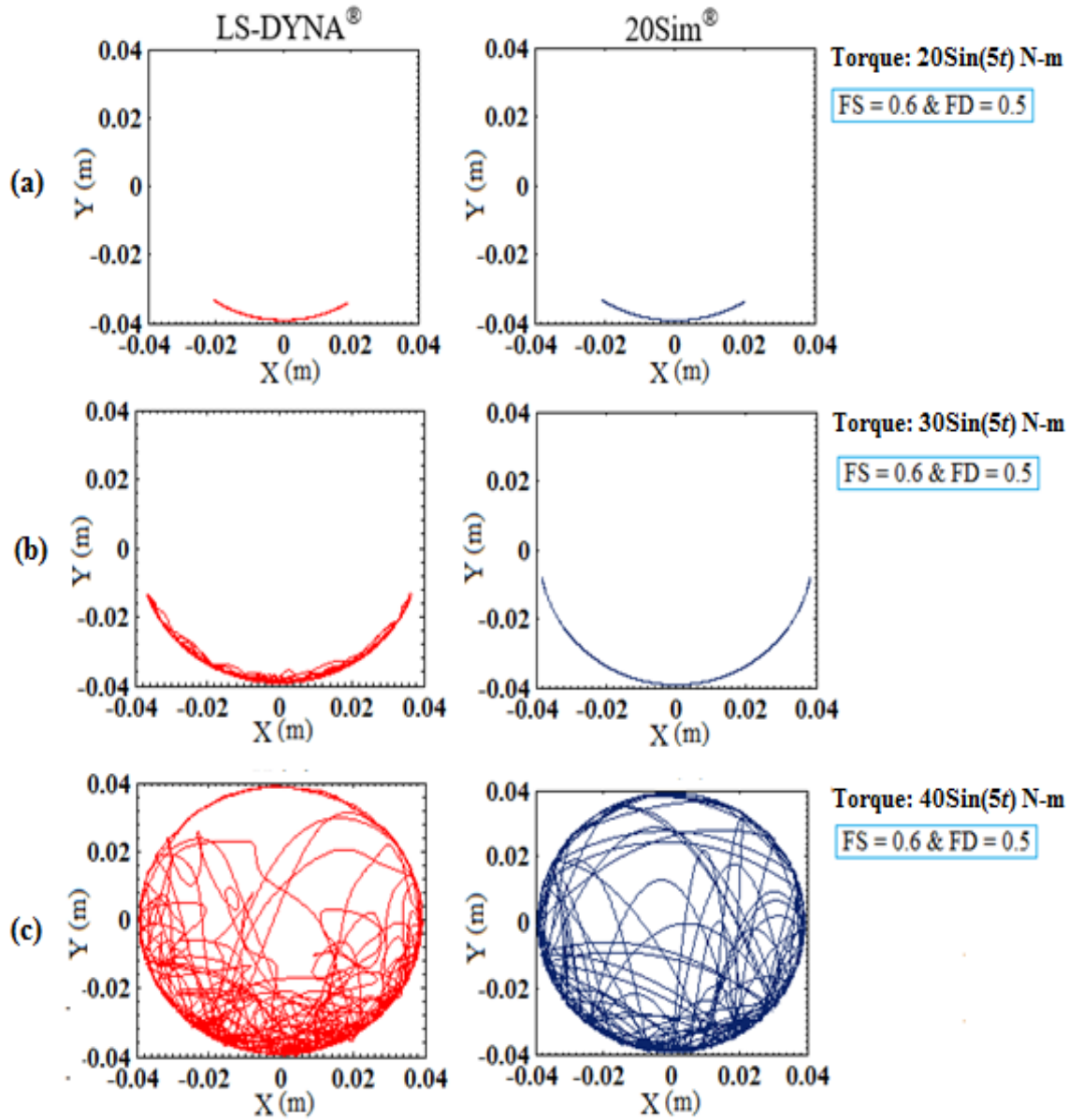

Figure 5.17: The shaft center whirling orbit for different applied torque.

5.4 Multi-body bond graph simulation of buckling of pipes inside wellbore

A 100 m drillpipe inside of a wellbore wall shown in Fig. 5.18 has been modeled both in LS-DYNA® and 20Sim® software. Fig. 5.19 depicts the model geometry in LS-DYNA®. A total of 50 body segments and 200 beam elements has been used for modeling the pipe dynamics in 20Sim® and LS-DYNA®, respectively. The automatic nodes (beam nodes) to surface (wellbore wall) contact type has been chosen in LS-DYNA®. The simulation results for a rotating shaft with 16 rad/sec speed subjected to compressive loads are shown in Figs. 5.20-5.25.

The sinusoidal buckling occurs when the axial force is 150 kN (Fig. 5.20). When the load increases to 200 kN, full helical buckling with six coils develops (Fig. 5.21). The similarity between the 20Sim® and LS-DYNA® models can be identified both in Fig. 5.20 and Fig. 5.21 animation plots. The *x*-displacement of the pipe center at 50 m length distance obtained from LS-DYNA® and 20Sim® when the pipe is rotating at a speed of 16 rad/sec and the applied axial force is 150 kN are plotted in Fig. 5.22. Although the displacements are not exactly same for the two simulations, the trajectories of the pipe center geometry (Fig. 5.23) are very close. The pipe center motion shown in Fig. 5.23 can be categorized as snaking motion.

Fig. 5.24 shows the *x*-displacement of the pipe center when the applied axial force increases to 200 kN. The displacements obtained from LS-DYNA® and 20Sim® are almost the same. The trajectories of the pipe center geometry plotted in Fig. 5.25 are also very close for the two simulations and the motion of the pipe center orbit can be categorized as whirling motion.

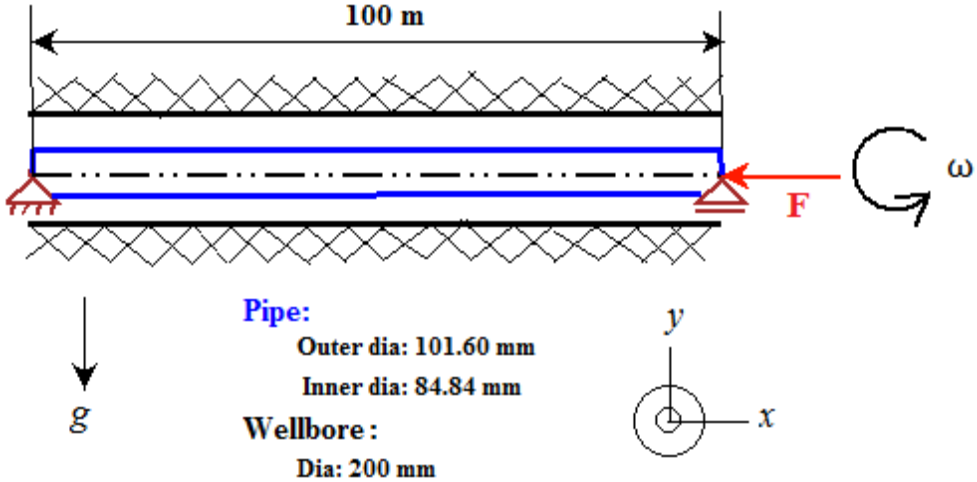

Figure 5.18: Sketch of the buckling test case.

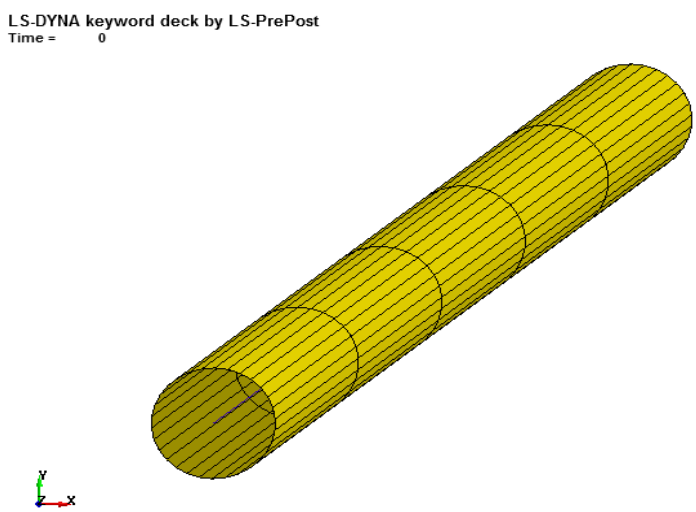

Figure 5.19: Pipe inside wellbore model in LS-DYNA®.

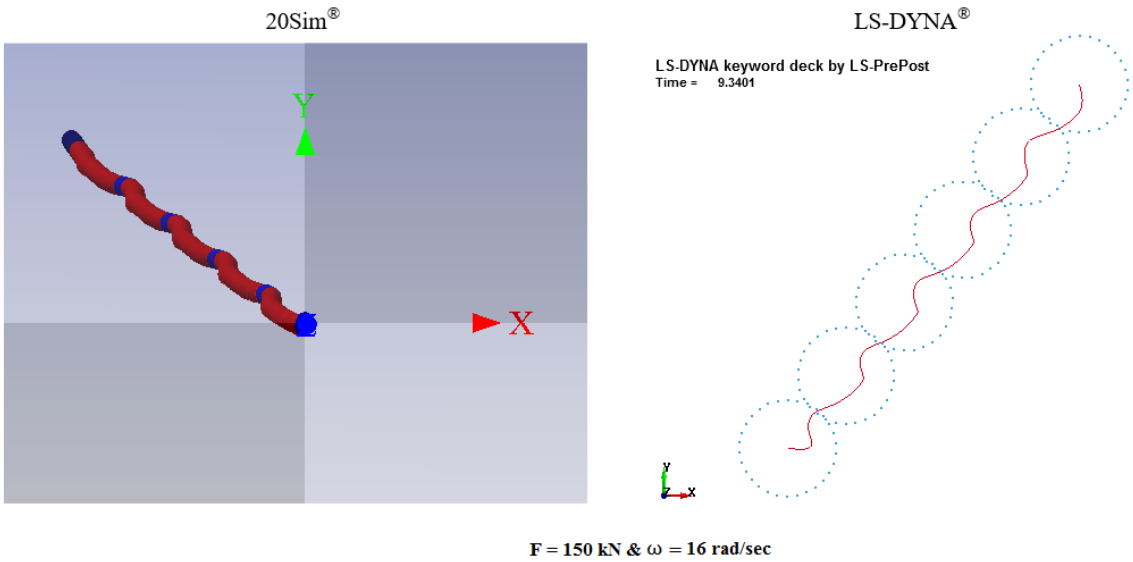

Figure 5.20: Sinusoidal buckling (snaking motion) animation.

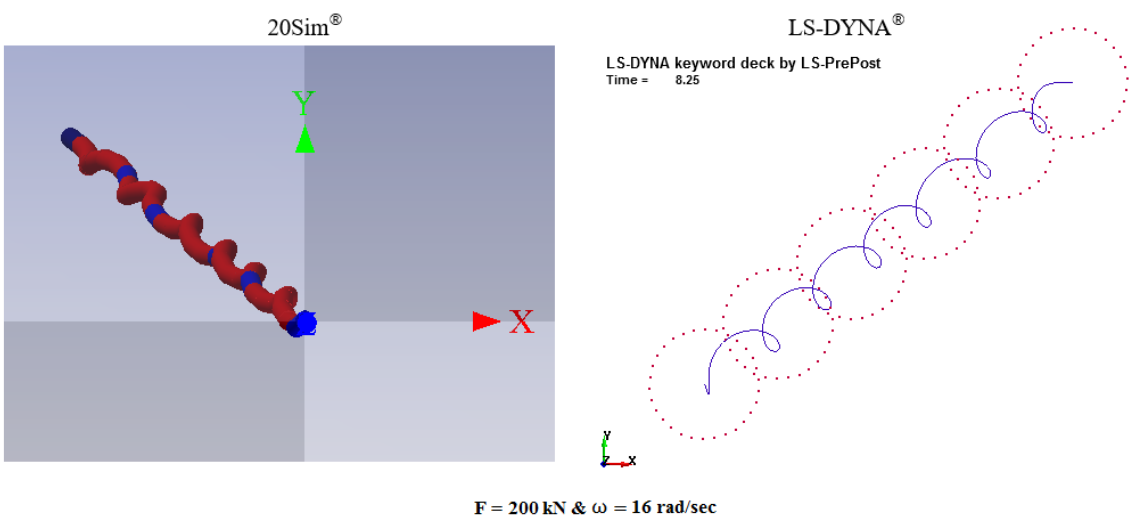

Figure 5.21: Helical buckling (whirling motion) animation.

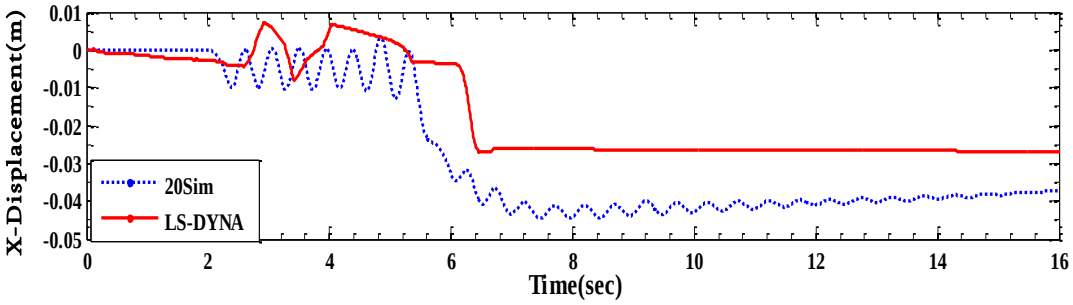

Figure 5.22: The x-displacement of pipe center at 50 m length distance when 150 kN applied load and 16 rad/sec rotation speed.

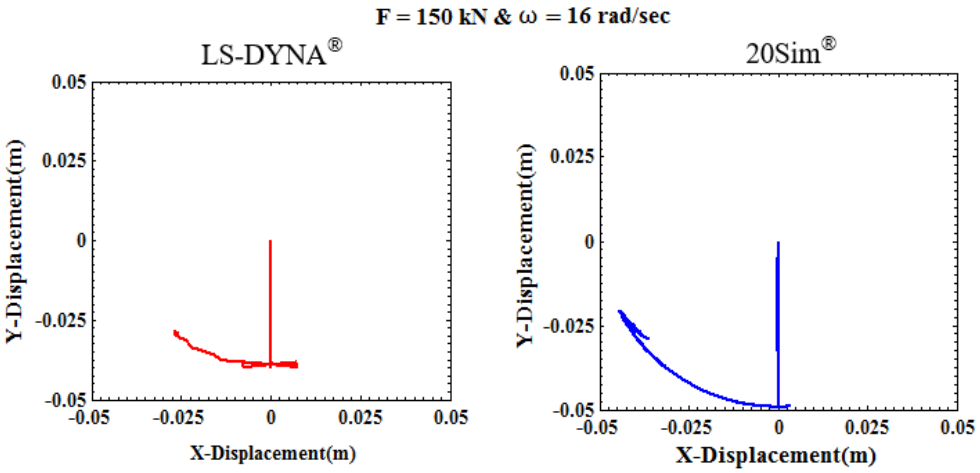

Figure 5.23: The trajectory of pipe center at 50 m length distance when 150 kN applied load and 16 rad/sec rotation speed.

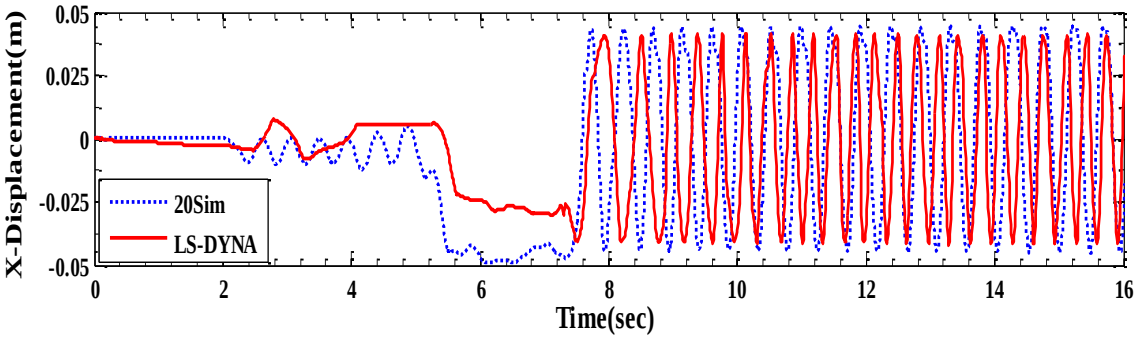

Figure 5.24: The x-displacement of pipe center at 50 m length distance when 200 kN applied load and 16 rad/sec rotation speed.

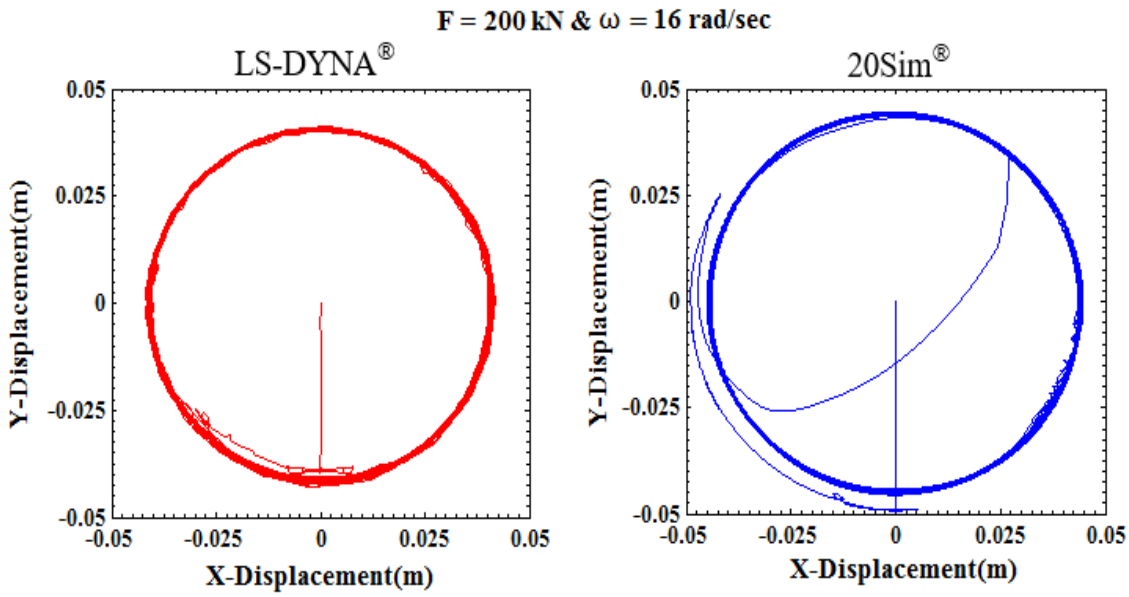

Figure 5.25: The trajectory of pipe center at 50 m length distance when 200 kN applied load and 16 rad/sec rotation speed.

The proposed multi-body bond graph approach for drillpipe modeling can therefor capture the pipe buckling inside wellbore wall that are most important for predicting and analyzing vibration related drilling problems. The model will be used in the next section simulation for capturing the 3D dynamics of horizontal BHA.

5.5 Demonstration of complete horizontal model

The system being modeled consists of drill pipes (DP), heavy weight drill pipes (HWDP), “subs” such as navigation and logging tools, collars, mud motor, the drill bit and the rock (formation). “Motor HS”, which is run by drilling mud, rotates the drill bit with respect to the rest of the string. Drilling fluid is circulated in the drillstring and the annular space between the drillstring and the wellbore. The drilling fluid is characterized by the flow rate developed by the mud pumps. The top of the drillstring is subject to a tension force, applied through the surface cables. Rotary motion is applied by a three-phase ac induction motor, through a gear box, to the rotary table via the kelly. The essential components of the horizontal oilwell drillstring are shown in Fig. 5.26. The drillstring model is divided into two sections. Section One includes the vertical portion, curved portion and major horizontal portion. The 56 m long final horizontal portion (BHA) ending at the bit is called Section Two.

The Section One model includes decoupled axial and torsional dynamics. Lateral dynamics are ignored. A lumped-segment approach is used in the axial and torsional dynamic model. Both axial and torsional submodels have a total of 45 segments as shown in Table 5.2. In the axial submodel, hydrodynamic damping, due to drill fluid circulation in the drillstring and the annular space, is considered in the DP and HWDP. In the torsional model, the DP and HWDP dynamic models consider viscous damping which results from the contact between the drillstring surface and drilling fluid. In the vertical portion, the contact between drillstring and wellbore wall is neglected. For curved and horizontal portions the contact and friction between drillstring and wellbore wall are considered. The

curved portion of the drillstring is divided into 20 segments and each segment is assumed as having continuous contact with the wellbore surface as shown in Fig. 5.26.

The 56 m long horizontal BHA of the drillstring shown in Fig. 5.26 is modeled using three-dimensional multi-body dynamics. The contact-friction phenomena between drillstring and wellbore wall is considered. Table 5.3 summarizes the multibody segments for the BHA section.

The quasi-static rock-bit model discussed in Chapter 4 is used instead of a computationally intensive and difficult-to-parameterize complete dynamic representation.

Table 5.2: Summary of the lumped segments for section one

Name of Drillstring Portion	No. of Segments
Vertical [1700 m]	10
Curved [463 m]	20
Horizontal [2100 m]	15

Table 5.3: Summary of the multibody segments for section two

Name of Drillstring Components	No. of Segments
Bit [0.2 m]	1
Motor HS [8 m]	8
Collars [36 m]	20
SUB [1 m]	1
DP [10 m]	4
SUB [1 m]	1

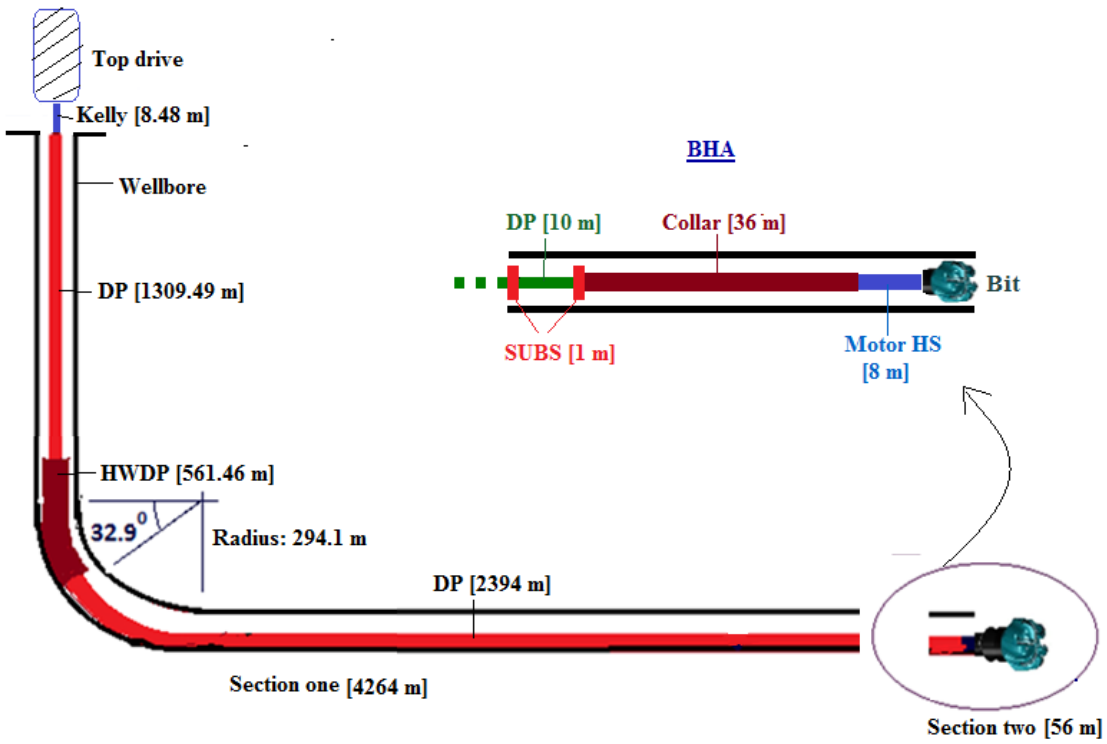

Figure 5.26: Schematic of the horizontal drillstring for simulation.

5.5.1 Simulation results

The bond graph model of the deviated drillstring has been developed in 20Sim®. The main objective of this simulation is to show the ability of the proposed three-dimensional BHA model to capture the coupling between axial, lateral and torsional oscillations near the bit. The bit-rock model has the capability to advance the bit and predict the ROP. Data from an actual well (Appx. B) is used for simulation. The simulation results for a 4320 m total drilled depth are shown in Figs. 5.27-5.35. The top of the drillstring is rotated at 5.2 rad/sec (or 50 rpm) while the mud motor is rotated at 13.7 rad/sec (or 131 rpm) (Fig. 5.27). Simulation results in Fig. 5.28 show that the drill bit rotates smoothly at 18.9 rad/sec (or

181 rpm) angular speed, which is the combined speed of the top drive and mud motor shown in Fig. 5.27. The surface torque required to overcome the cutting torque at bit and frictional torque while drilling is shown in Fig. 5.28. The constant WOB (Fig. 5.27) and bit speed provide a constant ROP that can be verified from the ROP plot in Fig. 5.28.

Figs. 5.29-5.32 show the trajectories of the geometric center of the bit, of the motor HS

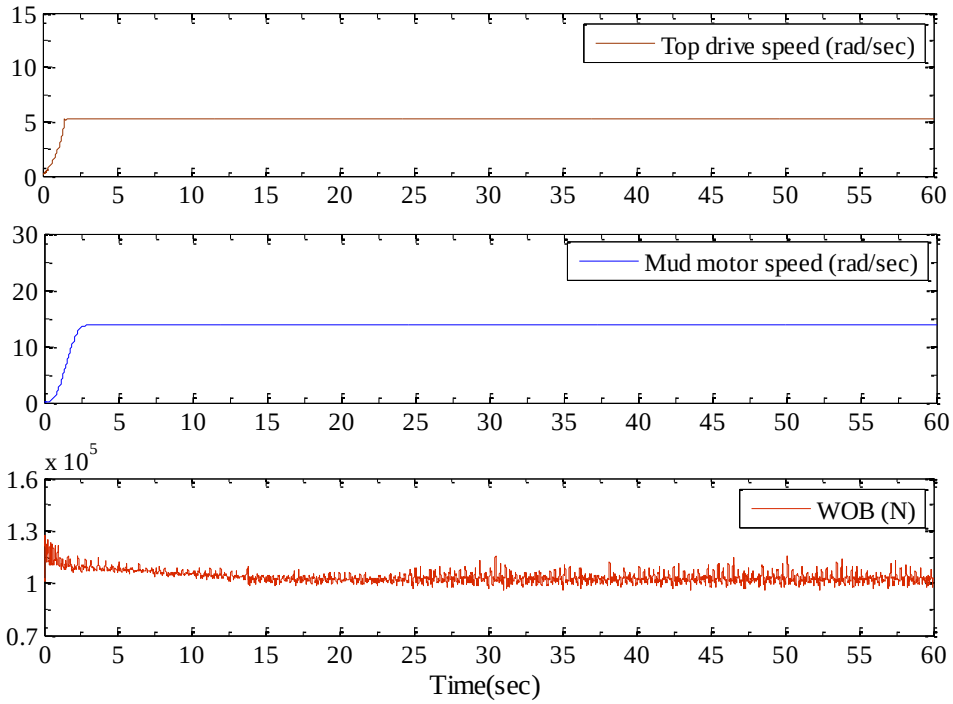

Figure 5.27: Simulation plots of top drive speed, mud motor speed and dynamic WOB.

4 m behind bit and of the collar 17 m and 28 m behind the bit. The trajectories show the bit and collar, when viewed in cross-section, are sliding up and down the borehole (snaking motion). But the motor HS segment is experiencing the lateral vibrations. High oscillation is identified in the bit whirling speed (Fig. 5.33). Also, higher contact force is found at the bit where the bit experiences high oscillations in whirl speed shown in Fig. 5.34. The

important finding from the simulation results is the presence of lateral shocks in the motor HS contact force shown in Fig. 5.34. A 20Sim® animation window screen capture is shown in Fig. 5.35.

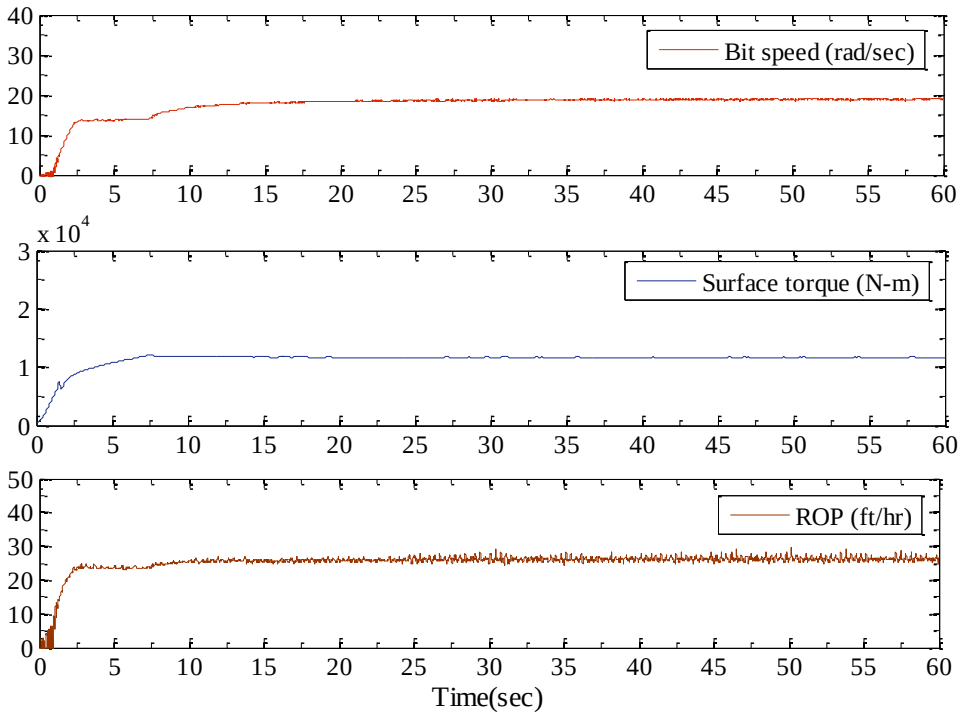

Figure 5.28: Simulation plots of bit speed, surface torque and instantaneous ROP.

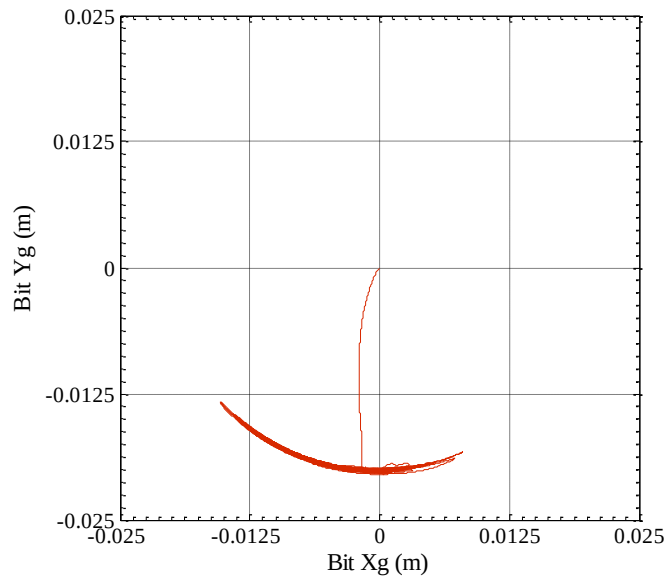

Figure 5.29: The trajectory of drill bit center

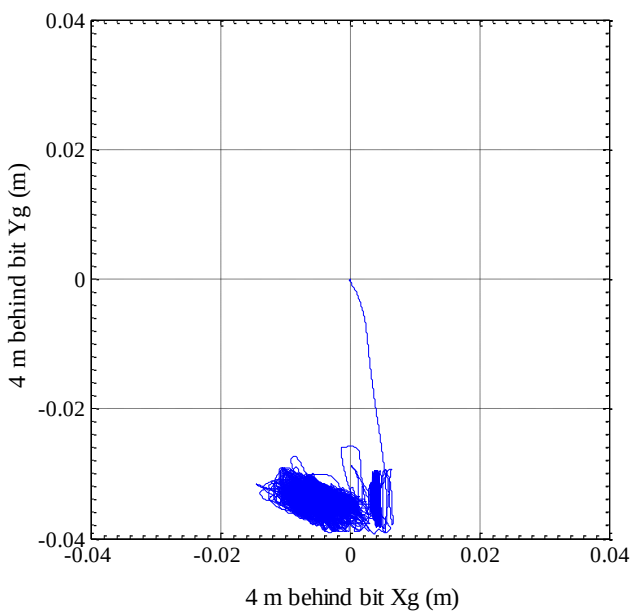

Figure 5.30: The trajectory of motor HS center at 4 m behind bit.

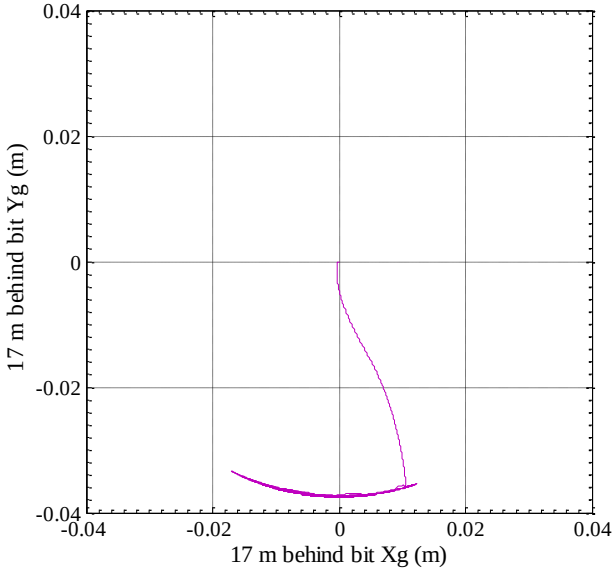

Figure 5.31: The trajectory of collar center at 17 m behind bit.

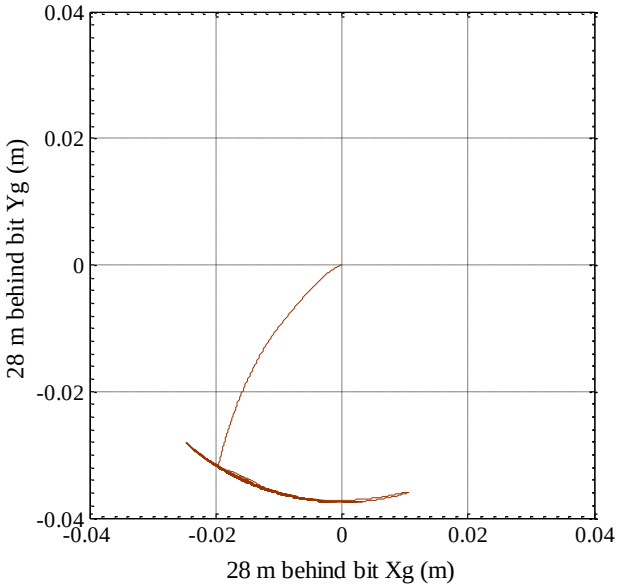

Figure 5.32: The trajectory of collar center at 28 m behind bit.

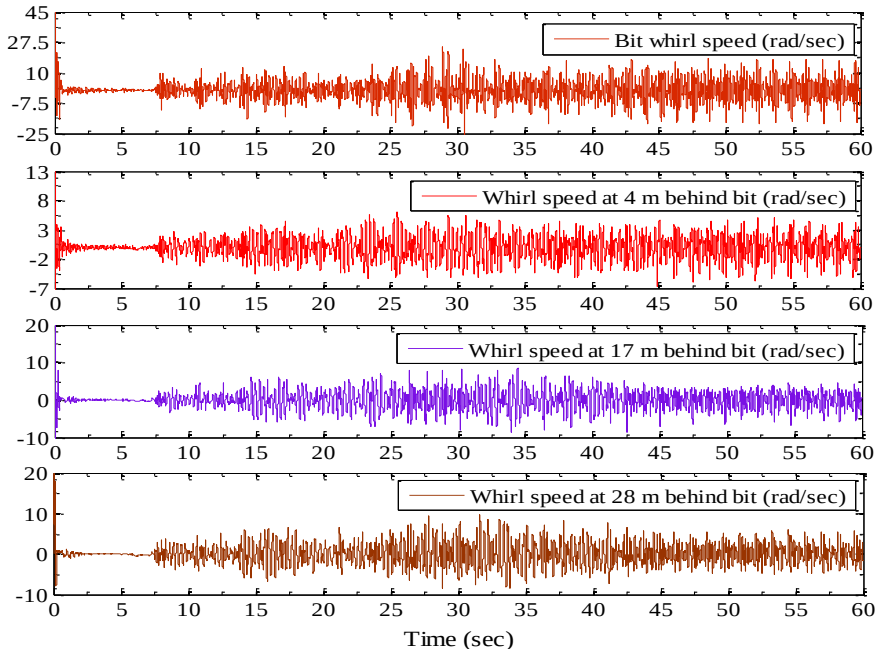

Figure 5.33: Whirl speed at bit, 4 m behind bit (motor HS), 17 m and 28 m behind bit (collar).

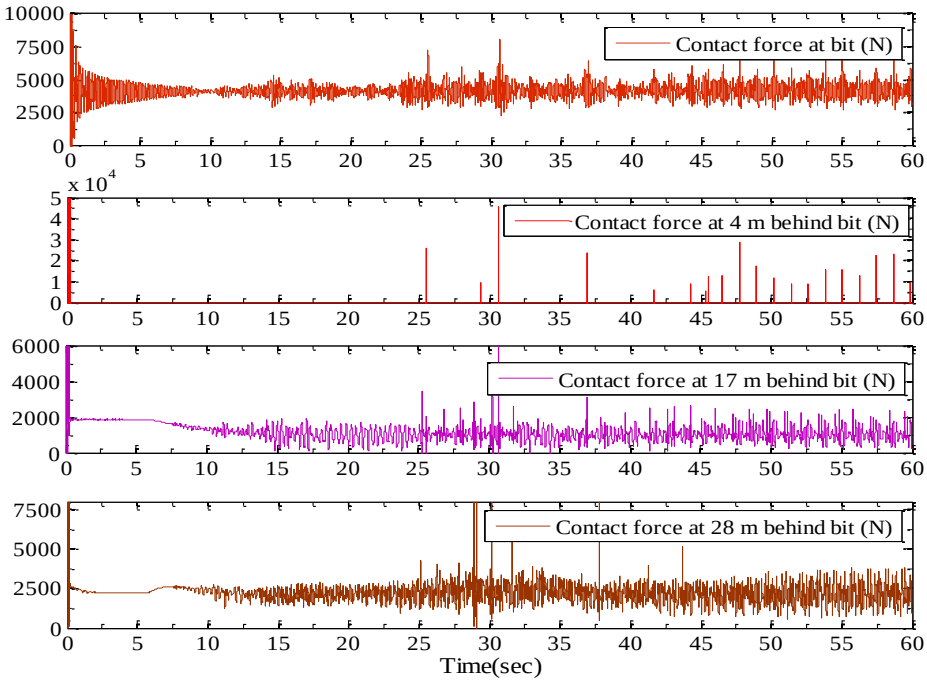

Figure 5.34: Contact force at bit, 4 m behind bit (motor HS), 17 m and 28 m behind bit (collar).

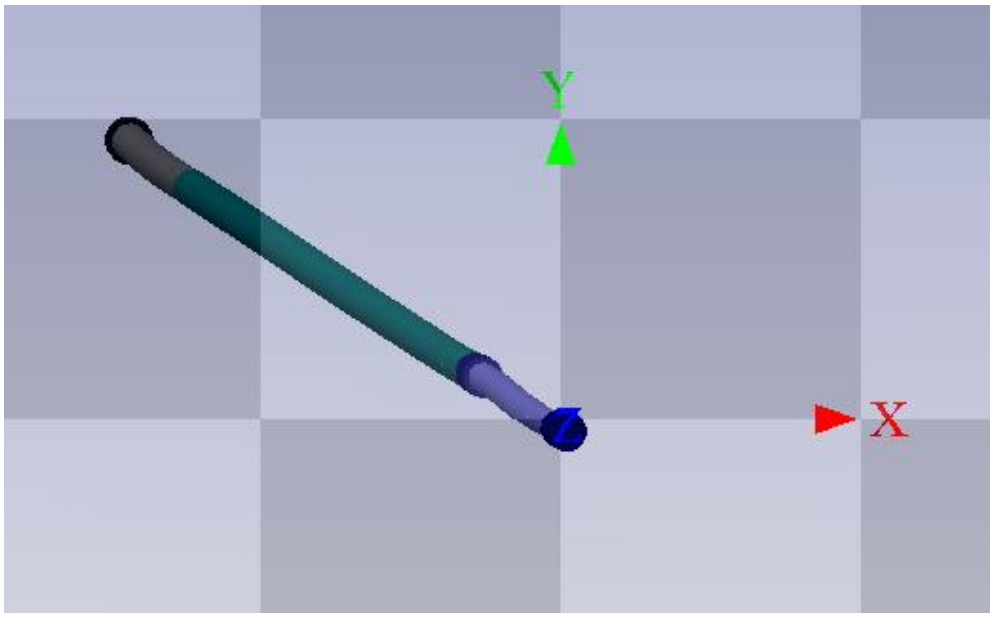

Figure 5.35: Animation plot of BHA in 20Sim®.

Application of the three-dimensional multi-body bond graph modeling approach for developing a horizontal oilwell pipe dynamics has been presented. The proposed dynamic model accounts the stick-slip whirl interaction phenomena at the contact between drillstring and wellbore wall. Several tests are conducted to predict the accuracy of the modeling approach for drillpipe dynamic responses. The model is able to predict the changing phase between sinusoidal and helical buckling. The model results have a very good agreement with the LS-DYNA® finite element model. Demonstration of a complete horizontal oilwell drillstring model has been presented. Simulation results show that the model able to capture the three-dimensional BHA dynamics. In the next section, the model will be used to simulate the effect of downhole tool, which is discussed in Chapter 4 as a means of decreasing frictional energy loss and increasing ROP, on the BHA lateral dynamics.

5.5.1.1 Effect of downhole tool on BHA lateral dynamics

The main objective of this simulation is to show the ability of the proposed model to predict the effect of axial excitation tool on the 3D motions, especially lateral dynamics, of the BHA. The different amplitudes and frequencies of AES force have been considered in the model simulation. Figs. 5.36-5.47 summarizes the comparison study of finding the optimum combination of amplitudes and frequencies of AES force. Figs. 5.36-5.39 show the performance of the AES force in improving WOB transfer and increasing ROP. The results have similarity with the Chapter 4 simulation results. Figs. 40-43 show the trajectories of the geometric center of the bit, of the mud motor at 4 m behind the bit, and of the collar 17 m and 28 m behind the bit for the case of different amplitudes and frequencies of AES force. As the AES force amplitude increases and frequency decreases the drill bit rolling distance path and the lateral vibration in the motor HS segment at behind the bit increase. There is no significant difference in the collar segment's rolling motions. The contact force results (Figs. 44-47) show that the amplitude contact force or lateral shock in BHA increases when the AES force amplitude increases and frequency decreases. The results show that the motor HS section behind the bit experiences severe lateral shocks. The Ryan Direction Service data sheet also shows the mud motor failures while drilling. Thus the horizontal drillstring model described herein is effective at predicting the effect of downhole tool parameters on drilling performance, decoupled axial and torsional vibrations throughout the string and 3D vibrations in the BHA.

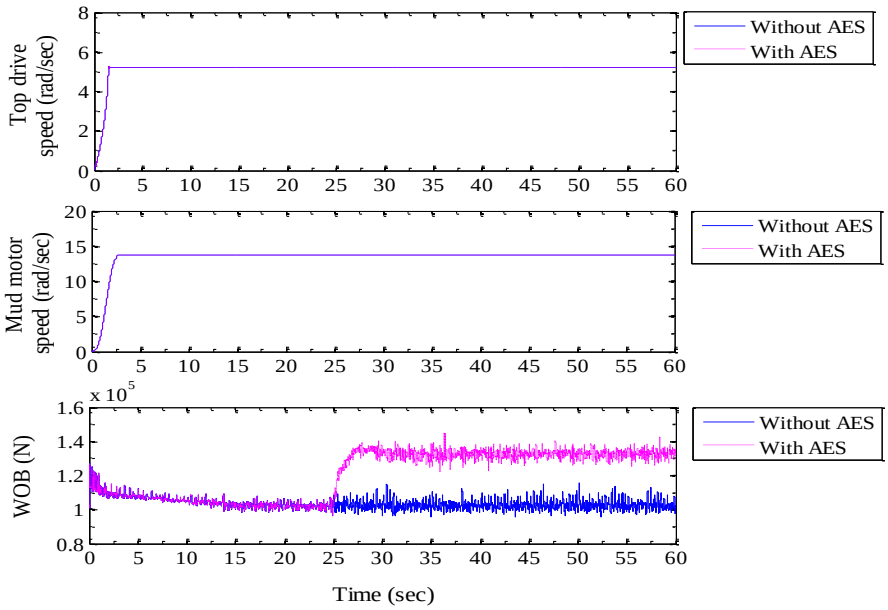

Figure 5.36: Top drive speed, mud motor speed and WOB for the case of without and with AES, 100sin(125*t*) kN.

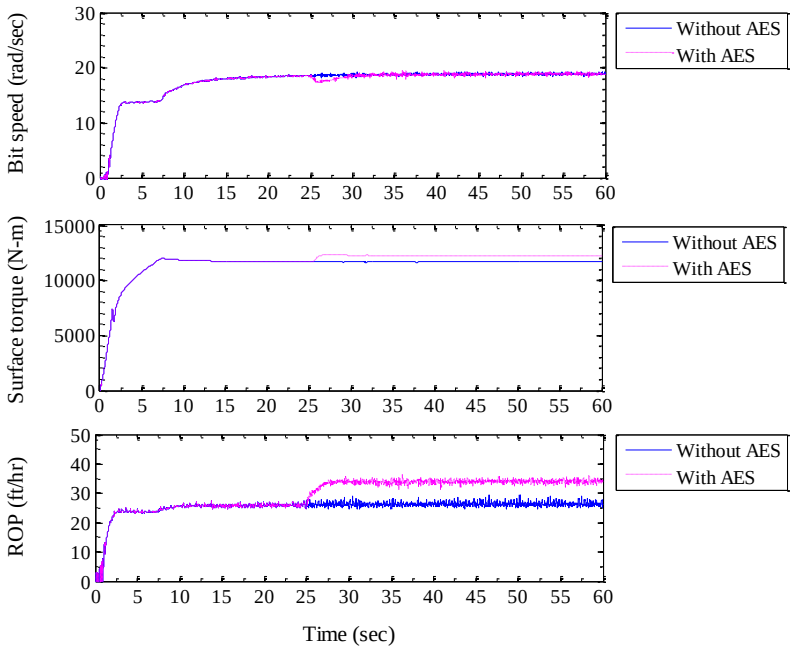

Figure 5.37: Surface torque, bit speed and ROP for the case of without and with AES, 100sin(125*t*) kN.

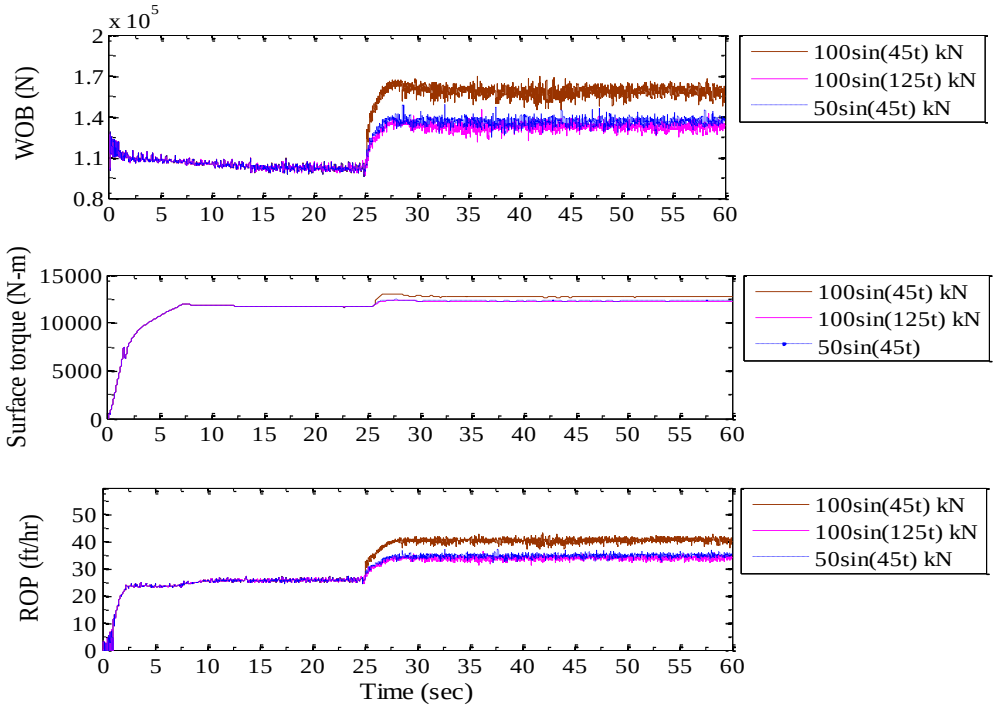

Figure 5.38: WOB, surface torque and ROP for different amplitudes and frequencies of AES force.

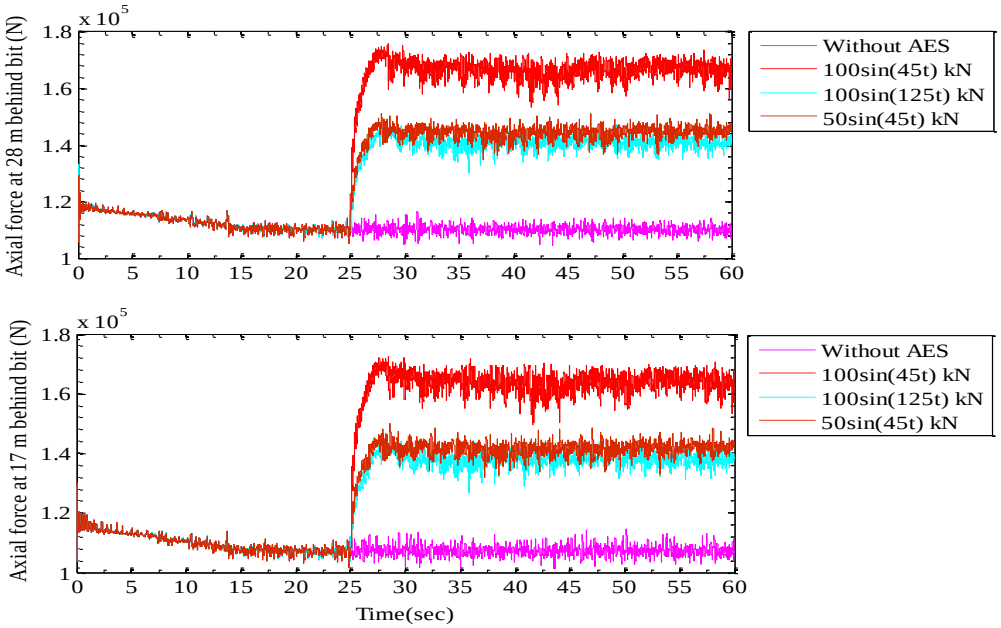

Figure 5.39: Axial force at 17 m and 28 m behind bit segments for the case of without and with AES.

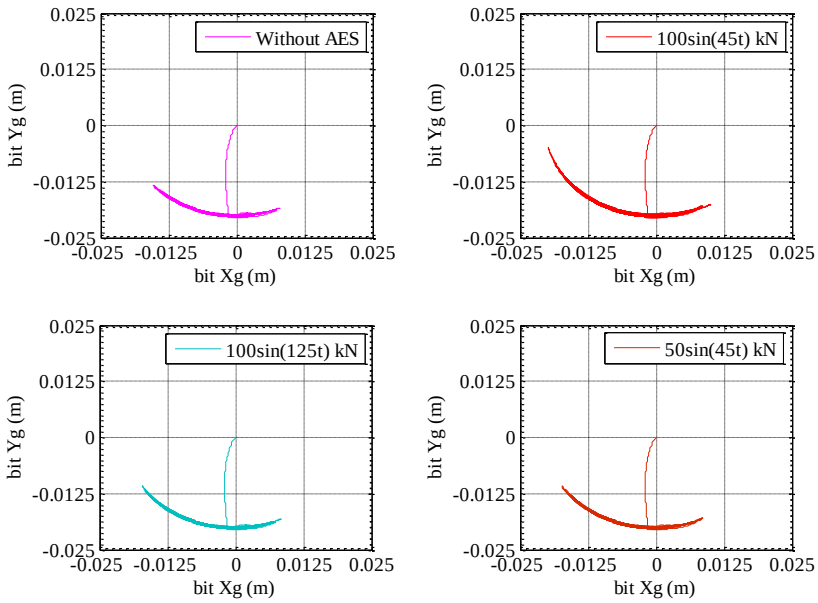

Figure 5.40: The trajectory of bit center for different amplitudes and frequencies of AES force.

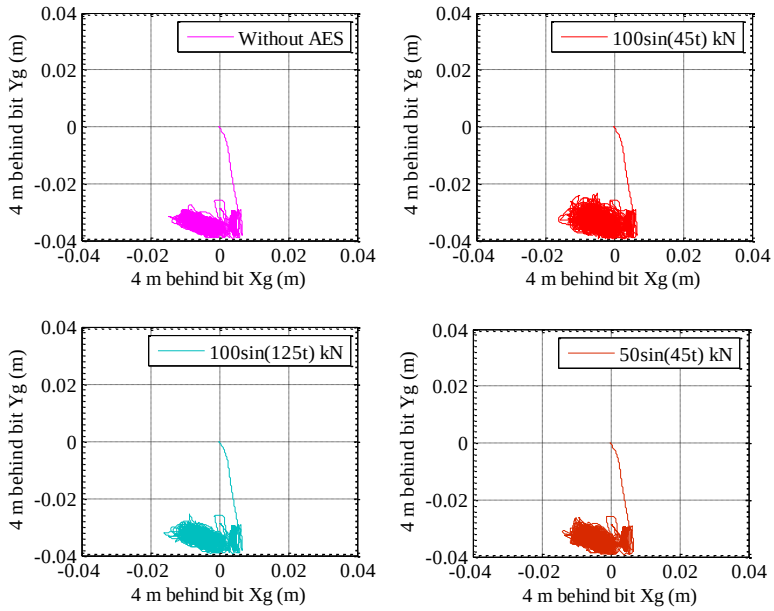

Figure 5.41: The trajectory of mud motor center at 4 m behind bit for different amplitudes and frequencies of AES force.

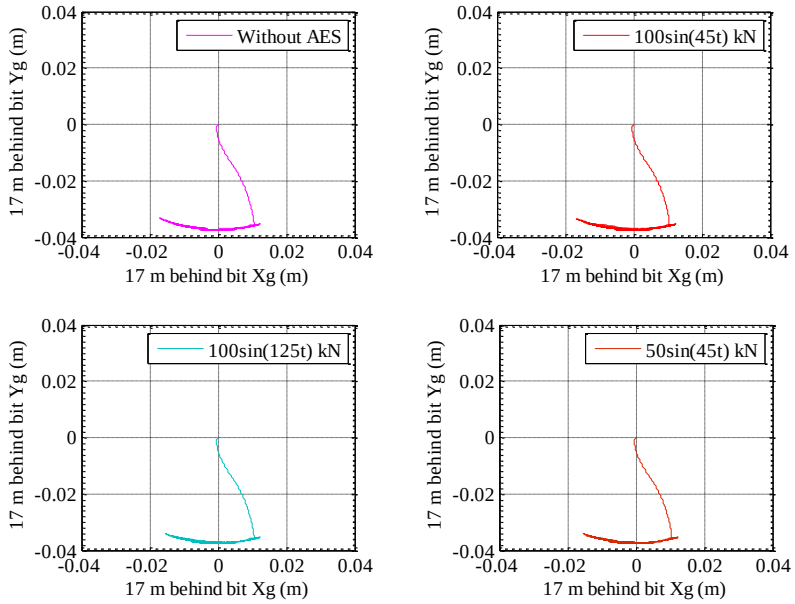

Figure 5.42: The trajectory of collar center at 17 m behind bit for different amplitudes and frequencies of AES force.

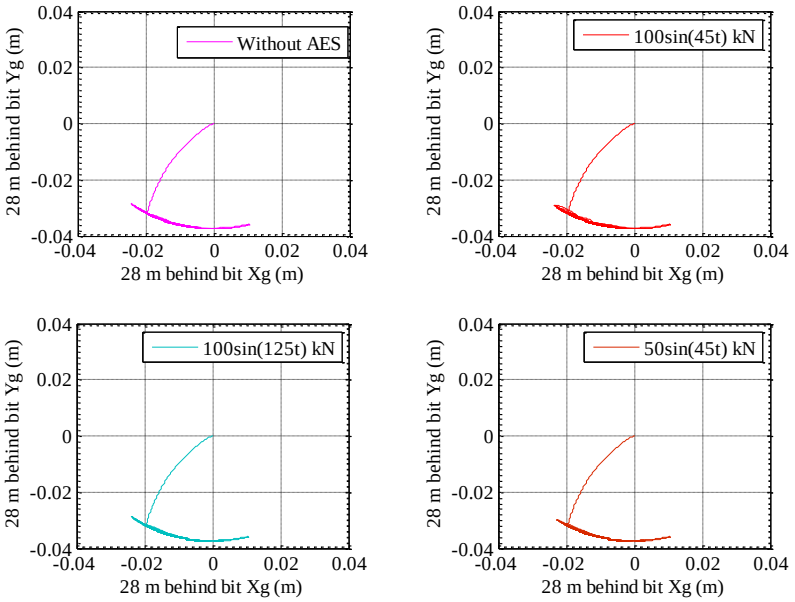

Figure 5.43: The trajectory of collar center at 28 m behind bit for different amplitudes and frequencies of AES force.

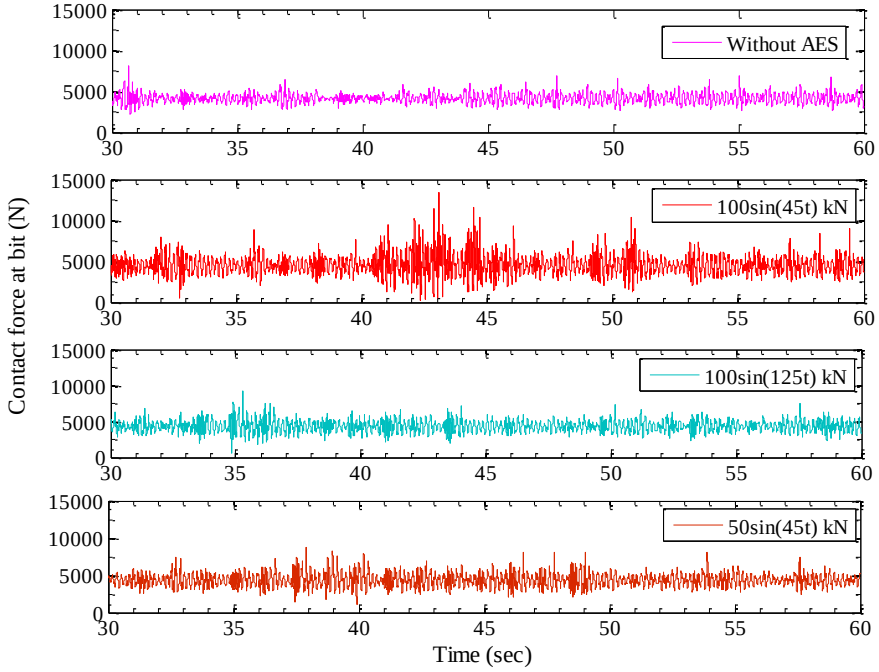

Figure 5.44: Contact force at bit for different amplitudes and frequencies of AES force.

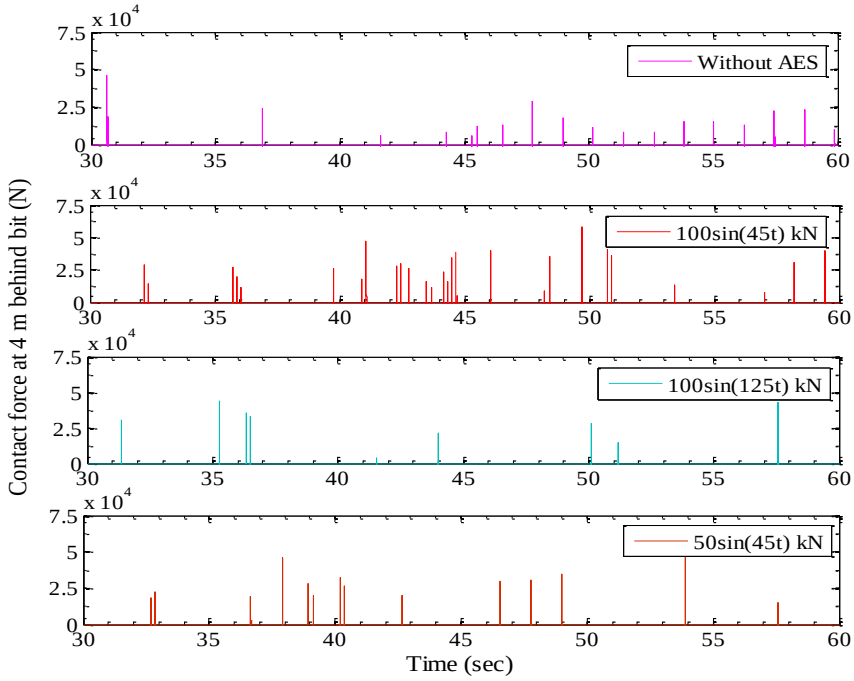

Figure 5.45: Contact force at 4 m behind bit (motor HS) for different amplitudes and frequencies of AES force.

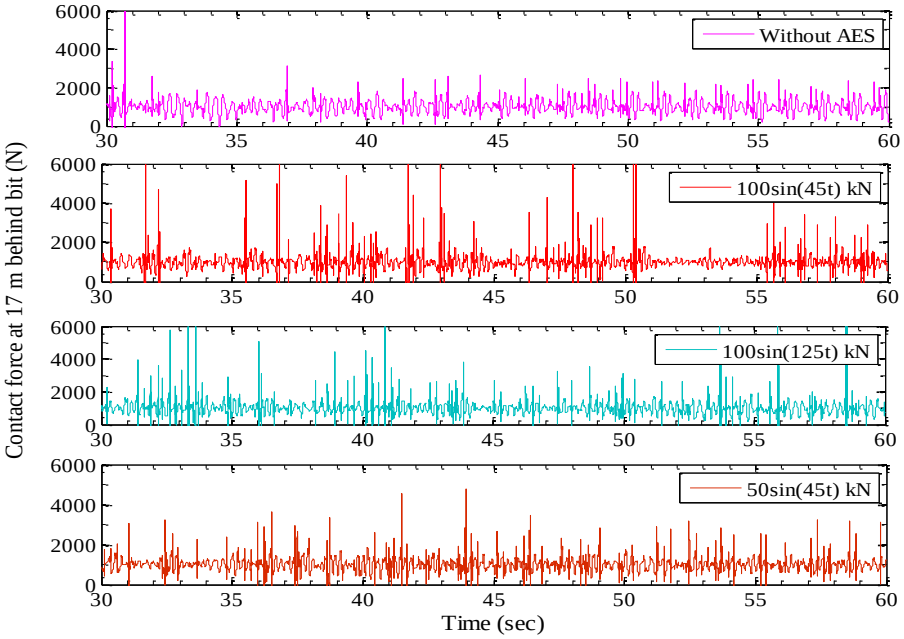

Figure 5.46: Contact force at 17 m behind bit (collar) for different amplitudes and frequencies of AES force.

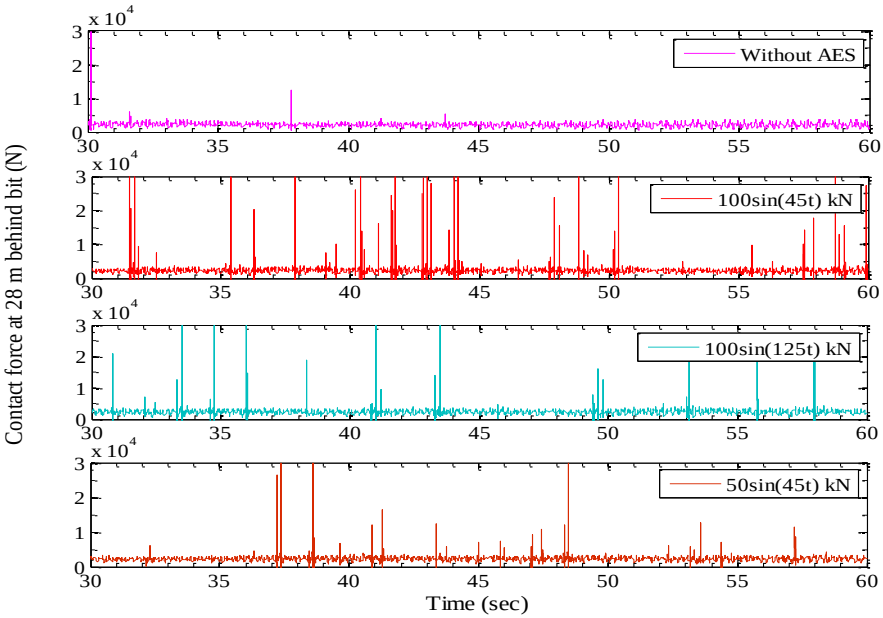

Figure 5.47: Contact force at 28 m behind bit (collar) for different amplitudes and frequencies of AES force.

This chapter work presents an application of a three-dimensional multi-body bond graph modeling approach for simulating vibration in a horizontal oilwell. The model includes three-dimensional multibody dynamic segments in the final horizontal section (BHA) ending at the bit, which allows prediction of coupled axial, torsional and lateral vibrations. The upper portions of the drillstring assume decoupled axial and torsional lumped segments. The behavior of the multi-body model was verified with an LS-DYNA® finite element model. The model accounts for the stick-slip and whirl interaction phenomena at the contact between the drillstring and wellbore wall. The model is able to predict the transition between sinusoidal and helical buckling as WOB changes. A complete horizontal oilwell drillstring simulation was demonstrated. Simulation results show that the model is able to predict three-dimensional BHA dynamic responses, and simulate the effect of a downhole axial vibration tool. The downhole tool was predicted to cause better weight transfer to the bit, with a low frequency and high amplitude force excitation giving best performance but increased risk of severe lateral shock. In the next chapter, the summary of the thesis work and the recommended future works will be presented.

6 Conclusions and Further Work

6.1 Thesis summary

Achieving an efficient yet predictive dynamic model for a deviated wellbore requires understanding the drillstring contact-friction with wellbore wall. This thesis considered the problem of developing drillstring contact-friction dynamics and provided a suitable approach to capture it. Although works already presented drillstring dynamics with this phenomenon, there remains a need for a coupled stick-slip and whirl model at the contact between rotary drillstring and wellbore to simulate the snaking and whirling motions of the BHA. Another limitation of existing work was the lack of a complete development of a deviated drillstring model which can capture top drive electric motor dynamics, vertical drillstring dynamics, curved drillstring dynamics, 3D BHA dynamics and a rock-bit interaction phenomena. In addition, existing models were unable to capture the effect of downhole tools such as Agitator® and mud motor on the 3D dynamics of BHA.

The central focus of this thesis was to develop a bond graph dynamic model of a complete deviated oilwell drilling to simulate the 3D motions of BHA. The first part, development of axial and torsional motions of a horizontal oilwell drilling, was achieved through the extension of author's previous vertical model with dynamic model of frictional torque/drag. The vertical model presented the dynamics of whole drillstring including both drill pipes and collars using a lumped segment approach. In addition to the axial vibration, torsional vibration, and axial-torsional coupling due to rock-bit interaction, the model

accounted for the self-weight effect, the associated tension and compression fields, viscous damping, hydrodynamic damping, and hydraulic forces due to drilling mud within the drillstring; an empirical treatment of rock-bit interaction, and top drive motor dynamics. A stick-slip friction model was used to simulate the friction drag and torque for axial and rotation motions, respectively. The stick-slip friction model also implemented in an LS-DYNA® FEM model to ensure that LS-DYNA® was a suitable validation environment for the later 3D multibody BHA submodel. A modified version of normal force calculation was presented for torque and drag prediction. The torque and drag results from the model were validated with field data from industry (Ryan Directional Drilling) collboration.

The second part, development the 3D dynamics of BHA, proved to be much more challenging than originally anticipated. A non-linear three dimensional multibody system approach was used to model the BHA dynamics. The effectiveness of the model was validated with LS-DYNA® FEM model. The model was extended to include stick-slip whirl phenomena due to contact between the rotating BHA and wellbore. The contact model incorporated stiff springs with discontinuous laws which provide no effort until the radial deflection exceeds the radial clearance between BHA and wellbore wall. Damping was also added into the model. The contact force generated from the model was compared with the FEM. The model was validated with dynamic FEM through comparisons of the response of an enclosed shaft under axially compressive load rotating inside the wellbore.

The third part, demonstration of complete horizontal oilwell drilling simulation was performed with the presence of downhole tools such as an axial excitation tool (e.g., Agitator®) and mud motor. The model predicted how axial and torsional bit-rock reactions

were propagated to the surface, and the role that lateral vibrations near the bit play in exciting those vibrations and stressing components in the BHA. The proposed model included the mutual dependence of these vibrations, which arose due to bit-rock interaction and friction dynamics between the drillstring and wellbore wall.

6.2 Summary of main results

1. The dynamics of an ac three phase induction motor were modeled and later used with a gear submodel as a more realistic of a top drive system. The no-load responses from the model of a 500 hp induction motor (3-phase, 4 pole, 2300 V) was presented. Both the transient and the steady-state responses of the motor were obtained from the proposed model. At steady-state, the rotor ran at the speed of very close to 1800 rpm. Later the motor model was used with the gear submodel as a representation of top drive system.
2. The vertical oilwell simulation results were very sensitive to the drill bit cutting coefficient. The higher cutting coefficient provided higher ROP, depth of cut and TOB. The downhole mud motor increased the bit speed and provided smooth drilling. Higher oscillation in the WOB amplitude was found at high bit speed. High stick-slip vibration at the bit was found in the absence of a mud motor. Stick-slip vibration was eliminated with an increase in top drive speed and lowering the applied WOB.
3. Wellbore friction parameters played an important role in the horizontal oilwell simulation. The rotating friction coefficients (static and dynamic) for drillstring

rotational motion differed from longitudinal friction coefficients (static and dynamic). The dynamic and static friction coefficients for CNRL HZ Septimus C9-21-81-19 oilwell drillstring axial motions simulation were recommended as 0.35 and 0.40, respectively. For torsional motion simulation the recommended values of dynamic and static friction coefficients were 0.2 and 0.25 respectively.

4. The lab experiments showed that an Agitator® downhole tool can be represented as a sinusoidal force. The oscillation frequency and pressure drop across the Agitator® tool (or force amplitude) increased with the drilling fluid flow rate.
5. The proposed 3D multi-body drill pipes dynamics model simulation results agreed with LS-DYNA® finite element analysis. The natural frequencies from the models matched reasonably well. The discrepancy between the models lateral deflections increased with the higher applied load. The proposed model provided less stiff than the LS-DYNA® model. The model was able to capture the pipe rotor dynamics.
6. The 3D multi-body bond graph approach for horizontal drillpipe modeling with stick-slip whirl interaction at the contact between horizontal drillpipe and borehole provided accepted accuracy to capture the pipe buckling phenomena. The model showed the ability to capture pipe rolling motion over the wellbore wall.
7. The simulation results from a complete horizontal oilwell drillstring model with 3D BHA dynamics captured the coupling between axial, lateral and torsional oscillations near the bit. The motor HS section at behind the bit experienced high lateral shocks. The results showed that the bit rolled over the wellbore.

8. The application of high amplitude and low frequency of downhole axial excitation force source (or Agitator®) provided better weight transfer to the bit and increased rate of penetration. A very high amplitude and a very low frequency force increased the contact force between BHA and borehole, and the chances of severe lateral shock to the BHA. Thus, the tuning study between downhole tool parameters and overall drilling performance was recommended.

6.3 Future work

This thesis was able to demonstrate the potential of efficiently creating bond graph dynamic models of a horizontal oilwell drillstring by extending the previous lumped segment vertical model work with the consideration of wellbore friction and 3D BHA multibody dynamics. Many opportunities for extending the impact of this work remain. The following is a list of issues that should be considered for the next stage of research.

6.3.1 Experimentally determine parameters for bit-rock interaction models

The interaction phenomena of drill bit with formation is one of the major excitation source of drilling vibrators. Drilling with drag bits on hard formation generates the most severe drillstring vibrations. Drag bit-rock interaction phenomena has received considerable attention in recent years with increasing use of polycrystalline diamond compact (PDC) bits in harder formations, and has motivated extensive research on this type of phenomena. Also the interaction model of the PDC bit with rock is very important to forecast the ROP of the bit.

The rock-bit interaction model should be experimentally parameterized to match field drilling data. A drilling experiment can be carried out using the drilling rig in the Advance Drilling Laboratory (ADL) at MUN in which a real PDC bit can be loaded under the assumption of a steady bit motion. The relationship of applied WOB, threshold WOB, bit rotary speed and drill fluid flow rate with the ROP, cutting torque on bit (TOB) and friction TOB of PDC bit should be considered. The type of lobe pattern generation on the cutting formation should be observed for determining the surface elevation function. In addition, this study should include the determination of formation stiffness and damping parameters. Multiple nonlinear regression analysis can be conducted on the basis of the experimental data; and a new bit-rock interaction model can be established.

For further validation a field case study can be performed to parameterize the model for various types of rock, PDC bits and bottom-hole pressure conditions, thereby increasing its predictive ability for modeling of a full scale PDC bit-rock interaction phenomena.

6.3.2 Experimentally validation of drillstring buckling model in curved/horizontal wellbore

Buckling of drillstrings can increase the risk of fatigue failure which are extremely costly during horizontal oilwell drilling. Also drillstring buckling may cause problems such as deviation control while drilling and ineffective axial load transfer to the bit. The developed bond graph model of 3D shaft dynamics in 20Sim® should be verified with experimental study. Thus an experimental setup can be built in the ADL at MUN to study buckling and post buckling behavior of pipes constrained in straight horizontal and curved

wellbore. With the increasing of axial load, pipes first buckle sinusoidally and then helically. An additional contact force and friction energy loss between the pipe and wellbore wall are induced due to the buckling, which are of major concern while drilling horizontal and extended reach drilling.

The experimental facility of the pipe buckling in curved/horizontal wells should allow to apply axial load at one end (free end) and to measure load at both ends (load end and fixed/pinned end) of the pipe. The displacement of the pipe at the load end should also be measured. The experimental facility should also allow to conduct experiments with static internal pressure. The effect of pipe end conditions (pinned or fixed), pipe size (especially outer diameter of pipe) and internal fluid pressure on the pipe buckling behavior in a curved/horizontal wellbore should be studied. Non-contact proximity sensors should be used to visualize lateral motion.

Verification of the lateral contact force model should be performed by using experimental measurement of lateral contact forces in order to compare axial force transfer. The contact gage can be designed and constructed to measure the lateral contact force. The contact gage will generate a force in the opposite direction to the lateral contact force of the pipe. If the pipe buckles laterally or into a helical shape, then an additional lateral contact force can develop between the pipe and the wellbore wall. The friction factor to the model can be estimated through back-calculation from the experimental results. Drag forces occurring at the curved sections of the wellbore can have significant control on axial force transfer. This work results will confirm the versatility and effectiveness of developed 20Sim® computer simulator for better understanding and solving buckling related

problems in the field. Finally, the model should be verified with field experiments or using field data from collaboration with oilwell drilling industry partners.

6.3.3 Experimentally determination of pipe-borehole friction factor in horizontal drilling with a bed of cuttings

One of the important aspects of drilling horizontal or extended reach wells is the friction between the drillpipes and borehole with the presence of cuttings that tend to deposit on the lower part of the horizontal annular section. An experimental setup should be built in ADL at MUN to find out the maximum friction factor that can arise from the presence of cuttings. The effect of cuttings size on the friction factor value should be studied.

The experimental facility should allow build up of a constant height solid bed along the test section. A drilling fluid flow loop should be connected with the setup. Experiments should be performed for different annular geometries, different values of solid/fluid properties, different pipe size and operational variables (particle diameter, rheology, fluid density and flow rate).

This work results will validate the developed 20Sim® computer simulator for better predicting the frictional torque and drag during the case of worst cutting removal system. The experimental facility can also be used to validate the hydrodynamic damping (axial) and viscous damping (torsional) for the case of fluid/solid flow instead of only drilling fluid flow which is one of the limitations in the current model.

6.3.4 Extension of the horizontal drillstring model to predict the fatigue in horizontal wells

Drill pipe fatigue is one of the major problems while drilling in short radius build sections of horizontal wells. It occurs when the maximum bending stress in pipes becomes larger than the fatigue limit. Buckling of drillstrings can increase the risk of fatigue failure. The current model should be extended to include pipe fatigue phenomena for monitoring the fatigue damage. The pipe fatigue damage should be determined by pipe bending stresses, rotating revolutions, and pipe S-N curves. The effect of pipe material, bit weight, penetration rate and other drilling variables on fatigue model should be investigated.

The extended model can be verified with the experimental study of rotating buckled pipe inside annulus. This work will extend the capability of the current model to monitor the effect of severe vibrations on pipe fatigue damage.

6.3.5 Experimentally determine parameters for downhole mud motor model

The downhole motor is a hydraulic-mechanical coupled system and driven by high pressure mud where the RPM depends on the mud flow rate. The current work has modeled the mud motor as a constant rotation input to the rotary drilling simulation model which does not represent the actual drilling conditions. Thus, a model of coupled hydro-mechanical mud motor model should be developed by performing the laboratory tests in ADL at MUN.

An experimental facility should be built that can allow flow of high pressure drilling fluid through the mud motor. The effect of mud flow rate and mud density on the motor

RPM should be measured and plotted. The corresponding pressure drop across the mud motor should also be measured to develop the hydraulic fluid line. This work will extend the ability of the current model to capture the effect of the mud flow rate on the drill bit rotation.

6.3.6 Extension of vertical drillstring model to include the effect of riser buckling on offshore drilling dynamics.

Offshore technology for Deep water drilling systems is becoming a focus with increasing demand for exploration of underwater oil and gas resources. The current model has to include the effect of riser buckling on the vertical drillstring dynamics for offshore drilling application. A buckled riser can increase the contact force between vertical drill pipe and riser which can significantly increase bending stress in pipes during drilling operations.

A riser or flexible pipe can be modeled by using 3D continuum FEM in LS-DYNA®. The model can be verified with the buckling response from experimental work. The effect of external pressure and internal pressure on the riser buckling should be studied. The riser model can also be developed by using 20Sim® 3D multibody dynamics (or 2D axial and lateral coupling) and can be combined with the current model. This work will be able to simulate offshore deviated oilwell drilling systems.

6.3.7 Experimentally determine parameters for axial excitation tool model

The experimental characterization of downhole axial excitation tool (or Agitator®) presented in this research work is limited to the low flow rate conditions. Also the experiment has been conducted without applying back pressure. An experimental facility should be built in ADL at MUN in order to predict actual force generation from the tool. The generating force profile can be used directly to the drillstring model to simulate the effect of downhole tool parameters on drilling dynamics. This work will allow the model to simulate the drilling model with the actual downhole tool generated force profile.

6.3.8 Validate the complete horizontal drilling dynamic simulator with MWD field data

To achieve accurate simulation, the model should be validated using MWD drilling dynamic tool data in the time domain with an adequate sampling rate. The study of dynamic behavior of the drill bit for various drilling conditions (hook load, RPM, mud properties and flow rate, BHA configuration, drill bit design, borehole parameters, and formation properties) should be conducted. The major drilling dynamics such as bit bounce, lateral vibrations, BHA/bit whirl, torque shocks, stick-slip and torsional oscillation should be measured and compared.

This work will allow the simulator to be used efficiently as a training tool for teaching drilling and MWD personnel, providing a better understanding and feeling for various phenomena and problems related to drilling dynamics.

6.4 Application for this work

The model developed in this thesis are computationally efficient and user friendly. Thus the model can be used for the following purposes.

- a model that can assist with well trajectory planning, and predict relationships between weight-on-bit, rotary speed, bit-bounce, and stick-slip.
- a model to design controllers to mitigate severe drillstring vibrations.
- a model to assist industry partners, and the industry in general, with predicting loads on downhole tools. Such a model would allow drillers to choose drilling parameters and tool locations to minimize the chances of failure.
- a model to use as a simulator for training purposes such as teaching drilling and MWD personnel to provide important insight into phenomena and problems related to drilling dynamics.

6.5 Final word

The development of an efficient yet predictive dynamic model for a deviated oilwell drillstring is a challenging research work. It is extremely multidisciplinary, requiring knowledge of top drive motor dynamics, contact-friction phenomena in the curved and horizontal section, 3D BHA dynamics, hydrodynamic damping and bit-rock interaction phenomena. The proposed model is computationally efficient and user friendly. The proposed research work of developing the use of a high-order lumped segment approximation, implemented using the bond graph method for which commercial software

exists which can be interfaced with widely used engineering software packages such as Matlab®. The research can be used to (a) understand and predict sensitivity of unwanted vibration modes such as stick-slip and bit-bounce to drilling parameters, (b) predict effect of downhole vibration tools on MWD tool life and on vibration of the drillstring as a whole, and (c) control of drillstring vibrations.

References

Aadnoy, B.S. (1998). Friction Analysis for Long-Reach Wells. SPE/IADC 39391 presented at *SPE/IADC Drilling Conference*, Dallas, Texas, USA.

Aadnoy, B.S. and Andersen, K. (2001). Design of Oil Wells Using Analytical Friction Models. *Journal of Petroleum Science and Engineering*.

Aadnoy, B.S., Fabiri, V.T. and Djurhuus, J. (2006). Construction of Ultralong Wells Using a Catenary Well Profile. SPE/IADC 98890 presented at the *SPE/IADC Drilling Conference*, Miami, USA.

Aadnoy, B.S. and Djurhuus, J. (2008). Theory and Application of a New Generalized Model for Torque and Drag. *SPE/IADC 114684 presented at the SPE/IADC Asia Pacific Drilling Technology Conference and Exhibition*, Jakarta, Indonesia.

Aadnoy, B.S., Fazaelizadeh, M. and Hareland, G. (2010). A 3-Dimensional Analytical Model for Wellbore Friction. *Journal of Canadian Petroleum Technology*.

Aarrestad, T.V. (1990). Effect of Steerable BHA on Drag and Torque in Wells. *SPE 20929 presented at Europec 90*, The Hague, Netherlands.

Aarrestad, T.V. and Blikra, H. (1994). Torque and Drag- Two Factors in Extended-Reach Drilling. *Journal of Petroleum Technology*.

Adewuya, O. A. and Pham, S. V. (1998). A Robust Torque and Drag Analysis Approach for Well Planning and Drillstring Design. *IADC/SPE Drilling Conference*. Dallas, Texas, USA.

Akinniranye, G., Megat, A., Elsweisy, H., Palacio, J., Poedjono, B. and Goobie, R. (2009). Implementation of a shock and Vibration Mitigation Process: Achieving Real-Time Solutions and Savings. *SPE Middle East Oil and Gas Show and Conference*, Bahrain.

Alfsen, T.E., Blikra, H. and Tjotta, H. (1993). Pushing the Limits for Extended-Reach Drilling, New World Record Well from Platform Statfjord C, Well C2. *SPE 26350 presented at the SPE Annual Technical Conference and Exhibition*, Houston.

Ali, A.A., Barton, S. and Mohanna, A. (2011). Unique Axial Oscillation Tool Enhances Performance of Directional Tools in Extended Reach Applications. *Presented at the Brasil Offshore Conference and Exhibition*, Macae, Brazil, June 14-17.

Allouche, E.N., Ariaratnam, S.T. and Lueke, J.S. (2000). Horizontal Directional Drilling: Profile of an Emerging Industry. *Journal of Construction Engineering and Management*.

Altamimi, I.M., Mokrani, S. and Zulfikaf, A.H. (2015). Axial Oscillation Tool Significantly Mitigates the Vibration Level and Enhances Drilling Performance in Conjunction with Standard RSS Systems. *Internation Petroleum Exhibition and Conference*, SPE, Abu Dhabi, UAE.

Amro, M.M. (2000). Causes and Remedies of Drillstring Failures While Drilling Medium radius Horizontal Wells (Field Study). *IADC/SPE Asia Pacific Drilling Technology*, Kuala Lumpur, Malaysia.

Bacarreza, L., Hornabrook, C., Khoo, C.C., Nevoy, H. and Japar N.J. (2008). The Snaking Wells in Champion West, Offshore Brunei. Best Practices for ERD Well Construction. *IADC/SPE Asia Pacific Drilling Technology Conference and Exhibition*, Jakarta, Indonesia.

Bailey, J. J., & Finnie, I. (1960). Analytical Study of Drill-string Vibration. *American Society of Mechanical Engineers -- Transactions -- Journal of Engineering for Industry Series B*, 82(2), 122–128.

Bailey, J.R., Biediger, A.O., Sundararaman, S., Carson, A.D., Elks, W.C. and Dupriest, F.E. (2008). Development and Application of a BHA Vibrations Model. *International Petroleum Technology Conference*, Kuala Lumpur, Malaysia.

Barton, S. and Lockley, R. (2008). Directional Success in the Canadian Rockies: Dynamic Tools Enable Accurate Comparison of Drill Bit Designs. *SPE Annual Technical Conference and Exhibition*, Denver, Colorado, USA.

Bert, D.R., Storaune, A. and Zheng, N. (2007). Case Study: Drillstring Failure Analysis and New Deep-Well Guidelines Lead to Success. *SPE Annual Technical Conference and Exhibition*, Anaheim, California, USA.

Breedveld, P.C. (1985). Proposition for an unambiguous vector bond graph notation. *Journal of Dynamic Systems, Measurement and Control*, Vol. 104, No. 3, pp. 267-270.

Breedveld, P. (2003). Bond Graphs. http://www-lar.deis.unibo.it/euron-geoplex-sumsch/files/ lectures_1/Breedveld/Breedveld_03_BGConcepts.pdf

Brett, J.F., Beckett, A.D., Holt, C.A. and Smith, D.L. (1989). Uses and Limitations of Drillstring Tension and Torque Models for Monitoring Hole Conditions. *SPE Drilling Engineering*.

Burgess, T.M., McDaniel, G.L. and Das, P.K. (1987). Improving BHA Tool Reliability with Drillstring Vibration Models: Field Experience and Limitations. *SPE/IADC Drilling Conference*, New Orleans, Louisiana, USA.

Canadian Association of Petroleum Producers (CAPP) (2012). Complied industry statistics 1981-2011. (http://www.capp.ca/).

Challamel, N., Sellami, H. and Chenevez, E. (2000). A stick-slip analysis based on rock/bit interaction: theoretical and experimental contribution. *In: Proceedings of the IADC/SPE#59230, SPE/IADC Conference*. New Orleans, Louisiana.

Chrisman, J., Orley, C., Hood, J., Stone, C., Leopold, N. and Taylor, R. (2012). Information from a Downhole Dynamics Tool Provides Real-Time Answers for Optimization While Drilling 10,000 ft Laterals in the Middle Bakken Formation of the Williston Basin. *SPE Annual Technical Conference and Exhibition*, San Antonio, Texas, USA.

Cook, R.L., Nicholson, J.W., Sheppard, M.C. and Westlake, W. (1989). First Real Time Measurements of Downhole Vibrations, Forces, and Pressures Used to Monitor Directional Drilling Operations. *SPE/IADC Drilling Conference*, New Orleans, Louisiana, USA.

D'Ambrosio, P., Bouska, R.R., Clarke, A., Laird, J., Mckay, J. and Edwards, S.T. (2012). Distributed Dynamics Feasibility Study. *IADC/SPE Drilling Conference and Exhibition*, San Diego, California, USA.

Dareing, D. W., & Livesay, B. J. (1968). Longitudinal and Angular Drill-string Vibrations with Damping. In ASME Meeting Pet-31, Sep 22-25 1968 (9). *American Society of Mechanical Engineers*. New York, NY, United States.

Downton, G., Klausen, T.S., Hendricks, A. and Pafitis, D. (2000). New Direction in Rotary Steerable Drilling. *Oilfield Review.*

Dunayevsky, V.A., Judzis, A. and Mills, W.H. (1985). Dynamic Stability of Drillstring under Fluctuating Weight-on-Bit. *Presented at the 60th Annual Technical Conference of the SPE*, Las Vegas, Nevada, USA.

Efteland, F., Coit, A.R. and McKenna, K.I. (2014). Surface Control Software Dramatically Mitigates Downhole Torsional Vibration in the Eagle Ford Shale Play as Validated by High-Speed Downhole Dynamics data. *SPE Annual Technical Conference and Exhibition*, Amsterdam, Netherlands.

Eronini, I.E. (1978). A Dynamic Model for Optimization and Control of Rock Drilling. *Ph.D. thesis*, University of California, Berkeley.

Gee, R., Hanley, C., Hussain, R., Canuel, L. and Martinez, J. (2015). Axial oscillation tools vs. lateral vibration tools for friction reduction What's the best way to shake the pipe, *SPE*, 173024 (2015).

Ghasemloonia, A., Rideout, D.G., Butt, S.D. (2013). Vibration analysis of a drillstring in vibration-assisted rotary drilling: finite element modeling with analytical validation. *ASME Journal of Energy Resources Technology*, Vol. 135, No. 3, 032902: 1-18.

Ghasemloonia, A., Rideout, D.G., Butt, S.D. (2015). A review of drillstring vibration modeling and suppression methods. *Journal of Petroleum Science and Engineering*, 131, pp. 150-164.

He, X., Halsey, G.W. and Kyllingstad, A. (1995). "Interactions between Torque and Helical Buckling in Drilling. *Annual Technical Conference & Exhibition*, Dallas, Texas.

Heisig, G. and Neubert, M. (2000). Lateral Drillstring Vibration in Extended-Reach Wells. *SPE/IADC Drilling Conference*, New Orleans, Louisiana, USA.

Ho, H.S. (1988). An Improved Modeling Program for Computing the Torque and Drag in Directional and Deep Wells. *SPE 18047 presented at the Annual Technical Conference and Exhibition*, Houston, Texas.

Hood, J.A., Leidland, B.T., Haldorsen, H. and Heisig, G. (2001). Aggressive Drilling Parameter Management Based on Downhole Vibration Diagnostics Boosts Drilling Performance in Difficult Formation. *SPE Annual Technical Conference and Exhibition*, New Orleans, Louisiana, USA.

Hutchinson, J.W. (2001). Shear coefficient for Timoshenko beam theory. *ASME Journal of Applied Mechanics*, Vol. 68, No. 1, pp. 87-92.

Jaggi, A., Upadhaya, S. and Chowdhury, A.R. (2007). Successful PDC/RSS Vibration Management Using Innovative Depth-of-Cut Control Technology: Panna Field, Offshore India. *SPE/IADC Drilling Conference*, Amsterdam, Netherlands.

Jansen, J.D. and Steen, L.V.D. (1995). Active damping of self excited torsional vibrations in oil well drillstrings. *Journal of Sound and Vibration*. 179(4), 647–668.

Janwadkar, S.S., Fortenberry, D.G., Robert, G.K., Kramer, M., Trichel, D.K., Rogers, T., Privott, S.A., Welch, B. and Isbell, M.R. (2006). BHA and Drillstring Maximizes Drilling Performance in Lateral Wells of Barnett Shale Gas Field on N. Texas. *SPE Gas Technology Symposium*, Calgery, Alberta, Canada.

Jardine, S., Malone, D. and Sheppard, M. (1994). Putting a Damper on Drilling's Bad Vibration, *Oilfield Review*.

Jerez, H. and Tilley, J. (2014). Advancements in Powered Rotary Steerable Technologies Result in Record-Breaking Runs. *SPE Latin American and Caribbean Petroleum Engineering Conference*, Maracaibo, Venezuela.

Johancsik, C.A., Friesen, D.B. and Dawson, R. (1984). Torque and Drag in Directional Wells- Prediction and Measurement, *Journal of Petroleum Technology*.

Karnopp, D. (1985). Computer Simulation of Stick-slip Friction in Mechanical Dynamic Systems. *ASME Journal of Dynamic Systems, Measurement and Control*, V. 107(1), pp. 647-668.

Karnopp, D. C., Margolis, D. L. and Rosenberg, R. C. (1990). System Dynamics: A Unified Approach, Wiley, New York.

Karnopp, D. C., Margolis, D. L. and Rosenberg, R. C. (1999). System Dynamics; Modeling and Simulation of Mechatronics Systems, 3rd edition, John Wiley & Sons, Inc., New York.

Karnoop, D.C., Margolis, D.L., Rosenberg, R.C. (2006). System Dynamics; Modeling and Simulation of Mechatronics Systems, 4th edition, John Wiley & Sons, Inc., New York, USA.

Karnopp, D.C. (2003). Understanding Induction Motor State Equations Using Bond Graphs. *International Conference on Bond Graph Modeling and Simulation*, Orlando, Florida.

Khulief, Y.A. and Al-Naser, H. (2005). Finite Element Dynamic Analysis of Drillstrings. Finite Elements in Analysis and Design, 41(13), 1270-1288.

Khulief, Y.A., Al-Sulaiman, F.A. and Bashmal, S. (2007). Vibration Analysis of Drillstrings with Self –excited Stick-slip Oscillations. *Journal of Sound and Vibration*, 299(3), 540-558.

Kyllingstad, A., & Halsey, G.W. (1988). A Study of Slip/Stick Motion of the Bit. *SPE Drilling Engineering*, 3(4).

Leine, R.I. (2000). Bifurcations in discontinuous mechanical systems of Filippov-type. *Ph.D. thesis*, Technical University of Eindhoven, Netherland.

Leine, R.I., Campen, D.H.V. and Keultjes, W.J.G. (2002). Stick-slip Whirl Interaction in Drillstring Dynamics. *Journal of Vibration and Acoustics*, Transections of the ASME, 124(2), 209-220.

Lenamond, C., Marques, L., Anderson, M. and Mota, S. (2005). *AADE National Technical Conference and Exhibition*, Houston, Texas, USA.

Lesage, M., Falconer, I.G. and Wick, C.J. (1988). Evaluating Drilling Practice in Deviated Wells with Torque and Weight Data. *SPE Drilling Engineering*.

Lesso, W.G., Mullens, E. and Daudey, J. (1989). Developing a Platform Strategy and Predicting Torque Losses for Modeled Directional Wells in the Amauligak Field of the Beaufort Sea. Canada. *SPE 19550 presented at the Annual Technical Conference and Exhibition*, San Antonio, Texas.

Lesso, B., Ignova, M., Zeineddine, F., Burks, J. and Welch, B. (2011). Testing the Combination of High Frequency Surface and Downhole Drilling Mechanics and Dynamics Data under a Variety of Drilling Conditions. *SPE/IADC Drilling Conference and Exhibition*, Amsterdam, Netherlands.

Lopez, E.M.N. (2010). Bit-sticking Phenomena in a Multidegree of Freedom Controlled Drillstring. *Drilling and Well Technology*, UK.

Luke, G.R. and Juvkam-Wold, H.C. (1993). Determination of True Hook Load and Line Tension under Dynamic Conditions. *SPE Drilling & completion*.

Macdonald, K.A., Bjune, J.V. (2007). Failure analysis of drillstrings. *Engineering Failure Analysis*, 14:1614-1666.

Maidla, E.E. and Wojtanowicz, A.K. (1987 a). Field Comparison of 2-D and 3-D Methods for the Borehole FrictionEvaluation in Directional Wells. *SPE 16663 presented at the Annual Technical Conference and Exhibition*, Dallas, Texas.

Maidla, E.E. and Wojtanowicz, A.K. (1987 b). Field Method of Assessing Borehole Friction for Directional Well Casing. *SPE 15696 presented at the Middle East Oil Show*, Manama, Bahrain.

Mantle, K. (2014). The Art of Controlling Wellbore Trajectory. *Oilfield review*, Schlumberger.

Margolis, D. (2004). Fixed causality slip-stick friction models for use in simulation of non-linear systems. *Journal of Systems and Control Engineering*, V. 216, part I.

McCormick, J. and Liu, G. (2012). Torque and Drag Modeling Advanced Techniques and Troubleshooting. *SPE Annual Technical Conference and Exhibition*, San Antonio, Texas, USA.

Millheim, K.K. and Apostal, M.C. (1981). The Effect of Bottomhole Assembly Dynamics on the Trajectory of a Bit. *Journal of Petroleum Technology*, S. 2323-2338.

Miraj, S.A., Kaarstad, E. and Aadnoy, B.S. (2011). Improvement of Torque-and-Drag Modeling in Long-Reach Wells. *Journal of Modern Applied Science, Published by Canadian Center of Science and Education*.

Navarro-Lopez, E.M. and Cortes, D. (2007). Avoiding Harmful Oscillations in a Drillstring through Dynamical Analysis. *Journal of Sound and Vibrations*. 307,152–171.

Opeyemi, A. A. and Pham, S.V. (1998). A Robust Torque and Drag Analysis Approach for Well Planning and Drill string Design. *SPE/IADC 39321 presented at SPE/IADC Drilling Conference*, Dallas, Texas, USA.

Ozpineci, B. and Tolbert, L.M. (2003). Simulink Implementation of Induction Machine Model – A Modular Approach. *IEEE*, pp 728-734.

Payne, M. L. and Abbassian, F. (1996). Advanced Torque-and-Drag Considerations in Extended-Reach Wells. *SPE Drilling and Completion*.

Pegasus Vertex, Inc. (2014). Torque and Drag: Concepts that Every Drilling and Completion Engineer Should Know.

Perreau, P.J., Rey-Fabret, I.F., Gomel, M.M. and Mabile, M.C. (1998). New Results in Real Time Prediction. *International Petroleum Exhibition and Conference*, Abu Dhabi, U.A.E.

Pogorelov, D., Mikheev, G., Lysikov, N., Ring, L., Gandikota, R., Abedrabbo, N. (2012). A multibody system approach to drill string dynamics modeling. *Presented at the ASME 2012 11th Biennial Conference on Engineering Systems Design and Analysis* (ESDA2012), Nantes, France, July 2-4.

Raap, C., Craig, A.D. and Graham, R. (2012). Drillpipe-Dynamics Measurements-Insight into Drillstring Dysfunctions. *SPE Annual Technical Conference and Exhibition*, Denver, Colorado, USA.

Rajnauth, J. and Jagai, T. (2012). Reduce Torsional Vibration and Improve Drilling Operations. *International Journal of Applied Science and Technology*, Vol. 2, No. 7.

Reiber, F., Vos, B. E. and Eide, S.E. (1999). On-Line Torque and Drag: A Real – Time Drilling Performance Optimization Tool. *SPE/IADC 52836 presented at the SPE/IADC Drilling Conference*, Amsterdam, Netherlands.

Richard, T., Germay, C. and Detournay, E. (2004). Self-excited Stick-slip Oscillations of Drill bits. *Mecanique* 332, 619–626.

Rideout, D.G., Stein, J.L. and Louca, L.S. (2008). Systematic Assessment of Rigid Internal Combustion Engine Dynamic Coupling. *Journal of Engineering for Gas Turbines and Power*, ASME, Vol. 130.

Rideout, D.G., Arvani, F., Butt, S.D. and Fallahi, E. (2013). Three-Dimensional Multi-Body Bond Graph Model for Vibration Control of Long Shafts-Application to Oilwell Drilling. *Integrated Modeling and Analysis in Applied Control and Automation*, Athens, Greece.

Rideout, D.G., Ghasemloonia, A., Arvani, F., Butt, S.D., 2015. An intuitive and efficient approach to integrated modeling and control of three-dimensional vibration in long shaft. *International Journal of Simulation and Process Modeling*, Vol. 10, No. 2, pp. 163-178.

Rubin, M.B., 2000. Cosserat Theories: Shell, Rods and Points. *Springer Netherlands*, August 31.

Ryan Directional Services, 2012. Personal communication with Ryan Directional Services, Calgery, AB.

Sack, J.,2011. A Case Study: Extended-Reach Laterals in the Denver-Julesburg Basin. Halliburton, *www.halliburton.com*.

Samantaray, A.K. (2006). About Bond Graphs – The System Modeling World.

Sampaio, R., Piovan, M.T. and Lozano, G.V. (2007). Coupled axial torsional vibrations of drillstring by means of nonlinear model. *Journal of Mechanics Research Communications*. 34, 497–502.

Samuel, R. and Yao, D. (2010). Vibration Analysis and Control with Hole-Enlarging Tools. *SPE Annual Technical Conference and Exhibition*, Florence, Italy.

Sarker, M., Rideout, D.G. and Butt, S.D. (2012a). Dynamic Model of an Oilwell Drillstring with Stick-slip and Bit-bounce Interaction. *10th International Conference on Bond Graph Modeling and Simulation*, Genoa, Italy.

Sarker, M., Rideout, D.G. and Butt, S.D. (2012b). Advantages of an LQR Controller for Stick-slip and Bit-bounce Mitigation in an Oilwell Drillstring. *International Mechanical Engineering Congress and Exposition*, Houston, TX, USA.

Sarker, M. (2012). Modelling, Simulation and Control of Stick-slip and Bit-bounce Vibration in an Oilwell Drillstring. *M.Eng. Thesis*, Memorial University of Newfoundland, Canada.

Sarker, M., Rideout, D.G., Butt, S.D. (2014). Dynamic modeling of horizontal shafts with annular surface contact and friction – application to oilwell drilling. *Presented at ASME International Mechanical Engineering Congress and Exposition*, Montreal, Quebec, Canada, November 14-20.

Sheppard, M.C., Wick, C. and Burgess, T. (1987). Designing Well Paths to Reduce Drag and Torque. SPE Drilling Enginering, pp. 344-350.

Skyles, L.P. and Amiraslani, Y.A. (2012). Converting Static Friction to Kinetic Friction to Drill Further and Faster in Directional Holes. *Presented at IADC/SPE Drilling Conference and Exhibition*, San Diego, California, USA, 6-8 March.

Sonowal, K., Bennetzen, B., Wong, P. and Isevcan, E. (2009). How Continuous Improvement Lead to the Longest Horizontal Well in the World. *SPE/IADC Drilling Conference and Exhibition*, Amsterdam, Netherlands.

Spanos, P.D., Chevallier, A.M., Politis, N.P., Payne, M.L. (2003). Oil and gas well drilling: a vibrations perspective. *Shock Vibration Digest*, 35(2): 85-103.

Sugiura, J. and Jones, S. (2007). Real-Time Stick-Slip and Vibration Detection for 8 1/2 in Hole-Size Rotary Steerable Tools in Deeper Wells and More Aggressive Drilling. *AADE National Technical Conference and Exhibition*, Houston, Texas, USA.

Sugiura, J. (2008). The Use of the Near-bit Vibration Sensor While Drilling Leads to Optimized Rotary-Steerable Drilling in Push-and Point-the-Bit Configurations. *SPE Asia Pacific Oil and Gas Conference and Exhibition*, Perth, Australia.

Tveitdal, T. (2011). Torque and Drag analysis of North Sea Wells Using New 3D Model. *Master's Thesis*, Faculty of Science and Technology, University of Stavanger, Stavanger, Norway.

Tucker, R.W. and Wang, C. (1999). An Integrated Model for Drill-string Dynamics. *Journal of Sound and Vibration*, 224(1), 123-165.

Wicks, N., Pabon, J. and Zheng, A. (2014). Modeling and Field Trials of the Effective Tractoring Force of Axial Vibration Tools. *Presented at the SPE Deepwater Drilling and Completions held in Galveston*, Texas, USA, September 10-11.

Wilson, T.P. and Yalcin, O. (1992). Two Double Azimuth-Double S-Shaped Wells Planned and Drilled Using Torque and Drag Modeling. *SPE/IADC 23848 presented at the SPE/IADC Drilling Conference*, New Orleans, Louisiana.

Wright, J., Borri, L., Simeone, D., Longo, J. and Weber, M. (2014). Nikaitchuq Project Vibration Mitigation Strategy. *SPE Western North American and Rocky Mountain Joint Regional Meeting*, Denver, Colorado, USA.

Yigit, A.S. and Christoforou, A.P. (2000). Coupled Torsional and Bending Vibrations of Actively Controlled Drillstring. *Journal of Sound and Vibration*, 234(1), 67-83.

Yigit, A.S. and Christoforou, A.P. (2006). Stick-slip and Bit-bounce Interaction in Oil-well Drillstrings. *Journal of Energy Resources Technology*, 128(4), 268-274.

Zamanian, M., Khadem, S.E. and Ghazavi, M.R. (2007). Stick-slip oscillations of drag bits by considering damping of drilling mud and active damping system. Journal of Petroleum Science Engineering. 59(3–4), 289–299.

Zare, J., Hashemi, S.J. and Rashed, G. (2011). Finite element analysis of drillstring lateral vibration. *Scientific Research and Essays*, Vol. 6(13), pp. 2682-2694.

Appendix A

Well information

Oil Company: Canadian Natural Resources Ltd.
Well: CNRL HZ Septimus C9-21-81-19
LSD: 09-21-081-19W6M
Rig: Precision Drilling Rig # 322

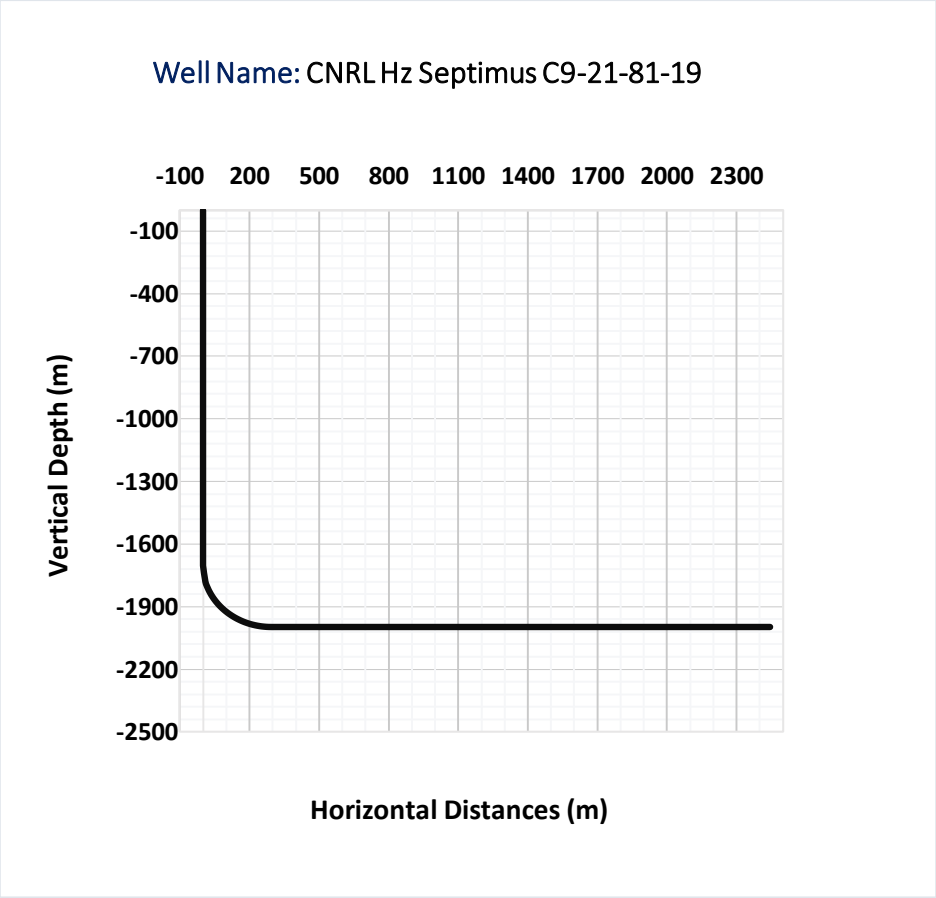

Figure A.1: Sketch of well profile

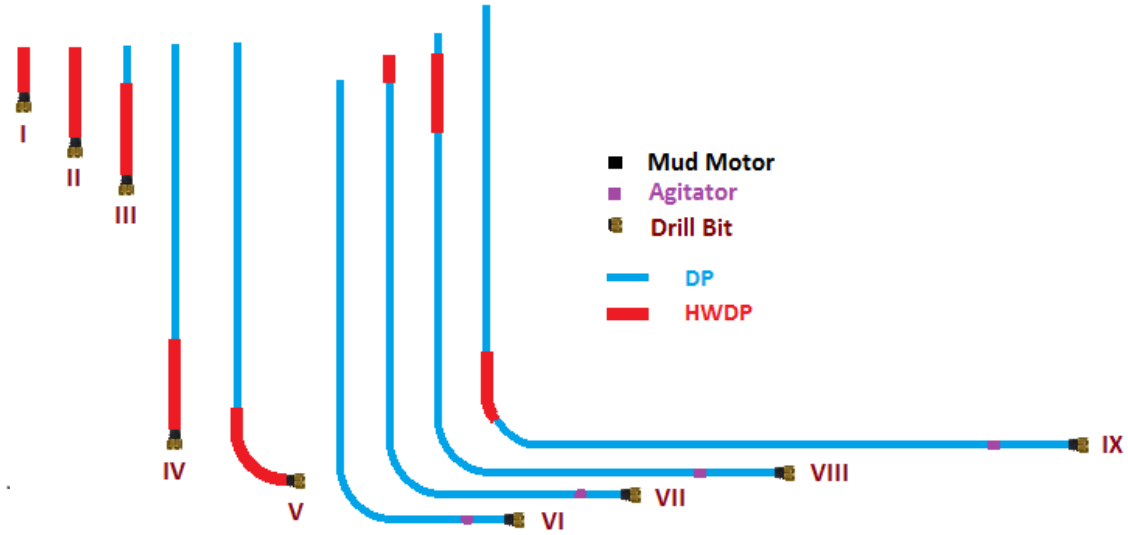

Figure A.2: Drillstring configurations in different depths.

Table A.1: Drillstring configuration chart

No.	Configurations
I (MD = 200m)	Bit + Motor + HWDP(200m)
II (MD = 620m)	Bit + Motor + HWDP(620m)
III (MD = 720m)	Bit + Motor + HWDP(620m) + DP (100m)
IV (MD = 1720m)	Bit + Motor + HWDP(620m) + DP (1100m)
V (MD = 2180m)	Bit + Motor + HWDP(620m) + DP (1560m)
VI (MD = 2300m)	Bit + Motor + Collar (50) + DP (300m) + Agitator + DP(1950m)
VII (MD = 2556m)	Bit + Motor + Collar (50) + DP (300m) + Agitator + DP(2113m) + HWDP(93m)
VIII (MD = 3062m)	Bit + Motor + Collar (50) + DP (300m) + Agitator + DP(2113m) + HWDP(561m) + DP(38m)
IX (MD = 4340m)	Bit + Motor + Collar (50) + DP (600m) + Agitator + DP(1819m) + HWDP(561m) + DP(1310m)

Appendix B

Simulation data

Table B.1: Data used in rotary drilling simulation.

Parameters	Values	Parameters	Values
Drillstring data		Surface elevation amplitude, s_0	0.001 m
Cable and derrick spring constant	9.3×10^{6} N/m	Bit factor, b	1
Swivel and derrick mass	7031 kg	Cutting coefficient ξ, C_1, C_2	1, 1.35×10^{-8}, -1.9×10^{-4}
Kelly length	15 m	Frictional coefficient μ_0, α,β, γ & ν	0.06, 2, 1, 1 & 0.01
Kelly outer diameter	0.379 m	Threshold force, W_{fs}	10000 N
Kelly inner diameter	0.0825 m	***Hydraulic data***	
DP outer diameter	0.101 m (4 in)	Mud fluid density, ρ_m	1198 kg/m^3
DP inner diameter	0.0848 m (3.34 in)	Mud flow rate, Q	$Q_m + Q_a \sin(qt)$ m^3/s
HWDP outer diameter	0.171 m (6.75 in)	Mean mud flow rate, Q_m	0.022 m^3/s
HWDP inner diameter	0.0571 m (2.25 in)	Mud flow pulsation amplitude, Q_a	0.002 m^3/s
SUB outer diameter	0.136 m (5.354 in)	Freq. of variation in mud flowrate, q	25.13 rad/s
SUB inner diameter	0.057 m (2.244 in)	Equivalent fluid viscosity for fluid resistance to rotation μ_e	30×10^{-3} Pa-s
Collar outer diameter	0.125 m (4.921 in)	Weisbach friction factor outside drill pipe or collar, α_a	0.017
Collar inner diameter	0.06 m (2.362 in)	Weisbach friction factor inside drill pipe or collar, α_p	0.017
Motor HS outer diameter	0.121 m (4.763 in)	***Motor data***	
Motor HS inner diameter	0.0 m (0.0 in)	V, f, P	2300 V, 377 rad/s, 4 pole
Drillstring material	Steel	L_{ls}, L_{lr}	0.0032 H, 0.0032 H
Wellbore diameter	0.18 m (7.086 in)	L_m	0.14329 H
Drill bit-rock data		R_s, R_r	0.262, 0.187
Bit type	PDC (Single cutter)	J_m, R_m	11.06 kg-m^2 , 0.05 Ω
Drill bit diameter	0.159 m (6.259 in)		
Drill bit mass	65 kg		
Rock stiffness	1.16×10^{9} N/m		
Rock damping	1.50×10^{5} N-s/m		

Appendix C

20Sim® model programming codes

Material properties

```
parameters
    real e = 211000000000;          // modulus of elasticity, N/m2
    real g = 80e9;                  // shear modulus, Pa
    real steel_density = 7860;      // steel density, kg/m3
    real Nu = 0.3;                  // poisson ratio
variables
    real global rho;
    real global E;
    real global G;
    real global nu;
equations
    rho = steel_density;
    E = e;
    G = g;
    nu = Nu;
```

Mud fluid properties

```
parameters
    real mud_rho = 1200;                    // mud density kg/m3
    real Friction_factor_outer = 0.017;     // weisbach friction factor outside drii pipe or collar
    real Friction_factotor_inner = 0.017;   // weisbach friction factor inside drii pipe or collar
variables
    real global mud_density;
    real global friction_factor_outer;
    real global friction_factor_inner;
equations
    mud_density = mud_rho;
    friction_factor_outer = Friction_factor_outer;
    friction_factor_inner = Friction_factotor_inner;
```

Mud flow rate

```
parameters
    real Qm = 0.022;            // mean mud flow rate,
    real Qa = 0.002;            // mud flow pulsation amplitude,
    real q = 25.13 {rad/s};     // frequency of variations in mud flowrate
variables
    boolean hidden change;
    real hidden half;
    real global Q;              // Volume rate of flow of drilling mud'
```

```
equations
    "calculate at least 2 points per cycle to get a triangle"
    half = pi / q;
    change = frequencyevent (half, half / 2);

    "calculate the sine wave"
    Q = Qm + Qa * sin ( q * time);
```

Induction motor constant

```
parameters
    real Voltage = 2300;                // volt
    real frequency = 377;
    real pole = 2;                      // 4 pole i.e two pairs
    real L_ls = 0.003199;               // output value unit H, hp
    real L_m = 0.14329;
    real L_lr = 0.003199;
    real R_s = 0.262;
    real R_r = 0.187;
    real J_m = 11.06;                   // kg.m^2
    real R_m = 0.05;                    // N.m.s
    real desire_speed = 5.2;
variables
    real global V;
    real global f;
    real global Lls;
    real global Lm;
    real global Ls;
    real global Llr;
    real global Lr;
    real global Rs;
    real global Rr;
    real global P;
    real global Jm;
    real global Rm;
    real global gear_ratio;
equations
    V = Voltage;
    f = frequency;
    P = pole;
    Lls = L_ls;
    Lm = L_m;
    Ls = Lls + Lm;
    Lr = Llr + Lm;
    Llr = L_lr;
    Rs = R_s;
    Rr = R_r;
    Jm = J_m;
    Rm = R_m;

    gear_ratio = 188.4/desire_speed;
```

Rock-bit constant

```
parameters
    real r = 0.0795;              // bit radius
    real zeta = 1;                //parameters
    real c1 =  0.5e-08;           //parameters
    real c2 = -1.9e-04;           //parameters
    real alpha = 2;               //parameters
    real beta = 1;                //parameters
    real gama = 1;                //parameters
    real munot = 0.06;            //parameters
    real nu = 0.01;               //parameters
    real Kc = 1.16e09;            // Berea Sandstone rock stiffness N.m
    real R = 1.5e05;
    real bit_mass = 65;
    real bit_flow_area = 2.3865e-04;
variables
    real global bit_radius;
    real global Zeta;
    real global C1;
    real global C2;
    real global Alpha;
    real global Beta;
    real global Gama;
    real global Munot;
  real global Nu;
    real global rock_compliance;
    real global rock_damping;
    real global Bit_Mass;
    real global Bit_Inertia;
    real global bit_nozzle_radius;
equations
    bit_radius = r;
    Zeta = zeta;
    C1 = c1;
    C2 = c2;
    Alpha= alpha;
    Beta = beta;
    Gama = gama;
    Munot = munot;
    Nu = nu;
    rock_compliance = 1/Kc;
    rock_damping = R;
    Bit_Mass = bit_mass;
    Bit_Inertia = 0.5 * Bit_Mass * bit_radius^2;
    bit_nozzle_radius = (bit_flow_area/3.14159)^0.5;
```

Bouyancy factor

```
parameters
    real bouyancy_fac = 0.85;          // wellbore radius, m
variables
    real global BF;
```

```
equations
    BF = bouyancy_fac;
```

Wellbore size

```
parameters
    real r_w = 0.10;                // wellbore radius, m
variables
    real global wellbore_radius;
equations
    wellbore_radius = r_w;
```

Drillstring dimensions

```
parameters
    //Kelly
    real kelly_oD = 0.101;
    real kelly_iD = 0.082;
    real kelly_mat_Damp = 2000;     // material damping, Axial per unit length
    real kelly_mat_tor_Damp = 100;  // material damping, torsional
    //DP
    real DP_OD = 0.101;
    real DP_ID   = 0.082;
    real DP_mat_Damp = 2000;     // material damping
    real DP_mat_tor_Damp = 100;  // material damping, torsional
    //HWDP
    real HWDP_OD = 0.132;
    real HWDP_ID    = 0.060;
    real HWDP_mat_Damp = 3000;     // material damping
    real HWDP_mat_tor_Damp = 150;  // material damping, torsional
    real Torsion_viscosity_resis = 30e-03;    // equivalent viscosity  for fluid resistance to rotation, pa.sec
variables
    // Kelly
    real global kelly_OD;
    real global kelly_ID;
    real global kelly_area_inertia;
    real global kelly_area;
    real global kelly_Mat_damp;
    real global kelly_Mat_tor_damp;
    //DP
    real global dp_OD;
    real global dp_ID;
    real global DP_area_inertia;
    real global DP_area;
    real global dp_Mat_damp;
    real global dp_Mat_tor_damp;
    //HWDP
    real global hwdp_OD;
    real global hwdp_ID;
    real global HWDP_area_inertia;
    real global HWDP_area;
    real global hwdp_Mat_damp;
```

```
    real global hwdp_Mat_tor_damp;
    real global torsion_viscosity_resis;
equations
    // Kelly
    kelly_OD = kelly_oD;
    kelly_ID = kelly_iD;
    kelly_area = 3.1416*((kelly_OD/2)^2 - (kelly_ID/2)^2);
    kelly_area_inertia = 0.5 * 3.1416* ((kelly_OD/2)^4 - (kelly_ID/2)^4);
    kelly_Mat_damp = kelly_mat_Damp;
    kelly_Mat_tor_damp = kelly_mat_tor_Damp;
    // DP
    dp_OD = DP_OD;
    dp_ID = DP_ID;
    DP_area = 3.1416*((dp_OD/2)^2 - (dp_ID/2)^2);
    DP_area_inertia = 0.5 * 3.1416* ((dp_OD/2)^4 - (dp_ID/2)^4);
    dp_Mat_damp = DP_mat_Damp;
    dp_Mat_tor_damp = DP_mat_tor_Damp;
    // HWDP
    hwdp_OD = HWDP_OD;
    hwdp_ID = HWDP_ID;
    HWDP_area = 3.1416*((hwdp_OD/2)^2 - (hwdp_ID/2)^2);
    HWDP_area_inertia = 0.5 * 3.1416* ((hwdp_OD/2)^4 - (hwdp_ID/2)^4);
    hwdp_Mat_damp = HWDP_mat_Damp;
    hwdp_Mat_tor_damp = HWDP_mat_tor_Damp;
    torsion_viscosity_resis = Torsion_viscosity_resis;
```

Vertical drillstring portion constants

```
parameters
    // kelly
    real kelly_L = 10;                  // length of kelly, m
    real Kelly_n = 1;                           // number of segments for kelly
    // DP
    real dp1_L = 1300;              // length of drillpipe, m
    real dp1_n = 6;             // number of segments for drillpipe
    //HWDP
    real hwdp1_L = 390;             // Straight section length of HWDP, m
    real hwdp1_n = 3;               // number of segments for straight HWDP
variables
    real global rho;
    real global E;
    real global G;
    // Kelly
    real global kelly_n;
    real global kelly_delx;
    real global kelly_OD;
    real global kelly_ID;
    real global kelly_area_inertia;
    real global kelly_area;
    real global kelly_Mat_damp;         // material damping per unit length
    real global kelly_Mat_tor_damp;     // material damping per unit length
    real global kelly_mass_inertia;
    real global kelly_torsion_comp;
```

```
    real global kelly_mass;
    real global kelly_axial_comp;
    real global kelly_mat_damp;
    real global kelly_mat_tor_damp;
    // DP
    real global DP1_L;
    real global DP1_n;
    real global DP1_delx;
    real global dp_OD;
    real global dp_ID;
    real global DP_area_inertia;
    real global DP_area;
    real global dp_Mat_damp;        // material damping per unit length
    real global dp_Mat_tor_damp;    // material damping per unit length
    real global DP1_mass_inertia;
    real global DP1_torsion_comp;
    real global DP1_torsion_fluid_resis;
    real global DP1_mass;
    real global DP1_axial_comp;
    real global DP1_mat_damp;
    real global DP1_mat_tor_damp;
    // HWDP
    real global HWDP1_L;    // Straight section
    real global HWDP1_n;
    real global HWDP1_delx;
    real global hwdp_OD;
    real global hwdp_ID;
    real global HWDP_area_inertia;
    real global HWDP_area;
    real global hwdp_Mat_damp;      // material damping per unit length
    real global hwdp_Mat_tor_damp;  // material damping per unit length
    real global HWDP1_mass_inertia;
    real global HWDP1_torsion_comp;
    real global HWDP1_torsion_fluid_resis;
    real global HWDP1_mass;
    real global HWDP1_axial_comp;
    real global HWDP1_mat_damp;
    real global HWDP1_mat_tor_damp;
    real global torsion_viscosity_resis;
    real global wellbore_radius;
equations
    // Kelly
    kelly_n = Kelly_n;
    kelly_delx = kelly_L / kelly_n;
    kelly_mass_inertia = 0.5 * rho * kelly_area * kelly_delx * ((kelly_OD/2)^2 + (kelly_ID/2)^2);
    kelly_torsion_comp = kelly_delx/(G*kelly_area_inertia);
    kelly_mass = rho * kelly_area * kelly_delx;
    kelly_axial_comp = kelly_delx/(E * kelly_area);
    kelly_mat_damp = kelly_Mat_damp*kelly_delx;
    kelly_mat_tor_damp = kelly_Mat_tor_damp*kelly_delx;
    // DP
    DP1_L = dp1_L;
    DP1_n = dp1_n;
```

```
DP1_delx = dp1_L / dp1_n;
DP1_mass_inertia = 0.5 * rho * DP_area * DP1_delx * ((dp_OD/2)^2 + (dp_ID/2)^2);
DP1_torsion_comp = DP1_delx/(G*DP_area_inertia);
DP1_torsion_fluid_resis = (2*3.1416* torsion_viscosity_resis * (dp_OD/2)^3 /(wellbore_radius - (dp_OD/2)))* DP1_delx;
DP1_mass = rho * DP_area * DP1_delx;
DP1_axial_comp = DP1_delx/(E * DP_area);
DP1_mat_damp = dp_Mat_damp*DP1_delx;          // axial model
DP1_mat_tor_damp = dp_Mat_tor_damp*DP1_delx;
// HWDP
HWDP1_L = hwdp1_L;
HWDP1_n = hwdp1_n;
HWDP1_delx = hwdp1_L / hwdp1_n;
HWDP1_mass_inertia = 0.5 * rho * HWDP_area * HWDP1_delx * ((hwdp_OD/2)^2 + (hwdp_ID/2)^2);
HWDP1_torsion_comp = HWDP1_delx/(G*HWDP_area_inertia);
HWDP1_torsion_fluid_resis = (2*3.1416* torsion_viscosity_resis * (hwdp_OD/2)^3 /(wellbore_radius - (hwdp_OD/2)))* HWDP1_delx;
HWDP1_mass = rho * HWDP_area * HWDP1_delx;
HWDP1_axial_comp = HWDP1_delx/(E * HWDP_area);
HWDP1_mat_damp = hwdp_Mat_damp*HWDP1_delx;          // axial model
HWDP1_mat_tor_damp = hwdp_Mat_tor_damp*HWDP1_delx;
```

Curved drillstring portion constants

```
parameters
    // DP
    // Curved Section
    real dp2_L = 289;                  // length of drillpipe, m
    real dp2_n = 13;               // number of segments for drillpipe
    //HWDP
    real hwdp2_L = 171;                // Curved section length of HWDP, m
    real hwdp2_n = 7;                  // number of segments for curved HWDP
variables
    real global rho;
    real global E;
    real global G;
    // DP
    real global DP2_L;
    real global DP2_n;
    real global DP2_delx;
    real global dp_OD;
    real global dp_ID;
    real global DP_area_inertia;
    real global DP_area;
    real global dp_Mat_damp;        // material damping per unit length
    real global dp_Mat_tor_damp;    // material damping per unit length

    real global DP2_mass_inertia;
    real global DP2_torsion_comp;
    real global DP2_torsion_fluid_resis;
    real global DP2_mass;
```

```
    real global DP2_axial_comp;
    real global DP2_mat_damp;
    real global DP2_mat_tor_damp;
    // HWDP
    real global HWDP2_L;    // Curved Section
    real global HWDP2_n;
    real global HWDP2_delx;
    real global hwdp_OD;
    real global hwdp_ID;
    real global HWDP_area_inertia;
    real global HWDP_area;
    real global hwdp_Mat_damp;      // material damping per unit length
    real global hwdp_Mat_tor_damp;  // material damping per unit length
    real global HWDP2_mass_inertia;
    real global HWDP2_torsion_comp;
    real global HWDP2_torsion_fluid_resis;
    real global HWDP2_mass;
    real global HWDP2_axial_comp;
    real global HWDP2_mat_damp;
    real global HWDP2_mat_tor_damp;
    real global torsion_viscosity_resis;
    real global wellbore_radius;
equations
    // DP
    DP2_L = dp2_L;
    DP2_n = dp2_n;
    DP2_delx = dp2_L / dp2_n;
    DP2_mass_inertia = 0.5 * rho * DP_area * DP2_delx * ((dp_OD/2)^2 + (dp_ID/2)^2);
    DP2_torsion_comp = DP2_delx/(G*DP_area_inertia);
    DP2_torsion_fluid_resis = (2*3.1416* torsion_viscosity_resis * (dp_OD/2)^3 /(wellbore_radius -
(dp_OD/2)))* DP2_delx;
    DP2_mass = rho * DP_area * DP2_delx;
    DP2_axial_comp = DP2_delx/(E * DP_area);
    DP2_mat_damp = dp_Mat_damp*DP2_delx;          // axial model
    DP2_mat_tor_damp = dp_Mat_tor_damp*DP2_delx;
    // HWDP
    HWDP2_L = hwdp2_L;
    HWDP2_n = hwdp2_n;
    HWDP2_delx = hwdp2_L / hwdp2_n;
    HWDP2_mass_inertia = 0.5 * rho * HWDP_area * HWDP2_delx * ((hwdp_OD/2)^2 +
(hwdp_ID/2)^2);
    HWDP2_torsion_comp = HWDP2_delx/(G*HWDP_area_inertia);
    HWDP2_torsion_fluid_resis = (2*3.1416* torsion_viscosity_resis * (hwdp_OD/2)^3 /(wellbore_radius
- (hwdp_OD/2)))* HWDP2_delx;
    HWDP2_mass = rho * HWDP_area * HWDP2_delx;
    HWDP2_axial_comp = HWDP2_delx/(E * HWDP_area);
    HWDP2_mat_damp = hwdp_Mat_damp*HWDP2_delx;          // axial model
    HWDP2_mat_tor_damp = hwdp_Mat_tor_damp*HWDP2_delx;
```

Horizontal drillstring portion constants

```
parameters
    // DP
```

```
    // Horizontal section
    real dp3_L = 1520;              // length of drillpipe, m, Before agitator
    real dp3_n = 15;            // number of segments for drillpipe, Before agitator
    real dp4_L = 600;               // length of drillpipe, m, After agitator
    real dp4_n = 6;             // number of segments for drillpipe, After agitator
variables
    real global rho;
    real global E;
    real global G;
    // DP
    real global DP3_L;
    real global DP3_n;
    real global DP3_delx;
    real global DP4_L;
    real global DP4_n;
    real global DP4_delx;
    real global dp_OD;
    real global dp_ID;
    real global DP_area_inertia;
    real global DP_area;
    real global dp_Mat_damp;        // material damping per unit length
    real global dp_Mat_tor_damp;    // material damping per unit length
    real global DP3_mass_inertia;
    real global DP3_torsion_comp;
    real global DP3_torsion_fluid_resis;
    real global DP3_mass;
    real global DP3_axial_comp;
    real global DP3_mat_damp;
    real global DP4_mass_inertia;
    real global DP4_torsion_comp;
    real global DP4_torsion_fluid_resis;
    real global DP4_mass;
    real global DP4_axial_comp;
    real global DP4_mat_damp;
    real global DP1_mat_tor_damp;
    real global DP2_mat_tor_damp;
    real global DP3_mat_tor_damp;
    real global DP4_mat_tor_damp;
    real global torsion_viscosity_resis;
    real global wellbore_radius;
equations
    // DP
    DP3_L = dp3_L;
    DP4_L = dp4_L;

    DP3_n = dp3_n;
    DP4_n = dp4_n;
    DP3_delx = dp3_L / dp3_n;
    DP4_delx = dp4_L / dp4_n;
    DP3_mass_inertia = 0.5 * rho * DP_area * DP3_delx * ((dp_OD/2)^2 + (dp_ID/2)^2);
    DP4_mass_inertia = 0.5 * rho * DP_area * DP4_delx * ((dp_OD/2)^2 + (dp_ID/2)^2);
    DP3_torsion_comp = DP3_delx/(G*DP_area_inertia);
    DP4_torsion_comp = DP4_delx/(G*DP_area_inertia);
```

```
    DP3_torsion_fluid_resis = (2*3.1416* torsion_viscosity_resis * (dp_OD/2)^3 /(wellbore_radius -
(dp_OD/2)))* DP3_delx;
    DP4_torsion_fluid_resis = (2*3.1416* torsion_viscosity_resis * (dp_OD/2)^3 /(wellbore_radius -
(dp_OD/2)))* DP4_delx;
    DP3_mass = rho * DP_area * DP3_delx;
    DP4_mass = rho * DP_area * DP4_delx;
    DP3_axial_comp = DP3_delx/(E * DP_area);
  DP4_axial_comp = DP4_delx/(E * DP_area);
    DP3_mat_damp = dp_Mat_damp*DP3_delx;          // axial model
    DP4_mat_damp = dp_Mat_damp*DP4_delx;          // axial model
    DP3_mat_tor_damp = dp_Mat_tor_damp*DP3_delx;
    DP4_mat_tor_damp = dp_Mat_tor_damp*DP4_delx;
```

Drillstring build section angle constants

```
parameters
    real curv_radius = 294.1;
variables
    real global HWDP_Alpha;
    real global DP_Alpha;
    real global HWDP2_n;
    real global DP2_n;
    real global HWDP2_delAlpha;
    real global DP2_delAlpha;
    real global DP2_L;
    real global HWDP2_L;
    real global Curv_radius;
    //HWDP
    real global HWDP_alpha_01;
    real global HWDP_alpha_02;
    real global HWDP_alpha_03;
    real global HWDP_alpha_04;
    real global HWDP_alpha_05;
    real global HWDP_alpha_06;
    real global HWDP_alpha_07;
    // DP
    real global DP_alpha_01;
    real global DP_alpha_02;
    real global DP_alpha_03;
    real global DP_alpha_04;
    real global DP_alpha_05;
    real global DP_alpha_06;
    real global DP_alpha_07;
    real global DP_alpha_08;
    real global DP_alpha_09;
    real global DP_alpha_10;
    real global DP_alpha_11;
    real global DP_alpha_12;
    real global DP_alpha_13;
equations
```

```
    Curv_radius = curv_radius;
    HWDP_Alpha = HWDP2_L /Curv_radius;
    DP_Alpha = DP2_L/Curv_radius;
    HWDP2_delAlpha = HWDP_Alpha/HWDP2_n;
    DP2_delAlpha = DP_Alpha/DP2_n;
    // HWDP
    HWDP_alpha_01 = 0 + HWDP2_delAlpha/2;
    HWDP_alpha_02 = HWDP_alpha_01 + HWDP2_delAlpha;
    HWDP_alpha_03 = HWDP_alpha_02 + HWDP2_delAlpha;
    HWDP_alpha_04 = HWDP_alpha_03 + HWDP2_delAlpha;
    HWDP_alpha_05 = HWDP_alpha_04 + HWDP2_delAlpha;
    HWDP_alpha_06 = HWDP_alpha_05 + HWDP2_delAlpha;
    HWDP_alpha_07 = HWDP_alpha_06 + HWDP2_delAlpha;
    // DP
    DP_alpha_01 = HWDP_alpha_07 + DP2_delAlpha;
    DP_alpha_02 = DP_alpha_01 + DP2_delAlpha;
    DP_alpha_03 = DP_alpha_02 + DP2_delAlpha;
    DP_alpha_04 = DP_alpha_03 + DP2_delAlpha;
    DP_alpha_05 = DP_alpha_04 + DP2_delAlpha;
    DP_alpha_06 = DP_alpha_05 + DP2_delAlpha;
    DP_alpha_07 = DP_alpha_06 + DP2_delAlpha;
    DP_alpha_08 = DP_alpha_07 + DP2_delAlpha;
    DP_alpha_09 = DP_alpha_08 + DP2_delAlpha;
    DP_alpha_10 = DP_alpha_09 + DP2_delAlpha;
    DP_alpha_11 = DP_alpha_10 + DP2_delAlpha;
    DP_alpha_12 = DP_alpha_11 + DP2_delAlpha;
    DP_alpha_13 = DP_alpha_12 + DP2_delAlpha;
```

Friction constant

```
parameters
    real K = 1e07;
    real C = 100000;
    real Mu_s = 0.4;
    real Mu_k = 0.35;
    real Mu_st = 0.25;
    real Mu_kt = 0.20;
    real v_Threshold = 0.0005;
variables
    real global mu_s;
    real global mu_k;
    real global mu_st;
    real global mu_kt;
    real global k;
    real global c;
    real global v_threshold;
equations
    mu_s = Mu_s;
    mu_k = Mu_k;
    mu_st = Mu_st;
    mu_kt = Mu_kt;
    k = K;
    c = C;
```

```
    v_threshold = v_Threshold;
```

Swivel constants

```
parameters
    real Swivel_mass = 7031;  // mass of swivel, kg
variables
    real global swivel_mass;
equations
    swivel_mass = Swivel_mass;
```

Downhole axial excitation tool (or Agitator®) constants

```
parameters
    real agi_L = 9;                 // length of drillpipe, m, After agitator
    real agi_n = 1;                 // number of segments for drillpipe, After agitator
variables
    real global rho;
    real global E;
    real global G;
    // DP
    real global Agi_L;
    real global Agi_n;
    real global Agi_delx;
    real global hwdp_OD;
    real global hwdp_ID;
    real global HWDP_area_inertia;
    real global HWDP_area;
    real global hwdp_Mat_damp;      // material damping per unit length
    real global hwdp_Mat_tor_damp;  // material damping per unit length
    real global agi_mass_inertia;
    real global agi_torsion_comp;
    real global agi_torsion_fluid_resis;
    real global agi_mass;
    real global agi_axial_comp;
    real global agi_mat_damp;
    real global agi_mat_tor_damp;


    real global torsion_viscosity_resis;
    real global wellbore_radius;
equations
    // DP
    Agi_L = agi_L ;
    Agi_n = agi_n;
    Agi_delx = agi_L / agi_n;
    agi_mass_inertia = 0.5 * rho * HWDP_area * Agi_delx * ((hwdp_OD/2)^2 + (hwdp_ID/2)^2);
    agi_torsion_comp = Agi_delx/(G*HWDP_area_inertia);
    agi_torsion_fluid_resis = (2*3.1416* torsion_viscosity_resis * (hwdp_OD/2)^3 /(wellbore_radius -
(hwdp_OD/2)))* Agi_delx;
```

```
    agi_mass = rho * HWDP_area * Agi_delx;
    agi_axial_comp = Agi_delx/(E * HWDP_area);
    agi_mat_damp = hwdp_Mat_damp*Agi_delx;          // axial model
    agi_mat_tor_damp = hwdp_Mat_tor_damp*Agi_delx;
```

Motor HS 3D segment constants

```
parameters
    real HS_L = 8;                  // length of drillcollar, m
    real HS_N = 8;                  // number of segments for drillcollar
    real HS_od = 0.121;
    real HS_ID   = 0.0;
    real HS_r = 10000;
    real HS_rt = 500;
    real HS_rfluid = 5;
    real HS_rfluid_tor = 0.1;
variables
    real global rho;
    real global E;
    real global G;
    real global nu;
    real HS_A;
    real HS_m;
    real global HS_M[3,3];
    real global HS_rA_G[3,1];
    real global HS_rB_G[3,1];
    real HS_Iz;
    real HS_Ix;
    real HS_Iy;
    real global HS_I[3,3];
    real global HS_K_bend;
    real HS_K_axial;
    real HS_K_shear;
    real HS_K_torsion;
    real global HS_K[3,3];
    real global HS_Kt[3,3];
    real HS_J;
    real global HS_R[3,3];
    real global HS_Rt[3,3];
    real global HS_Rfluid[3,3];
    real global HS_Rfluid_tor[3,3];
    real global HS_delx;
    real HS_X;
    real global HS_OD;
    real global sub_delx;
    real global pipe_delx;
    real global collar_delx;
    real global HS_zo1[3,1],HS_zo2[3,1],HS_zo3[3,1],HS_zo4[3,1];
    real global HS_zo5[3,1],HS_zo6[3,1],HS_zo7[3,1],HS_zo8[3,1];
    real global HS_r_EI;
    real global HS_del;
```

```
    real global wellbore_radius;
equations
    HS_delx = HS_L/HS_N;
    HS_OD = HS_od;
    HS_del = wellbore_radius - HS_OD/2;
    HS_zo1 = [0;0;-(2*sub_delx+4*pipe_delx+20*collar_delx+HS_delx/2)];
    HS_zo2 = [0;0;-(2*sub_delx+4*pipe_delx+20*collar_delx+3*HS_delx/2)];
    HS_zo3 = [0;0;-(2*sub_delx+4*pipe_delx+20*collar_delx+5*HS_delx/2)];
    HS_zo4 = [0;0;-(2*sub_delx+4*pipe_delx+20*collar_delx+7*HS_delx/2)];
    HS_zo5 = [0;0;-(2*sub_delx+4*pipe_delx+20*collar_delx+9*HS_delx/2)];
    HS_zo6 = [0;0;-(2*sub_delx+4*pipe_delx+20*collar_delx+11*HS_delx/2)];
    HS_zo7 = [0;0;-(2*sub_delx+4*pipe_delx+20*collar_delx+13*HS_delx/2)];
    HS_zo8 = [0;0;-(2*sub_delx+4*pipe_delx+20*collar_delx+15*HS_delx/2)];
    HS_A = 3.1416*((HS_OD/2)^2 - (HS_ID/2)^2);
    HS_X = 6*(((HS_OD/2)^2+(HS_ID/2)^2)^2*(1+nu)^2)/(7*(HS_ID/2)^4+34*(HS_ID/2)^2*
(HS_OD/2)^2+7*(HS_OD/2)^4+nu*(12*(HS_ID/2)^4+48*(HS_ID/2)^2*(HS_OD/2)^2+12*(HS_OD/2)^4
)+nu^2*(4*(HS_ID/2)^4+16*(HS_ID/2)^2*(HS_OD/2)^2+4*(HS_OD/2)^4));
     //X = 10 * (1 + nu) / (12 + (11 * nu)); // for rectangular section
     HS_K_shear = HS_X * HS_A * G / HS_delx;
     HS_m = rho * HS_A * HS_delx;
     HS_rA_G = [0; 0; HS_delx/2];
    HS_rB_G = [0; 0; -HS_delx/2];
    HS_M = [HS_m,0,0;0,HS_m,0;0,0,HS_m];
    HS_Iz = 0.5 * HS_m * ((HS_OD/2)^2 + (HS_ID/2)^2);
    HS_Ix = (HS_m * ((3 * ((HS_OD/2)^2 + (HS_ID/2)^2)) + (HS_delx)^2)) / 12;
    HS_Iy = (HS_m * ((3 * ((HS_OD/2)^2 + (HS_ID/2)^2)) + (HS_delx)^2)) / 12;
    HS_I = [HS_Ix,0,0;0,HS_Iy,0;0,0,HS_Iz];
    HS_J = ((HS_OD/2)^4 - (HS_ID/2)^4) * 3.1416 *0.5;
    HS_K_axial = (E * HS_A) / HS_delx;
    HS_K_torsion = (G * HS_J) / HS_delx;
    HS_K_bend = (E * 3.1416*((HS_OD)^4 - (HS_ID)^4) / 64) / HS_delx;
    HS_K = [HS_K_shear,0,0;0,HS_K_shear,0;0,0,HS_K_axial];
    HS_Kt = [HS_K_bend,0,0;0,HS_K_bend,0;0,0,HS_K_torsion];
    HS_R = [HS_r,0,0;0,HS_r,0;0,0,HS_r];
    HS_Rt = [HS_rt,0,0;0,HS_rt,0;0,0,HS_rt];
    HS_Rfluid = [4,0,0;0,4,0;0,0,HS_rfluid];
    HS_Rfluid_tor = [0,0,0;0,0,0;0,0,HS_rfluid_tor];
    HS_r_EI = HS_OD/(2*(E * 3.1416*((HS_OD)^4-(HS_ID)^4)/64));
```

Pipes 3D segment constants

```
Parameters
    real pipe_L = 10;              // length of drillcollar, m
    real pipe_N = 4;               // number of segments for drillcollar
    real pipe_od = 0.101;
    real pipe_ID = 0.082;
    real pipe_r = 10000;
    real pipe_rt = 500;
    real pipe_rfluid = 5;
    real pipe_rfluid_tor = 0.1;
variables
    real global rho;
    real global E;
```

```
    real global G;
    real global nu;
    real pipe_A;
    real pipe_m;
    real global pipe_M[3,3];
    real global pipe_rA_G[3,1];
    real global pipe_rB_G[3,1];
    real pipe_Iz;
    real pipe_Ix;
    real pipe_Iy;
    real global pipe_I[3,3];
    real global pipe_K_bend;
    real pipe_K_axial;
    real pipe_K_shear;
    real pipe_K_torsion;
    real global pipe_K[3,3];
     real global pipe_Kt[3,3];
    real pipe_J;
    real global pipe_R[3,3];
    real global pipe_Rt[3,3];
    real global pipe_Rfluid[3,3];
    real global pipe_Rfluid_tor[3,3];
    real global pipe_delx;
    real pipe_X;
    real global pipe_OD;
    real global sub_delx;
    real global pipe_zo1[3,1],pipe_zo2[3,1],pipe_zo3[3,1],pipe_zo4[3,1];
    real global pipe_r_EI;
    real global pipe_del;
    real global wellbore_radius;
equations
    pipe_delx = pipe_L/pipe_N;
    pipe_OD = pipe_od;
    pipe_del = wellbore_radius - pipe_OD/2;
    pipe_zo1 = [0;0;-(sub_delx+pipe_delx/2)];
    pipe_zo2 = [0;0;-(sub_delx+3*pipe_delx/2)];
    pipe_zo3 = [0;0;-(sub_delx+5*pipe_delx/2)];
    pipe_zo4 = [0;0;-(sub_delx+7*pipe_delx/2)];
    pipe_A = 3.1416*((pipe_OD/2)^2 - (pipe_ID/2)^2);
    pipe_X                                                                                                                                                                                                                                                                                                                                                                                                                                                                                                                                                                                                                                                                                                                                                                                                                                                                                                                                                                                                                                                                                                                                                                                                                                                                                                                                                                                                                                                                                                                                                                                                                                                                                                                                                                                                                                                                                                                                                                                                                                                                                                                                                                                                                                                                                                                                                                                                                                                                                                                                                                                                                                                                                                                                                                                                                                                                                                                                                                                                                                                                                                                                                                                                                                                                                                                                                                                                                                                                                                                                                                                                                                                                                                                                                                                                                                                                                                                                                                                                                                                                                                                                                                                                                                                                                                                                                                                                                                                                                                                                                                                                                                                                                                                                                                                                                                                                                                                                                                                                                                                                                                                                                                                                                                                                                                                                                                                                                                                                                                                                                                                                                                                                                                                                                                                                                                                                                                                                                                                                                                                                                                                                                                                                                                                                                                                                                                                                                                                                                                                                                                                                                                                                                                                                                                                                                                                                                                                                                                                                                                                                                                                                                                                                                                
= 6*(((pipe_OD/2)^2+(pipe_ID/2)^2)^2*(1+nu)^2)/(7*(pipe_ID/2)^4+34*(pipe_ID/2)^2*(pipe_OD/2)^2+7*(pipe_OD/2)^4+nu*(12*(pipe_ID/2)^4+48*(pipe_ID/2)^2*(pipe_OD/2)^2+12*(pipe_OD/2)^4)+nu^2*(4*(pipe_ID/2)^4+16*(pipe_ID/2)^2*(pipe_OD/2)^2+4*(pipe_OD/2)^4));
  //X = 10 * (1 + nu) / (12 + (11 * nu)); // for rectangular section
    pipe_K_shear = pipe_X * pipe_A * G / pipe_delx;
    pipe_m = rho * pipe_A * pipe_delx;
    pipe_rA_G = [0; 0;pipe_delx/2];
    pipe_rB_G = [0; 0; -pipe_delx/2];
    pipe_M = [pipe_m,0,0;0,pipe_m,0;0,0,pipe_m];
    pipe_Iz = 0.5 * pipe_m * ((pipe_OD/2)^2 + (pipe_ID/2)^2);
    pipe_Ix = (pipe_m * ((3 * ((pipe_OD/2)^2 + (pipe_ID/2)^2)) + (pipe_delx)^2)) / 12;
    pipe_Iy = (pipe_m * ((3 * ((pipe_OD/2)^2 + (pipe_ID/2)^2)) + (pipe_delx)^2)) / 12;
    pipe_I = [pipe_Ix,0,0;0,pipe_Iy,0;0,0,pipe_Iz];
```

```
    pipe_J = ((pipe_OD/2)^4 - (pipe_ID/2)^4) * 3.1416 *0.5;
    pipe_K_axial = (E * pipe_A) / pipe_delx;
    pipe_K_torsion = (G * pipe_J) / pipe_delx;
    pipe_K_bend = (E * 3.1416*((pipe_OD)^4 - (pipe_ID)^4) / 64) / pipe_delx;
    pipe_K = [pipe_K_shear,0,0;0,pipe_K_shear,0;0,0,pipe_K_axial];
    pipe_Kt = [pipe_K_bend,0,0;0,pipe_K_bend,0;0,0,pipe_K_torsion];
    pipe_R = [pipe_r,0,0;0,pipe_r,0;0,0,pipe_r];
    pipe_Rt = [pipe_rt,0,0;0,pipe_rt,0;0,0,pipe_rt];
    pipe_Rfluid = [4,0,0;0,4,0;0,0,pipe_rfluid];
    pipe_Rfluid_tor = [0,0,0;0,0,0;0,0,pipe_rfluid_tor];
    pipe_r_EI = pipe_OD/(2*(E * 3.1416*((pipe_OD)^4-(pipe_ID)^4)/64));
```

Bit 3D segment constants

```
parameters
      real bit_L = 0.2;                 // length of drillcollar, m
      real bit_N = 1;                 // number of segments for drillcollar
      real bit_od = 0.159;
      real bit_ID    = 0.0;
      real bit_r = 10000;
      real bit_rt = 500;
      real bit_rfluid = 5;
      real bit_rfluid_tor = 0.1;
variables
      real global rho;
      real global E;
      real global G;
      real global nu;
      real bit_A;
      real bit_m;
  real global bit_M[3,3];
      real global bit_rA_G[3,1];
      real global bit_rB_G[3,1];
  real bit_Iz;
  real bit_Ix;
  real bit_Iy;
  real global bit_I[3,3];
      real global bit_K_bend;
      real bit_K_axial;
      real bit_K_shear;
      real bit_K_torsion;
  real global bit_K[3,3];
  real global bit_Kt[3,3];
      real bit_J;
      real global bit_R[3,3];
      real global bit_Rt[3,3];
      real global bit_Rfluid[3,3];
      real global bit_Rfluid_tor[3,3];
      real global bit_delx;
      real bit_X;
      real global bit_OD;
      real global sub_delx;
```

```
    real global pipe_delx;
    real global collar_delx;
    real global HS_delx;
    real global bit_zo1[3,1];
    real global bit_r_EI;
    real global bit_del;
    real global wellbore_radius;
equations
    bit_delx = bit_L/bit_N;
    bit_OD = bit_od;
    bit_del = wellbore_radius - bit_OD/2;
    bit_zo1 = [0;0;-(2*sub_delx+4*pipe_delx+20*collar_delx+8*HS_delx+bit_delx/2)];
    bit_A = 3.1416*((bit_OD/2)^2 - (bit_ID/2)^2);
    bit_X = 6*(((bit_OD/2)^2+(bit_ID/2)^2)^2*(1+nu)^2)/(7*(bit_ID/2)^4+34*(bit_ID/2)^2*
(bit_OD/2)^2+7*(bit_OD/2)^4+nu*(12*(bit_ID/2)^4+48*(bit_ID/2)^2*(bit_OD/2)^2+12*(bit_OD/2)^4)+
nu^2*(4*(bit_ID/2)^4+16*(bit_ID/2)^2*(bit_OD/2)^2+4*(bit_OD/2)^4));
  //X = 10 * (1 + nu) / (12 + (11 * nu)); // for rectangular section
    bit_K_shear = bit_X * bit_A * G / bit_delx;
    bit_m = rho * bit_A * bit_delx;
    bit_rA_G = [0; 0; bit_delx/2];
    bit_rB_G = [0; 0; -bit_delx/2];
    bit_M = [bit_m,0,0;0,bit_m,0;0,0,bit_m];
      bit_Iz = 0.5 * bit_m * ((bit_OD/2)^2 + (bit_ID/2)^2);
      bit_Ix = (bit_m * ((3 * ((bit_OD/2)^2 + (bit_ID/2)^2)) + (bit_delx)^2)) / 12;
      bit_Iy = (bit_m * ((3 * ((bit_OD/2)^2 + (bit_ID/2)^2)) + (bit_delx)^2)) / 12;
      bit_I = [bit_Ix,0,0;0,bit_Iy,0;0,0,bit_Iz];
      bit_J = ((bit_OD/2)^4 - (bit_ID/2)^4) * 3.1416 *0.5;
      bit_K_axial = (E * bit_A) / bit_delx;
      bit_K_torsion = (G * bit_J) / bit_delx;
      bit_K_bend = (E * 3.1416*((bit_OD)^4 - (bit_ID)^4) / 64) / bit_delx;
      bit_K = [bit_K_shear,0,0;0,bit_K_shear,0;0,0,bit_K_axial];
      bit_Kt = [bit_K_bend,0,0;0,bit_K_bend,0;0,0,bit_K_torsion];
     bit_R = [bit_r,0,0;0,bit_r,0;0,0,bit_r];
     bit_Rt = [bit_rt,0,0;0,bit_rt,0;0,0,bit_rt];
     bit_Rfluid = [4,0,0;0,4,0;0,0,bit_rfluid];
     bit_Rfluid_tor = [0,0,0;0,0,0;0,0,bit_rfluid_tor];
     bit_r_EI = bit_OD/(2*(E * 3.1416*((bit_OD)^4-(bit_ID)^4)/64));
```

Contact spring-damper constants

```
parameters
    real k_w = 1e9;
    real c_w = 300000;
variables
    real global kw;
    real global cw;
equations
    kw = k_w;
    cw = c_w;
```

Motor speed constants

```
parameters
    real w_M = 13.7;
```

```
variables
    real global motor_speed;
equations
    motor_speed = w_M;
```

TOB effort source codes

```
variables
    real flow;
    real phidot_function;
    real ROP;
    real depth_of_cut;
    real global bit_radius;
    real global Zeta;
    real global C1;
    real global C2;
    real global Alpha;
    real global Beta;
    real global Gama;
    real global Munot;
    real global Nu;
    real global avg_WOB;
    real global Desired_table_speed;
equations
    phidot_function = Munot*(tanh(phidot)+Alpha*phidot/(1+Beta*(phidot)^(2*Gama))+Nu*phidot);
    if WOB <= 5000 then
     ROP = 0;
     depth_of_cut = 0;
     if phidot == 0.0 then
        p.e = 0;
     else
        p.e = WOB*bit_radius*phidot_function;
     end;
  else
     if phidot == 0.0 then
        ROP = 0;
        p.e = WOB*bit_radius*phidot_function + 5000;
     else
        if phidot < 0 then
           ROP = 0;
           p.e = WOB*bit_radius*phidot_function;
        else
           ROP = C1*(WOB)*phidot^0.5;
           depth_of_cut = (2*3.1415926*ROP)/phidot;
           p.e = WOB*bit_radius*phidot_function +
(WOB)*bit_radius*Zeta*(depth_of_cut/bit_radius)^0.5;
        end;
     end;
  end;
flow = p.f;
rate_of_penetration = ROP;
```

Rock compliance codes

```
variables
    real global rock_compliance;
    real global rock_damping;
equations
    X = int(p.f);
    if X >=0 then
        p.e = (1/rock_compliance) * X + rock_damping*p.f;
    else
        p.e = 0;
    end;
WOB = p.e;
```

Surface elevation source codes

```
parameters
    real S0 = 0.0001;
    real b = 1;

equations
    if phidot < 0 then
        S_vel = 0;
    else
      S_vel =  S0 * (b * phidot) * cos (b* phi);
  end;
```

Appendix D

LS-DYNA® FEM programming codes

Natural frequency LS-DYNA® model reduced input codes

```
*KEYWORD MEMORY=900000000
*TITLE
*CONTROL_IMPLICIT_DYNAMICS
   imass    gamma     beta   tdybir   tdydth   tdybur    irate
      1       0.0       0.0     0.0     1.0E28 1.0E28       0
*CONTROL_IMPLICIT_EIGENVALUE
   neig   center    lflag   lftend    rflag   rhtend   eigmth   shfscl
    500     0.0       0   -1.0E29       0    1.0E29       2      0.0
   isolid   ibeam   ishell  itshell   mstres   evdump
      0       0        0       0        0        0
*CONTROL_IMPLICIT_GENERAL
   imflag     dt0    imform    nsbs     igs    cnstn    form   zero_v
     1       5.0E-4     2        1        2        0        0        0
*CONTROL_IMPLICIT_SOLUTION
   nsolvr   ilimit   maxref    dctol    ectol    rctol    lstol   abstol
     2        11       15      0.001    0.01   1.0E10   0.89    1.0E-10
  dnorm   diverg    istif   nlprint   nlnorm   d3itctl   cpchk
     2       1        1       0        2        0        0
  arcctl   arcdir   arclen   arcmth   arcdmp   arcpsi   arcalf   arctim
     0       0       0.0       1        2        0        0        0
  lsmtd    lsdir    irad     srad     awgt     sred
     1       2       0.0      0.0      0.0      0.0
*CONTROL_IMPLICIT_SOLVER
  lsolvr   lprint   negev    order    drcm    drcprm   autospc   autotol
     4       2        2        0        4       0.0       1        0.0
  lcpack   mtxdmp
     2       0
*CONTROL_TERMINATION
  endtim   endcyc   dtmin   endeng   endmas
   0.025     0       0.0     0.0      1.0E8
*DATABASE_BINARY_D3PLOT
    dt       lcdt    beam    npltc   psetid
  0.001      0        0        0        0
   ioopt
     0
*BOUNDARY_SPC_SET_ID
     id                          heading
     0                          Fixed BC
   nsid     cid     dofx     dofy     dofz     dofrx    dofry    dofrz
     1       0       1        1        1        1        1        1
*SET_NODE_LIST_TITLE
   Fixed BC node
   sid     da1     da2     da3     da4    solver
    1      0.0     0.0     0.0     0.0    MECH
   nid1    nid2    nid3    nid4    nid5    nid6    nid7    nid8
    1       0       0       0       0       0       0       0
*LOAD_BODY_Z
   lcid     sf     lciddr     xc      yc      zc      cid
    1      1.0      0       0.0     0.0     0.0      0
*PART
    title
 10m Drillpipe
   pid    secid    mid    eosid    hgid    grav   adpopt    tmid
    1       1       1       0        0       0       0        0
*SECTION_BEAM_TITLE
```

```
beam
   secid    elform      shrf   qr/irid       cst     scoor       nsm
      1         5           1.0        2           1       0.0         0.0
     ts1           ts2           tt1         tt2
   0.1016    0.1016   0.08484   0.08484
*MAT_ELASTIC_TITLE
Steel
     mid        ro         e          pr        da        db    not used
      1    7850.0   2.1E11    0.3       0.0       0.0        0
*DEFINE_CURVE_TITLE
gravity
      lcid      sidr       sfa       sfo      offa      offo    dattyp     lcint
       1         0         1.0       1.0       0.0       0.0         0         0
       a1                  o1
       0.0               9.81
       2.0               9.81
*ELEMENT_BEAM
*NODE
*END
```

Lateral deflection LS-DYNA® model reduce input codes

```
*KEYWORD MEMORY=100000000
*TITLE
*CONTROL_DYNAMIC_RELAXATION
      nrcyck     drtol    drfctr    drterm    tssfdr    irelal     edttl       idrflg
      250        1.0E-2  0.995    0.000     0.000         0      4.0E-2         0
*CONTROL_TERMINATION
      endtim    endcyc     dtmin    endeng    endmas
       8.0          0         0.000     0.000      1.0E+8
*DATABASE_GLSTAT
     dt              binary      lcur     ioopt
    1.0E-2         0              0         1
*DATABASE_NODOUT
     dt              binary      lcur     ioopt   option1   option2
     1.0E-2         0              0         1        0.000         0
*DATABASE_RCFORC
     dt              binary      lcur     ioopt
    1.0E-2         0              0         1
*DATABASE_BINARY_D3PLOT
     dt             lcdt      beam     npltc    psetid
    1.0E-3         0         0          0         0
    ioopt
    0
*DATABASE_HISTORY_NODE_ID
 400Force end
 300two third
 200middle
*BOUNDARY_SPC_SET
     nsid       cid      dofx      dofy      dofz     dofrx     dofry     dofrz
       1         0         1           1           1         1           1           1
*SET_NODE_LIST_TITLE
NODESET(SPC) 1
     sid       da1       da2       da3       da4    solver
      1        0.0       0.0       0.0       0.0     MECH
     nid1      nid2      nid3      nid4      nid5      nid6      nid7      nid8
       1         0         0         0         0         0         0         0
*LOAD_BODY_Z
     lcid        sf       lciddr        xc        yc        zc       cid
      1          1.0         0     0.000     0.000     0.000         0
*LOAD_NODE_POINT
     nid       dof      lcid        sf       cid        m1        m2        m3
     400         2         2        1.0         0         0         0         0
*PART
     pid     secid       mid     eosid      hgid      grav    adpopt      tmid
     1         3          2          0          0          0          0          0
```

```
*SECTION_BEAM_TITLE
beam
     secid    elform      shrf   qr/irid       cst     scoor       nsm
       3         5           1.0         2          1       0. 0         0.0
     ts1       ts2       tt1                tt2
  0.1016  0.1016   8.4840E-2     8.4840E-2
*MAT_PLASTIC_KINEMATIC_TITLE
plastic kinematic
     mid        ro         e           pr      sigy           etan      beta
      2       7850      2.1E+11  0.3     1.5E+11     0.000     0.000
     src        srp        fs          vp
    0.000     0.000     0.000     0.000
*DEFINE_CURVE_TITLE
gravity
     lcid      sidr       sfa       sfo      offa      offo    dattyp
     1          0         1.0      1.0       0.0       0.0        0
     a1                  o1
     0.000             9.810000
     8.000000         9.810000
*DEFINE_CURVE_TITLE
Lateral Load
     lcid      sidr       sfa       sfo      offa      offo    dattyp
       2        0         1.0      1.0       0.0       0.0        0
     a1                  o1
     0.0                 0
     4.0                500
     8.0                500
*ELEMENT_BEAM
*NODE
*END
```

Pipe rotor dynamics LS-DYNA® model reduce inputs codes

```
*KEYWORD
*TITLE
*CONTROL_DYNAMIC_RELAXATION
     nrcyck     drtol      drfctr    drterm    tssfdr    irelal     edttl    idrflg
      250        0.001     0.995       0.0       0.0        0         0.04        0
*CONTROL_TERMINATION
     endtim    endcyc     dtmin    endeng    endmas
     50.0        0           0.0        0.0        1.0E8
*DATABASE_ABSTAT
     dt         binary      lcur     ioopt
     0.01        0           0         1
*DATABASE_GLSTAT
     dt         binary      lcur     ioopt
     0.01        0           0         1
*DATABASE_NODOUT
     dt          binary      lcur     ioopt   option1   option2
     0.01        0           0         1         0.0         0
*DATABASE_RCFORC
     dt          binary      lcur     ioopt
     0.01        0           0         1
*DATABASE_BINARY_D3PLOT
     dt          lcdt      beam     npltc    psetid
     0.01        0          0          0         0
     ioopt
     0
*DATABASE_HISTORY_NODE
*BOUNDARY_PRESCRIBED_MOTION_NODE_ID
0Shaft top end rotation
     nid       dof       vad      lcid       sf       vid     death      birth
       1        7         0         2         1.0      0       1.0E28      0.0
*BOUNDARY_SPC_SET_ID
0shaft top end BC
nsid      cid      dofx      dofy      dofz     dofrx     dofry     dofrz
```

```
    4       0       1       1       1       1       1       0
*SET_NODE_LIST_TITLE
shaft top end BC set
    sid     da1     da2     da3     da4   solver
    4       0.0     0.0     0.0     0.0     MECH
    nid1    nid2    nid3    nid4    nid5    nid6    nid7    nid8
    1       0       0       0       0       0       0       0
*PART
10mShaft
    pid    secid    mid    eosid    hgid    grav   adpopt    tmid
    1       1       1       0       0       0       0       0
*SECTION_BEAM_TITLE
beam for shaft
    secid   elform    shrf   qr/irid    cst    scoor    nsm
      1       5       1.0       2       1      0.0      0.0
    ts1       ts2      tt1       tt2
   0.1016   0.1016   0.08484   0.08484
*MAT_PLASTIC_KINEMATIC_TITLE
plastic kinematic steel
    mid      ro       e      pr     sigy     etan    beta
      1   7850    2.1E11   0.3   2.5E8     0.0     0.0
    src     srp      fs      vp
     0.0     0.0     0.0     0.0
*PART
Disk
    pid    secid    mid    eosid    hgid    grav   adpopt    tmid
      3       3       3       0       0       0       0       0
*SECTION_SHELL_TITLE
shell for disk
    secid   elform    shrf     nip    propt  qr/irid   icomp   setyp
      3       2       1.0       2      1.0      0       0       1
    t1       t2       t3       t4      nloc    marea    idof   edgset
    0.01    0.01    0.01    0.01     0.0     0.0      0.0      0
*MAT_ELASTIC_TITLE
Elastic for Disk
    mid      ro       e       pr      da      db    not used
      3   7850    1.0E13   0.3     0.0     0.0      0
*PART
ecentric Mass
    pid    secid    mid    eosid    hgid    grav   adpopt    tmid
     4       4       4       0       0       0       0       0
*SECTION_SOLID_TITLE
solid for mass
   secid   elform     aet
    4       1         0
*MAT_ELASTIC_TITLE
mat for mass
     mid      ro       e        pr      da      db    not used
      4   25000    2.1E11   0.3     0.0     0.0      0
*SECTION_SHELL_TITLE
Shell for Wall
     secid   elform    shrf     nip    propt  qr/irid   icomp   setyp
      2       2       1.0       2      1.0      0       0       1
     t1       t2       t3       t4      nloc    marea    idof   edgset
    0.02    0.02    0.02    0.02     0.0     0.0      0.0      0
*MAT_RIGID_TITLE
Rigid
    mid      ro       e        pr       n   couple      m    alias
      2   7850    2.1E11   0.30000001    0.0     0.0     0.0
    cmo     con1     con2
     0.0      0       0
    lco or a1      a2      a3      v1      v2      v3
     0.0          0.0     0.0     0.0     0.0     0.0
*DEFINE_CURVE_TITLE
Gravity
    lcid    sidr     sfa     sfo     offa    offo   dattyp   lcint
```

```
    1       0      1.0      1.0      0.0      0.0       0       0
    a1              o1
    0.0         9.81000042
    50.0         9.81000042
*DEFINE_CURVE_TITLE
Rotation
    lcid     sidr      sfa      sfo     offa     offo   dattyp    lcint
      2        0      1.0      1.0      0.0      0.0        0        0
     a1              o1
     0.0             0.0
    10.0            10.0
    50.0            10.0
*DEFINE_CURVE_TITLE
damping
    lcid     sidr      sfa      sfo     offa     offo   dattyp    lcint
      3        0      1.0      1.0      0.0      0.0        0        0
           a1              o1
            0.0            1.0
           50.0            1.0
*SET_NODE_LIST_TITLE
shaft disk constrain set
     sid      da1      da2      da3      da4   solver
      1      0.0      0.0      0.0      0.0   MECH
*SET_NODE_LIST_TITLE
mass disk constrain set
    sid      da1      da2      da3      da4   solver
     2      0.0      0.0      0.0      0.0   MECH
*CONSTRAINED_NODAL_RIGID_BODY_SPC_TITLE
shaft disk constrain
    pid      cid     nsid    pnode     iprt   drflag   rrflag
      5        0        1        0        0        0        0
    cmo     con1     con2
     0.0        0        0
*CONSTRAINED_NODAL_RIGID_BODY_SPC_TITLE
mass disk constrain
    pid      cid     nsid    pnode     iprt   drflag   rrflag
    6        0        2        0        0        0        0
    cmo     con1     con2
     0.0        0        0
*DAMPING_GLOBAL
    lcid   valdmp      stx      sty      stz      srx      sry      srz
     3     0.0        0.25     0.25   162.487    0.1      0.1    102.28
*ELEMENT_SOLID
*ELEMENT_SHELL
*ELEMENT_BEAM
*NODE
*END
```

Contact LS-DYNA® model reduce input codes

```
*KEYWORD
*TITLE
*CONTROL_CONTACT
    slsfac   rwpnal   islchk   shlthk   penopt   thkchg    orien   enmass
     0.0      0.0        2        2        1        0        1        0
    usrstr   usrfrc   nsbcs   interm    xpene   ssthk     ecdt  tiedprj
      0        0        0        0      4.0        0        0        0
    sfric    dfric     edc      vfc       th    th_sf   pen_sf
     0.0      0.0      0.0      0.0      0.0      0.0      0.0
    ignore   frceng  skiprwg   outseg  spotstp  spotdel  spothin
      0        0        0        0        0        0      0.0
    isym    nserod   rwgaps   rwgdth   rwksf    icov   swradf   ithoff
      0        0        1      0.0      1.0        0      0.0        0
   shledg   pstiff   ithcnt   tdcnof   ftall   unused   shltrw
      0        0        0        0        0      0.0
```

```
*CONTROL_DYNAMIC_RELAXATION
    nrcyck    drtol     drfctr   drterm   tssfdr   irelal    edttl   idrflg
     250      0.001     0.995    0.01     1.0      0         0.04    1
*CONTROL_TERMINATION
    endtim   endcyc    dtmin    endeng   endmas
     0.5     0          0.0      0.0      0.0
*DATABASE_GLSTAT
    dt          binary     lcur     ioopt
    0.001       0          0        1
*DATABASE_RCFORC
    dt          binary     lcur     ioopt
    0.001       0          0        1
*DATABASE_BINARY_D3PLOT
    dt          lcdt     beam     npltc    psetid
    0.001       0        0        0        0
    ioopt
     0
*BOUNDARY_SPC_SET
     nsid     cid     dofx     dofy     dofz     dofrx    dofry    dofrz
      1       0       1        1        1        1        1        1
*SET_NODE_LIST_TITLE
NODESET(SPC) 1
     sid     da1     da2     da3     da4    solver
      1      0.0     0.0     0.0     0.0    MECH
*LOAD_BODY_Z
     lcid     sf     lciddr     xc     yc     zc     cid
      1       1.0    0          0.0    0.0    0.0    0
*CONTACT_SURFACE_TO_SURFACE_ID
     cid                                                title
      1
     ssid     msid     sstyp     mstyp    sboxid    mboxid     spr     mpr
      1       2        3         3        0         0          0       0
     fs       fd       dc        vc       vdc       penchk     bt      dt
     0.3      0.2      250       1.2E8    20.0      0          0.0     1.0E20
     sfs      sfm      sst       mst      sfst      sfmt       fsf     vsf
     1.0      1.0      0.0       0.0      1.0       1.0        1.0     1.0
*PART
Solid Shaft
     pid     secid     mid     eosid     hgid     grav     adpopt     tmid
      1       1        1       0         0        0        0          0
*SECTION_SOLID_TITLE
Solid for Shaft
    secid    elform     aet
      1       2         0
*MAT_ELASTIC_TITLE
Mat for Shaft
    mid      ro       e        pr       da       db  not used
      1      80000    2.1E11   0.3      0.0      0.0      0
*PART
Shell Wall
    pid     secid     mid     eosid     hgid     grav     adpopt     tmid
      2       2       3       0         0        0        0          0
*SECTION_SHELL_TITLE
shell for wall
    secid    elform     shrf     nip     propt    qr/irid    icomp    setyp
      2       2         1.0      3       1.0      0          0        1
    t1       t2       t3       t4       nloc     marea     idof     edgset
    0.02     0.02     0.02     0.02     0.0      0.0       0.0      0
*MAT_RIGID_TITLE
Rigid for Wall
     mid      ro       e        pr       n        couple       m     alias
      3       7850     2.1 E11  0.3      0.0      0.0          0.0
     cmo      con1     con2
     0.0      0        0
    lco or a1     a2       a3       v1       v2       v3
     0.0          0.0      0.0      0.0      0.0      0.0
```

```
*DEFINE_CURVE_TITLE
gravity
    lcid      sidr       sfa       sfo      offa      offo    dattyp     lcint
       1         0       1.0       1.0       0.0       0.0         0         0
              a1                  o1
             0.0          9.81000042
             0.5          9.81000042
*ELEMENT_SOLID
*ELEMENT_SHELL
*NODE
*END
```

Rolling motion LS-DYNA® model reduce input codes

```
*KEYWORD
*TITLE
*CONTROL_CONTACT
    slsfac    rwpnal    islchk    shlthk    penopt    thkchg     orien    enmass
     0.0       0.0         2         2         1         0         1         0
    usrstr    usrfrc    nsbcs    interm     xpene     ssthk      ecdt   tiedprj
       0         0         0         0       4.0         0         0         0
    sfric     dfric       edc       vfc        th     th_sf    pen_sf
     0.0       0.0       0.0       0.0       0.0       0.0       0.0
    ignore    frceng   skiprwg    outseg   spotstp   spotdel   spothin
       0         0         0         0         0         0       0.0
    isym    nserod    rwgaps    rwgdth     rwksf      icov    swradf    ithoff
       0         0         1       0.0       1.0         0       0.0         0
    shledg    pstiff    ithcnt    tdcnof     ftall    unused    shltrw
       0         0         0         0         0       0.0
*CONTROL_DYNAMIC_RELAXATION
    nrcyck     drtol    drfctr    drterm    tssfdr    irelal     edttl    idrflg
     250     0.001     0.995      0.01       1.0         0      0.04         1
*CONTROL_TERMINATION
    endtim    endcyc     dtmin    endeng    endmas
    10.0         0       0.0       0.0       0.0
*DATABASE_GLSTAT
    dt    binary      lcur     ioopt
   0.001         0         0         1
*DATABASE_NODOUT
    dt    binary      lcur     ioopt   option1   option2
   0.001         0         0         1       0.0         0
*DATABASE_RCFORC
    dt    binary      lcur     ioopt
   0.001         0         0         1
*DATABASE_BINARY_D3PLOT
    dt      lcdt      beam     npltc    psetid
   0.001         0         0         0         0
    ioopt
       0
*DATABASE_HISTORY_NODE
    id1       id2       id3       id4       id5       id6       id7       id8
    448      1891         0         0         0         0         0         0
*BOUNDARY_SPC_SET_ID
0Wall Fixed BC
    nsid       cid      dofx      dofy      dofz     dofrx     dofry     dofrz
       1         0         1         1         1         1         1         1
*SET_NODE_LIST_TITLE
Wall Fixed BC Nodes
     sid       da1       da2       da3       da4    solver
       1       0.0       0.0       0.0       0.0MECH
*BOUNDARY_SPC_SET
     nsid       cid      dofx      dofy      dofz     dofrx     dofry     dofrz
       6         0         1         0         0         0         0         0
*SET_NODE_LIST_TITLE
NODESET(SPC) 6
```

```
     sid       da1       da2       da3       da4    solver
       6       0.0       0.0       0.0       0.0MECH
     nid1      nid2      nid3      nid4      nid5      nid6      nid7      nid8
     448      1891         0         0         0         0         0         0
*LOAD_BODY_Z
     lcid        sf    lciddr        xc        yc        zc       cid
       1       1.0         0       0.0       0.0       0.0         0
*LOAD_NODE_POINT
     nid       dof      lcid        sf       cid        m1        m2        m3
     448         5         3       1.0         0         0         0         0
    1891         5         3       1.0         0         0         0         0
*CONTACT_AUTOMATIC_SURFACE_TO_SURFACE
    ssid      msid     sstyp     mstyp    sboxid    mboxid       spr       mpr
       1         2         3         3         0         0         0         0
      fs        fd        dc        vc       vdc    penchk        bt        dt
    0.6       0.5       250    1.2E8      20.0         0       0.0      1. 0E20
     sfs       sfm       sst       mst      sfst      sfmt       fsf       vsf
     1.0       1.0       0.0       0.0       1.0       1.0       1.0       1.0
*PART
Solid Shaft
     pid     secid       mid     eosid      hgid      grav    adpopt      tmid
       1         1         1         0         0         0         0         0
*SECTION_SOLID_TITLE
Solid for Shaft
     secid    elform       aet
       1         2         0
*MAT_ELASTIC_TITLE
Mat for Shaft
     mid        ro         e        pr        da        db  not used
       1    150000    2.1E11       0.3       0.0       0.0         0
*PART
Rigid Wall
     pid     secid       mid     eosid      hgid      grav    adpopt      tmid
       2         2         3         0         0         0         0         0
*SECTION_SHELL_TITLE
shell for wall
     secid    elform      shrf       nip     propt   qr/irid     icomp     setyp
       2         2       1.0         3       1.0         0         0         1
      t1        t2        t3        t4      nloc     marea      idof    edgset
    0.02      0.02      0.02      0.02       0.0       0.0       0.0         0
*MAT_RIGID_TITLE
Rigid for Wall
     mid        ro         e        pr         n    couple         m     alias
       3      7850    2.1E11       0.3       0.0       0.0       0.0
     cmo      con1      con2
     0.0         0         0
    lco or a1       a2        a3        v1        v2        v3
     0.0       0.0       0.0       0.0       0.0       0.0
*DEFINE_CURVE_TITLE
gravity
     lcid      sidr       sfa       sfo      offa      offo    dattyp     lcint
       1         0       1.0       1.0       0.0       0.0         0         0
            a1                  o1
             0.0          9.81000042
            10.0          9.81000042
*DEFINE_CURVE_TITLE
Torque Curve
     lcid      sidr       sfa       sfo      offa      offo    dattyp     lcint
       3         0       1.0      10.0       0.0       0.0         0         0
*SET_NODE_LIST_TITLE
NODESET(SPC) 3
     sid       da1       da2       da3       da4    solver
       3       0.0       0.0       0.0       0.0MECH
     nid1      nid2      nid3      nid4      nid5      nid6      nid7      nid8
     448      1891         0         0         0         0         0         0
*SET_NODE_LIST_TITLE
```

```
NODESET(CNRB)
     sid      da1      da2      da3      da4    solver
      4      0.0      0.0      0.0      0.0     MECH
*SET_NODE_LIST_TITLE
NODESET(CNRB)
     sid      da1      da2      da3      da4    solver
      5      0.0      0.0      0.0      0.0     MECH
*CONSTRAINED_NODAL_RIGID_BODY
     pid      cid     nsid    pnode     iprt    drflag    rrflag
      3        0        4        0        0        0         0
*CONSTRAINED_NODAL_RIGID_BODY
     pid      cid     nsid    pnode     iprt    drflag    rrflag
      4        0        5        0        0        0         0
*ELEMENT_SOLID
*ELEMENT_SHELL
*NODE
*END
```

Pipe buckling inside wellbore LS-DYNA® model reduced input codes

```
*KEYWORD
*TITLE
*CONTROL_DYNAMIC_RELAXATION
    nrcyck     drtol    drfctr    drterm    tssfdr    irelal     edttl    idrflg
     250       0.001    0.995      0.0       0.0        0        0.04       0
*CONTROL_TERMINATION
    endtim    endcyc     dtmin    endeng    endmas
     25.0        0        0.0       0.0       1.0E8
*DATABASE_ABSTAT
    dt    binary     lcur    ioopt
   0.01    0          0       1
*DATABASE_GLSTAT
    dt    binary     lcur    ioopt
   0.01    0          0       1
*DATABASE_NCFORC
    dt    binary     lcur    ioopt
   0.01    0          0       1
*DATABASE_NODOUT
    dt    binary     lcur    ioopt   option1   option2
   0.01    0          0       1       0.0        0
*DATABASE_RCFORC
    dt    binary     lcur    ioopt
   0.01    0          0       1
*DATABASE_BINARY_D3PLOT
    dt      lcdt     beam    npltc    psetid
   0.01    0         0        0        0
    ioopt
     0
*DATABASE_HISTORY_NODE
    id1      id2      id3      id4      id5      id6      id7      id8
     1       50      100      150      200      250      300      350
    400      75      125      175      225      275      325      375
*BOUNDARY_PRESCRIBED_MOTION_NODE_ID
 1End (Z=0) Rotation BC
    nid      dof      vad     lcid       sf      vid    death      birth
     1        7        0        2       1.0       0    1. 0E28     0.0
*BOUNDARY_SPC_SET_ID
 0End (Z=0) BC
    nsid      cid     dofx     dofy     dofz    dofrx    dofry    dofrz
     1        0        1        1        1        0        0        0
*SET_NODE_LIST_TITLE
 End (Z=0) Node
    sid      da1      da2      da3      da4    solver
     1       0.0      0.0      0.0      0.0    MECH
    nid1     nid2     nid3     nid4     nid5     nid6     nid7     nid8
     1        0        0        0        0        0        0        0
```

```
*BOUNDARY_SPC_SET_ID
0End (Z=100) BC
    nsid     cid    dofx    dofy    dofz   dofrx   dofry   dofrz
       2       0       1       1       0       0       0       0
*SET_NODE_LIST_TITLE
 End (Z=100) Node
    sid     da1     da2     da3     da4  solver
      2     0.0     0.0     0.0     0.0    MECH
    nid1    nid2    nid3    nid4    nid5    nid6    nid7    nid8
    400       0       0       0       0       0       0       0
*BOUNDARY_SPC_SET_ID
 0Wall Ends BC
    nsid     cid    dofx    dofy    dofz   dofrx   dofry   dofrz
       4       0       1       1       1       1       1       1
*SET_NODE_LIST_TITLE
 wallBC set
    sid     da1     da2     da3     da4  solver
      4     0.0     0.0     0.0     0.0    MECH
*LOAD_BODY_Y
    lcid      sf  lciddr      xc      yc      zc     cid
       1     1.0       0     0.0     0.0     0.0       0
*LOAD_NODE_POINT
    nid     dof    lcid      sf     cid      m1      m2      m3
    400       3       4    -1.0       0       0       0       0
*CONTACT_AUTOMATIC_NODES_TO_SURFACE_ID
 1Shaft and wall contact
    ssid    msid   sstyp   mstyp  sboxid  mboxid     spr     mpr
       1       2       3       3       0       0       1       1
      fs      fd      dc      vc     vdc  penchk      bt      dt
     0.2     0.1   250.0 12000.0    40.0       0     0.0  1.0E20
     sfs     sfm     sst     mst    sfst    sfmt     fsf     vsf
     1.0     1.0     0.0     0.0     1.0     1.0     1.0     1.0
*PART
 DrillPipe
    pid   secid     mid   eosid    hgid    grav  adpopt    tmid
       1       1       1       0       0       0       0       0
*SECTION_BEAM_TITLE
 beam for shaft
    secid  elform    shrf  qr/irid     cst   scoor     nsm
       1       4     1.0       2       1     0.0     0.0
    ts1     ts2     tt1     tt2
  0.1016  0.1016 0.08484 0.08484
*MAT_PLASTIC_KINEMATIC_TITLE
 plastic kinematic steel
    mid      ro       e      pr    sigy    etan    beta
       1  7850.0  2.1E11     0.3  2.5E8     0.0     0.0
    src     srp      fs      vp
    0.0     0.0     0.0     0.0
*PART
 Wall
    pid   secid     mid   eosid    hgid    grav  adpopt    tmid
       2       2       3       0       0       0       0       0
*SECTION_SHELL_TITLE
 Shell for Wall
    secid  elform    shrf     nip   propt  qr/irid   icomp   setyp
       2       2     1.0       3     1.0       0       0       1
    t1      t2      t3      t4    nloc   marea    idof  edgset
    0.04    0.04    0.04    0.04     0.0     0.0     0.0       0
*MAT_PLASTIC_KINEMATIC_TITLE
 wall01
    mid      ro       e      pr    sigy    etan    beta
       3  5850.0   2.1E8     0.3  2.5E8     0.0     0.0
    src     srp      fs      vp
    0.0     0.0     0.0     0.0
*MAT_RIGID_TITLE
 Rigid
```

```
     mid       ro        e         pr        n      couple        m     alias
       2     7850.0   2.1E11   0.3      0.0      0.0          0.0
     cmo      con1      con2
      0.0        0         0
     lco or a1       a2       a3       v1       v2       v3
      0.0             0.0      0.0      0.0      0.0      0.0
*DEFINE_CURVE_TITLE
Gravity
    lcid     sidr      sfa      sfo     offa     offo    dattyp    lcint
       1        0      1.0      1.0      0.0      0.0        0        0
    a1                o1
    0.0         9.81000042
    25.0         9.81000042
*DEFINE_CURVE_TITLE
Rotation
      lcid     sidr      sfa      sfo     offa     offo    dattyp    lcint
       2        0       1.0      16.0    0.0      0.0        0        0
     a1                o1
    0.0               0.0
    2.0               0.0
   7.0               1.0
   25.0               1.0
*DEFINE_CURVE_TITLE
damping
      lcid     sidr      sfa      sfo     offa     offo    dattyp    lcint
       3        0       1.0      1.0      0.0      0.0        0        0
     a1                o1
     0.0               1.0
    25.0               1.0
*DEFINE_CURVE_TITLE
Axial load Curve
      lcid     sidr      sfa      sfo        offa      offo    dattyp    lcint
       4        0       1.0   150000.0   0.0       0.0        0        0
     a1                o1
     0.0               0.0
     2.0               0.0
     7.0               1.0
     25.0               1.0
*DAMPING_GLOBAL
    lcid    valdmp      stx      sty      stz      srx      sry      srz
       3      0.0     0.01     0.01      0.1     0.01     0.01      0.1
*ELEMENT_SHELL
*ELEMENT_BEAM
*NODE
*END
```